A High-Performance, Catalog-Driven Approach to Light Curve Extraction for Wide-Field Photometric Surveys

By

Robert J. Siverd Jr.

Dissertation

Submitted to the Faculty of the

Graduate School of Vanderbilt University

in partial fulfillment of the requirements

for the degree of

DOCTOR OF PHILOSOPHY

in

Astrophysics

August 9, 2019

Nashville, Tennessee

Approved:

Keivan G. Stassun, Ph.D.

Andreas Berlind, Ph.D.

David Weintraub, Ph.D.

Joshua Pepper, Ph.D.

ACKNOWLEDGMENTS

I'd like to offer special thanks to Dr. Keivan Stassun for the years of advice, supervision, and encouragement without which I could not have come this far. I wish to extend this gratitude to Dr. Andreas Berlind, Dr. Joshua Pepper, and Dr. David Weintraub who have invested significant time and energy to help me reach this far and for helping me develop as a scientist.

I am also extremely grateful for the loving support of family and friends (Mom, Dad, Veronica, and Amanda especially) that has helped keep me going through this years-long journey. I couldn't have done it without you!

This project makes use of data from the KELT survey, including support from The Ohio State University, Vanderbilt University, and Lehigh University, along with the KELT follow-up collaboration. Construction of KELT-N was supported by the National Aeronautics and Space Administration under grant No. NNG04GO70G issued through the Origins of Solar Systems program. KELT-South is hosted by the South African Astronomical Observatory and we are grateful for their ongoing support and assistance.

This work uses observations made at the South African Astronomical Observatory (SAAO). This work includes data taken at The McDonald Observatory of The University of Texas at Austin. This work makes use of observations from the LCOGT network. The TRES and KeplerCam observations were obtained with partial support from the Kepler Mission through NASA Cooperative Agreement NNX11AB99A with the Smithsonian Astrophysical Observatory.

This work has made use of NASA's Astrophysics Data System, the Extrasolar Planet Encyclopedia at exoplanet.eu [Schneider et al., 2011], the NASA Exoplanet Archive, the Exoplanet Orbit Database at exoplanets.org, the SIMBAD database operated at CDS, Strasbourg, France, and the VizieR catalogue access tool, CDS, Strasbourg, France.

We make use of Filtergraph, an online data visualization tool developed at Vander-

bilt University through the Vanderbilt Initiative in Data-intensive Astrophysics (VIDA). We acknowledge with thanks the variable star observations from the AAVSO International Database contributed by observers worldwide and used in this research. This research was made possible through the use of the AAVSO Photometric All-Sky Survey (APASS), funded by the Robert Martin Ayers Sciences Fund and NSF AST-1412587.

We also used data products from the Widefield Infrared Survey Explorer, which is a joint project of the University of California, Los Angeles; the Jet Propulsion Laboratory/California Institute of Technology, which is funded by the National Aeronautics and Space Administration; the Two Micron All Sky Survey, which is a joint project of the University of Massachusetts and the Infrared Processing and Analysis Center/California Institute of Technology, funded by the National Aeronautics and Space Administration and the National Science Foundation; and the European Space Agency (ESA) mission *Gaia* (http://www.cosmos.esa.int/gaia), processed by the *Gaia* Data Processing and Analysis Consortium (DPAC, http://www.cosmos.esa.int/web/gaia/dpac/consortium). Funding for the DPAC has been provided by national institutions, in particular the institutions participating in the *Gaia* Multilateral Agreement. MINERVA is a collaboration among the Harvard-Smithsonian Center for Astrophysics, The Pennsylvania State University, the University of Montana, and the University of New South Wales. MINERVA is made possible by generous contributions from its collaborating institutions and Mt. Cuba Astronomical Foundation, The David & Lucile Packard Foundation, National Aeronautics and Space Administration (EPSCOR grant NNX13AM97A), The Australian Research Council (LIEF grant LE140100050), and the National Science Foundation (grants 1516242 and 1608203). Any opinions, findings, and conclusions or recommendations expressed are those of the author and do not necessarily reflect the views of the National Science Foundation. This work was partially supported by funding from the Center for Exoplanets and Habitable Worlds. The Center for Exoplanets and Habitable Worlds is supported by the Pennsylvania State University, the Eberly College of Science, and the Pennsylvania Space Grant Consortium.

TABLE OF CONTENTS

Appendix

LIST OF TABLES

LIST OF FIGURES

Figure Page

LIST OF ABBREVIATIONS

2MASS	Two Micron All Sky Survey
ADU	Analog-to-Digital Unit
BLS	Boxcar Least-Squares
CCD	Charge-coupled device
CDE	Catalog-Driven Extraction
FITS	Flexible Image Transport System
FWHM	Full-Width at Half Maximum
HDU	(FITS) Header + Data Unit
HWHM	Half-Width at Half Maximum
IQR	Inter-Quartile Range
KELT	Kilodegree Extremely Little Telescope
MAD	Median Absolute Deviation
MAR	Median Absolute Residual
PSF	Point Spread Function
RMS	Root Mean Square
RMSD	Root-Mean-Square Deviation
SNR	Signal-to-Noise Ratio
TFA	Trend Filtering Algorithm

Chapter 1

Introduction

The Kilodegree Extremely Little Telescope project (KELT) is an ongoing nearly-all-sky photometric survey built to discover transiting exoplanets orbiting bright stars. Using small-aperture, wide-field telescopes in Sonoita, AZ, USA and Sutherland, South Africa, KELT is able to monitor $\sim 70\%$ of the sky at $\sim 1\%$ precision for $7.5 < V < 10$ stars at a cadence of 30 - 60 minutes [Pepper et al., 2007, 2012]. Roughly 25 transiting exoplanets have been discovered with this system over its past ten years of operation.

Despite the large quantity of high-quality data obtained and the suitability of these data for many scientific applications, adoption of KELT data into the broader community has been fairly slow. A number of ancillary (non-transiting, non-exoplanet) science projects have used of different KELT data sets but such work usually involves people who have direct connections to members of the KELT team. This is probably a reflection of the proprietary knowledge necessary to extract useful science from KELT data in its common forms. Slight changes to the way we organize and manage our data internally could probably improve this situation significantly and spur wider adoption and use of KELT data within the astronomy community.

Similar changes would likely also have a positive impact on the core KELT mission of exoplanet discovery. For example, inflexibility in how stars and candidates are treated makes it difficult to combine data from the overlapping regions of adjacent fields, reducing discovery power. Related issues arise that limit our ability to identify blends during candidate selection often leads to wasted telescope time in follow-up.

A set of key changes to infrastructure, methods, software, and behavior loosely referred to as "Catalog-Driven Extraction" (CDE hereafter) was devised both in response to the struggles noted above and to a sense of increasing competition for planet discoveries from

other surveys such as TESS and MASCARA (Ricker et al. 2015, Talens et al. 2017c). The implementation of these changes has been my primary focus for nearly a year. With coding nearly complete and initial testing successful, the focus now shifts to identifying the most efficient way to employ these tools. An outline of the remainder of this dissertation follows below.

Chapter 2 describes the first transiting substellar companion discovered by the KELT survey: a 27-Jupiter-mass brown dwarf in a short-period orbit around a rapidly rotating host star. Transiting brown dwarfs are significantly rarer than their Hot Jupiter cousins and were not believed to reside in systems such as this one. In addition to the precise brown dwarf mass and radius measurements, this work also helped illustrate how radial velocity techniques can be used effectively with a rapidly rotating host star. Over time, this technique has become the workhorse method for exoplanet confirmation around hot host stars.

Chapter 3 describes the serendipitous observation of bright, nearby supernova SN2014J by the KELT survey telescope and the extraction of a high-fidelity light curve of the event. The unique combination of high-SNR and high cadence enabled the application of new constraints on the supernova environment.

Chapter 4 details the discovery of the transiting exoplanet KELT-19Ab, a Jupiter-sized planet in a retrograde orbit around a hot, bright, rapidly rotating star with a distant stellar companion. The host itself appears to be a metal-enriched Am star. If that status is confirmed, this would be the first such specimen known to host an exoplanet. Combined with other unusual system properties, this is an excellent candidate for further study.

Chapter 5 describes Catalog-Driven Extraction (CDE), a set of significant changes and improvements to existing KELT survey data management and reduction methods designed to deliver improved data quality and facilitate data sharing with the astronomy community. Chapter 5 begins with a primer on the photometry methods used by the KELT survey and an overview of the shortcomings present in the current (legacy) system. This is followed by an

overview of CDE procedures, detailed descriptions of data processing methods, a description of final data products produced and a final summary of the CDE system improvements. Concluding remarks follow in Chapter 6.

Chapter 2

KELT-1b: a Strongly Irradiated, Highly Inflated, Short Period, 27 Jupiter-Mass Companion Transiting a Mid-F Star

2.1 Introduction

The most information-rich exoplanetary systems are those in which the companion happens to transit in front of its parent star. Transiting systems are enormously useful for enabling detailed measurements of a seemingly endless array of physical properties of extrasolar planets and their host stars (see reviews by Winn 2009, 2010). The most basic properties that can be measured using transiting planets are the planet mass and radius, and so average density. These parameters alone allow for interesting constraints on the internal composition and structure of planets [Guillot, 2005, Fortney et al., 2007a,b, Rogers and Seager, 2010, Miller and Fortney, 2011]. In addition to these basic parameters, transiting planets enable the study of their atmospheres [Seager and Sasselov, 2000, Charbonneau et al., 2002, Vidal-Madjar et al., 2003, Seager and Deming, 2010] and thermal emission [Deming et al., 2005, Charbonneau et al., 2005, Knutson et al., 2008]. They also allow measurement of planetary and stellar oblateness, rotation rate, and spin-orbit alignment [Seager and Hui, 2002, Spiegel et al., 2007, Carter and Winn, 2010, Rossiter, 1924, McLaughlin, 1924, Winn et al., 2005, Gaudi and Winn, 2007]. Transiting planets may also be searched for associated rings and moons [Brown et al., 2001, Barnes and Fortney, 2004, Tusnski and Valio, 2011]. Further, variations in transit timing may indicate the presence of other bodies in the system [Holman and Murray, 2005, Agol et al., 2005, Steffen and Agol, 2005, Ford and Gaudi, 2006, Ford and Holman, 2007, Kipping, 2009]. With sufficiently precise observations, one may constrain the presence of planets with masses smaller than that of the Earth [Agol and Steffen, 2007, Carter and Winn, 2010].

The high scientific value of transiting planet systems motivated the first dedicated wide-

field transit surveys, which by now have identified over 100 transiting systems (TrES, Alonso et al. 2004; XO, McCullough et al. 2006; HATNet, Bakos et al. 2007; SuperWASP, Collier Cameron et al. 2007a, QES, Alsubai et al. 2011). Although there is substantial diversity in their design, strategy, and sensitivity, these surveys can be grossly characterized as having relatively small cameras with apertures of order 10 cm, and detectors with relatively wide fields-of-view of tens of square degrees. These surveys are primarily sensitive to giant, close-in planets with radii $R_P \gtrsim 0.5 R_{\rm Jup}$ and periods of $P \lesssim 10$ d, orbiting relatively bright FGK stars with $V \sim 10-12$.

The space-based missions CoRoT [Baglin, 2003] and Kepler [Borucki et al., 2010] have dramatically expanded the parameter space of transit surveys, enabling the detection of planets with sizes down to that of the Earth and below, planets with periods of several years, and planets orbiting a much broader range of host stars. Furthermore, their large target samples have allowed the detection of rare and therefore interesting planetary systems. These missions have already announced over 50 confirmed planets, and the Kepler mission has announced an additional ~ 2300 candidates [Batalha et al., 2013], most of which are smaller than Neptune. Notable individual discoveries include the first detection of a transiting Super-Earth [Léger et al., 2009], the detection of a 'temperate' gas giant with a relatively long period of ~ 100 days [Deeg et al., 2010], the first multi-planet transiting systems [Steffen et al., 2010, Holman et al., 2010, Latham et al., 2011, Lissauer et al., 2011], the first circumbinary planets [Doyle et al., 2011, Welsh et al., 2012], and the detection of planets with radius of $\lesssim R_\oplus$ [Muirhead et al., 2012, Fressin et al., 2012].

Although Kepler and CoRoT have revolutionized our understanding of the demographics of planets, the opportunities for follow-up of the systems detected by these missions are limited. By design, both missions primarily monitor relatively faint stars with $V \gtrsim 12$. Consequently, many of the follow-up observations discussed above that are generically enabled by transiting systems are not feasible for the systems detected by Kepler and CoRoT. Detailed characterization of the majority of these systems will therefore be difficult or im-

possible. There is thus an ongoing need to discover transiting planets orbiting the bright stars, as well as to increase the diversity of such systems.

All else being equal, the brightest stars hosting transiting planets are the most valuable. Larger photon flux permits more instruments and/or facilities to be employed for follow-up, allows subtler effects to be probed, reduces statistical uncertainties, and generally allows for improved or more extensive calibration procedures that help to control systematic errors. Furthermore, brighter stars are also easier to characterize, and are more likely to have pre-existing information, such as proper motions, parallaxes, metallicities, effective temperatures, angular diameters, and broadband colors.

The majority of the brightest ($V \lesssim 8$) FGK dwarfs in the sky have been monitored using precision radial velocity surveys for many years, and as a result most of the giant planets with periods of less than a few years orbiting these stars have already been discovered (e.g., Wright et al. 2012). A smaller subset of these stars have been monitored over a shorter time baseline with the sensitivity needed to detect Neptune- and SuperEarth-mass planets. Because of the low a priori transit probability for all but short period planets, the transiting systems constitute a very small fraction of this sample. To date, seven planets first discovered via radial velocity have subsequently been discovered to also transit; all of the host stars for these planets are brighter than $V = 9$. Although there are projects that aim to increase this sample [Kane et al., 2009], the overall yield is expected to be small.

Because RV surveys generically require spectroscopic observations that are observationally expensive and must be obtained in series, it is more efficient to discover transiting planets around the much more abundant fainter stars by first searching for the photometric transit signal, and then following these up with targeted RV observations to eliminate false positives and measure the planet mass. However, in order to compensate for the rarity and low duty cycle, many stars must be monitored over a long time baseline. Photometric transit surveys that target brighter stars therefore require larger fields of view. Most of the original transit surveys had fields of view and exposure times that were optimized to de-

tect planets orbiting stars with $V \gtrsim 10$. Indeed, only ~ 20 transiting planets orbiting stars with $V \leq 10$ are currently known (~ 40 with $V \lesssim 11$). Of those with $V \leq 10$, $\sim 40\%$ were originally detected by RV surveys.

The Kilodegree Extremely Little Telescope-North (KELT-North) transit survey [Pepper et al., 2007] was designed to detect giant, short-period transiting planets orbiting the brightest stars that are not readily accessible to RV surveys. Pepper et al. [2003] determined the optimal hardware setup specifically to detect transiting planets orbiting stars with $V \sim 8-10$, and based on the specified design requirements in that paper, the KELT-North survey telescope system was constructed using off-the-shelf, high-end consumer equipment. In fact, as the current detection demonstrates, KELT has exceeded its design goals, and is sensitive to transiting systems in some favorable cases down to $V \sim 12$.

In addition to the goal of filling in the magnitude gap between radial velocity and other transit surveys, the KELT-North survey also has the potential to detect fainter systems with $V \gtrsim 10$ that are in the magnitude range of previous surveys, but were missed or overlooked for various reasons. The detection discussed in this paper is an example of this opportunity. Here the fact that the KELT-North survey is only now starting to vet candidates, more than eight years after the first candidates were announced by other transit surveys, can be seen an advantage. In particular, previous surveys have established the existence of massive brown dwarf companions [Deleuil et al., 2008, Irwin et al., 2010, Bouchy et al., 2011b, Johnson et al., 2011, Bouchy et al., 2011a], and have demonstrated the feasibility of detecting low-mass companions to hot, rapidly rotating stars [Collier Cameron et al., 2010a]. Partially in response to these results, the KELT-North survey deliberately broadened our search targets to include hot and/or rapidly-rotating stars, which were previously neglected by many transit surveys. The evolving perception of what kinds of stars constitute viable transit search targets played an interesting role in the discovery of KELT-1b, as discussed in §2.3.2.

The KELT-North survey has been collecting data since September 2006, and has ac-

quired a sufficient number of high-quality images to detect transit candidates. We have been systematically identifying and vetting transit candidates since February 2011, and in this paper we report our first confirmed low-mass transiting companion, which we designate KELT-1b. KELT-1b has a mass of ~ 27 M_J, and we will therefore follow convention and refer to it as a 'brown dwarf' throughout the majority of this paper. However, as we discuss in §2.6.1, we are, in fact, agnostic about its true nature and therefore how it should be categorized.

The outline of this paper is as follows. In order to introduce the survey and provide the appropriate context for our discovery, in §2.2 we summarize the properties of the KELT-North survey and our procedure for candidate selection. In §2.3 we review the observations of KELT-1, starting with the properties of the candidate in the KELT-North data, and then summarize the follow-up photometry, spectroscopy, and high-contrast imaging. §2.5 describes our analysis and characterization of the host star and its substellar companion. In §2.6 we provide a speculative discussion of the possible implications of this unique system for theories of the emplacement and tidal evolution of short-period substellar companions, models of the structure and atmosphere of brown dwarfs, and the demographics of substellar companions to stars. We briefly summarize in §2.7.

For quick reference, Table 2.1 lists the values of the light curve statistics used to select KELT candidates, Table 2.2 provides a summary of the observations of the KELT-1 system, Table 2.3 lists various collected properties and measurements of the KELT-1 host star, Table 2.4 lists median values and 68% confidence intervals for the physical and orbital parameters of the KELT-1 system, Table 2.5 lists median values and 68% confidence intervals for the light curve and radial velocity parameters of the KELT-1 system, Table 2.6 lists the inferred transit times, Tables 2.7 and 2.8 list the radial velocity and bisector measurements, and Tables 2.9-2.17 list the photometric measurements.

Table 2.1: KELT-North BLS Candidate Selection Criteria

Signal Detection Efficiency	SDE>7.0	Depth	$\delta < 0.05$
Signal to Pink-noise	SPN>7.0	χ^2 ratio	$\frac{\Delta\chi^2}{\Delta\chi^2_-} > 1.5$
Fraction from one night	$f_{1n} < 0.8$	Duty cycle	$q < 0.1$

Table 2.2: Summary of KELT-1 Observations

Observatory	UT Dates	No. of Obs	Wavelength	Section; Table
Photometry, Transit:				
PvdKO	2011-12-03 –– 2011-12-04	151	i	§2.3.4.1; T2.9
ULMO	2011-12-03 –– 2011-12-04	110	r	§2.3.4.2; T2.10
HAO	2011-12-10	266	i	§2.3.4.3; T2.11
FLWO	2011-12-16	362	z	§2.3.4.4; T2.12
ULMO	2011-12-31 –– 2012-01-01	162	r	§2.3.4.2; T2.13
FLWO	2012-01-07	459	i	§2.3.4.4; T2.14
Photometry, Secondary Eclipse:				
ULMO	2011-12-02	115	i	§2.3.4.2
FTN/LCOGT	2011-12-30	72	PS-Z[a]	§2.3.4.5
ULMO	2012-01-04	121	i	§2.3.4.2
Spectroscopy, Orbit:				
FLWO/TRES	2011-11-09 –– 2012-02-05	23	3900-8900Å	§2.3.3; T2.7
Spectroscopy, Rossiter-McLaughlin:				
FLWO/TRES	2012-01-07	42	3900-8900Å	§2.3.3; T2.8
Adaptive Optics Imaging:				
Keck/NIRC2	2012-01-07		H, K'	§2.3.5

Notes:
ULMO: University of Louisville Moore Observatory;
PvdKO: Peter van de Kamp Observatory;
HAO: Hereford Arizona Observatory;
FLWO: Fred Lawrence Whipple Observatory;
FTN: Faulkes Telescope North;
LCOGT: Las Cumbres Observatory Global Telescope Network;
[a] Pan-STARRS-Z

Table 2.3: KELT-1 Stellar Properties

Parameter	Description (Units)	Value	Source	Ref.
Names		TYC 2785-2130-1		
		GSC 02785-02130		
		2MASS J00012691+3923017		
α_{J2000}		00:01:26.92	Tycho	1
δ_{J2000}		+39:23:01.7	Tycho	1
B_T		11.363 ± 0.065	Tycho-2	2
V_T		10.701 ± 0.057	Tycho-2	2
J		9.682±0.022	2MASS	3
H		9.534±0.030	2MASS	3
K		9.437±0.019	2MASS	3
WISE1		12.077±0.022	WISE	4
WISE2		12.732±0.020	WISE	4
WISE3		14.655±0.030	WISE	4
μ_α	Proper Motion in RA (mas yr^{-1})	-10.1 ± 0.7	NOMAD	5
μ_δ	Proper Motion in Dec. (mas yr^{-1}) ...	-9.4 ± 0.7	NOMAD	5
γ_{abs}	Absolute Systemic RV (km s^{-1})	-14.2 ± 0.2	This Paper	
.....	Spectral Type	F5±1	This Paper	
d	Distance (pc)	263 ± 14	This Paper	
.....	Age (Gyr)	1.75 ± 0.25	This Paper	
A_V	Visual Extinction	0.18 ± 0.10	This Paper	
(U^a, V, W)	Galactic Space Velocities (km s^{-1}) ...	(19.9±1.1,-9.6±0.5, -2.6±0.9)	This Paper	
M_{cz}	Mass of Convective Zone ($M_\odot$)	$[2.8 \pm 0.4] \times 10^{-4}$	This Paper	
R_{cz}	Base of the Convective Zone ($R_\odot$) ...	1.31 ± 0.03	This Paper	
C_*	Total Moment of Inertia (cgs)	$[1.18 \pm 0.04] \times 10^{54}$	This Paper	
C_{cz}	Convection Zone Moment of Inertia (cgs)	$[3.2 \pm 0.7] \times 10^{51}$	This Paper	

(1) Hog et al. [1998]; (2) Høg et al. [2000]; (3) Skrutskie et al. [2006], Cutri et al. [2003a];
(4) Wright et al. [2010], Cutri and et al. [2012b]; (5) Zacharias et al. [2004].
[a] We adopt a right-handed coordinate system such that positive U is toward the Galactic center.

Table 2.4: Median values and 68% confidence intervals for the Physical and Orbital Parameters of the KELT-1 System

Variable	Description (Units)	Value ($e \neq 0$)	Value ($e \equiv 0$)
Stellar Parameters:			
M_* .	Mass ($M_\odot$)	1.335 ± 0.063	1.332 ± 0.063
R_* .	Radius ($R_\odot$)	$1.471^{+0.045}_{-0.035}$	$1.460^{+0.039}_{-0.030}$
L_* ..	Luminosity ($L_\odot$)	$3.51^{+0.25}_{-0.21}$	$3.46^{+0.23}_{-0.19}$
ρ_* ..	Density (cgs)	$0.594^{+0.027}_{-0.042}$	$0.608^{+0.019}_{-0.039}$
$\log g$.	Surface gravity (cgs)	$4.228^{+0.014}_{-0.021}$	$4.234^{+0.012}_{-0.018}$
$T_{\rm eff}$.	Effective temperature (K) ...	6516 ± 49	6516 ± 49
[Fe/H]	Metallicity	0.052 ± 0.079	0.052 ± 0.073
$v \sin I_*$	Rotational velocity (m s^{-1}) ..	56000 ± 2000	56000 ± 2000
λ ..	Spin-orbit alignment (degrees) .	2 ± 16	1 ± 15
Planetary Parameters:			
e ..	Eccentricity	$0.0100^{+0.010}_{-0.0070}$	$--$
ω_* .	Argument of periastron (degrees)	65^{+72}_{-74}	$--$
P ..	Period (days)	1.217513 ± 0.000015	1.217513 ± 0.000015
a ..	Semi-major axis (AU)	0.02472 ± 0.00039	0.02470 ± 0.00039
M_P .	Mass (M_J)	27.38 ± 0.93	27.37 ± 0.92
R_P .	Radius (R_J)	$1.116^{+0.038}_{-0.029}$	$1.108^{+0.034}_{-0.025}$
ρ_P .	Density (cgs)	$24.5^{+1.5}_{-2.1}$	$25.0^{+1.3}_{-1.9}$
$\log g_P$	Surface gravity	$4.736^{+0.017}_{-0.025}$	$4.743^{+0.014}_{-0.022}$
T_{eq} .	Equilibrium temperature (K) ..	2423^{+34}_{-27}	2416^{+30}_{-24}
Θ ..	Safronov number	$0.907^{+0.028}_{-0.032}$	$0.915^{+0.024}_{-0.028}$
$\langle F \rangle$.	Incident flux (10^9 erg s^{-1} cm^{-2})	$7.83^{+0.45}_{-0.34}$	$7.73^{+0.39}_{-0.30}$

2.2 The KELT-North Survey

Because this is the first paper from the KELT-North survey, we describe the survey, selection criteria, and follow-up observations and reduction methodology in some detail. Readers who are not interested in these details, but are rather primarily interested in the properties and implications of the KELT-1b system, can skip to §2.5.

2.2.1 KELT-North Instrumentation and Survey Strategy

The KELT-North survey instrument consists of a collection of commercially-available equipment, chosen to meet the requirements of Pepper et al. [2003] and tuned to find the few brightest stars with transiting planets in the Northern sky. The optical system consists of an Apogee AP16E (4K x 4K 9μm pixels) thermo-electrically cooled CCD camera attached using a custom mounting plate to a Mamiya camera lens with 80mm focal length and 42mm aperture (f/1.9). The resultant field of view of the detector is $26^\circ \times 26^\circ$ at roughly $23''$per pixel, allowing simultaneous observation of nearly 40,000 stars in typical high Galactic latitude fields. The medium-format image size is markedly larger than the CCD detector (which measures 37×37mm) which greatly reduces the severity of vignetting across the large field of view. At the same time, the small aperture permits longer exposures, which improve observing efficiency (assuming fixed camera read-out time). A Kodak Wratten #8 red-pass filter is mounted in front of the lens to further reduce the impact of atmospheric reddening (which primarily affects blue wavelengths) on our photometry. The resultant bandpass resembles a widened Johnson-Cousins *R*-band. This optical system is mounted atop a Paramount ME robotic mount from Software Bisque on a fixed pier at Winer Observatory in Sonoita, AZ (Latitude $31^\circ\ 39'56.08''$N, Longitude $110^\circ\ 36'06.42''$W, elevation 1515.7 meters). See Pepper et al. [2007] for additional details about the system hardware.

The primary KELT-North transit survey consists of 13 fields centered at 31.7° dec-

Table 2.5: Median values and 68% confidence intervals for the Lighcurve and Radial Velocity Parameters of the KELT-1 System

Parameter	Description (Units)	Value
RV Parameters:		
T_C ...	Time of inferior conjunction (BJD_{TDB})	$2455914.1628^{+0.0023}_{-0.0022}$
T_P ...	Time of periastron (BJD_{TDB})	$2455914.08^{+0.24}_{-0.25}$
K ...	RV semi-amplitude ($m\ s^{-1}$)	4239 ± 52
K_R ...	RM amplitude ($m\ s^{-1}$)	343 ± 13
$M_P \sin i$.	Minimum mass (M_J)	27.34 ± 0.92
M_P/M_* .	Mass ratio	0.01959 ± 0.00040
u....	RM linear limb darkening	$0.5861^{+0.0046}_{-0.0043}$
γ_0 ...	zero point for Orbital RVs (Table 2.7) ($m\ s^{-1}$) .	-14200 ± 49 (stat.)$\pm$200 (sys.)
γ_1 ...	zero point for RM RVs (Table 2.8) ($m\ s^{-1}$) ..	-14200^{+56}_{-59} (stat.)$\pm$200 (sys.)
$e \cos \omega_*$.	.....	$0.0019^{+0.0091}_{-0.0060}$
$e \sin \omega_*$.	.....	$0.0044^{+0.011}_{-0.0063}$
$f(m1,m2)$	Mass function (M_J)	0.01006 ± 0.00037
Transit Parameters:		
R_P/R_* .	Radius of the planet in stellar radii	$0.07806^{+0.00061}_{-0.00058}$
a/R_* ..	Semi-major axis in stellar radii	$3.619^{+0.055}_{-0.087}$
i....	Inclination (degrees)	$87.6^{+1.4}_{-1.9}$
b....	Impact parameter	$0.150^{+0.11}_{-0.088}$
δ....	Transit depth	$0.006093^{+0.000096}_{-0.000090}$
T_{FWHM} .	FWHM duration (days)	0.10645 ± 0.00045
τ....	Ingress/egress duration (days)	$0.00873^{+0.00049}_{-0.00020}$
T_{14} ...	Total duration (days)	$0.11526^{+0.00069}_{-0.00059}$
P_T ...	A priori non-grazing transit probability	$0.2564^{+0.0079}_{-0.0055}$
$P_{T,G}$ ..	A priori transit probability	$0.2998^{+0.0093}_{-0.0065}$
$T_{C,0}$ ..	transit time for PvdKO UT 2011-12-03 (BJD_{TDB})	2455899.5549 ± 0.0010
$T_{C,1}$ ..	transit time for ULMO UT 2011-12-03 (BJD_{TDB})	$2455899.55408 \pm 0.00044$
$T_{C,2}$ ..	transit time for HAO UT 2011-12-10 (BJD_{TDB})	$2455905.63860^{+0.00084}_{-0.00082}$
$T_{C,3}$ ..	transit time for FLWO UT 2011-12-16 (BJD_{TDB})	$2455911.72553 \pm 0.00045$
$T_{C,4}$ ..	transit time for ULMO UT 2011-12-31 (BJD_{TDB})	$2455927.55574^{+0.00040}_{-0.00042}$
$T_{C,5}$ ..	transit time for FLWO UT 2012-01-07 (BJD_{TDB})	$2455933.64320^{+0.00041}_{-0.00039}$
$u_{1Sloani}$.	linear limb-darkening coefficient	$0.2146^{+0.0046}_{-0.0042}$
$u_{2Sloani}$.	quadratic limb-darkening coefficient	$0.3170^{+0.0038}_{-0.0033}$
$u_{1Sloanr}$.	linear limb-darkening coefficient	$0.2865^{+0.0052}_{-0.0045}$
$u_{2Sloanr}$.	quadratic limb-darkening coefficient	$0.3274^{+0.0032}_{-0.0026}$
$u_{1Sloanz}$.	linear limb-darkening coefficient	$0.1646^{+0.0044}_{-0.0041}$
$u_{2Sloanz}$.	quadratic limb-darkening coefficient	$0.3074^{+0.0031}_{-0.0028}$
Secondary Eclipse Parameters:		
T_S ...	Time of eclipse (BJD_{TDB})	$2455913.5559^{+0.0063}_{-0.0050}$
b_S ...	Impact parameter	$0.152^{+0.12}_{-0.089}$
$T_{S,FWHM}$	FWHM duration (days)	$0.1074^{+0.0023}_{-0.0014}$
τ_S ...	Ingress/egress duration (days)	$0.00886^{+0.00052}_{-0.00029}$
$T_{S,14}$ ..	Total duration (days)	$0.1164^{+0.0026}_{-0.0017}$
P_S ...	A priori non-grazing eclipse probability	$0.2529^{+0.0059}_{-0.0026}$
$P_{S,G}$ ..	A priori eclipse probability	$0.2957^{+0.0071}_{-0.0031}$

Table 2.6: KELT-1b Transit Times

Epoch	T_C	σ_{T_C}	O-C	(O-C)/σ_{T_C}	Obs.
-8	2455899.55496	88	187.11	2.11	PvdKO
-8	2455899.55407	37	110.56	2.96	ULMO
-3	2455905.63858	72	-147.70	-2.04	HAO
2	2455911.72553	38	-196.27	-5.10	FLWO
15	2455927.55574	35	37.52	1.05	ULMO
20	2455933.64320	34	34.05	0.98	FLWO

Table 2.7: KELT-1 Orbital Radial Velocities and Bisectors

BJD_{TDB}	RV ($m\,s^{-1}$)	σ_{RV} ($m\,s^{-1}$)	Bisector ($m\,s^{-1}$)	σ_{BS} ($m\,s^{-1}$)
2455874.861355	-10305.7	193.3	103.9	152.2
2455876.751353	-18142.8	182.9	121.5	106.7
2455884.783908	-10927.0	275.9	189.6	90.1
2455885.723564	-10514.3	238.3	56.0	140.3
2455887.750071	-18276.1	213.7	75.6	130.1
2455888.709891	-16515.4	173.4	-61.1	117.0
2455900.658271	-11719.3	222.0	-55.7	84.4
2455901.773451	-10631.5	366.7	-41.6	108.3
2455904.764448	-18413.6	180.2	-29.4	124.5
2455905.598058	-13110.9	190.2	127.0	74.8
2455911.618841	-11898.5	240.3	165.9	84.3
2455912.633163	-10246.8	325.6	-33.0	160.8
2455930.604440	-13935.0	216.2	67.7	74.6
2455931.588925	-18254.2	210.1	131.8	46.3
2455932.584867	-17274.7	190.9	-158.3	75.2
2455934.572100	-10040.1	248.2	-53.4	82.5
2455935.671466	-11233.9	334.9	-293.1	130.6
2455936.607043	-16403.1	307.3	-34.7	209.3
2455937.570378	-18296.0	156.2	4.3	68.5
2455940.565265	-10305.4	224.9	-210.3	102.9
2455957.622238	-10005.3	267.8	-123.9	97.2
2455960.657124	-17866.6	297.0	10.2	171.4
2455962.599920	-9968.9	235.1	9.8	121.1

Notes. Radial velocities and bisector spans with uncertainties for spectra taken with TRES at FLWO on nights outside of transit. Times are for mid-exposure and are in the BJD_{TDB} standard [Eastman et al., 2010]. RVs are approximately on an absolute scale, and the uncertainties have been scaled based on a global fit to the data. See §2.3.3 and §2.5.2 for details.

Table 2.8: KELT-1 RM Radial Velocities and Bisectors

BJD_{TDB}	RV ($m\,s^{-1}$)	σ_{RV} ($m\,s^{-1}$)	Bisector ($m\,s^{-1}$)	σ_{BS} ($m\,s^{-1}$)
2455933.561465	12352.9	180.5	53.5	109.8
2455933.565146	12544.0	215.7	178.0	141.5
2455933.568838	12660.8	201.8	10.2	145.3
2455933.573282	12565.8	190.2	218.3	130.1
2455933.576973	12906.4	159.9	91.7	122.5
2455933.580654	12948.6	214.2	11.1	151.7
2455933.585237	12884.8	167.9	78.0	124.5
2455933.588917	12709.2	152.7	211.0	149.3
2455933.592609	12922.4	180.6	59.1	108.3
2455933.596983	12893.1	154.8	50.0	134.5
2455933.600664	12591.3	112.0	74.2	81.3
2455933.604355	13057.7	190.5	34.8	113.6
2455933.608765	13254.4	93.4	266.9	129.1
2455933.612457	12858.8	135.4	4.4	122.2
2455933.616137	13326.5	111.8	90.8	63.0
2455933.621194	13524.8	152.7	148.1	114.1
2455933.624875	13718.2	128.5	53.1	99.4
2455933.628555	13756.6	139.9	19.5	137.3
2455933.633034	13880.6	138.6	22.5	115.4
2455933.636714	13844.8	115.0	177.2	130.4
2455933.640406	14203.6	131.7	45.2	124.7
2455933.645035	14292.8	142.4	0.4	82.1
2455933.648715	14320.5	144.9	20.9	88.2
2455933.652396	14319.4	172.8	188.0	86.4
2455933.656869	14520.7	147.6	10.8	87.1
2455933.660555	14793.0	136.8	234.2	104.5
2455933.664235	14810.5	126.0	117.8	71.0
2455933.668887	14923.9	135.6	183.6	88.4
2455933.672567	15059.7	172.7	37.9	136.2
2455933.676248	15021.1	103.3	21.6	112.4
2455933.680761	15430.5	139.5	211.8	76.4
2455933.684453	15333.1	180.1	82.2	198.6
2455933.688133	15296.7	140.7	52.1	108.0
2455933.692820	15561.8	155.9	164.2	135.4
2455933.696501	15374.8	205.1	237.5	142.5
2455933.700192	15283.4	311.1	699.1	412.4
2455933.704648	15615.1	144.2	157.8	119.1
2455933.708340	15314.0	217.0	54.8	133.8
2455933.712020	15762.7	218.2	181.9	114.5
2455933.716464	15772.2	218.7	206.9	147.1
2455933.720145	16075.3	179.0	245.7	210.6
2455933.723836	15779.8	181.1	33.8	160.4

Radial velocities and bisector spans with uncertainties for spectra taken with TRES at FLWO on the night of the primary transit on UT 2012-01-07. Times are for mid-exposure and are in the BJD_{TDB} standard [Eastman et al., 2010]. RVs are approximately on an absolute scale, and the uncertainties have been scaled based on a global fit to the data. See §2.3.3 and §2.5.2 for details.

Table 2.9: Relative Photometry from PvdKO on UT 2011 December 03 (i)

BJD_{TDB}	Relative Flux	Uncertainty
2455899.454080	1.00112	0.00177
2455899.455342	0.99986	0.00177
2455899.456603	0.99606	0.00206
2455899.457865	0.99556	0.00218
2455899.459138	1.00147	0.00192
2455899.460399	0.99946	0.00163
2455899.461661	0.99686	0.00162
2455899.462934	1.00004	0.00190
2455899.464207	1.00294	0.00221
2455899.465468	0.99780	0.00175

This photometry has been corrected for a linear trend with air mass, and normalized by the fitted out-of-transit flux. See §2.5.2. This table is published in its entirety in the electronic edition. A portion is shown here for guidance regarding its form and content.

Table 2.10: Relative Photometry from ULMO on UT 2011 December 03 (r)

BJD_{TDB}	Relative Flux	Uncertainty
2455899.475596	1.00155	0.00091
2455899.476984	1.00058	0.00091
2455899.478361	0.99852	0.00089
2455899.479738	1.00015	0.00091
2455899.481115	1.00175	0.00089
2455899.482493	1.00039	0.00089
2455899.483870	1.00020	0.00089
2455899.485259	1.00144	0.00089
2455899.486636	0.99967	0.00089
2455899.488014	1.00099	0.00091

This photometry has been corrected for a linear trend with air mass, and normalized by the fitted out-of-transit flux. See §2.5.2. This table is published in its entirety in the electronic edition. A portion is shown here for guidance regarding its form and content.

Table 2.11: Relative Photometry from HAO on UT 2011 December 10 (i)

BJD_{TDB}	Relative Flux	Uncertainty
2455905.540572	0.99833	0.00250
2455905.541132	0.99667	0.00250
2455905.541712	1.00321	0.00252
2455905.542272	1.00209	0.00243
2455905.542842	1.00116	0.00243
2455905.543412	0.99931	0.00243
2455905.543972	1.00078	0.00243
2455905.544542	0.99829	0.00242
2455905.545112	0.99994	0.00243
2455905.545692	0.99800	0.00250

This photometry has been corrected for a linear trend with air mass, and normalized by the fitted out-of-transit flux. See §2.5.2. This table is published in its entirety in the electronic edition. A portion is shown here for guidance regarding its form and content.

Table 2.12: Relative Photometry from FLWO on UT 2011 December 16 (z)

BJD_{TDB}	Relative Flux	Uncertainty
2455911.612185	1.00109	0.00154
2455911.612983	1.00230	0.00154
2455911.613516	1.00009	0.00154
2455911.614002	1.00177	0.00154
2455911.614488	0.99899	0.00154
2455911.615078	1.00118	0.00154
2455911.615564	1.00159	0.00154
2455911.616051	0.99953	0.00154
2455911.616560	1.00155	0.00154
2455911.617081	1.00066	0.00154

This photometry has been corrected for a linear trend with air mass, and normalized by the fitted out-of-transit flux. See §2.5.2. This table is published in its entirety in the electronic edition. A portion is shown here for guidance regarding its form and content.

Table 2.13: Relative Photometry from ULMO on UT 2011 December 31 (r)

BJD_{TDB}	Relative Flux	Uncertainty
2455927.468704	0.99844	0.00145
2455927.470335	0.99820	0.00125
2455927.471713	0.99925	0.00116
2455927.473090	1.00005	0.00105
2455927.474467	0.99994	0.00099
2455927.475844	1.00105	0.00092
2455927.477233	0.99940	0.00090
2455927.478610	1.00084	0.00086
2455927.479987	0.99960	0.00086
2455927.481365	0.99849	0.00084

This photometry has been corrected for a linear trend with air mass, and normalized by the fitted out-of-transit flux. See §2.5.2. This table is published in its entirety in the electronic edition. A portion is shown here for guidance regarding its form and content.

Table 2.14: Relative Photometry from FLWO on UT 2012 January 7 (i)

BJD_{TDB}	Relative Flux	Uncertainty
2455933.568776	1.00164	0.00184
2455933.569101	0.99893	0.00184
2455933.569459	1.00032	0.00184
2455933.569830	1.00046	0.00184
2455933.570200	0.99947	0.00184
2455933.570536	1.00032	0.00184
2455933.570871	1.00131	0.00184
2455933.571195	1.00074	0.00184
2455933.571531	0.99764	0.00184
2455933.571867	1.00003	0.00184

This photometry has been corrected for a linear trend with air mass, and normalized by the fitted out-of-transit flux. See §2.5.2. This table is published in its entirety in the electronic edition. A portion is shown here for guidance regarding its form and content.

Table 2.15: Relative Photometry from ULMO on UT 2011 December 2 (i)

BJD_{TDB}	Relative Flux	Uncertainty
2455897.65499	1.00097	0.00145
2455897.65721	0.99944	0.00134
2455897.65859	0.99993	0.00140
2455897.65997	0.99930	0.00141
2455897.66134	1.00078	0.00140
2455897.66273	1.00023	0.00138
2455897.66411	1.00137	0.00134
2455897.66549	0.99971	0.00138
2455897.66686	0.99978	0.00140
2455897.66824	0.99970	0.00140

This photometry has been normalized and corrected for a linear trend with time. See §2.5.4. This table is published in its entirety in the electronic edition. A portion is shown here for guidance regarding its form and content.

Table 2.16: Relative Photometry from FTN/LCOGT on UT 2011 December 30 (PS-Z)

BJD_{TDB}	Relative Flux	Uncertainty
2455925.730250	0.99855	0.00078
2455925.731230	1.00045	0.00078
2455925.732210	0.99953	0.00078
2455925.733190	1.00032	0.00078
2455925.734190	1.00069	0.00078
2455925.735170	1.00000	0.00078
2455925.739770	1.00089	0.00078
2455925.740700	0.99925	0.00078
2455925.741670	0.99874	0.00078
2455925.742660	0.99933	0.00078

This photometry has been normalized and corrected for a linear trend with time. See §2.5.4. This table is published in its entirety in the electronic edition. A portion is shown here for guidance regarding its form and content.

Table 2.17: Relative Photometry from ULMO on UT 2012 January 4 (*i*)

BJD_{TDB}	Relative Flux	Uncertainty
2455930.50268	1.00020	0.00111
2455930.50487	1.00126	0.00110
2455930.50624	0.99911	0.00110
2455930.50762	0.99970	0.00111
2455930.50901	1.00139	0.00116
2455930.51039	1.00146	0.00111
2455930.51177	0.99958	0.00111
2455930.51314	1.00016	0.00111
2455930.51452	1.00098	0.00111
2455930.51590	1.00085	0.00111

This photometry has been normalized and corrected for a linear trend with time. See §2.5.4. This table is published in its entirety in the electronic edition. A portion is shown here for guidance regarding its form and content.

lination, spanning all 24 hours of right ascension. Including the slight overlap between fields, the total survey area is $\approx 40\%$ of the Northern sky. Survey observations consist of 150-second exposures with a typical per-field cadence of 15-30 minutes. The KELT-North telescope has been collecting survey data in this manner since September 2006, and to date has acquired between 5000 and 9300 images per field. Given this quantity of data and the typical achieved photometric precision of $\sim 1\%$ for $V \lesssim 11$, the KELT-North survey is able to detect short-period giant transiting planets orbiting most FGK stars with magnitudes from saturation near $V \sim 8$ down to $V \sim 12$.

2.2.2 KELT-North Pipeline

Relative photometry is generated from flat-fielded images using the ISIS image subtraction package (Alard and Lupton 1998, Alard 2000, see also Hartman et al. 2004), in combination with point-spread function fitting using the stand-alone DAOPHOT II [Stetson, 1987, 1990]. Although highly effective, the image subtraction procedures are highly computer-intensive. To improve reduction performance, the default ISIS scripts were modified to facilitate distributed image reduction across many computers in parallel. ISIS oper-

ation in this fashion permits thorough exploration of various reduction parameters, which would be intractable if executed serially. Other elements of the ISIS reduction package have also been modified or replaced with more robust alternatives. For example, the standard ISIS source-identification routines and utilities are ill-equipped to deal with the nature and ubiquity of aberrations in KELT-North images. In response, we have replaced the ISIS 'extract' utility with the popular SExtractor program [Bertin and Arnouts, 1996]. A more complete explanation of these modifications and driver scripts that implement them are available online[1].

2.2.3 KELT-North Candidate Selection

Once we have the light curves created by ISIS for all of the DAOPHOT-identified point sources in the reference image, we begin a series of post-processing steps before doing the initial candidate selection. To begin, we convert the ISIS light curves from differential flux to instrumental magnitude using the results of the DAOPHOT photometry on the reference image. We also apply 5σ iterative clipping to all of the light curves at this stage; this typically removes $\sim 0.6\%$ of the data points. All of the uncertainties for the converted and clipped light curves in a given field are then scaled as an ensemble. The scaling is chosen such that the $\chi^2/\mathrm{dof} = 1$ for the main locus of the light curves on a magnitude versus χ^2/dof plot. Typically this scaling is around a factor of 1.2, implying that the uncertainties are somewhat underestimated.

We next attempt to match all of the DAOPHOT-identified point sources in the reference image to stars in the Tycho-2 catalog. We obtain a full-frame WCS with sub-pixel accuracy on our reference frame using Astrometry.net [Lang et al., 2010]. Using this solution, we match stars by taking the closest Tycho-2 entry within $45''$. This typically generates matches for 98% of the Tycho-2 stars within each field. A successful Tycho-2 match also will provide a 2MASS ID. We use the proper motions and JHK apparent magnitudes from

[1] http://astro.phy.vanderbilt.edu/~siverdrj/soft/is3/index.html

these two catalogs.

We next attempt to match all of the DAOPHOT-identified point sources in the reference image to stars in the Tycho-2 catalog. We obtain a full-frame WCS with sub-pixel accuracy on our reference frame using Astrometry.net [Lang et al., 2010]. Using this solution, we match stars by taking the closest Tycho-2 entry within 45″. This typically generates matches for 98% of the Tycho-2 stars within each field. A successful Tycho-2 match also will provide a 2MASS ID. We use the proper motions and JHK apparent magnitudes from these two catalogs.

With this catalog information, we next identify and exclude giant stars by means of a reduced proper motion (H_J) diagram [Gould and Morgan, 2003]. Following the specific prescription of Collier Cameron et al. [2007c], we place each of our matched stars on a J vs. H_J plot. We compute the reduced proper motion of a star as

$$H_J = J + 5\log(\mu/\text{mas yr}^{-1}) \tag{2.1}$$

and determine the star to be a giant if it fails to satisfy

$$\begin{aligned} H_J \quad > \quad & -141.25(J-H)^4 + 473.18(J-H)^3 \\ & -583.6(J-H)^2 + 313.42(J-H) - 43.0 \end{aligned} \tag{2.2}$$

This process leaves us with anywhere from 10,000 to 30,000 catalog-matched putative dwarf stars and subgiants (hereafter dwarfs) per field, depending primarily on the location of the field relative to the Galactic plane.

The dwarfs are then run through the Trend Filtering Algorithm [TFA, Kovács et al., 2005][2] to reduce systematic noise. We select a new set of detrending stars for each light curve by taking the 150 closest stars – outside of a 20 pixel exclusion zone centered on

[2]We used the versions of TFA and BLS (described later) found in the VARTOOLS package [Hartman et al., 2008].

the star being detrended – that are within two instrumental magnitudes of the star being detrended.

KELT's Paramount ME is a German Equatorial mount, which requires a "flip" as it tracks stars past the meridian. Therefore, the optics and detector are rotated 180 degrees with respect to the stars between observations in the Eastern and Western hemispheres, and detector defects, optical distortions, PSF shape, flat fielding errors, etc., for a given star can be completely different. This requires us to treat observations in the East and West essentially as two separate instruments. Thus the preceding steps (magnitude conversion, error scaling, dwarf identification, TFA) are each performed separately on the East and West images of each field. After the dwarf stars in the East and West have been run through TFA, we then combine the two light curves of each target into one East+West light curve. We first match stars from the East and the West pointings by their Tycho IDs, and then determine the error-weighted scaling factor of the Western light curve needed to match the error-weighted mean instrumental magnitude of the East light curve.

All of the light curves from the matched Tycho dwarf stars in a field are given an internal ID. We next search the combined East+West light curves of the dwarfs for transit-like signals using the box-fitting least squares algorithm (BLS; Kovács et al. 2002). We use a custom version of BLS modified to skip over integer and half integer multiples of the sidereal day to reduce the effect of spurious signals due to diurnal systematics and their aliases on the BLS statistics. We perform selection cuts along six of the statistics that are output by the VARTOOLS implementation of the BLS algorithm: signal detection efficiency SDE, signal to pink noise SPN[3], the fraction of transit points from one night f_{1n}, depth δ, the ratio of $\Delta\chi^2$ for the best transit model to best inverse transit model $\Delta\chi^2/\Delta\chi^2_-$ [Burke et al., 2006], and the fraction of the orbit spent in transit or duty cycle q. In order to determine the appropriate threshold values for these statistics, we injected realistic transit signals with a range of properties into a large sample of light curves, and then attempted to

[3]See Kovács et al. [2002] and Hartman et al. [2009], respectively, for the definitions of SDE and SPN

recover these using the BLS algorithm. We then determined the values of these statistics that roughly maximize the overall detection efficiency while minimizing the number of spurious detections. The final adopted values are given in Table 2.1.

In addition to the cuts we make on the BLS statistics, we also impose restrictions on the effective temperature and inferred density of the candidate host stars. For the temperature, we require that $T_{\rm eff} < 7500$K. We calculate the stellar effective temperature of each candidate from its 2MASS $J-K$ colors. We used the Yonsei-Yale isochrones [Demarque et al., 2004b] at 5 Gyr with solar metallicity and no alpha enhancement to create a simple polynomial fit for $T_{\rm eff}$ as a function of $J-K$:

$$\begin{aligned} \log T_{\rm eff} &= 3.94808 - 0.7353(J-K) \\ &\quad +1.0116(J-K)^2 - 0.8334(J-K)^3. \end{aligned} \tag{2.3}$$

As we have conducted our follow-up spectroscopy, we have found that this relation generally predicts $T_{\rm eff}$ to within ~ 100K for $T_{\rm eff} \lesssim 7000$K and to within ~ 300K for stars with $T_{\rm eff} = 7000-7500$K.

We also require that the stellar density, ρ_*, as inferred from the BLS transit fit to the KELT-North light curve, to be within 1.0 dex of the stellar density calculated for each star using its $J-K$ colors, assuming the star is on the main sequence. A large disparity in the observed versus the calculated density is indicative of a blend or of a giant that made it through the reduced proper motion cuts [Seager and Mallén-Ornelas, 2003]. Again using the Yonsei-Yale isochrones at 5 Gyr with solar metallicity and no alpha enhancement, we made a fit for density as a function of $J-K$:

$$\begin{aligned} \log(\rho_{*,\rm calc}/\rho_\odot) &= -1.00972 + 2.82824(J-K) \\ &\quad -1.19772(J-K)^2. \end{aligned} \tag{2.4}$$

We require that this value be within 1.0 dex of the stellar density we calculate from the

KELT-North lightcurve

$$\log \rho_{*,\mathrm{obs}} = \log \left[\frac{3}{G\pi^2 q^3 P^2} \right], \tag{2.5}$$

where P and q are the orbital period and duty cycle (transit duration relative to the period) as returned by BLS. This equation assumes circular orbits and that the companion mass is much smaller than the host star mass, $M_P \ll M_*$. Also, because BLS does not attempt to fit for the ingress/egress duration, and furthermore KELT-North data typically do not resolve the ingress or egress well, we are not able to determine the transit impact parameter and thus the true stellar radius crossing time. Equation 2.5 therefore implicitly assumes an equatorial transit, and so formally provides only an upper limit to the true stellar density. For a transit with an impact parameter of $b = 0.7$, the true density is ~ 0.5 dex smaller than that inferred from Equation 2.5.

All of the light curves that pass these selection criteria are designated as candidates, and a number of additional diagnostic tests are then performed on them, including Lomb-Scargle (LS, Lomb 1976, Scargle 1982) and AoV [Schwarzenberg-Czerny, 1989, Devor, 2005] periodograms. The results of these tests, the values of the BLS statistics, the light curves themselves, as well as a host of additional information, are all collected into a web-page for each candidate. Members of the team can then use this information to vote on the true nature of the candidate (probable planet, eclipsing binary, sinusoidal variable, spurious detection, blend or other). All candidates with at least one vote for being a probable planet are then discussed, and the most promising are then passed along for follow-up photometry, reconnaissance spectroscopy, or both.

2.3 Observations

2.3.1 KELT-North Photometry, Candidate Identification, and Vetting Overview

KC20C05168 emerged as a strong candidate from the analysis of the combined light curves from stars in the overlap area between fields 1 and 13. The KC20C05168 light

curve contains 8185 epochs distributed over ~ 4.2 years, between UT October 25, 2006 and UT December 28, 2010, with a weighted RMS of 9.8 millimagnitudes (mmag). This RMS is typical for KELT-North light curves of stars with this magnitude ($V \sim 10.7$). A strong BLS signal was found at a period of $P \simeq 1.2175$ days, with a depth of $\delta \simeq 3.8$ mmag, and detection statistics SPN=8.53, SDE=12.41, $q = 0.09$, $\Delta\chi^2/\Delta\chi^2_- = 2.06$, and $\log(\rho_{*,obs}/\rho_{*,cal}) = -0.06$. The phased KELT-North light curve is shown in Figure 2.1. A significant signal also appeared in SuperWASP data [Butters et al., 2010] of this star at the same period. The KELT-North data exhibit some evidence for out-of-transit variability at the mmag level and exhibit some relatively weak peaks in the LS and AoV periodograms, but we did not consider these signals to be strong enough to warrant rejection of the candidate. In addition, the depth of the photometric transit signal in the original KELT-North light curve is substantially smaller than we find in the high-precision follow-up data (see §2.3.4). Further analysis indicates that the out-of-transit variability and smaller depth were likely due to a minor problem with the original data

Based on the strength of the K20C05168 signal, the estimated effective temperature of the host star of $T_{\rm eff} \sim 6500$K, and the fact that the star was sufficiently isolated in a DSS image, we submitted the candidate for reconnaissance spectroscopy with the Tillinghast Reflector Echelle Spectrograph (TRES; Fűrész 2008) on the 1.5m Tillinghast Reflector at the Fred Lawrence Whipple Observatory (FLWO) on Mount Hopkins in Arizona. The first observation on UT November 9, 2011 at the predicted quadrature confirmed the $T_{\rm eff}$ estimate of the star, and also demonstrated that it was a slightly evolved dwarf with $\log g \sim 4$, and that it was rapidly rotating with $v \sin I_* \sim 55$ km s^{-1}. A second observation was obtained on UT November 11, 2011 separated by ~ 1.9 days, or ~ 1.54 in phase, from the first observation and thus sampled the opposite quadrature. The two observations exhibited a large and significant radial velocity shift of ~ 8 km s^{-1}, consistent with a brown dwarf companion.

Efforts to obtain photometric follow-up during the primary transit and secondary eclipse

were then initiated. Concurrently, additional spectra with TRES were taken to characterize the spectroscopic orbit. In addition, we obtained adaptive optics imaging of the target to search for close companions. Finally, once we were fairly confident that the signals were due to a low-mass transiting companion, we obtained continuous spectroscopic time series with TRES during the primary transits on UT December 21, 2011 and UT January 7, 2012 for the purposes of measuring the Rossiter-McLaughlin (RM) effect. All of these observations are described in greater detail in the subsequent sections and summarized in Table 2.2.

2.3.2 Previous Identification of the Photometric Candidate by HATNet

KELT-1b was also recognized as a photometric transiting planet candidate by the HATNet project, based on observations obtained in 2006. In September 2009 the candidate HTR162-002 was forwarded to D. Latham's team for spectroscopic follow up. An initial observation with TRES confirmed that the target was a late F main-sequence star, as expected from 2MASS color $J - K_s$=0.245. The synthetic template with $T_{\rm eff} = 6250$K and $\log g = 4.0$ and assumed solar metallicity, gave the best match to the observed spectrum. However, that first TRES spectrum also revealed that the star was rotating rapidly, with $v \sin I_* = 55$ km s^{-1}. At that time, D. Latham's team routinely put aside candidates rotating more rapidly than about $v \sin I_* = 30$ km s^{-1}, arguing that it would not be possible to determine velocities with a precision sufficient for an orbital solution for a planetary companion.

HTR162-002 remained on the HATNet "don't observe with TRES" list until it was independently rediscovered by the KELT-North team and was forwarded to D. Latham's team as candidate KC20C05168 in November 2011 for spectroscopic follow up with TRES. During the intervening 26 months, there were two relevant developments in the procedures and tools used by Latham's team, both resulting from contributions by L. Buchhave. The first development, enabled by convenient tools in the observing website, was the practice

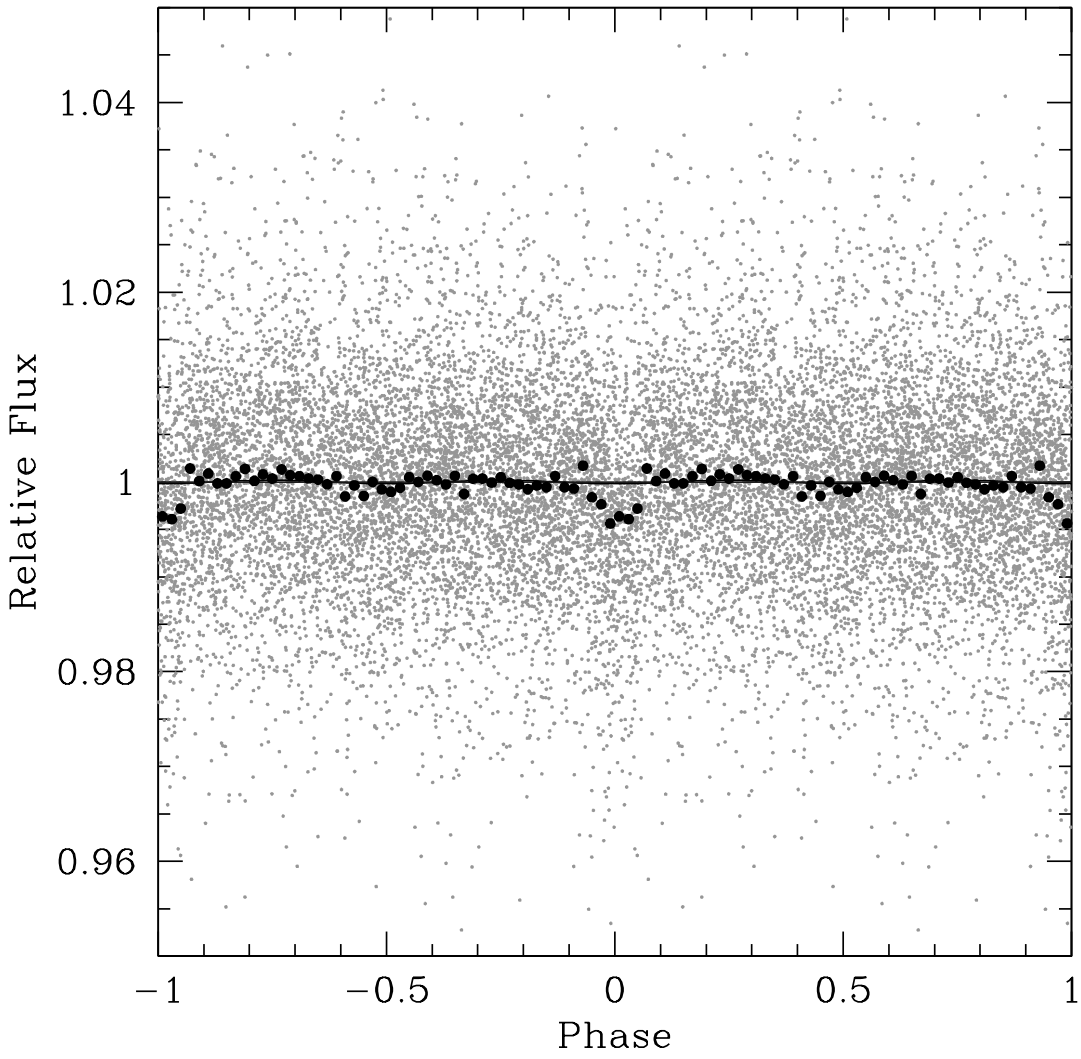

Figure 2.1: The KELT-North light curve of KELT-1 phased to the BLS determined period of $P = 1.2175$ days is shown in the grey points. The black points show the data binned 0.02 in phase.

of observing new candidates only near opposite quadratures, according to the discovery ephemeris and assuming circular orbits. The second development was a much improved procedure for deriving radial velocities for rapidly-rotating stars, initially motivated by the Kepler discovery of hot white dwarfs transiting rapidly-rotating A stars [Rowe et al., 2010]. As it turned out, the second observation of KC20C05168 with TRES described above was taken before the first observation was reviewed, so the candidate was not relegated to the rejected list due to its rapid rotation before the opposite quadrature was observed. When the results were reviewed after the second observation, the evidence for a significant radial velocity shift between the two observations was obvious, despite the rapid rotation, therefore suggesting that the unseen companion was probably a brown dwarf, if not a giant planet.

It should also be recognized that over the 26 months since the first observation of HTR162-002, the attitude against pursuing rapidly rotating stars as possible hosts for transiting planets had gradually softened among the exoplanet community. An important development was the demonstration that slowly-rotating subgiants that have evolved from rapidly-rotating main-sequence A stars do occasionally show the radial-velocity signatures of orbiting planetary companion (e.g., Johnson et al. 2007). A second insight came from the demonstration that the companion that transits the rapidly-rotating A star WASP-33 must be a planet, using Doppler imaging [Collier Cameron et al., 2010a]. Finally, the discovery of transiting brown dwarf companions suggested the possibility of detecting their large amplitude RV signals even when they orbit stars with large $v \sin I_*$ and thus poor RV precision.

In the early days of wide-angle photometric surveys for transiting planets, Latham's team had established procedures for handling candidates forwarded for spectroscopic follow up by more than one team. Such duplications were fairly common, and the goal was to assign credit to the initial discovery team, which was especially important in an era when few transiting planets had been confirmed. By the time it was noticed in mid December

2011 that KC20C05168 was the same as HTR162-002, the KELT-North team already had in hand a convincing orbital solution from TRES and high-quality light curves from several sources, confirming that KELT-1b was indeed a substellar companion.

2.3.3 Spectroscopy from FLWO/TRES

A total of 81 spectra of KELT-1 were taken using the TRES spectrograph on the 1.5m Tillinghast Reflector at FLWO. These were used to determine the Keplerian parameters of the spectroscopic orbit, measure bisector variations in order to exclude false positive scenarios, measure the spectroscopic parameters of the primary, and measure anomalous RV shift of the stellar spectral lines as the companion transits in front of the rapidly-rotating host star, i.e., the RM effect [Rossiter, 1924, McLaughlin, 1924]. The TRES spectrograph provides high resolution, fiber-fed echelle spectroscopy over a bandpass of $3900-8900$Å[Fűrész, 2008]. The observations obtained here employed the medium fiber for a resolution of $R \sim 44,000$. The data were reduced and analyzed using the methods described in Quinn et al. [2012] and Buchhave et al. [2010].

A subset of six spectra were combined in order to determine the spectroscopic parameters of the host star using the Spectral Parameter Classification (SPC) fitting program (Buchhave et al., in preparation). SPC cross-correlates the observed spectrum against a grid of synthetic Kurucz [Kurucz, 1979] spectra. This analysis yielded $T_{\rm eff} = 6512 \pm 50$K, $\log g = 4.20 \pm 0.10$, [Fe/H]$= 0.06 \pm 0.08$, and $v \sin I_* = 55.2 \pm 2\,{\rm km\ s^{-1}}$. These parameters were used as priors for the joint global fit to the RV, RM, and photometric data as described in §2.5.2.

Spectra were taken at a range of phases in order to characterize the spectroscopic orbit and search for bisector span variations indicative of a blend. One of these spectra happened to be taken during a primary transit on UT 2011-11-18, and so was not used in the analysis because it is likely to be affected by the RM effect. The RV and bisector data for the remaining 23 spectra are listed in Table 2.7. These observations span ~ 88 days from UT

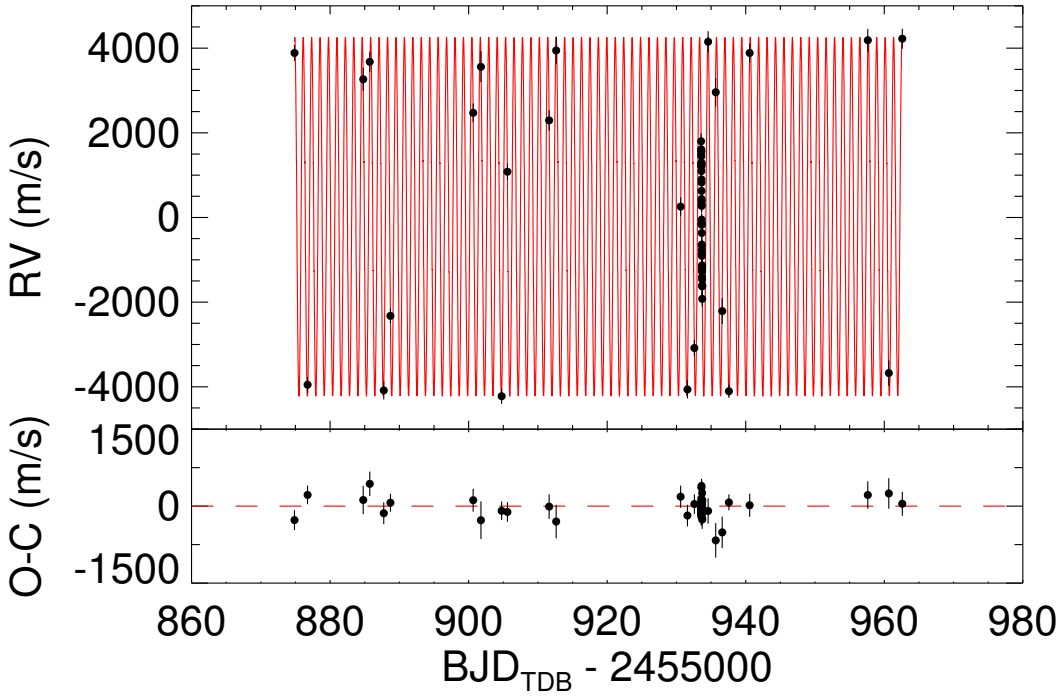

Figure 2.2: Top panel: the points with uncertainties show the measured RVs for KELT-1 as a function of time in $\mathrm{BJD_{TDB}}$. The barycentric velocity of the system, as determined from the model fit shown in the solid line (see §2.5.2), has been been subtracted from the data. Bottom panel: the residuals from the model fit.

2011-11-09 through UT 2012-02-05. The uncertainties on the listed radial velocities have been scaled by a factor of 1.214 based on an independent fit to these data, as described in §2.5.2. The scaled median RV uncertainty is ~ 230 m s^{-1}. The uncertainties in the bisector measurements have not been scaled. The median bisector uncertainty is ~ 110 m s^{-1}.

Time series spectroscopy was obtained with TRES on two different nights of primary transits in order to measure the spin-orbit alignment of the companion via the RM effect. Fifteen observations were obtained on UT 2011-12-21 and forty-two observations on UT 2012-01-07. Conditions were relatively poor for the first run, resulting in a factor ~ 2 larger uncertainties and incomplete coverage of the transit. We therefore decided not to include these data in our final analysis, although we confirmed that this has no effect on our final inferred parameters. The RV and bisector data for the RM run on UT 2012-01-07 are listed

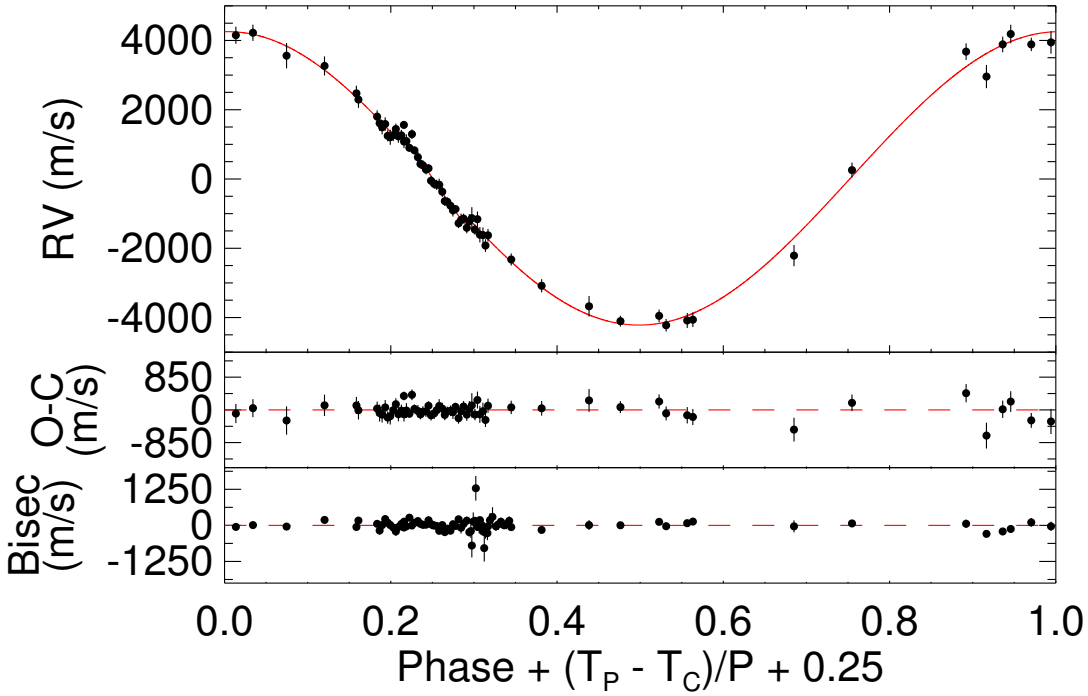

Figure 2.3: Points with uncertainties show the measured RVs for KELT-1 relative to the barycentric velocity of the system, phased to the best-fit period as determined from the model fit shown in the solid line (see §2.5.2). The phases are normally referenced to the time of periastron (T_P), but have been shifted such that a phase of 0.25 corresponds to the time of inferior conjunction T_C or transit. RV data near this phase show deviations from the Keplerian expectation due to the RM effect, which was included in the model. Middle panel: the residuals of the RV data from the model fit. Bottom panel: bisector spans as a function of phase.

in Table 2.8. The RV uncertainties have been scaled by a factor of 0.731, also based on the global model fit described in §2.5.2. We note that the majority of the χ^2 for these data are due to a few outliers. The median scaled RV uncertainty is ~ 160 m s^{-1}. The bisector uncertainties were not scaled.

All of the RV and bisector measurements used in the subsequent analysis are shown as a function of epoch of observation in $\mathrm{BJD_{TDB}}$ in Figure 2.3. The measurements phased to the best-fit companion period from the joint fit to photometric and RV data are shown in Figure 2.3, demonstrating the very high signal-to-noise ratio with which the RV signal of the companion was detected, and the good phase coverage of the orbit. A detail of the RV

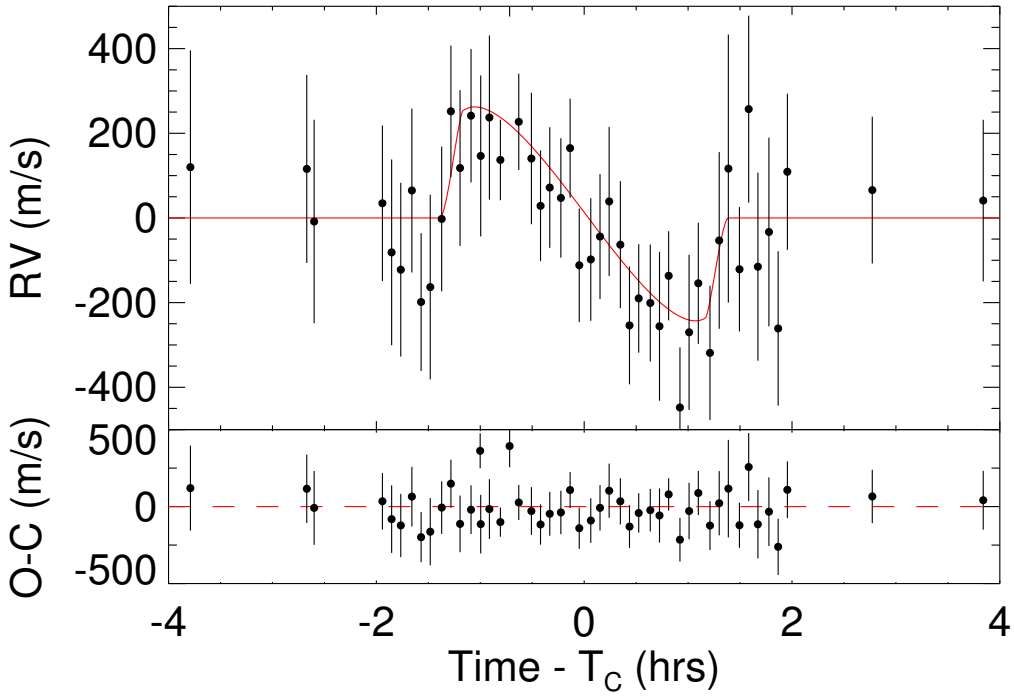

Figure 2.4: Top panel: the points with uncertainties show the measured RVs relative to the barycentric velocity of the system for KELT-1, as a function of the time since transit T_C, for data taken near T_C. The Keplerian RV variation as determined from the best-fit model has been removed from both the data and model. Data taken within ~ 1.4 hours of T_C occur during transit, and are thus strongly affected by the RM effect. The shape of the RM signal indicates that the projected obliquity of the host star with respect to the orbit is small. Bottom panel: the residuals of the data to the RM fit.

data near the time primary transit with the orbital (Doppler) RV signal removed is shown in Figure 2.4, showing the clear detection of the RM effect and a suggestion that the orbit normal is well aligned with the projected stellar spin axis.

Finally, we determined the absolute radial velocity of the system barycenter using a simple circular orbit fit to radial velocities determined from the full set of spectra, which were determined using a single order near the Mg b line. (Note that the relative RVs used for determining the orbit were determined using the full, multi-order analysis of the spectra.) The zero point correction to these velocities were determined using contemporaneous monitoring of five RV standard stars. The final value we obtain is $\gamma_{\rm obs} = -14.2 \pm 0.2$ km s^{-1}, where the uncertainty is dominated by the systematic uncertainties in the absolute velocities of the standard stars. This zero point, along with the global fit to the data in §2.5.2, were used to place the instrumental relative radial velocities on an absolute scale. Therefore, the RVs listed in Tables 2.7 and 2.8 are on an absolute scale.

2.3.4 Follow-Up Photometry

We obtained high-precision follow-up photometry of KELT-1 in order to confirm the K20C05168 transit signal, search for evidence of a strongly wavelength-dependent transit depth indicative of a stellar blend, and search for evidence of a secondary eclipse. Also, these data enable precision measurements of the transit depth, ingress/egress duration, and total duration, in order to determine the detailed parameters of the KELT-1 system. In all, we obtained coverage of 9 complete and 4 partial primary transits, and two complete and one partial secondary eclipse, using six different telescopes in all. Many of these data were taken under relatively poor conditions and/or suffer from strong systematics. We therefore chose to include only a subset for the final analysis, including six of the primary transits and the three secondary eclipses. In the following subsections, we detail the observatories and data reduction methods used to obtain these data. The dates, observatories, and filters for these data sets are summarized in Table 2.2. The light curves for the primary transits

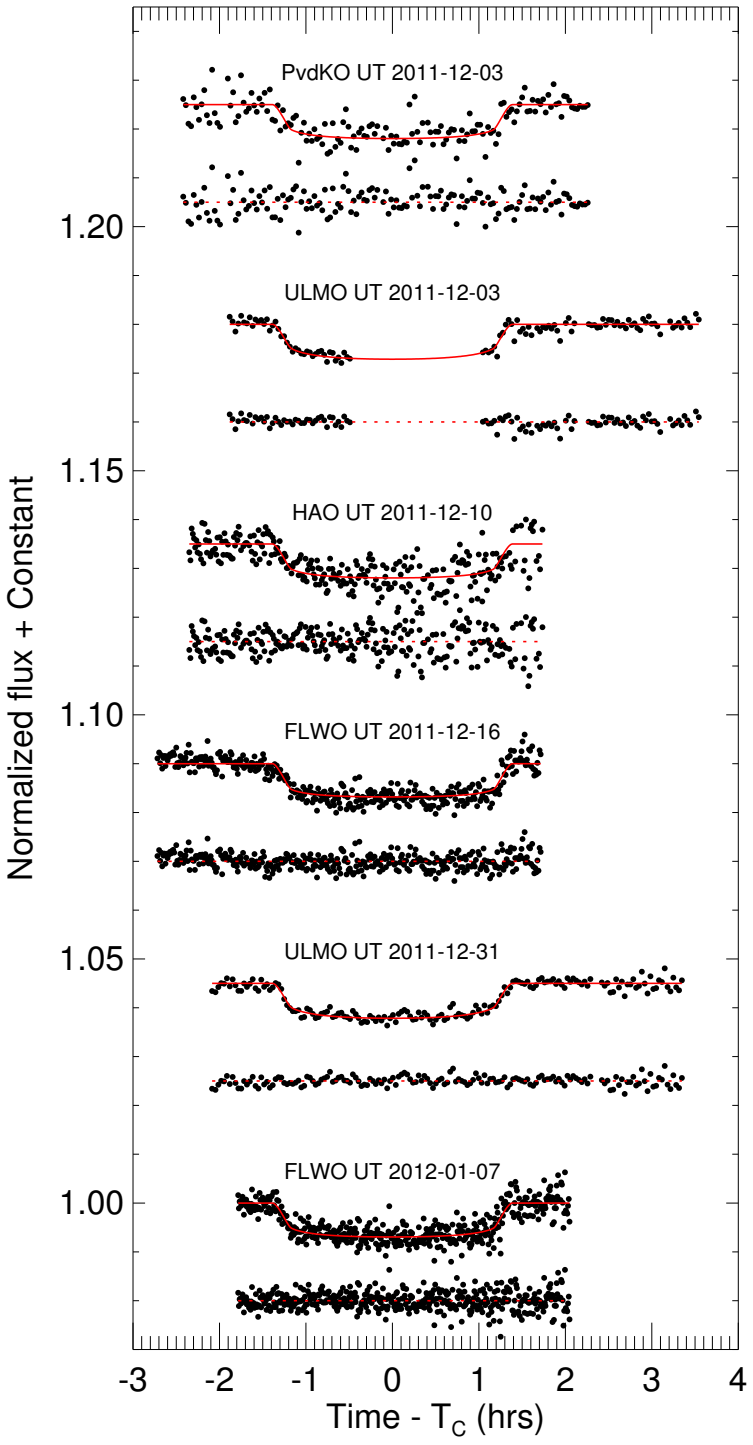

Figure 2.5: Points show the relative flux as a function of time from transit (T_C) for the six sets of follow-up observations of transits we analyze here. The data sets are labeled and summarized in Table 2.2. The data are normalized by the fitted out-of-transit flux, and a linear trend with air mass has been removed (see §2.5.2). In addition, an arbitrary offset has been applied to each light curve for clarity. For each observation, we plot the data above and the residuals below. In all cases, the solid lines show the model fit from the analysis in §2.5.2.

are displayed in Figure 2.5 and the data are listed in Tables 2.9 through 2.13, whereas the light curves for the secondary eclipse are displayed in Figure 2.6 and the data are listed in Tables 2.15 through 2.17.

2.3.4.1 Peter van de Kamp Observatory (PvdKO)

Data on the primary transit starting on UT 2011-12-03 were acquired with the 0.6-meter, f/7.8 Ritchey-Chrétien telescope at the Peter van de Kamp Observatory at Swarthmore College (Swarthmore, PA, USA). The telescope is equipped with an Apogee U16M CCD with 4096x4096 9-micron pixels, giving a field of view 26 arcminutes on a side. Available filters are 50mm-square Johnson-Cousins $UBVR_cI_c$ and SDSS *ugriz*, both from Omega Optical. The telescope is autoguided to minimize photometric errors from imperfect flatfielding, keeping the centroid shift of each star to within typically 3-4 pixels over the course of a night. The observations used here were obtained with the *i* filter and used 2x2 binning, giving a binned pixel scale of $0.76''$/ pixel.

The data were reduced in IRAF using standard procedures for flat-fielding (with twilight sky flats) and dark and bias subtraction. Aperture photometry was performed, and then differential magnitudes for the target star were calculated using an ensemble of comparison stars in the same field, chosen to minimize the scatter in the final light curve.

2.3.4.2 University of Louisville Moore Observatory (ULMO)

Data on the primary transits starting UT 2011-12-03 and 2011-12-31, and on the secondary eclipses starting 2011-12-02 and 2012-01-04, were obtained with the University of Louisville Moore Observatory RC24 telescope (MORC24) located near Brownsboro, Kentucky. MORC24 is a RC Optical Systems Ritchey-Chrétien 0.6 m telescope on an equatorial fork mount. The telescope is equipped with an Apogee U16M 4096×4096 pixel CCD camera which has a focal plane scale of $0.''39$ pixel^{-1} and a field of view (FOV) of $26.'3 \times 26.'3$. The UT 2011-12-03 and 2011-12-31 data were obtained using an Astrodon

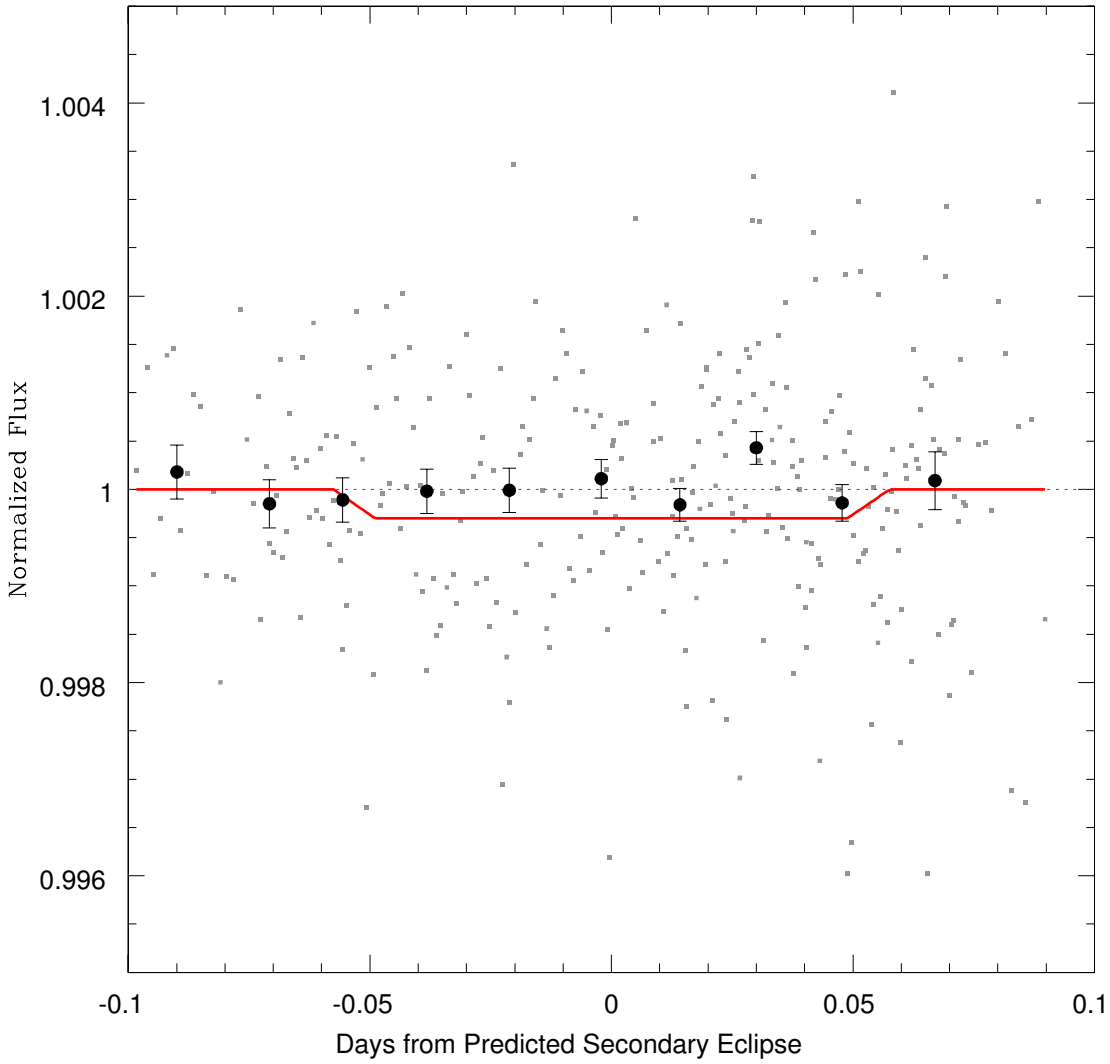

Figure 2.6: Gray points show the combined i and Pan-STARRS-Z relative photometry of KELT-1 as a function of the predicted time of secondary eclipse of KELT-1b (T_S), obtained from the observatories listed in Table 2.2. The data have been corrected for a linear trend with air mass and normalized by the zero point of the linear fit (see §2.5.4). The larger circles with error bars show the binned observations. Note we do not fit to the binned data; these are shown for the purposes of illustration only. The over plotted example light curve is the secondary eclipse depth we would expect if KELT-1b had a geometric albedo of $A_g = 0.1$ and instantaneously reradiated its incident stellar flux ($f' = 2/3$). We would have detected this event with a confidence level of $\gtrsim 95\%$.

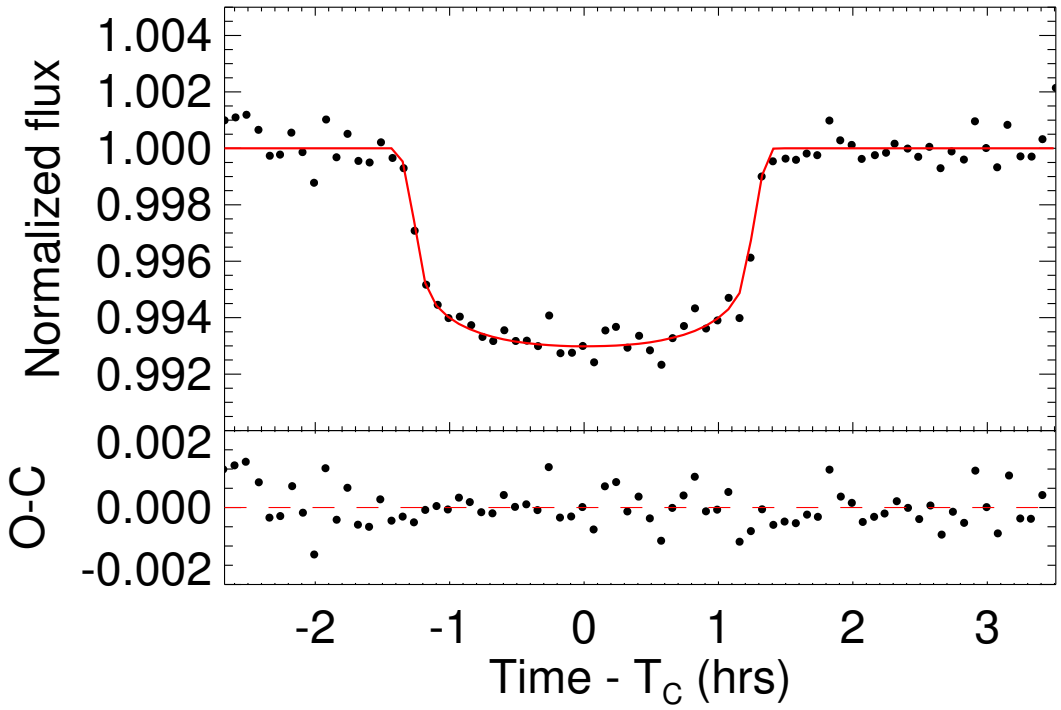

Figure 2.7: Top panel: the points show the six data sets displayed in Figure 2.5, combined and binned in 5 minute intervals. Since these data sets were taken with different filters and have different systematics, we do *not* use this combined light curve for analysis, but rather show it for the purposes of illustrating the overall quality and statistical constraining power of the ensemble of follow-up light curves. The solid red curve shows the six transit models for each of the individual fits combined and binned in 5 minute intervals the same way as the data. Bottom panel: the residuals of the binned light curve from the binned model in the top panel.

Photometrics Sloan r filter, while the other two sets of data were obtained using an Astrodon Photometrics Sloan i filter. The MORC24 mount has excellent free-running tracking, so we did not use a separate guide camera. Instead, minor telescope pointing corrections are made after each exposure by comparing the CCD pixel coordinates of the centroid of the target star to its initial position on the CCD. KELT-1b was held to within 3-4 pixels of the starting position on the CCD throughout each observing session. Since KELT-1b is separated from its nearest detectable neighbor in DSS2 imagery by $\sim 18''$, we were able to defocus the telescope to allow for longer exposures without the risk of blending from the neighbor star. An exposure time of 100 s was used for all observations, resulting in a 120 s cadence when combined with the 20 s CCD readout time.

We used AstroImageJ (Collins & Kielkopf 2012, in preparation) to calibrate the image data. The algorithm includes bias subtraction, CCD non-linearity correction, dark subtraction, and flat-field division. AstroImageJ was also used to perform aperture photometry using a circular aperture. An aperture size and an ensemble of comparison stars in the same field were chosen to minimize the scatter in the final light curves. AstroImageJ provides the option to use a standard fixed radius aperture or a variable radius aperture based on the measured FWHM of the target star in each image of the series. When a star is well separated from other stars, the variable aperture option tends to reduce photometric scatter under observing conditions that result in significant changes to the PSF during the observing session. The variable aperture produced optimal results for all four MORC24 KELT-1b light curves.

For the observations starting on UT 2011-12-02, cirrus clouds were present during the first half of the observations, and air mass ranged from 1.16 at the start of observations to 3.19 at the end. For the observations starting on UT 2011-12-04, skies were clear until clouds moved in about 30 minutes after ingress. The clouds cleared just prior to egress, however, sky transparency remained highly variable until about an hour after egress. Air mass ranged from 1.05 at the beginning of observations to 1.40 at the end. Although guid-

ing was maintained through the cloud cover, data during that time have been removed. For the observations starting on UT 2011-12-31, skies were clear with minimal variations in transparency. Air mass ranged from 1.00 at the beginning of observations to 2.17 at the end. For the observations on UT 2012-01-04, cirrus clouds were present during the second half of the observations, and air mass ranged from 1.03 at the start of observations to 1.96 at the end.

2.3.4.3 Hereford Arizona Observatory (HAO)

Data on the primary transit starting UT 2011-12-10 were obtained at the Hereford Arizona Observatory, HAO (observatory code G95 in the IAU Minor Planet Center). This is a private observatory in Southern Arizona consisting of a 14-inch Meade LX-200 GPS telescope equipped with a SBIG ST-10XME CCD, a focal reducer and a 10-position filter wheel with SDSS filters *ugriz*. The telescope and dome are operated via buried cables, permitting automation of observing sessions. Calibrations usually employ a master flat frame obtained during dusk prior to the observing session. The field-of-view (27 x 18 arcminutes) is sufficient for the use of approximately two dozen stars as candidates for reference in a typical field. The observations reported here were obtained with the *i* filter.

The data were reduced and a light curve was generated as follows. An artificial star was inserted in each image before photometry readings for the purpose of monitoring smooth extinction as well as extra extinction events caused by thin clouds, dew formation, and atmospheric seeing degradations that could swell the PSF beyond the photometry aperture circle. Photometry magnitude readings were made by the program MaxIm DL and imported to a spreadsheet, where several steps of manual reduction were completed. The first was to solve for an extinction model (including a temporal extinction trend) based on the sum of all candidate reference star fluxes versus air mass. Second, subsets of reference stars were evaluated for suitability, by toggling individual stars ”on and off” in order to determine the subset that minimize the RMS scatter in the target star light curve.

Finally, the light curve for the target was fitted using a model for systematic effects and a transit signature. Systematics were represented by a temporal trend and air mass curvature (AMC). The AMC is caused by the target star having a color that differs from the flux-weighted color of the reference stars. The transit parameters were depth, total duration, ingress/egress duration, and a parameter related to the stellar limb darkening. The solution was obtained by minimizing the χ^2 of the fit. Outliers were identified using an objective rejection criterion based on deviations from the model solution. Finally, the light curve is corrected for extinction and systematic effects and scaled to the out-of-transit model flux.

2.3.4.4 FLWO/KeplerCam

Data on the primary transits on UT 2011-12-16 and 2012-01-07 were obtained with KeplerCam on the 1.2m telescope at FLWO. KeplerCam has a single 4K $\times$ 4K Fairchild CCD with a pixel scale of 0.366 arcseconds per pixel, for a total FOV of 23.1 x 23.1 arcminutes. A full transit was observed on UT 2011-12-16 with clear conditions. Observations were obtained in the SDSS z filter with 30-second exposures. We also obtained a full transit on UT 2012-01-07 and observations were obtained with the SDSS i filter with 15-second exposures. Clouds came in at the end of the transit and as a result there is some increased scatter in the out-of-transit baseline. The data were reduced using a light curve reduction pipeline outlined in Carter et al. [2011] which uses standard IDL techniques.

2.3.4.5 Las Cumbres Observatory Global Telescope Network (LCOGT)

Data on the secondary eclipse on UT 2011-12-30 were obtained with the 2.0m Faulkes Telescope North (FTN) telescope, which is located on Haleakala on the island of Maui in Hawaii. The FTN telescope is part of the Las Cumbres Observatory Global Telescope Network [4]. These observations were made using the 4K $\times$ 4K Spectral camera (Fairchild Imaging CCD486 BI) in bin 2x2 mode for a faster readout together with the PanSTARRS-

[4] http://lco.global

Z filter. As scintillation noise becomes significant (>1 millimag) in exposures shorter than ~30 sec for telescopes of this aperture, the exposure time was kept to 60 sec and the telescope defocused to avoid saturation of the target while ensuring sufficient signal-to-noise ratio in the comparison stars. These data were debiased, dark-subtracted and flat fielded by the LCOGT offline pipeline (developed by the Astrophysics Research Institute at Liverpool John Moores) and aperture photometry was carried out using the stand-alone DAOPHOT II [Stetson, 1987, 1990]. Differential photometry was then computed using an ensemble of 15 comparison stars.

2.3.5 Keck Adaptive Optics Imaging

To further assess the multiplicity of KELT-1, we acquired adaptive optics images using NIRC2 (PI: Keith Matthews) at Keck on UT 2012-01-07. Our observations consist of dithered frames taken with the K' ($\lambda_c = 2.12\mu$m) and H ($\lambda_c = 1.65\mu$m) filters. We used the narrow camera setting to provide fine spatial sampling of the stellar point-spread function. The total on-source integration time was 81 seconds in each bandpass.

Images were processed by replacing hot pixel values, flat-fielding, and subtracting thermal background noise. No companions were identified in individual raw frames during the observations; however, upon stacking the images we noticed a point source (8σ) to the south-east of KELT-1. Figure 2.8 shows the final processed K' image. Inspection of the companion location showed that its separation from the star does not change with wavelength, demonstrating that it is not a speckle. This object is too faint and close to the primary to be detected with seeing-limited images.

We performed aperture photometry to estimate the relative brightness of the candidate tertiary, finding $\Delta H = 5.90 \pm 0.10$ and $\Delta K' = 5.59 \pm 0.12$. An $H - K' = 0.4 \pm 0.2$ color is consistent with spectral-types M1-L0 [Leggett et al., 2002, Kraus and Hillenbrand, 2007]. If the candidate is bound to KELT-1 and thus at the same distance of 262 ± 14pc and suffers the same extinction of $A_V = 0.18 \pm 0.10$ (see §2.5.1), then we estimate its absolute

H magnitude to be $M_H = 8.31 \pm 0.15$, corresponding to a M4-5 spectral type, consistent with its color (see, e.g., the compilation of Kirkpatrick et al. 2012).

We also measured an accurate position of the companion relative to the star by fitting a Gaussian model to each of the point-spread function cores. After correcting for distortion in the NIRC2 focal plane [5], and adopting a plate scale value of 9.963 ± 0.006 mas pix^{-1} and instrument orientation relative to the sky of $0.13^\circ \pm 0.02^\circ$ [Ghez et al., 2008], we find a separation of $\rho = 588 \pm 1$ mas and position angle $PA = 157.4^\circ \pm 0.2^\circ$ east of north. If it is bound to KELT-1, it has a projected physical separation of $\sim 154 \pm 8$ AU, and a period of ~ 1700 years assuming a circular, face-on orbit.

We used the Galactic model from Dhital et al. [2010] to assess the probability that the companion is an unrelated star (i.e., a chance alignment). The model uses empirical number density distributions to simulate the surface density of stars along a given line-of-sight and thus determine probability of finding a star within a given angular separation from KELT-1. We estimate an a priori probability of $\sim 0.05\%$ of finding a star separated by $\lesssim 0.59''$ from KELT-1b. We therefore conclude that the companion is likely to be a bona fide, physically associated binary system. With a total proper motion of ~ 20 mas/year, it will be possible to definitively determine whether the candidate tertiary is physically associated with KELT-1 within one year.

We note that the companion is unresolved in our follow-up primary transit photometry, and thus in principle leads to a dilution of the transit signal and a bias in the parameters we infer from a fit to the photometry described in §2.5.2. However, the effect is negligible. As we discuss in the next section, we are confident that the primary is being eclipsed. Thus the fractional effect on the transit depth is of the same order as the fractional contribution of the companion flux to the total flux, which is $< 1\%$.

[5] http://www2.keck.hawaii.edu/inst/nirc2/forReDoc/post_observing/dewarp/

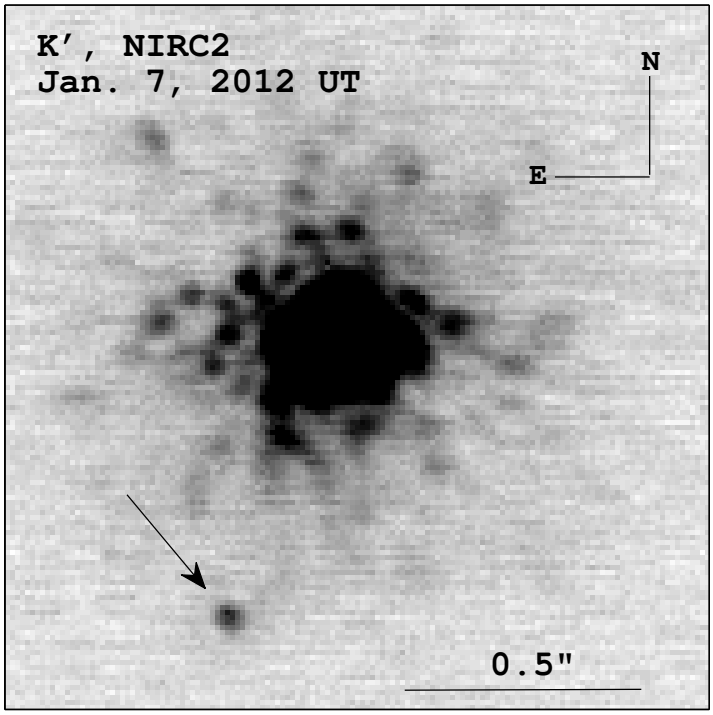

Figure 2.8: Keck AO image of KELT-1 taken with NIRC2 on UT 2012-01-07 in the K' filter. North is up and East is to the left. A $0.5''$bar is shown for scale. A faint companion with $\Delta K' = 5.59 \pm 0.12$ located $\sim 558 \pm 1$ mas to the southeast is clearly visible.

2.4 Evidence Against a Blend Scenario

One of the many challenges of photometric surveys for transiting planets is the relatively high rate of astrophysical false positives, blended eclipsing stellar binary or triple systems that can mimic some of the observable signatures of transiting low-mass companions to single stars. In the case of the KELT-North survey, one generically expects a higher rate of false positives as compared to other wide-field transit surveys such as HATNet or SuperWASP, because of the poorer image quality arising from the comparatively smaller aperture, larger pixel scale, and wider FOV. For KELT-1 in particular, the extreme properties of the companion, relatively high $v \sin I_*$ of the primary, and the fact that the primary is somewhat evolved, are all reminiscent of false positives that have been reported in previous surveys, e.g., Mandushev et al. [2005].

In the case of KELT-1b, however, we have a number of lines of evidence that strongly disfavor a blend scenario.

The most compelling arguments against blend scenarios arise from the spectra. First is the lack of strong evidence for bisector span variations. The lower panel of Figure 2.3 shows the bisector variations phased to the best-fit period of the companion as determined from the joint fit to the RV and photometry data described in §2.5.2. There is no evidence for bisector variations correlated with the orbital phase of the companion. The weighted RMS of the bisector spans, excluding the data taken on UT 2012-01-07, is ~ 120 m s^{-1}, only $\sim 30\%$ larger than would be expected based on the native uncertainties, and a factor of ~ 30 times smaller than the RMS of the RV measurements themselves. Figure 2.9 shows the bisector spans as a function of radial velocity relative to the system barycenter. There is no strong correlation; the correlation coefficient is only -0.17. In contrast, Figure 2.10 shows data taken on the night of UT 2012-01-07, which covered the primary transit. For the subset of these data taken within 0.03 days of the transit center (approximately the middle half of the transit), there is a clear correlation between the radial velocity and the bisector variations, with a correlation coefficient of 0.68. This is expected since the anomalous

radial velocity shift from the RM effect is due to a distortion of the rotationally-broadened stellar spectral lines as the planet progressively occults the light from different parts of the face of the star. Indeed, the second piece of evidence that the transit signatures are indeed due to a small companion occulting the primary star is the RM signal itself (Fig. 2.4), which has an amplitude consistent with the apparent transit depth and spectroscopically-determined $v \sin I_*$.

Third, photometric observations in several different filters (*riz*) are all consistent with the primary transit having nearly the same depth, and are well-modeled by transits of a dark companion across a star with the limb darkening consistent with its spectroscopically measured $T_{\rm eff}$ and $\log g$ (see Section 2.5.2).

Fourth, photometric observations at the predicted time of superior conjunction reveal no evidence for a secondary eclipse at the $\lesssim 1$ mmag level. These first two pieces of evidence tend to exclude or strongly disfavor blend scenarios in which the observed transits are due to diluted eclipses of a much fainter and redder eclipsing binary (e.g., O'Donovan et al. 2006).

Finally, our adaptive optics imaging does not reveal any sources further than $\sim 0\farcs25$ from the primary that could be both blended with it in seeing-limited images *and* cause transits at the observed depth of $\sim 1\%$. The one source we do detect, the putative tertiary, has a flux ratio relative to the primary of only $\sim 0.5\%$ in the near-IR, and is likely considerably fainter in the optical, and thus is too faint to explain the observed transits.

We did not perform any detailed modeling to determine the viability of specific blend scenarios. We defer here to Bakos et al. [2012], who argue that such analyses are generally unnecessary in situations in which there are no significant bisector variations, the transit ingress/egress durations are short compared to the total duration, and the radial velocity variations phase with the predicted transit ephemeris.

We conclude that all of the available data are best explained as due to a Jupiter-sized, brown dwarf companion transiting a rapidly-rotating mid-F star, with little or no evidence

for significant contamination from blended sources. Under this assumption, we proceed in the following section to analyze these data in order to determine the physical properties of the KELT-1 host star and its short-period, low-mass companion.

2.5 Characterization of the Star, Companion, and Orbit

2.5.1 Properties of the Host Star

Table 2.3 lists various collected properties and measurements of the KELT-1 host star. Many these have been culled from the literature, and the remainder are derived in this section. In summary, KELT-1 is a mildly evolved, solar-metallicity, mid-F star with an age of $\sim 1.5-2$ Gyr located at a distance of ~ 260 pc, with kinematics consistent with membership in the thin disk.

We construct an empirical spectral energy distribution (SED) of KELT-1 using optical fluxes in the B_T and V_T passbands from the Tycho-2 catalog [Høg et al., 2000], near-infrared (IR) fluxes in the J, H and Ks passbands from the 2MASS Point Source Catalog [Skrutskie et al., 2006, Cutri et al., 2003a], and near- and mid-IR fluxes in the four WISE passbands [Wright et al., 2010, Cutri and et al., 2012b]. This SED is shown in 2.11. We fit this SED to NextGen models from Hauschildt et al. [1999] by fixing the values of $T_{\rm eff}$, $\log g$ and [Fe/H] inferred from the global fit to the light curve and RV data as described in §2.5.2 and listed in Table 2.4, and then finding the values of the visual extinction A_V and distance d that minimizes χ^2. We find $A_V = 0.18 \pm 0.10$ and $d = 262 \pm 14$pc, with a $\chi^2 = 10.5$ for 6 degrees of freedom, indicating a reasonable fit ($P(> \chi^2) \sim 10\%$). We also performed a fit to the SED without priors, finding $T_{\rm eff} = 6500 \pm 400$K, $A_V = 0.20 \pm 0.15$, $\log g = 4.25 \pm 0.75$ and [Fe/H]$= -0.5 \pm 0.5$, consistent with the constrained fit. There is no evidence for an IR excess.

We note that the quoted statistical uncertainties on A_V and d are likely to be underestimated, because we have not accounted for the uncertainties in values of $T_{\rm eff}$, $\log g$ and

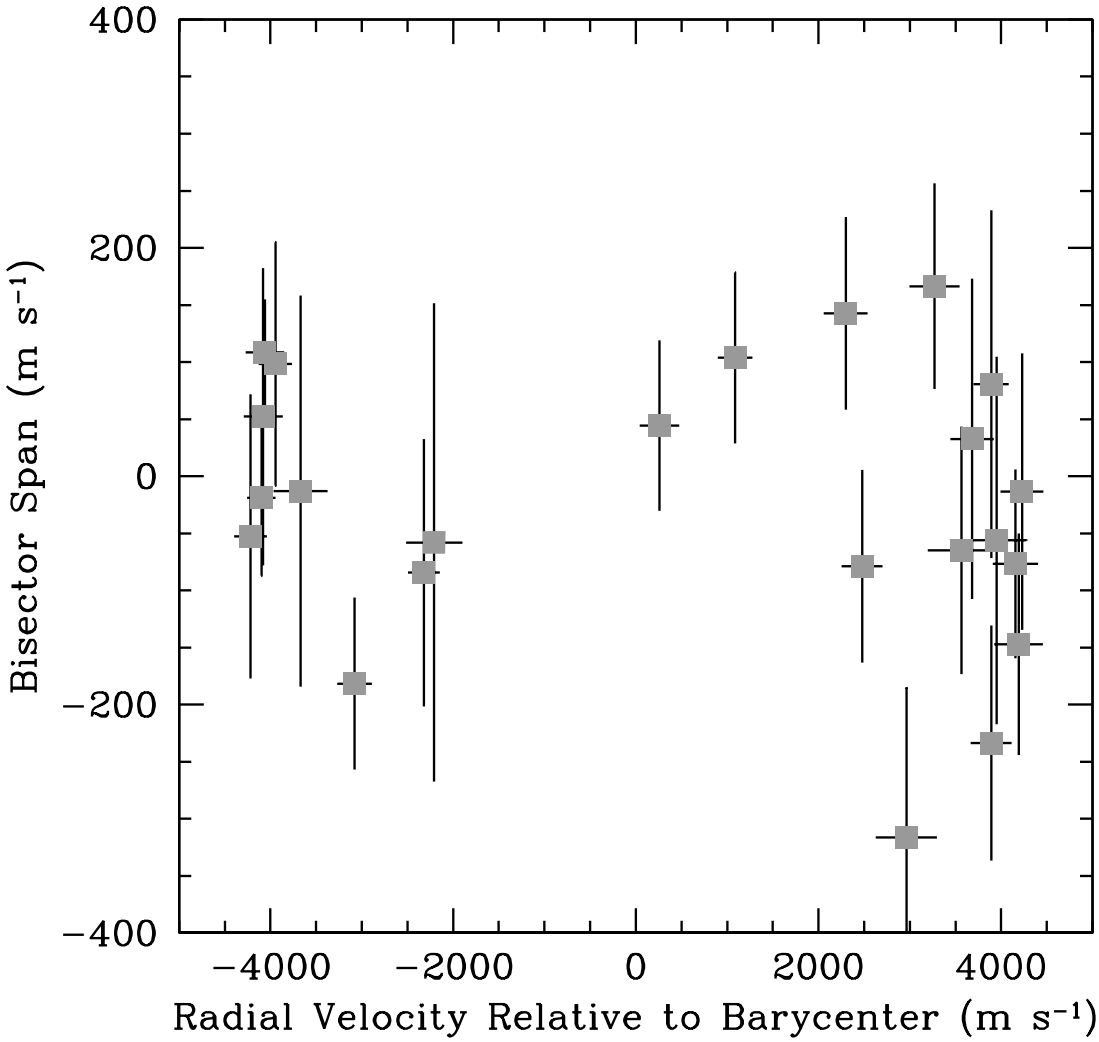

Figure 2.9: Bisector spans versus the RV relative to the system barycenter, excluding observations taken on the night of the transit on UT 2012-01-07. There is no evidence of a significant correlation between the bisector and RV variations, and the rms of the bisector span variations is ~ 30 times smaller than the rms of the RV measurements.

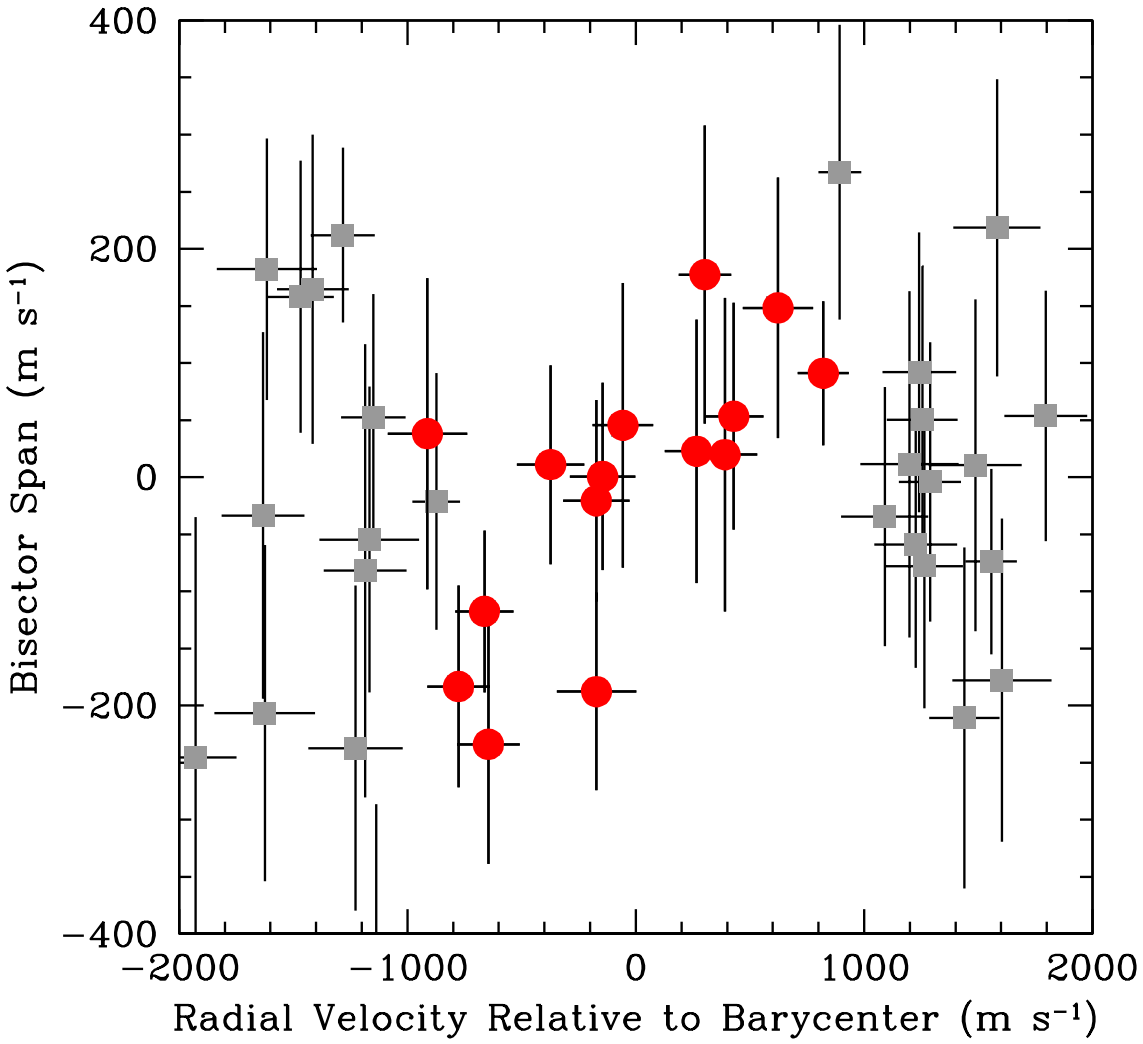

Figure 2.10: Bisector spans vs. the RV relative to the system barycenter for observations taken on the night of the transit on UT 2012-01-07. The red circles are the subset of those data that were taken within 0.03 days of the center of the transit, roughly corresponding to the middle half of the full transit duration. Note that these data are strongly correlated with the RV variations due to the RM effect.

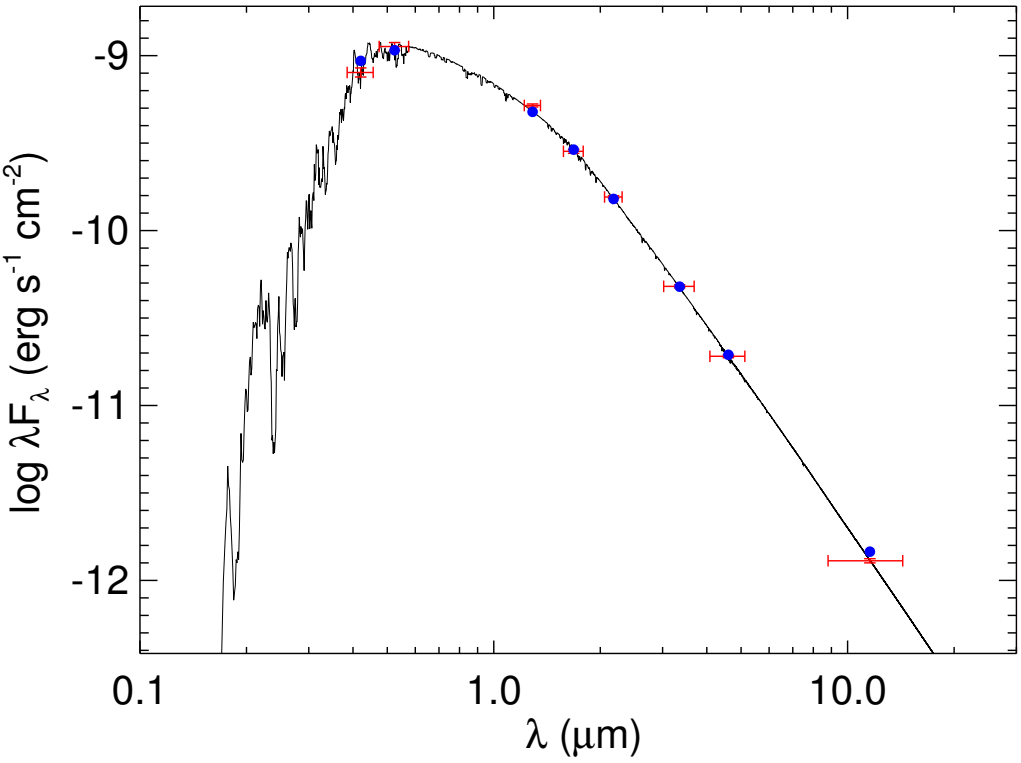

Figure 2.11: The red errorbars indicate measurements of the flux of the KELT-1 host star in various optical and IR passbands. The vertical errorbar indicates the photometric uncertainty, whereas the horizontal errorbar indicates the effective width of the passband. The solid curve is the best-fit theoretical SED from the NextGen models of Hauschildt et al. [1999], assuming $T_{\rm eff}$, $\log g$ and [Fe/H] fixed at the values in Table 2.4, with A_V and d allowed to vary. The blue dots are the predicted passband-integrated fluxes of the best-fit theoretical SED.

[Fe/H] used to derive the model SED. Furthermore, it is likely that alternate model atmospheres would predict somewhat different SEDs and thus values of the extinction and distance.

In Figure 2.12 we plot the predicted evolutionary track of KELT-1 on a theoretical HR diagram ($\log g$ vs. $T_{\rm eff}$), from the Yonsei-Yale stellar models [Demarque et al., 2004b]. Here, again we have used the values of M_* and [Fe/H] derived from the global fit (§2.5.2 and Table 2.4). We also show evolutionary tracks for masses corresponding to the ± 1 σ extrema in the estimated uncertainty. In order to estimate the age of the KELT-1 system, we compare these tracks to the values of $T_{\rm eff}$ and $\log g$ and associated uncertainties as determined from the global fit. These intersect the evolutionary track for a fairly narrow range of ages near ~ 2 Gyr. The agreement between the prediction from the evolutionary track at this age and the inferred temperature and surface gravity for KELT-1 is remarkably good, but perhaps not entirely surprising. The values of $T_{\rm eff}$, $\log g$, [Fe/H] and M_* were all determined in the global fit to the light curve and RV data in §2.5.2, which uses the empirical relations between ($T_{\rm eff}$, $\log g$, [Fe/H]) and (M_*, R_*) inferred by Torres et al. [2010] as priors on the fit, in order to break the well-known degeneracy between M_* and R_* for single-lined spectroscopic eclipsing systems. These empirical relations are known to reproduce the constraints between these parameters imposed by the physics of stellar evolution quite well (see, e.g., Section 8 in Torres et al. 2010).

Based on its $T_{\rm eff}$ and $J-K$ and the empirical table of spectral type versus color and $T_{\rm eff}$ for main-sequence from Kenyon and Hartmann [1995], we infer the spectral type of KELT-1 to be F5 with an uncertainty of roughly ± 1 spectral type.

We determined the Galactic U,V,W space velocities of the KELT-1 system using the proper motion of $(\mu_\alpha, \mu_\delta) = (-10.1 \pm 0.7, -9.4 \pm 0.7)$ mas yr^{-1} from the NOMAD catalog [Zacharias et al., 2004], the distance of $d = 262 \pm 14$ pc from our SED fit described above, and the barycentric radial velocity of the system as determined from the TRES observations (§2.3.3) of $\gamma_{abs} = -14.2 \pm 0.2$ km/s. We used a modification of the IDL routine `GAL_UVW`,

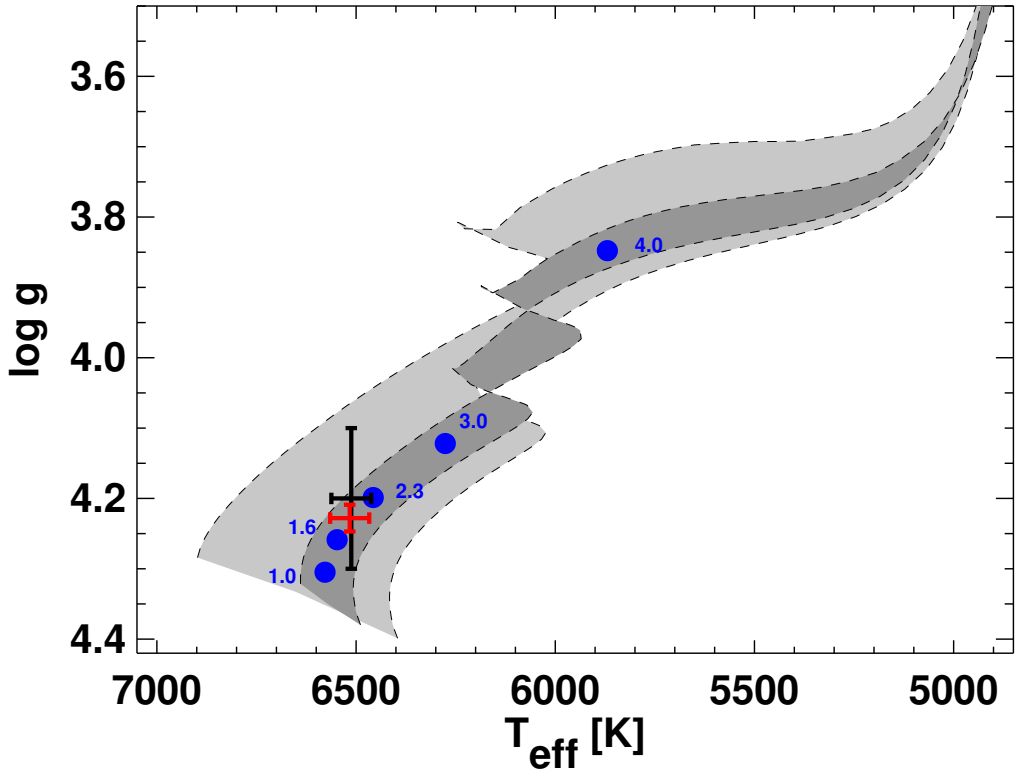

Figure 2.12: Theoretical H-R diagram based on Yonsei-Yale stellar evolution models [Demarque et al., 2004b]. The inner two sets of dashed tracks (shaded darked gray) represent the tracks for the extreme range of the 1σ uncertainties on $M_\star$ and [Fe/H] for the host star, as inferred from the joint fit described in §2.5.2, specifically $M_\star = 1.335 \pm 0.063\,\mathrm{M}_\odot$ and $[\mathrm{Fe/H}] = 0.052 \pm 0.079$. The red cross shows the best-fit $T_{\rm eff} = 6516 \pm 49$K and $\log g = 4.228^{+0.014}_{-0.021}$ from the final analysis. The black cross shows the inferred $T_{\rm eff}$ and $\log g$ from the spectroscopic analysis alone. The blue dots represent the location of the star for various ages in Gyr. The host star is slightly evolved with a probable age of ~ 2 Gyr, although a similar analysis with a different stellar evolutionary model prefers a slightly younger age of ~ 1.75Gyr. The outer two sets of dashed tracks (shaded light gray) show the range inferred using the spectroscopic constraints alone.

which is itself based on the method of Johnson and Soderblom [1987]. We adopt the correction for the Sun's motion with respect to the Local Standard of Rest from Coşkunoğlu et al. [2011a], and choose a right-handed coordinate system such that positive U is toward the Galactic Center. We find $(U,V,W) = (19.9 \pm 1.1, -9.6 \pm 0.5, -2.6 \pm 0.9)$ km s^{-1}, consistent with membership in the thin disk [Bensby et al., 2003]. We note also that the distance of KELT-1 from the Galactic plane is ~ 80 pc.

Finally, we use the solar evolutionary models of Guenther et al. [1992], updated with input physics from van Saders and Pinsonneault [2012], to gain some insight into the detailed structure of the host star. Fixing the mass and metallicity at the values determined from the global fit (§2.5.2 and Table 2.4), we evolved the model forward until the model $\log g$ and $T_{\rm eff}$ approximately matched the values inferred for KELT-1. We found that ages of $\sim 1.5 - 1.75$ Gyr best matched the available constraints, and thus this model prefers a somewhat younger age than the Yale-Yonsei model of (Fig. 2.12, Demarque et al. 2004b). We therefore decided to adopt an age of 1.75 ± 0.25 Gyr, consistent with both estimates. For this range of ages, the models of Guenther et al. [1992] predict a radius of the base of the convective zone of $R_{cz} = 1.30 \pm 0.03$ $R_\odot$, and a very small mass for the convective zone of $M_{cz} = [2.8 \pm 0.14] \times 10^{-5}$ $M_\odot$, as expected given the effective temperature of $T_{\rm eff} \sim 6500$K. In addition, the moment of inertia for the star and convective zone are $C_* = [1.15 \pm 0.04] \times 10^{54}$ g cm^2 and $C_{cz} = [3.2 \pm 0.6] \times 10^{51}$ g cm^2, respectively. We can also write the moment of inertia of the star as $C_* = \alpha_* M_* R_*^2$ with $\alpha_* = 0.0422$ [Guenther et al., 1992]. We will use these to estimate the angular momenta of the star, companion and orbit in §2.6.2.

2.5.2 System Properties Derived from a Joint Fit

It is well known that a joint fit to high-quality RVs and transit photometry of a transiting planet system allows one to determine the mass and radius of the star and planet, as well as the semi-major axis of the orbit, in principle to very high precision, up to a per-

fect one-parameter degeneracy [Seager and Mallén-Ornelas, 2003]. This degeneracy arises because the duration, depth, and shape of the primary transit, when combined with the eccentricity, longitude of periastron, and period of the planet from RV data, allow one to precisely estimate the density of the primary star ρ_*, but not M_* or R_* separately. Breaking this $M_* - R_*$ degeneracy generally requires imposing some external constraint, such as a theoretical mass-radius relation [Cody and Sasselov, 2002, Seager and Mallén-Ornelas, 2003], or constraints from theoretical isochrones (e.g., Bakos et al. 2012). In principle, a measurement of $\log g$ from a high-resolution spectrum can be used to break the degeneracy, but in practice these measurements are generally not competitive with the constraint on ρ_* and often have systematic uncertainties that are comparable to the statistical uncertainties.

We fitted the RV and transit data using a modified version of the IDL fitting package EXOFAST [Eastman et al., 2013]. The approach of EXOFAST to breaking the $M_* - R_*$ degeneracy is similar to the method described in, e.g., Anderson et al. [2012], but with significant differences. We will review it briefly here, but point the reader to Eastman et al. [2013] for more details. We fitted the RV and transit data simultaneously with a standard Keplerian and transit [Mandel and Agol, 2002] model using a modified MCMC method (described in more detail below). In addition to the standard fitting parameters, we also included $T_{\rm eff}, \log g$, [Fe/H] as proposal parameters. We then included priors on the measured values of $T_{\rm eff}, \log g$, [Fe/H] as determined from analysis of the TRES spectra and given in §2.3.3. In addition, we included priors on M_* and R_*, which are based on the empirical relations between ($T_{\rm eff}, \log g$, [Fe/H]) and (M_*, R_*) determined by Torres et al. [2010]. These priors essentially break the $M_* - R_*$ degeneracy, as they provide similar constraints as isochrones, i.e., they encode the mapping between the M_*, [Fe/H] and age of a star to its $T_{\rm eff}$ and $\log g$ as dictated by stellar physics.

We fitted the 6 primary transits, Doppler RV, stellar parameters, and RM effect simultaneously using EXOFAST, which employs a Differential Evolution Markov Chain Monte Carlo (DE-MC) method [Ter Braak, 2006]. We converted all times to the $\rm BJD_{TDB}$ stan-

dard [Eastman et al., 2010], and then at each step in the Markov Chain, we converted them to the target's barycentric coordinate system (ignoring relativistic effects). Note the final times were converted back to $\mathrm{BJD_{TDB}}$ for ease of use. This transformation accurately and transparently handles the light travel time difference between the RVs and transits.

First, we fitted the Doppler RV data independently to a simple Keplerian model, ignoring the RM data taken on UT 2012-01-07. At this stage, we did not include any priors on the stellar parameters, as they do not affect the RV-only fit. We scaled the uncertainties such that the probability that the χ^2 was larger than the value we achieved, $P\left(>\chi^2\right)$, was 0.5, to ensure the resulting parameter uncertainties were roughly accurate. For a uniform prior in eccentricity, we found the orbit is consistent with circular, with a 3σ upper limit of $e < 0.04$. Nevertheless, in order to provide conservative estimates for the fit parameters, we allowed for a non-zero eccentricity in our final fit. However, to test the effect of this assumption, we repeated the final fit forcing $e = 0$. We also investigated the possibility of a slope in the RVs, but found it to be consistent with zero, so we did not include this in the final fit.

Next, we fitted each of the 4 transits individually, including a zero point, $F_{0,i}$ and air mass detrending variable, $C_{0,i}$ for each of the i transits. The air mass detrending coefficient was significant ($> 1\sigma$) for all but 1 transit, so for consistency, we included it for all. After finding the best fit with AMOEBA [Nelder and Mead, 1965], we scaled the errors for each transit such that $P\left(>\chi^2\right) = 0.5$. At this stage, we included the priors on the stellar parameters as described above.

Next, we performed a combined fit to all the data, including a prior on the projected stellar rotation velocity ($v \sin I_* = 55.2 \pm 2$ km s^{-1}) from the spectra[6], and a prior on the period from the KELT-North discovery light curve ($P = 1.217513 \pm 0.000015$ days). Because it is usually systematics in the RV data that vary over long time scales (due to a

[6]The prior on $v \sin I_*$ improves the determination of the spin-orbit alignment angle λ [Gaudi and Winn, 2007]. We also performed a fit without this prior, finding results that were roughly consistent with, although less precise than, those with the prior.

combination of instrumental drift and stellar jitter) that ultimately set the error floor to the RVs, we expect the uncertainties of densely packed observations to be smaller than the RMS of all observations, but with a systematic offset relative to the rest of the orbit. Therefore, we fitted a separate zero point during the RM run, and also scaled the errors on the RVs during transit to force $P\left(>\chi^2\right) = 0.5$ for those subsets of points. $P\left(>\chi^2\right)$depends on the number of degrees of freedom, but it is not obvious how many degrees of freedom there are in the RM run – technically, the entire orbit and the transit affect the $\chi^2$of the RM (13 parameters), but the freedom of the RM measurements to influence most of those parameters is very limited, when fit simultaneously with the transits. Indeed, even $v \sin I_*$ is constrained more by the spectroscopic prior than the RM in this case, which means there are only two parameters (the projected spin-orbit alignment, λ, and the zero point, γ) that are truly free. To be conservative, we subtracted another degree of freedom to encompass all the other parameters on which the RM data has a slight influence, before scaling the errors.

The RM data were modeled using the Ohta et al. [2005] analytic approximation with linear limb darkening. At each step in the Markov Chain, we interpolated the linear limb darkening tables of Claret and Bloemen [2011] based on the chain's value for $\log g$, $T_{\rm eff}$, and $[{\rm Fe/H}]$ to derive the linear limb-darkening coefficient, u. We assumed the V band parameters to approximate the bandpass of TRES, though we repeated the exercise in the B-band with no appreciable difference in any of the final parameters. Note that we do *not* fit for the limb-darkening parameters, as the data are not sufficient to constrain them directly. The uncertainties in all the limb-darkening parameters provided in Table 2.5 arise solely from the scatter in $\log g$, $T_{\rm eff}$, $[{\rm Fe/H}]$. We assume no error in the interpolation of the limb-darkening tables.

In order to search for Transit Timing Variations (TTVs), during the combined fit, we fitted a new time of transit, $T_{C,i}$ for each of the i transits. Therefore, the constraint on T_C and P (quoted in Tables 2.5 and 2.4, respectively) come from the prior imposed from the

KELT-North light curve and the RV data, not the follow up light curves. Using these times to constrain the period during the fit would artificially reduce any observed TTV signal. A separate constraint on T_C and P follows from fitting a linear ephemeris to the transit times, as discussed in §2.5.3. It is the result from this fit that we quote as our final adopted ephemeris.

The results from this global fit are summarized in Tables 2.4 and 2.5. We also show the results for the physical parameters assuming $e = 0$ in Table 2.4; the differences between the fixed and free eccentricity fits are always smaller than their uncertainties, and generally negligible for most of these parameters. The values of $T_{\rm eff}$, $\log g$, and [Fe/H] we infer from the global fit are in agreement with the values measured directly from the TRES spectra to within the uncertainties. Since the spectroscopic values were used as priors in the global fit, this generally indicates that there is no tension between the value of ρ_* inferred from the light curve and RV data, and the spectroscopic values. The median value and uncertainty for $T_{\rm eff}$ is nearly unaffected by the global fit. While the median value for [Fe/H] has changed slightly, the uncertainty is very similar to that from the input prior. On the other hand, the uncertainty in $\log g$ from the global fit is a factor of $\gtrsim 5$ smaller than the uncertainty from the spectroscopic measurement. This is not surprising, since the constraint on ρ_* from the RV and light curve data provides a strong constraint on $\log g$ via the relations of Torres et al. [2010].

Following papers by the HATNet collaboration (e.g., Bakos et al. 2011, Hartman et al. 2011), we also present in Table 2.4 our estimates of the median values and uncertainties for a number of derived physical parameters of the system that may be of interest, including the planet equilibrium temperature assuming zero albedo and perfect redistribution T_{eq}, the average amount of stellar flux at the orbit of the companion $\langle F \rangle$, and the Safronov number $\Theta = (a/R_p)(M_P/M_*)$ (e.g., Hansen and Barman 2007). In addition, in Table 2.5 we quote our estimates of various fit parameters and intermediate derived quantities for the Keplerian RV fit, the primary transits, and the secondary eclipse.

We note that the final uncertainties we derive for M_*, R_*, $\log g$ and ρ_* are relatively small, $\sim 2\% - 5\%$. These uncertainties are similar to those found for other transiting planet systems using methods similar to the one used here (e.g., Anderson et al. 2012). Specifically, these methods derive physical parameters from a fit to the light curve and RV data, which simultaneously imposes an empirical constraint between the M_*, R_* and $T_{\rm eff}, \log g$ and [Fe/H] ultimately derived from Torres et al. [2010]. This constraint helps to break the $M_* - R_*$ degeneracy pointed out by Seager and Mallén-Ornelas [2003] and discussed above, and ultimately dictates our final uncertainty on M_* and R_* (and thus M_P and R_P). In particular, our spectroscopic measurement of $\log g$ provides a much weaker constraint. Given that our results rely so heavily on the Torres et al. [2010] relations, it is worthwhile to ask to what extent our parameters and uncertainties might be affected should these relations be systematically in error. First, as already noted, these empirical relations are known to agree well with stellar isochrones in general [Torres et al., 2010], and for KELT-1 in particular (Fig. 2.12). Second, analyses using stellar isochrones rather than empirical relations produce similar uncertainties on M_* and R_* (e.g., Bakos et al. 2011), suggesting that the small uncertainties we derive are not a by-product of our methodology. Finally, Southworth [2009] demonstrated that the results of the analysis of 14 transiting systems with several different sets of isochrones generally agree to within a few percent. We therefore conclude that our results are likely accurate, with systematic errors at the level of our statistical uncertainties (a few percent).

2.5.3 System Ephemeris and Transit Timing Variations

Table 2.6 lists the measured transit times for each of the six modeled transits, and Figure 2.13 shows the residuals of these times from a fit to a linear ephemeris. The best fit has

$$\begin{aligned} T_C(\mathrm{BJD_{TDB}}) &= 2455909.292797 \pm 0.00024 \\ P &= 1.2175007 \pm 0.000018, \end{aligned} \tag{2.6}$$

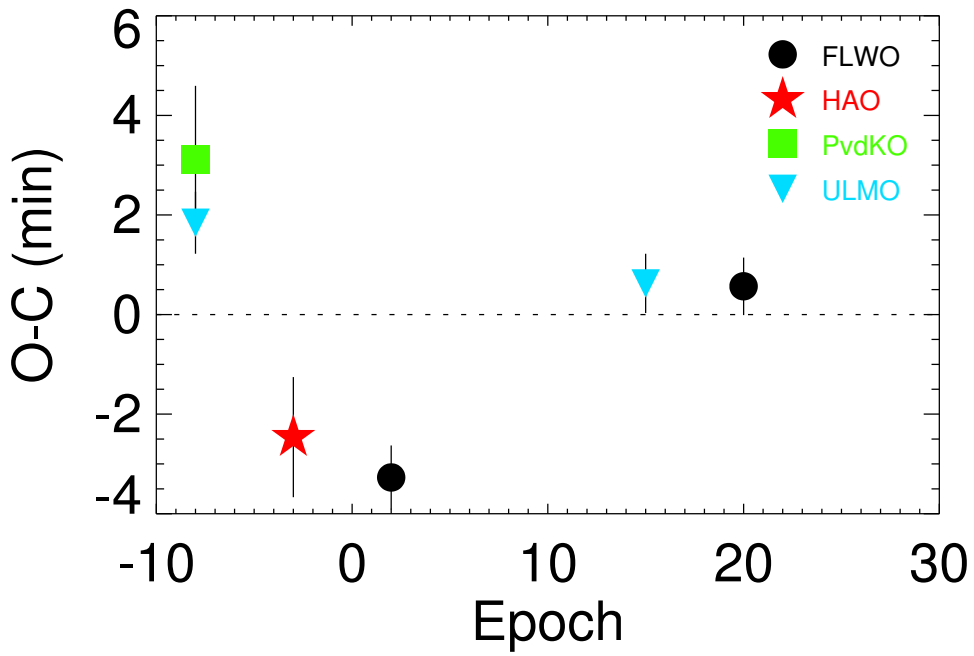

Figure 2.13: The residuals of the transit times from the best-fit (linear) ephemeris. The transit times are given in Table 2.6.

which is consistent with the ephemeris derived from the KELT-North light curve alone. The $\chi^2 = 44.9$ for the linear fit with 4 degrees of freedom is formally quite poor. This is mostly driven by one nominally significant (5σ) outlier, specifically for the transit observed on UT 2011-12-16 from FLWO. We note that the faint companion to KELT-1, if indeed bound, is too distant to explain such large TTVs.

We have taken great care to ensure the accuracy of our clocks and our conversion, and the fact that the residuals from different observatories roughly follow the same trend in time suggests that a catastrophic error in the observatory clock cannot be blamed. Since we fit the trend with air mass simultaneously with the transit, the potentially-large covariance between it and the transit time should be accurately reflected in the quoted uncertainties [Eastman et al., 2013]. Nevertheless, our MCMC analysis does not adequately take into account the effect of systematic uncertainties, and in particular we do not account for cor-

related uncertainties [Pont et al., 2006b, Carter and Winn, 2009], which could skew the transit time of a given event substantially. And, given the results from Kepler which suggest the rarity of such transit timing variations [Steffen et al., 2012], we are reluctant to over-interpret this result. Nevertheless, this is an interesting target for future follow-up.

2.5.4 Secondary Eclipse Limits

We observed the predicted secondary eclipses of KELT-1b assuming $e = 0$ on UT 2011 December 2, 2011 December 30, and 2012 January 4. In none of the three were we able to detect a secondary eclipse. The observations on 2011 December 2 and on 2012 January 4 were taken from the ULMO Observatory in i. On both nights we were able to observe through the predicted ingress and egress of the potential secondary. The two i-band light curves have a combined 236 data points, and show an rms scatter of 1.56 mmag. The observations on 2011 December 30 were taken with the FTN telescope in Pan-STARRS-Z. In this case, we were only able to begin observations half way through the predicted secondary eclipse. This Z-band light curve has 72 points, and an RMS scatter of 0.75 mmag.

We used the system parameters derived from the joint fit (§2.5.2) to fit our three observations. Since we did not detect a secondary eclipse, we used these fits to explore the combination of heat redistribution efficiency and Bond albedo A_B that would give rise to a secondary eclipse depth that is inconsistent with our data. To do so, we calculated the secondary eclipse depths we would expect for a range of redistribution efficiencies and albedos, and then fit a secondary eclipse model with the predicted depth to all three of our observations simultaneously.

In calculating the expected secondary eclipse depths, we made the assumption that both the star and the planet were blackbodies. We also assumed that the planet was a grey Lambert sphere, so the geometric albedo $A_g = (2/3)A_B$, and the spherical albedo is constant as a function of wavelength. Following Seager [2010], we parametrized the heat

redistribution efficiency as f', which is 1/4 in the case of uniform redistribution, and 2/3 in the case of no redistribution. We note that in between these two extremes f' is not easily related to the amount of heat redistribution, i.e., $f' = 0.45$ does not imply half of the incident stellar energy is redistributed around the planet.

To test these expected secondary eclipse depths against our observations, we fit simple trapezoidal eclipse curves with the expected depths to all three datasets simultaneously. Under our assumptions, the depth, timing, shape, and duration of the secondary eclipse are all determined by the parameters derived from the global fit and our specified values of A_B and f'. We then fit this model to our data, allowing for a normalization and a linear trend in the flux with time. We used the $\Delta\chi^2$ between the best fit eclipse model and the best constant fit, which itself was allowed a free slope and offset, to evaluate the detectability of each of the secondary eclipse depths. We used the χ^2 distribution to transform these $\Delta\chi^2$ values into detection probabilities. Figure 2.6 shows an example light curve against a median binned version of our data. This particular curve is the secondary eclipse we would expect if KELT-1b had $A_B = 0.1$, and instantaneously re-radiated its incident stellar flux, i.e., $f' = 2/3$. We would have detected this event with more than 95% confidence.

Figure 2.14 shows the results of our exploration of the heat redistribution versus Bond albedo parameter space. The orange section corresponds to eclipse depths detectable at less than the 68% confidence, the light orange is for depths detectable with 68-90% confidence, light yellow is for 90-95%, and the white contains depths that would have been detected at greater than 95% confidence. The particular shapes of the contours on this plot come from the competing effects of reflection and blackbody emission from KELT-1b on the depth of the secondary eclipse. Along the very bottom of the figure the Bond albedo is zero, and thus there is only thermal emission. We see the strong change in eclipse depth as amount of heat redistribution decreases, thus causing the temperature and eclipse depth for KELT-1b to increase. Along the top of the figure, where the Bond albedo is 0.75, the reflected starlight dominates the blackbody emission such that changing the redistribution efficiency

has little effect on the eclipse depth.

Slightly more than half of the allowed parameter space in Figure 2.14 would have caused secondary eclipses detectable in our data at greater than 90% confidence, while almost all would have been detected at more than 68% confidence. Since we did not see a secondary eclipse in our observations, we conclude that KELT-1b either it has a non-zero albedo, or it must redistribute some heat from the day side, or both. Formally, the scenario that is most consistent with our data is that KELT-1b has both a low Bond albedo and is very efficient at redistributing heat away from its day side, however we are reluctant to draw any strong conclusions based on these data.

2.6 Discussion

From our global fit to the light curves and RVs, we find that KELT-1b is a low-mass companion with a measured mass $M_P = 27.23^{+0.50}_{-0.48}$ M_J and radius $R_P = 1.110^{+0.032}_{-0.022}$ R_J. It is on a circular orbit with a semimajor axis of $a = 0.02466 \pm 0.00016$AU. The host KELT-1 is a mildly evolved mid-F star with a mass $M_* = 1.324 \pm 0.026\ M_\odot$, radius $R_* = 1.462^{+0.037}_{-0.024}\ R_\odot$, effective temperature $T_{\rm eff} = 6518 \pm 50$ K, and a likely age of $\sim 1.5 - 2$Gyr. Because of its small semimajor axis and hot host, KELT-1b receives a large stellar insolation flux of $\langle F \rangle = 7.81^{+0.42}_{-0.33} \times 10^9$ erg s^{-1} cm^{-2}, implying a high equilibrium temperature of $T_{eq} = 2422^{+32}_{-26}$ K assuming zero albedo and perfect redistribution. Both the surface gravity and density of KELT-1b are substantially higher than that of its host star, and higher than we would expect for a stellar object. We find that the orbit normal of KELT-1b is well-aligned with the projected rotation axis of its host star, with a projected alignment angle of $\lambda = 2 \pm 16$ degrees.

Even among the large and diverse menagerie of known transiting exoplanets and low-mass companions, KELT-1b is unique. First, it is one of only 7 unambiguous objects with mass the range $\sim 13 - 80$ M_J that are known to transit stars. Among these, it has the shortest period, and orbits the brightest host star ($V = 10.7$). In addition, there is potentially a stellar

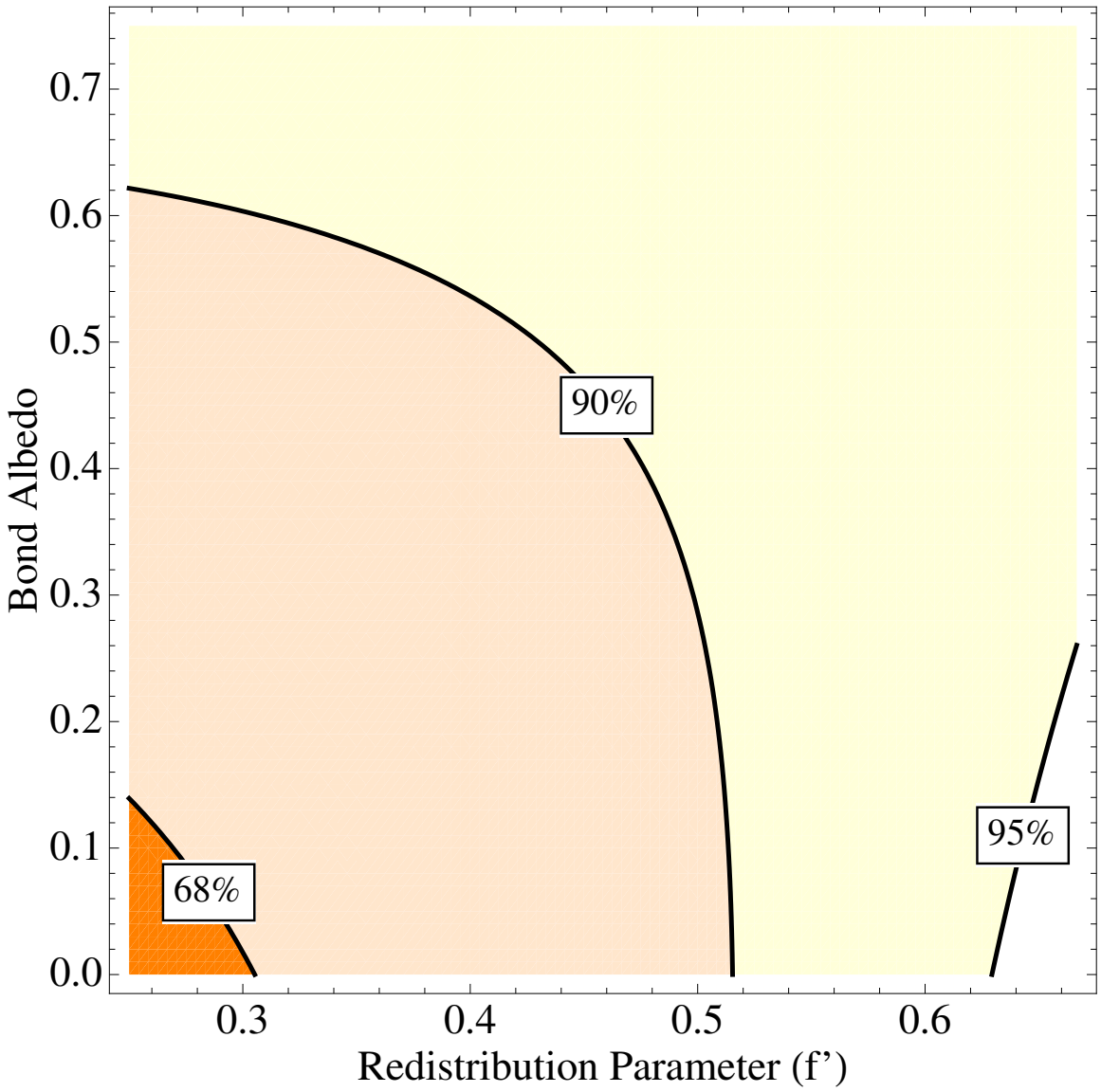

Figure 2.14: Values of the heat redistribution parameter f' and Bond albedo A_B that are excluded at a given confidence level based on the data taken during the secondary eclipse shown in Figure 2.6. The f' parameter describes the efficiency of heat redistribution, and is 1/4 in the case of uniform redistribution, and 2/3 in the case of no redistribution. In between these two extremes f' is not easily related to the amount of heat redistribution. Contours where the eclipse depths are detectable at the 68%, 90%, and 95% confidence level (left to right) are indicated.

M dwarf companion to the primary. For all these reasons, KELT-1b is likely to be a very interesting object for further study, and we expect it will provide a benchmark system to test theories of the emplacement and evolution of short period companions, as well the physics of tidal dissipation and irradiated atmospheres of substellar objects. We will discuss some of these ideas briefly.

2.6.1 Brown Dwarf or Supermassive Planet? KELT-1b and the Brown Dwarf Desert

Is KELT-1b a brown dwarf (BD) or a is it a suppermassive planet? By IAU convention, brown dwarfs (BDs) are defined to have masses between the deuterium burning limit of ~ 13 M_J [Spiegel et al., 2011] and the hydrogen burning limit of ~ 80 M_J (e.g., Burrows et al. 1997). Less massive objects are defined to be planets, whereas more massive objects are stars. By this definition, KELT-1b is a low-mass BD. However, it is interesting to ask whether or not KELT-1b could have plausibly formed in a protoplanetary disk, and therefore might be more appropriate considered a "supermassive planet" [Schneider et al., 2011]. More generally, it is interesting to consider what KELT-1b and systems like it may tell us about the formation mechanisms of close companions with masses in the range of $10 - 100 M_J$.

One of the first results to emerge from precision Doppler searches for exoplanets is the existence of a BD desert, an apparent paucity brown dwarf companions to FGK stars with periods less than a few years, relative to the frequency of stellar companions in the same range of periods [Marcy and Butler, 2000]. Subsequent studies uncovered planetary companions to such stars in this range of periods in abundance [Cumming et al., 2008], indicating that the BD desert is a local nadir in the mass function of companions to FGK stars. The simplest interpretation is that this is the gap between the largest objects that can form in a protoplanetary disk, and the smallest objects that can directly collapse or fragment to form a self-gravitating object in the vicinity of a more massive protostar. Therefore, the location of KELT-1b with respect to the minimum of the brown dwarf mass function might

plausibly provide a clue to its origin.

2.6.1.1 Comparison Sample of Transiting Exoplanets, Brown Dwarfs, and Low-mass Stellar Companions

In order to place the parameters of KELT-1b in context, we construct a sample of transiting exoplanets, BDs, and low-mass stellar companions to main sequence stars. We focus only on transiting objects, which have the advantage that both the mass and radius of the companions are precisely known[7]. We collect the transiting exoplanet systems from the Exoplanet Data Explorer (exoplanets.org, Wright et al. 2011), discarding systems for which the planet mass is not measured. We supplement this list with known transiting brown dwarfs [Deleuil et al., 2008, Johnson et al., 2011, Bouchy et al., 2011b,a, Anderson et al., 2011]. We do not include the system discovered by [Irwin et al., 2010], because a radius measurement for the brown dwarf was not possible. We also do not include 2M0535−05 [Stassun et al., 2007], because it is a young, double BD system. We add several transiting low-mass stars near the hydrogen burning limit [Pont et al., 2005, 2006a, Beatty et al., 2007]. We adopt the mass of XO-3b from the discovery paper [Johns-Krull et al., 2008], which is $M_P = 13.1 \pm 0.4$ M_J, which straddles the deuterium burning limit [Spiegel et al., 2011]. However, later estimates revised the mass significantly lower to $M_P = 11.8 \pm 0.6$ [Winn et al., 2008]. We will therefore categorize XO-3b as an exoplanet.

The disadvantage of using samples culled from transit surveys is that the sample size is much smaller, and transit surveys have large and generally unquantified selection biases (e.g., Gaudi et al. 2005, Fressin et al. 2009), particularly ground-based transit surveys. We emphasize that such biases are almost certainly present in the sample we construct. We

[7] In contrast, for companions detected only via RVs, only the minimum mass is known. Of course, one can make an estimate of the posterior probability distribution of the true mass given a measured minimum mass by adopting a prior for the distribution of inclinations (e.g., Lee et al. 2011). However, this procedure can be particularly misleading in the case of BDs: if BDs are indeed very rare, then objects with minimum mass in the BD desert are more likely to be stellar companions seen at low inclination. Anecdotally, in those cases where constraints on the inclinations can be made, companions with minimum mass near the middle of the brown dwarf desert often do turn out to be stars (e.g., Sahlmann et al. 2011, Fleming et al. 2012).

have therefore made no effort to be complete. The comparisons and suggestions we make based on this sample should not be considered definitive, but rather suggestive.

Figure 2.15 places KELT-1b among the demographics of known transiting companions to main sequence stars, focusing on massive exoplanets, BDs, and low-mass stars with short periods of $\lesssim 30$ days. KELT-1b has the tenth shortest period of any transiting exoplanet or BD known. It has the sixth shortest period among giant ($M_P \gtrsim 0.1$ M_J) planets, with only WASP-19b, WASP-43b, WASP-18b, WASP-12b, OGLE-TR-56b, and HAT-P-23b having shorter periods. KELT-1b is more massive by a factor ~ 3 than the most massive of these, WASP-18b [Hellier et al., 2009]. KELT-1b has a significantly shorter period than any of the previously known transiting brown dwarfs, by a factor of $\gtrsim 3$. KELT-1b therefore appears to be located in a heretofore relatively unpopulated region of the $M_P - P$ parameter space for transiting companions.

Although the KELT-1 system is relatively unique, it is worth asking if there are any other known systems that bear some resemblance to it. The $M_P \simeq 18\,M_J$, $P \simeq 1.3$ day RV-discovered companion to the M dwarf HD 41004B [Zucker et al., 2003] has similar minimum mass and orbit as KELT-1b, however the host star is obviously quite different. Considering the host star properties as well, perhaps the closest analogs are WASP-18b [Hellier et al., 2009], WASP-33b [Collier Cameron et al., 2010a], and KOI-13b [Mazeh et al., 2012, Mislis and Hodgkin, 2012]. All three of these systems consist of relatively massive ($M_p \gtrsim 3$ M_J) planets in short ($\lesssim 2$ day) orbits around hot ($T_{\rm eff} \gtrsim 6500$ K) stars.

The mass of KELT-1b (~ 27 M_J) is close to the most arid part of the BD desert, estimated to be at a mass of 31^{+25}_{-18} M_J according to Grether and Lineweaver [2006]. Thus, under the assumption that the BD desert reflects the difficulty of forming objects with this mass close to the parent star under *any* formation scenario, KELT-1b may provide an interesting case to test these various models. For disk scenarios, gravitational instability can likely form such massive objects, but likely only at much larger distances [Rafikov, 2005, Dodson-Robinson et al., 2009, Kratter et al., 2010]. The maximum mass possible from

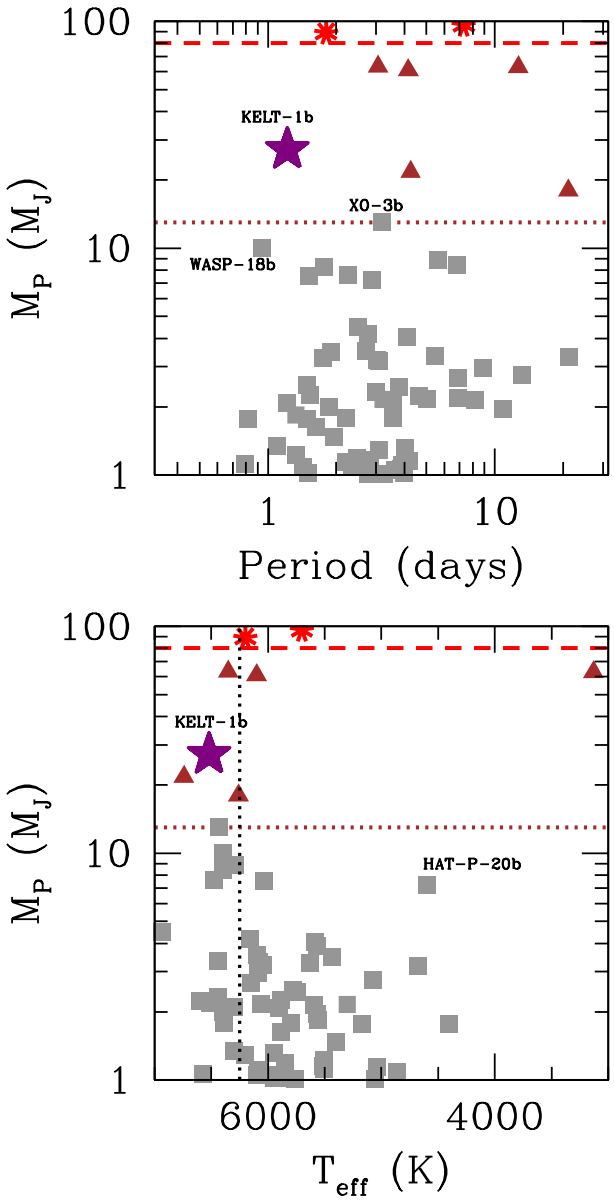

Figure 2.15: Top panel: mass vs. period for the known transiting companions to main-sequence stars with companion masses in the range $1-100$ M_J. An estimate of the deuterium burning limit [Spiegel et al., 2011] is shown as the horizontal dotted line, while the hydrogen burning limit is shown as the horizontal dashed line. Brown dwarfs are shown as triangles, exoplanets as squares, and low-mass stars as asterisks. KELT-1b is shown as the large star. It is the shortest period transiting brown dwarf currently known. Bottom panel: mass vs. host star effective temperature $T_{\rm eff}$ for the sample of transiting companions shown in the top panel. As suggested by Bouchy et al. [2011a], there is some evidence that massive ($M_P \gtrsim 5$ M_J companions are preferentially found around hot ($T_{\rm eff} \gtrsim 6000$K) stars, and KELT-1b follows this possible trend. The vertical line shows the division between hot and cool stars of $T_{\rm eff} = 6250$K suggested by Winn et al. [2010]. Note that we exclude the BD companion to NLTT 41135 [Irwin et al., 2010], and the double BD transit system 2M0535−05 [Stassun et al., 2007] in this and subsequent plots.

core accretion is poorly understood, but may be as large as ~ 40 M_J [Mordasini et al., 2009]. The possibility of significant migration of KELT-1b from its birth location to its present position must also be considered, particularly given the existence of a possible stellar companion to KELT-1 (§2.3.5). This possibility complicates the interpretation of the formation of KELT-1b significantly. For example, it has been suggested that brown dwarf companions are more common at larger separations [Metchev and Hillenbrand, 2009]; thus KELT-1b may have formed by collapse or fragmentation at a large separation, and subsequently migrated to its current position via the Kozai-Lidov mechanism [Kozai, 1962, Lidov, 1962].

One clue to the origin of KELT-1b and the BD desert may be found by studying the frequency of close BD companions to stars as a function of the stellar mass or temperature. Figure 2.15 shows the mass of known transiting short period companions as a function of the effective temperature of the host stars. As pointed out by Bouchy et al. [2011a], companions with $M_P \gtrsim 5\ M_{\rm Jup}$ appear to be preferentially found around hot stars with $T_{\rm eff} \gtrsim 6000$ K, and KELT-1b follows this trend. Although these hot stars are somewhat more massive, the most dramatic difference between stars hotter and cooler than 6000 K is the depth of their convection zones. This led Bouchy et al. [2011a] to suggest that tides may play an important role in shaping the frequency and distribution of massive exoplanet and brown dwarf companions to old stars. Some evidence for this has been reported by Winn et al. [2010], who argue that hot ($T_{\rm eff} \geq 6250$K) stars with close companions preferentially have high obliquities, suggesting that if the emplacement mechanisms are similar for all stars, tidal forces must later serve to preferentially bring cool host stars into alignment. Figure 2.16 shows the distribution of spin-orbit alignments for transiting planets versus the host star effective temperature. KELT-1b falls in the group of hot stars with *small* obliquities. Interestingly the other massive $\gtrsim 5\ M_{\rm Jup}$ planets are also located in this group.

We discuss the possible formation and evolutionary history of KELT-1b, and the likely role of tides in this history, in more detail below. We remain agnostic about the classifica-

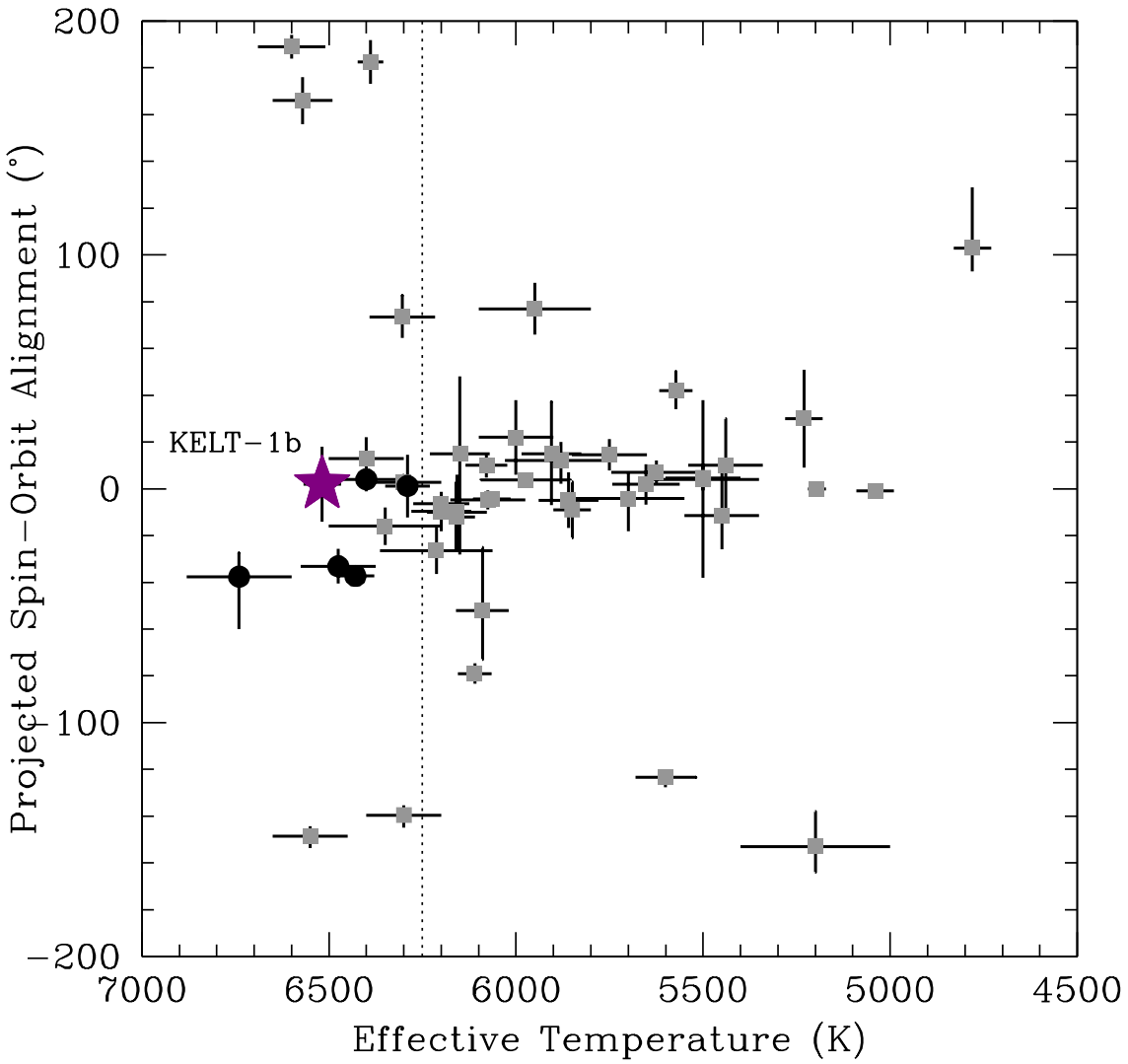

Figure 2.16: Projected spin-orbit alignment angle λ for transiting planets as measured by the RM effect vs. the effective temperature of the host star, following Winn et al. [2010]. The grey squares show exoplanets with mass $M_P < 5\ M_{\rm Jup}$, whereas the black circles show those with $M_P > 5 M_{\rm Jup}$. KELT-1b, shown with a star, is the first transiting brown dwarf with a RM measurement. Its orbit normal is consistent with being aligned with the projected host star spin axis. The dotted vertical line shows the suggested dividing line between hot and cool stars by Winn et al. [2010].

tion of KELT-1b as a brown dwarf or supermassive planet.

2.6.2 Tides, Synchronization, and Kozai Emplacement

Given the relatively large mass and short orbital period of KELT-1b, it seems probable that tides have strongly influenced the past evolution of the system, and may continue to be affecting its evolution. The literature on the influence of tides on exoplanet systems is vast (see, e.g., Rasio et al. 1996, Ogilvie and Lin 2004, Jackson et al. 2008, Leconte et al. 2010, Matsumura et al. 2010, Hansen 2010, for but a few examples), and there appears to be little consensus on the correct treatment of even the most basic physics of tidal dissipation, with the primary uncertainties related to where, how, and on what time scale the tidal energy is dissipated.

While we are interested in evaluating the importance of tides on the evolution of the orbit of KELT-1b and the spin of KELT-1, delving into the rich but difficult subject of tides is beyond the scope of this paper. We therefore take a somewhat heuristic approach. Specifically, we construct a few dimensionless quantities that likely incorporate the primary physical properties of binary systems that determine the scale of tidal evolution, but do not depend on the uncertain physics of energy dissipation. Specifically, we define,

$$\mathscr{T}_a \equiv \frac{M_*}{M_P}\left(\frac{a}{R_*}\right)^5, \quad \text{and} \tag{2.7}$$

$$\mathscr{T}_{\omega_*} \equiv \left(\frac{M_*}{M_P}\right)^2\left(\frac{a}{R_*}\right)^3. \tag{2.8}$$

For some classes of theories of tidal dissipation and under some assumptions, $\mathscr{T}_a$ is proportional to the e-folding timescale for decay of the orbit, and $\mathscr{T}_{\omega_*}$ is proportional to the timescale for synchronization of the spin of the star with the companion orbital period. It is worthwhile to note that for transiting planet systems the combinations of parameters M_P/M_* and a/R_* are generally much better determined than the individual parameters. In particular, the ratio of the mass of the planet to that of the star is closely related to the

RV semi-amplitude K, whereas a/R_* is closely related to the ratio of the duration of the transit to the period [Winn, 2010]. Figure 2.17 shows $\mathscr{T}_a$ and $\mathscr{T}_{\omega_*}$ as a function of orbital period for the sample of transiting exoplanets, brown dwarfs, and low-mass stars discussed previously. KELT-1b has shorter timescales than nearly the entire sample of systems, with the exception of a few of the low-mass stars. We therefore expect tidal effects to be quite important in this system.

As a specific example, under the constant time lag model [Hut, 1981, Matsumura et al., 2010], and assuming dissipation in the star, zero eccentricity, zero stellar obliquity, and a slowly rotating star, the characteristic time scale for orbital decay due to tides is $\tau_{decay} \equiv a/|\dot{a}| = (12\pi)^{-1} Q'_* \mathscr{T}_a P$, where Q'_* is related to the dimensionless tidal quality factor. For KELT-1b, $\mathscr{T}_a \sim 3 \times 10^4$, and so $\tau_{decay} \sim 0.3$ Gyr for $Q'_* = 10^8$, clearly much shorter than the age of the system. Similarly, the time scale for spinning up the star by the companion is $\tau_{synch} \equiv \omega_*/|\dot{\omega}_*| \propto Q'_* \mathscr{T}_{\omega_*} P$ [Matsumura et al., 2010], and so is also expected to be short compared to the age of the system.

Given the expected short synchronization time scale and the fact that the expected time scale for tidal decay is shorter than the age of the system, it is interesting to ask whether or not the system has achieved full synchronization, thus ensuring the stability of KELT-1b. The measured projected rotation velocity of the star is $v \sin I_* = 56 \pm 2$ km s^{-1}, which given the inferred stellar radius corresponds to a rotation period of $P_* = 2\pi R_* \sin I_* / v \sin I_* = [1.322 \pm 0.053] \sin I_*$ days, which differs from the orbital period of KELT-1b by $\sim 2\sigma$ for $I_* = 90^\circ$. This is suggestive that the system is indeed synchronized. The small discrepancy could either be due to a slightly underestimated uncertainty on $v \sin I_*$, or the host could be moderately inclined by $I_* \sim [67 \pm 7]^\circ$. However, one might expect the obliquity of the star to be realigned on roughly the same time scale as the synchronization of its spin [Matsumura et al., 2010]. The stellar inclination can also be constrained by the precise shape of the transit light curve: lower inclinations imply higher rotation velocities, and thus increased oblateness and gravity brightening [Barnes, 2009]. Ultimately, the inclination is limited to

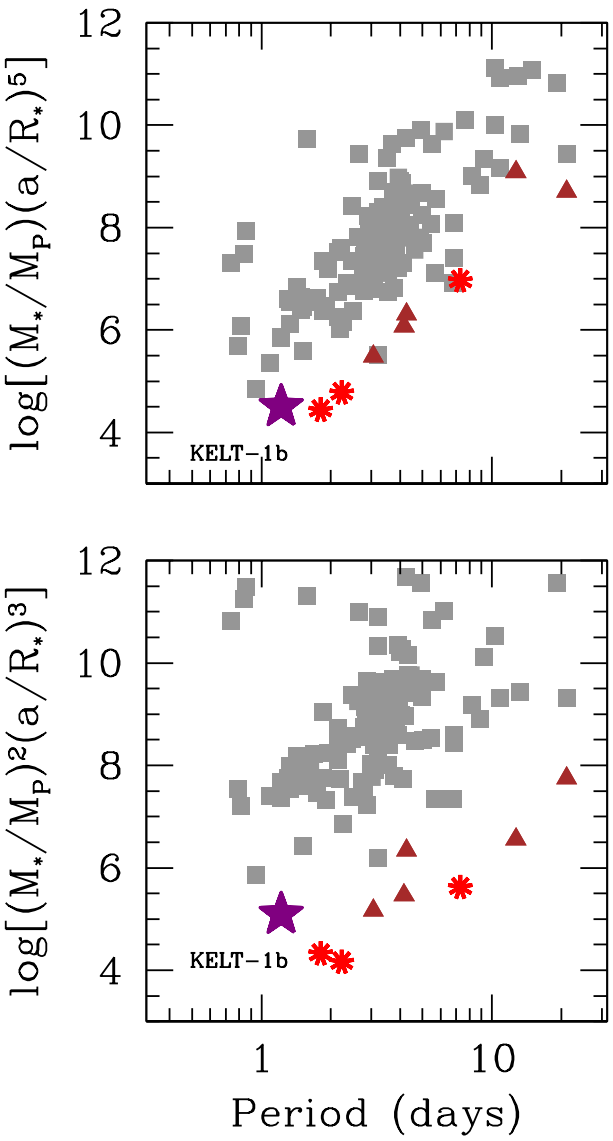

Figure 2.17: Dimensionless combinations of physical parameters that quantify the relative time scale for orbital tidal decay (top panel) and stellar spin-orbit synchronization (bottom panel) for different binary systems, as a function of the orbital period of the system. See §2.6.2 for an explanation and assumptions. Brown dwarfs are shown as triangles, exoplanets as squares, and low-mass stars as asterisks. KELT-1b is shown as the large star. Among known transiting exoplanets and brown dwarfs, it has the shortest characteristic time scale for orbital decay and synchronization.

$I_* \gtrsim 10^\circ$ in order to avoid break up.

We can also ask, given the known system parameters, if the system is theoretically expected to be able to achieve a stable synchronous state. A system is "Darwin stable" [Darwin, 1879, Hut, 1980] if its total angular momentum,

$$L_{tot} = L_{orb} + L_{\omega,*} + L_{\omega,P} \tag{2.9}$$

is more than the critical angular momentum of

$$L_{crit} \equiv 4 \left[\frac{G^2}{27} \frac{M_*^3 M_P^3}{M_* + M_P} (C_* + C_P) \right]^{1/4}, \tag{2.10}$$

where L_{orb} is the orbital angular momentum, L_{ω_*} is the spin angular momentum of the star, $L_{\omega,P}$ is the spin angular momentum of the planet, and $C_* = \alpha_* M_* R_*^2$ and $C_P = \alpha_P M_P R_P^2$ are the moments of inertia of the star and planet, respectively [Matsumura et al., 2010]. Since $C_P/C_* \sim (M_P/M_*)(R_P/R_*)^2 \sim 10^{-3}$, the contribution from the planet spin to the total angular momentum is negligible. We find $L_{tot}/L_{crit} = 1.029 \pm 0.014$, marginally above the critical value for stability. In addition, we find $(L_{\omega,*} + L_{\omega,P})/L_{orb} = 0.154 \pm 0.006$, which is smaller than the maximum value of $1/3$ required for a stable equilibrium [Hut, 1980]. Curiously, if we assume the star is already tidally synchronized, we instead infer $(L_{\omega,*} + L_{\omega,P})/L_{orb} = 0.167 \pm 0.004$, i.e., remarkably close to exactly one-half the critical value of 1/3.

Two additional pieces of information potentially provide clues to the evolutionary history of this system: the detection of a possible tertiary (§2.3.5; Fig.2.8), and the measurement of the RM effect (Fig. 2.4), demonstrating that KELT-1 has small projected obliquity. If the nearby companion to KELT-1 is indeed bound, it could provide a way of emplacing KELT-1b in a small orbit via the Kozai-Lidov mechanism [Kozai, 1962, Lidov, 1962]. If KELT-1b were originally formed much further from its host star, and on an orbit that was significantly misaligned with that of the putative tertiary, then its orbit might subsequently

be driven to high eccentricity via secular perturbations from the tertiary [Holman et al., 1997, Lithwick and Naoz, 2011, Katz et al., 2011]. If it reached sufficiently high eccentricity such that tidal effects became important at periastron, the orbit would be subsequently circularized at a relatively short period [Fabrycky and Tremaine, 2007, Wu et al., 2007, Socrates et al., 2012]. Nominally, one might expect the orbit of KELT-1b to be then left with a relatively large obliquity [Naoz et al., 2011]. The measured projected obliquity is $\lesssim 16$ degrees, implying that either the current true obliquity is small, or the star is significantly inclined (i.e., $I_* \sim 0$). However, if the star is significantly inclined, then the system cannot be synchronized. Perhaps a more likely alternative is that, after emplacement by the tertiary and circularization of the orbit, the system continued to evolve under tidal forces, with KELT-1b migrating inward to its current orbit while damping the obliquity of KELT-1 and synchronizing its spin period. Clearly, detailed simulations are needed to establish whether or not this scenario has any basis in physical reality.

2.6.3 Comparison to Theoretical Models of Brown Dwarfs

Transiting brown dwarfs provide one of the only ways to test and calibrate models of BD structure and evolution, which are used to interpret observations of the hundreds of free floating brown dwarfs for which no direct measurement of mass and radius is possible. Given that only 5 transiting brown dwarfs with radius measurements were previously known, KELT-1b potentially provides another important test of these models. Figure 2.18 shows the mass-radius relation for the known transiting companions to main-sequence stars with companion masses in the range $10-100\,M_J$. Being close to the minimum in the brown dwarf desert, the mass of KELT-1b begins to fill in the dearth of know systems between $\sim 20-60\,M_{\rm Jup}$. Furthermore, the formal uncertainty in its radius is only $\sim 2.5\%$, thereby allowing for a stringent test of models. In contrast, the two transiting BDs with similar masses, CoRoT-3b [Deleuil et al., 2008] and KOI-423b [Bouchy et al., 2011a], have much larger radius uncertainties, presumably due to the relative faintness of the host stars.

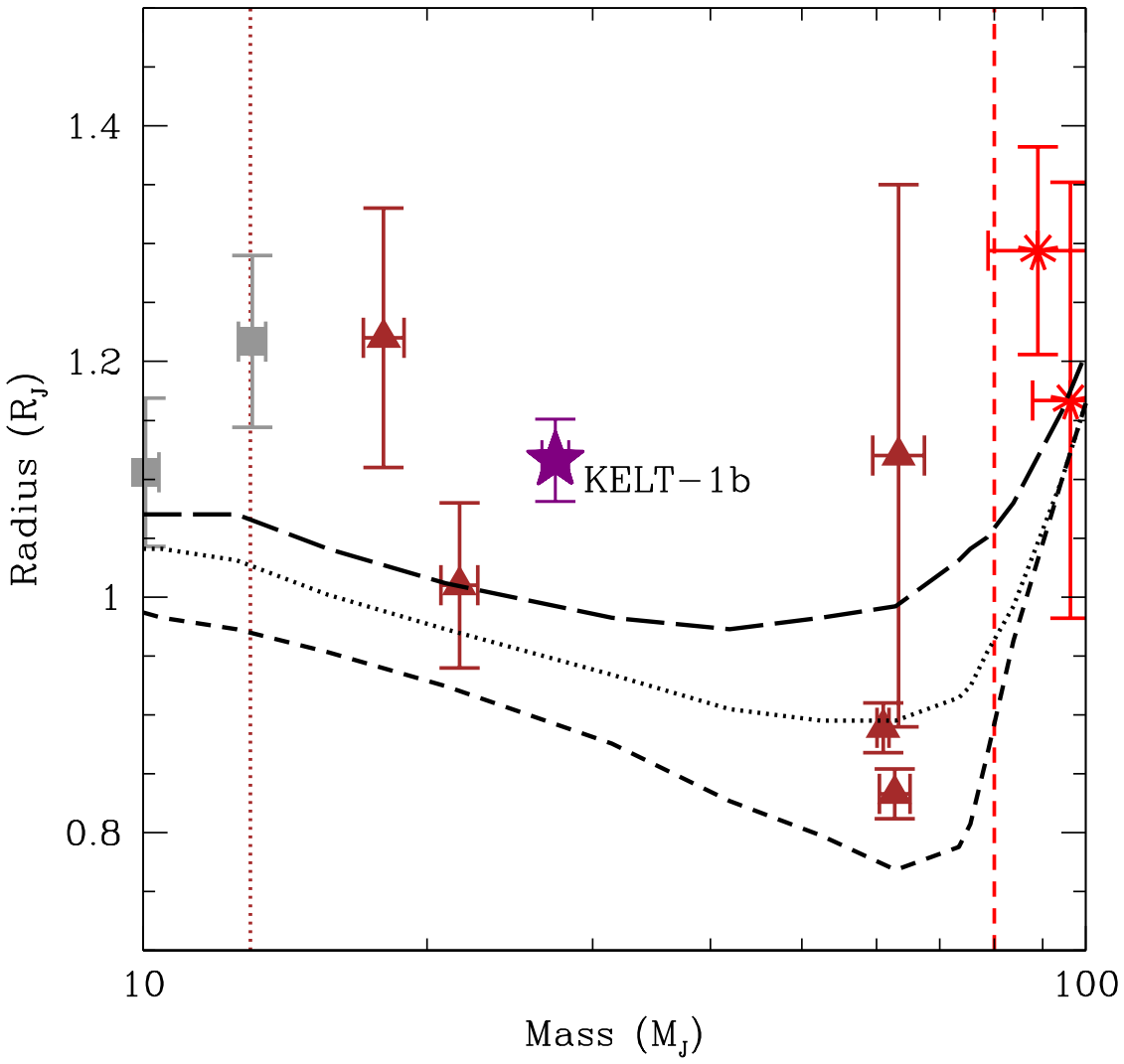

Figure 2.18: Radius vs. mass for the known transiting companions to main-sequence stars with companion masses in the range $10-100\,M_J$ that have measured radii. An estimate of the deuterium burning limit [Spiegel et al., 2011] is shown as the vertical dotted line, and the hydrogen burning limit is shown as the vertical dashed line. Brown dwarfs are shown as triangles, exoplanets as squares, and low-mass stars as asterisks. KELT-1b is shown as the large star. Predicted radii as a function of mass for isolated objects from the isochrones of Baraffe et al. [2003] are shown for an age of 5 Gyr (dashed), 1 Gyr (dotted), and 0.5 Gyr (long dashed); the true age of the KELT-1 system is almost certainly between 1 and 5 Gyr. Although stellar insolation is likely to increase the radii at fixed mass, Bouchy et al. [2011b] predict that the effect is small. KELT-1b therefore has an anomalously large radius.

Evolutionary models for isolated BDs generally predict that young (~ 0.5 Gyr) objects in the mass range $10-100$ $M_{\rm Jup}$ should have radii of $\sim R_{\rm Jup}$ (see the models of Baraffe et al. 2003 in Fig. 2.18). As these objects cool, however, their radii decrease, particularly for masses between 50 and 80 $M_{\rm Jup}$. After ~ 1 Gyr, all isolated objects with mass between 20-80 $M_{\rm Jup}$ are predicted to have radii $< R_{\rm Jup}$. The radius we measure for KELT-1b is $R_P = 1.110^{+0.032}_{-0.022}$ $R_{\rm Jup}$, which, at a mass of $M_P = 27.23^{+0.50}_{-0.48}$ $M_{\rm Jup}$, is ~ 7 σ and ~ 10 σ larger than the radius predicted by Baraffe et al. [2003] for ages of 1 Gyr and 5 Gyr, respectively. KELT-1b is strongly irradiated, which in principle can delay its cooling and contraction. However, Bouchy et al. [2011b] predict that the effect of insolation is small for brown dwarfs in this mass range, although their models were for a much more modest insolation corresponding to an equilibrium temperature of 1800 K (versus $\sim$ 2400K for KELT-1b). Therefore, given the estimated $1.5-2$ Gyr age of the system, KELT-1b is likely to be significantly inflated relative to predictions.

Using the benchmark double transiting BD 2M0535$-$05, Gómez Maqueo Chew et al. [2009] explore models in which brown dwarfs have large spots, which reduce the flux from their surface, thereby decreasing their effective temperatures and increasing their radii relative to those without spots (see also Bouchy et al. [2011b]). They find that these can lead to significantly inflated radii, but only for large spot filling factors of $\sim 50\%$, and for relatively young (~ 0.5 Gyr) systems. However, a detailed spectroscopic analysis of that system by Mohanty et al. [2010] and Mohanty and Stassun [2012], shows that surface spots cannot be present with such a large filling factor, and thus favor global structural effects such as strong internal magnetic fields (e.g., Mullan and MacDonald 2010). Many other mechanisms have been invoked to explain the inflated radii of some giant exoplanets (see Fortney and Nettelmann 2010 for a review), however it is not clear which, if any, of the many mechanisms that have proposed may also be applied to inflated brown dwarfs.

We would be remiss if we did not question whether we were erroneously inferring a large radius for the planet. In the past, such situations have arisen when there is a discrep-

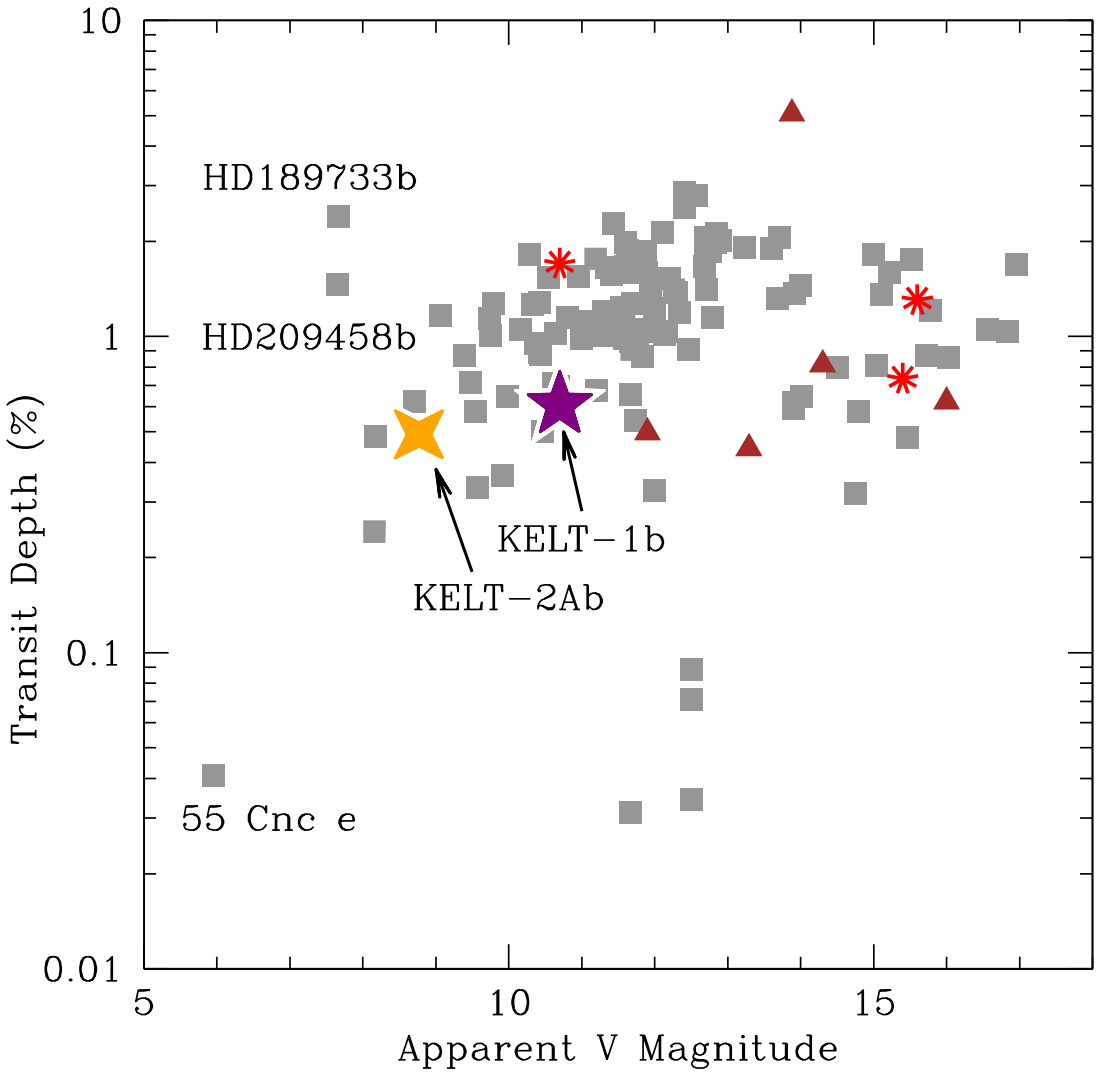

Figure 2.19: Transit depth assuming no limb darkening, i.e., $(R_P/R_*)^2$, as a function of the apparent V magnitude of the host star for a sample of transiting systems. Brown dwarfs are shown as triangles, exoplanets as squares, and low-mass stars as asterisks. KELT-1b is shown as the large star. All else being equal, objects in the top left provide the best targets for follow-up. KELT-1b has a similar transit depth as the other known transiting brown dwarfs, but is significantly brighter. Also labeled are some other benchmark systems. KELT-2b ($M_P \sim 1.5\ M_{\rm Jup}$) is shown as a large cross [Beatty et al., 2012].

ancy between the constraint on the stellar density from the light curve and the constraint on the stellar surface gravity of the star from spectroscopy (e.g., Johns-Krull et al. 2008, Winn et al. 2008). In our case, we find no such tension. The parameters of the star inferred from the spectroscopic data alone are in nearly perfect agreement with the results from the global analysis of the light curve, RV data, and spectroscopic constraints. We note that the effect of allowing a non-zero eccentricity also has a negligible effect on the inferred planetary radius. Finally, we reiterate that the faint companion detected in AO imaging (§2.3.5), which is unresolved in our follow-up photometry, has a negligible effect on our global fit and inferred parameters. Therefore, we believe our estimate of R_P is likely robust.

We conclude by noting that there is a need for predictions of the radii of brown dwarfs for a range of ages and stellar insolations, and it would be worthwhile to explore whether or not the inflation mechanisms that have been invented to explain anomalously large giant planets might work for much more massive and dense objects as well.

2.6.4 Prospects for Follow Up

Figure 2.19 compares the transit depth and apparent visual magnitude of the KELT-1 system ($\delta \sim 0.6\%$, $V = 10.7$) to the sample of transiting systems collected in §2.6.1.1 with available V magnitudes. KELT-1 is not particularly bright compared to the bulk of the known transiting exoplanet hosts. However, it is significantly brighter than the hosts of all known transiting brown dwarfs; the next brightest is WASP-30 [Anderson et al., 2011], which is ~ 1.2 magnitudes fainter. On the other hand, the depth of the KELT-1b transit is similar to that of the other known brown dwarfs.

The prospects for follow-up of KELT-1b are exciting, not only because of the brightness of the host, but also because of the extreme nature of the system parameters, in particular the relatively short orbital period, relatively large stellar radius, and relatively large amount of stellar irradiation received by the planet. Following Mazeh and Faigler [2010] and Faigler and Mazeh [2011], we can estimate the amplitudes of ellipsoidal variations A_{ellip}, Doppler

beaming A_{beam} (see also Loeb and Gaudi 2003), reflected light eclipses and phase variations A_{ref}, and thermal light eclipses and phase variations A_{therm},

$$A_{beam} = \alpha_{beam} 4 \left(\frac{K}{c} \right) \sim 5.7 \alpha_{beam} \times 10^{-5} \quad (2.11)$$

$$A_{ref} = \alpha_{ref} \left(\frac{R_P}{a} \right)^2 \sim 4.6 \alpha_{ref} \times 10^{-4} \quad (2.12)$$

$$A_{ellip} = \alpha_{ellip} \frac{M_P}{M_*} \left(\frac{R_*}{a} \right)^3 \sim 4.1 \alpha_{ellip} \times 10^{-4} \quad (2.13)$$

$$A_{therm} = \alpha_{therm} \left(\frac{R_P}{R_*} \right)^2 \left(\frac{R_*}{a} \right)^{1/2} \sim 3.2 \alpha_{therm} \times 10^{-3}, \quad (2.14)$$

where the expression for A_{therm} assumes observations in the Rayleigh-Jeans tail of both objects, and the expression for A_{ellip} assumes an edge-on orbit. The dimensionless constants α are defined in Mazeh and Faigler [2010], but to make contact with the secondary eclipse analysis in §2.5.4 we note that $\alpha_{ref} = A_g$ and $\alpha_{therm} = [f'(1-A_B)]^{1/4}$. All of these constants are expected to be of order unity, except for α_{ref}, which may be quite low for strongly irradiated planets, depending on wavelength [Burrows et al., 2008]. Based on previous results, all of these effects with the possible exception of Doppler beaming are likely to be detectable with precision photometry (see, e.g., Cowan et al. 2012). For ellipsoidal variations in particular, we expect $\alpha_{ellip} \sim 2$ and thus a relatively large amplitude of $A_{ellip} \sim 10^{-3}$. Furthermore, the detection of all these signals is facilitated by the short orbital period for KELT-1b.

The prospects for transmission spectroscopy are probably poorer, given the relatively small planet/star radius ratio (~ 0.078) and more importantly the large surface gravity for KELT-1b. For the optimistic case of $T_{eq} \simeq 2400$K assuming zero albedo and perfect redistribution, the scale height is only $H \sim kT/(\mu m_H g_P) \sim 16$ km, and thus will only lead to changes in the transit depth of order $\sim 2H/R_P \sim 0.04\%$.

2.7 Summary

We have presented the discovery of KELT-1b, the first transiting low-mass companion from the wide-field Kilodegree Extremely Little Telescope-North (KELT-North) transit survey. The host star KELT-1 is a mildly evolved, solar-metallicity, rapidly-rotating, mid-F star with an age of $\sim 1.5-2$ Gyr located at a distance of ~ 260 pc. The transiting companion is a low-mass brown dwarf or supermassive planet with mass $\sim 27\ M_{\rm Jup}$, on a very short period, circular orbit of $P \sim 1.2$ days.

In many ways, the KELT-1 system is quite unusual and extreme: KELT-1b receives a large amount of stellar insolation, is inflated relative to theoretical predictions, and raises strong tides on its host. The obliquity of KELT-1 is consistent with zero, and there is evidence that the spin of KELT-1 has been synchronized with the orbital period of KELT-1. Finally, there is a likely M-dwarf stellar companion to the KELT-1 system with a projected separation of ~ 150 AU. As the first definitively inflated transiting brown dwarf, KELT-1b demonstrates the need for models of brown dwarfs subject to a range of stellar insolations.

A plausible formation scenario for this system posits that KELT-1b formed on a much wider orbit, and was driven to a smaller semimajor axis by the tertiary via the Kozai-Lidov mechanism. The system then continued to evolve under strong tidal forces, with KELT-1b migrating inward to its current orbit, while damping the obliquity of KELT-1 and synchronizing its spin period.

The future evolution of the KELT-1 system may be spectacular. As KELT-1 continues to evolve and its radius increases, so will the tides raised on it by KELT-1b. Assuming KELT-1 is and remains tidally locked, as it cools it will develop a deep convective envelope, but be forced to rotate at an ever increasing rate. In ~ 2 Gyr, KELT-1 will have roughly the temperature of sun, but with a radius of $\sim 2\ R_\odot$ and a rotational velocity of ~ 100 km s^{-1}. At this point, KELT-1 will likely become an active RS CVn star [Walter and Bowyer, 1981]. Eventually, as KELT-1 reaches the base of the giant branch, it will swallow KELT-1b whole, likely resulting in a bright UV/X-ray and optical transient [Metzger et al., 2012].

Chapter 3

Observations of the M82 SN with the Kilodegree Extremely Little Telescope

3.1 Introduction

The study of supernovae to date has been mostly limited to cadences of days or longer. Exploring shorter time scales could shed new light on the nature of the progenitor system, the physics of the explosions, and possibly also the circumstellar environment. In the first study of its kind, Nugent et al. [2011], Bloom et al. [2012] used observations from the first hours of the optical onset of supernova (SN) SN 2011fe in M 101 to confirm the theoretical expectation that Type Ia supernovae (SNe Ia) are the result of thermonuclear explosions of compact objects, C/O white dwarfs. There is considerable debate concerning the possible systems leading to SNe Ia, in particular the core set ("normals") used as distance indicators in cosmology. A well-sampled lightcurve at early times could yield evidence of interaction with a donor star [e.g., Kasen, 2010], as expected from the single degenerate (SD) model [Whelan and Iben, 1973]. The double degenerate model (DD), where two white dwarfs merge [Tutukov and Yungelson, 1981, Iben and Tutukov, 1984, Webbink, 1984], could also leave a signature in the form of an accretion disk, lasting only for a very short period of time, not sampled by current observational surveys. Highly cadenced observations can also be used to explore the production of short-lived radioactive isotopes in the thermonuclear explosion, as well as the interaction between the ejecta and thin shells of circumstellar material surrounding the exploding star. SN 2014J, the closest "normal" SNIa since the beginning of modern CCD astronomy [Goobar et al., 2014a, Amanullah et al., 2014, Kelly et al., 2014, Marion et al., 2014, Foley et al., 2014, Brown et al., 2014], is a particularly well-suited object for high-precision studies that could help advance our understanding of these objects that are so crucial for cosmology.

3.2 Data and Methods

The M82 SN 2014J was serendipitously observed by the Kilodegree Extremely Little Telescope North (KELT-N) as part of its routine monitoring of the northern sky. The KELT-N telescope is a robotic telescope designed to search for transiting extrasolar planets around bright stars. The optical system consists of an Apogee AP16E CCD (4096×4096 9μm pixels) illuminated by a Mamiya wide-field, medium-format camera lens with 80mm focal length and 42mm aperture ($f/1.9$). The resulting images subtend $26^\circ \times 26^\circ$ at about 23" pixel^{-1}. It employs a Kodak Wratten #8 red-pass filter in front of the lens to mitigate the photometric effects of atmospheric reddening (which are most severe at blue wavelengths). The resulting bandpass resembles a widened Johnson-Cousins R band with effective wavelength $\lambda_{\rm eff} \approx 691$ nm and width ≈ 318 nm. This system is mounted on a Paramount ME robotic telescope mount. KELT-N typically achieves $\sim$1% r.m.s. photometric precision for $V \approx 8$–10, comparable to the brightness of M82 and of SN 2014J at peak brightness. The telescope hardware and operations are detailed more thoroughly in Pepper et al. [2007] and Siverd et al. [2012].

Since SN 2014J sits on top of a bright and highly spatially variable backround due to the underlying host galaxy, it was necessary to adjust our standard data reduction procedures which have been optimized for bright individual stars in the Milky Way. In this section we describe the data that were obtained with KELT-N, as well as the modifications to the standard calibration and data processing that were required for this object. We emphasize that the light curve of SN 2014J presented here is not strongly dependent on the specific choice of various data reduction parameters discussed below. Rather, our intent here is to fully document the detailed procedures that were required to extract a high quality light curve of SN 2014J from a telescope system that was designed and optimized for a very different type of object.

The final light curve that we present and analyze below is provided in Table 3.1.

Table 3.1: KELT light curve of SN 2014J

JD (TT)	Flux (ADU)	Error (ADU)
2456607.033097	-64.77650	171.68029
2456609.038233	127.30780	198.71798
2456611.033137	-207.46240	151.60861
2456616.011700	-55.97750	209.25459
2456616.026432	-80.47890	209.27662

The full table is provided in the electronic journal. A portion is shown here for guidance regarding form and content.

3.2.1 Data

KELT-N began observing new fields near the North Celestial Pole (NCP) in the fall of 2013. One of those fields by chance includes the bright galaxy M82. As part of its routine robotic observing operations, KELT-N observes the field containing M82 several times per night, on average, although the specific cadence varies from night to night depending on Moon and observing conditions. In particular, SN 2014J exploded near full moon. Due to KELT's normal strategy of avoiding observing fields near the full moon, we fortuitously obtained a larger-than-normal number of observations of the M82 field right around the time of explosion. Increased photometric noise in the KELT images of the M82 field due to increased sky brightness from the moon scatter was thus offset by an increased number of data points.

The KELT-North telescope uses a German Equatorial mount, causing a 180-degree rotation between images acquired on the East and West sides of the meridian. In addition, due to a tilt in the optical system, the KELT-North PSF variations are not circularly symmetric. It is therefore possible (and common) to see very different PSFs between East and West. At the location of M82, the effective West PSF size is $\sim 1/3$ smaller than its East counterpart. The smaller effective PSF area admits less sky flux and therefore has better precision, particularly among fainter sources that are dominated by sky flux. As a result, observations in

each orientation must be reduced independently. In order to avoid systematics associated with stitching together data from the two telescope orientations, in our analysis below we generally prefer to utilize the data from only the West orientation because in general the photometry is of higher quality. However we do incorporate the East orientation data as well for increased precision in our light curve feature timing measurements (see below).

In total, we have 1869 science-grade images (980 east, 889 west) acquired between 08 October 2013 and 14 June 2014 (JD 2456573.963 to 2456822.692). The 980 east images were acquired between 08 October 2013 and 01 April 2014 (JD 2456573.963 to 2456748.622) and the west images acquired between 10 November 2013 and 14 June 2014 (JD 2456607.033 to 2456822.692). The combined data set spans the nominal explosion time of JD 2456672.25 (UT) [see Zheng et al., 2014, and see also Sec. 3.3.1], the nominal peak time of JD 2456690.75 (UT), and well into the late-stage dimming of the event.

3.2.2 Dark and Flat Calibration

Nearly half of KELT-N dark frames during the season when SN 2014J was observed exhibit oscillating electrical noise with non-negligible amplitude, and with a length scale a few times larger than a typical point-spread-function full-width-at-half-maximum. This electrical noise arises from electronics that are activated only during dark frame acquisition and therefore does not affect the science frames. If the dark frames are stacked without correction, the resulting master dark frame exhibits pattern noise. In combination with pointing drift, these patterns induce correlated noise in light curves that is difficult to correct, particularly in a case such as SN 2014J where we hope to recover the pre- and post-explosion flux to the lowest levels possible.

Therefore, we generated a new, low-noise master dark frame using images from a previous season and used it to correct all images in this study. In each individual dark frame, we identified and removed the electrical noise in Fourier space. The resulting clean darks were level-matched to compensate for varying bias and then median-stacked with per-pixel

outlier rejection.

We flat-field the dark-subtracted science images with our standard master flat [see Siverd et al., 2012, for details of construction of the master flat].

3.2.3 Gradient Correction and Cloud Removal

After dark and flat calibration, we remove complex background spatial variations with a two-step process. Doing so before the image subtraction procedure prevents corruption of the convolution kernel and improves results, particularly with poor weather and high air mass (see below).

As the first stage of background removal, we remove the overall sky brightness gradient on the largest spatial scales. To do this, we fit a second-degree polynomial to each image with a Huber M-estimator [Huber, 1981], a robust regression procedure that automatically ignores contaminated (non-sky) pixels. We then subtract the best-fit polynomial from each image to remove large-scale sky gradients. Afterward, we add a constant such that the original median image value is restored.

After removing the large-scale gradient polynomial, we identify and mask extreme outliers (above 99th percentile) which include stars, passing airplanes, etc. We then apply a 201x201-pixel 45th percentile smooth to the masked image to map out sky variations on smaller spatial scales in a non-parametric way. We finally subtract the polynomial fit and smoothed image from the calibrated image and add a constant so that again the median image value is preserved.

3.2.4 Image Subtraction

The heart of the KELT light curve production process is image subtraction-based aperture photometry. In our standard procedure, KELT-N images are divided into 5x5 subframes of 816x816 pixels, each of which is processed separately. Unfortunately, by chance, M82 falls on an interior corner of the usual KELT-N subframes. This led to poor photomet-

ric results from our standard pipeline [see Siverd et al., 2012, for further details]. In order to improve the quality of the photometric extraction for SN 2014J, we chose to proceed with a single 816x816 subframe centered on M82, extracted after image registration. Then we proceeded to process this subframe via our usual image subtraction procedures with usual parameter choices. Importantly, we build our reference image exclusively from pre-explosion data to simplify the analysis as much as possible. Finally, we obtain an accurate WCS coordinate solution for our reference image using Astrometry.net [Lang et al., 2010].

In addition to the supernova, we extract light curves for numerous other stars in the area and use these to verify pipeline performance and estimate accurate photometric uncertainties. Including SN 2014J, we extracted 1874 Western and 1699 Eastern light curves. Because the supernova is not visible in our reference image, we adopt the R.A. and Dec coordinates from Goobar et al. [2014a] and convert these to pixel coordinates using the aforementioned reference image WCS.

3.2.5 Accurate Photometric Uncertainties

Due to optical vignetting and our preprocessing routines, the standard photometric uncertainties produced by our ISIS-based [Alard and Lupton, 1998, Alard, 2000] pipeline are often not reliable. Therefore, we instead determine the photometric uncertainties separately using a noise model fit to an ensemble of ~ 2000 nearby stars (see Figure 3.1). This process is complicated by two factors. First, the flux from SN 2014J changes significantly in time. Second, SN 2014J resides in front of a bright galaxy and thus "sees" a higher effective sky level than other sources in the area.

Our photometric uncertainty model includes Poisson noise contributions from both the source and the sky, plus an additive term due to unknown systematic errors. Mathetmatically, the RMS deviation (RMSD) is:

$$\mathrm{RMSD}(\bar{e}_{\star tot}, nPix, \bar{e}_{sky}) = \sigma_r + \frac{\sqrt{\bar{e}_{\star tot} + nPix \cdot \bar{e}_{sky}}}{\bar{e}_{\star tot}}$$

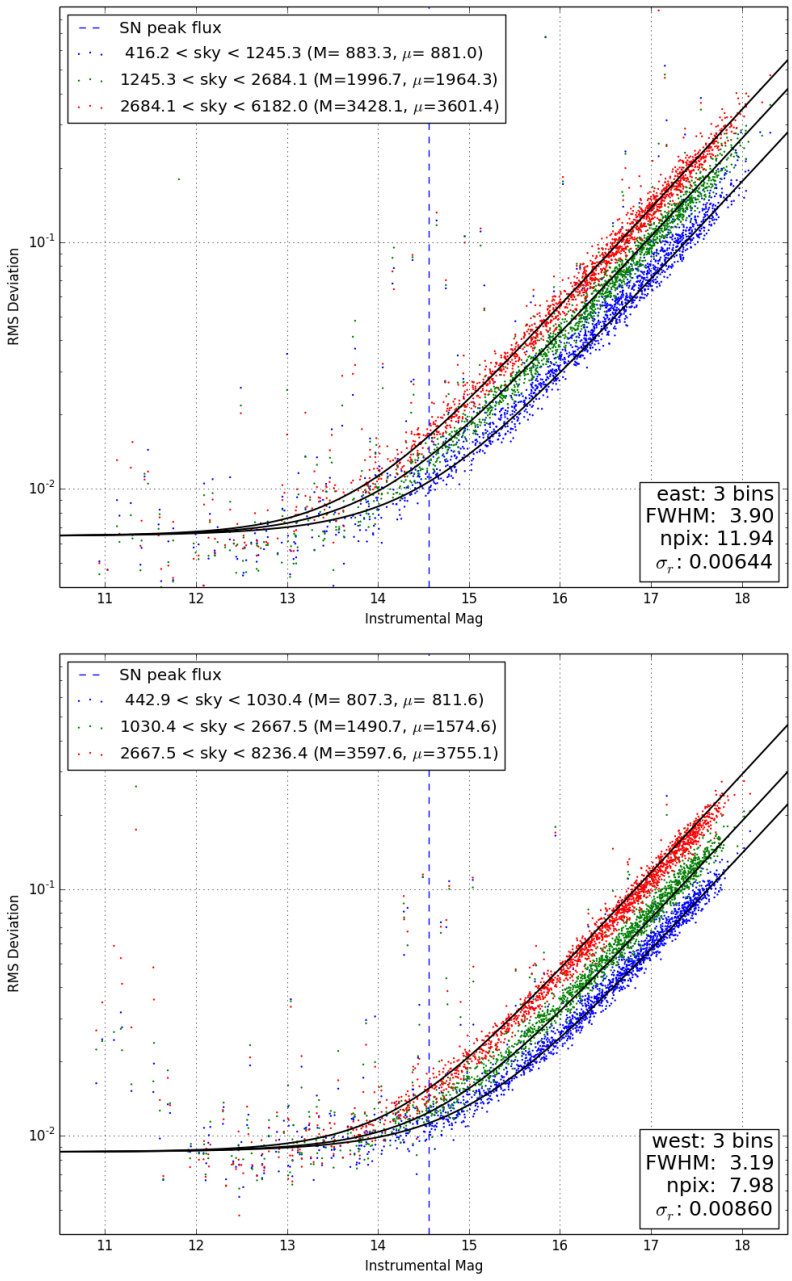

Figure 3.1: KELT noise model for east data (top) and west data (bottom). We characterize our photometric uncertainties empirically using an ensemble of nearly 2000 stars in the vicinity of M82. We find that the KELT-North photometric performance (i.e., light curve scatter as a function of source brightness and sky level) is well approximated by a Poisson noise aperture photometry model with a constant σ_r noise floor. Once the aperture area and noise floor are known, reliable photometric uncertainties may be calculated directly for any target.

where $e^-_{\star tot}$ is the total number of electrons in the star, nPix is the number of pixels in the photometric aperture, e^-_{sky} is the number of sky electrons per pixel, and σ_r is a constant noise floor due to unknown systematics. Though simplistic, this model provides a good description of the observed photometric uncertainty.

Due to the large pixel scale of KELT-N, sky level is a major contributor to the photometric uncertainty and the dominant contribution for sources fainter than $V \approx 10.5$. To capture the dependence on sky level, we create three (equal-N) bins of per-pixel sky counts and separately measure RMSD within each bin. We then fit the uncertainty model above to all three bins simultaneously to determine nPix and σ_r (see Fig. 3.1). For the east, we find nPix = 11.94 and σ_r = 0.00644. For the west, we find nPix = 7.98 and σ_r = 0.00860.

Based on reference image measurements, we adopt a a sky excess of 1360 counts for both eastern and western data. Combined with the nPix and σ_r values fit above, we are able to compute robust photometric uncertainties for each data point in our final SN 2014J light curves.

3.2.6 Conversion of Instrumental to Physical Flux Units

We empirically determine the relationship between KELT instrument response and physical flux in two steps. First, we combine KELT star fluxes with catalog data from Tycho-2 [Høg et al., 2000] and UCAC4 [Zacharias et al., 2013] to measure the offset between the KELT instrumental system and standard filters. We then use this offset to directly relate the KELT count rate to a flux-calibrated star in the Johnson system. We identified stars common to both KELT (east and west) object lists and cross-matched these with the Tycho-2 and UCAC4 catalogs. In total, we found 745 KELT sources with Tycho-2 and UCAC4 entries. We then robustly fit a straight line using the Theil-Sen estimator [Sen, 1968] to $(R - R_K)$ vs. $(B - V)$ to determine the KELT instrumental offset (Figure 3.2).

We assume for simplicity that SN 2014J has the color of an A0V star. An A0V star at 0th mag has R-band flux of 1.75×10^{-9} erg s^{-1} cm^{-2} Å^{-1} [Cox, 2000] and produces

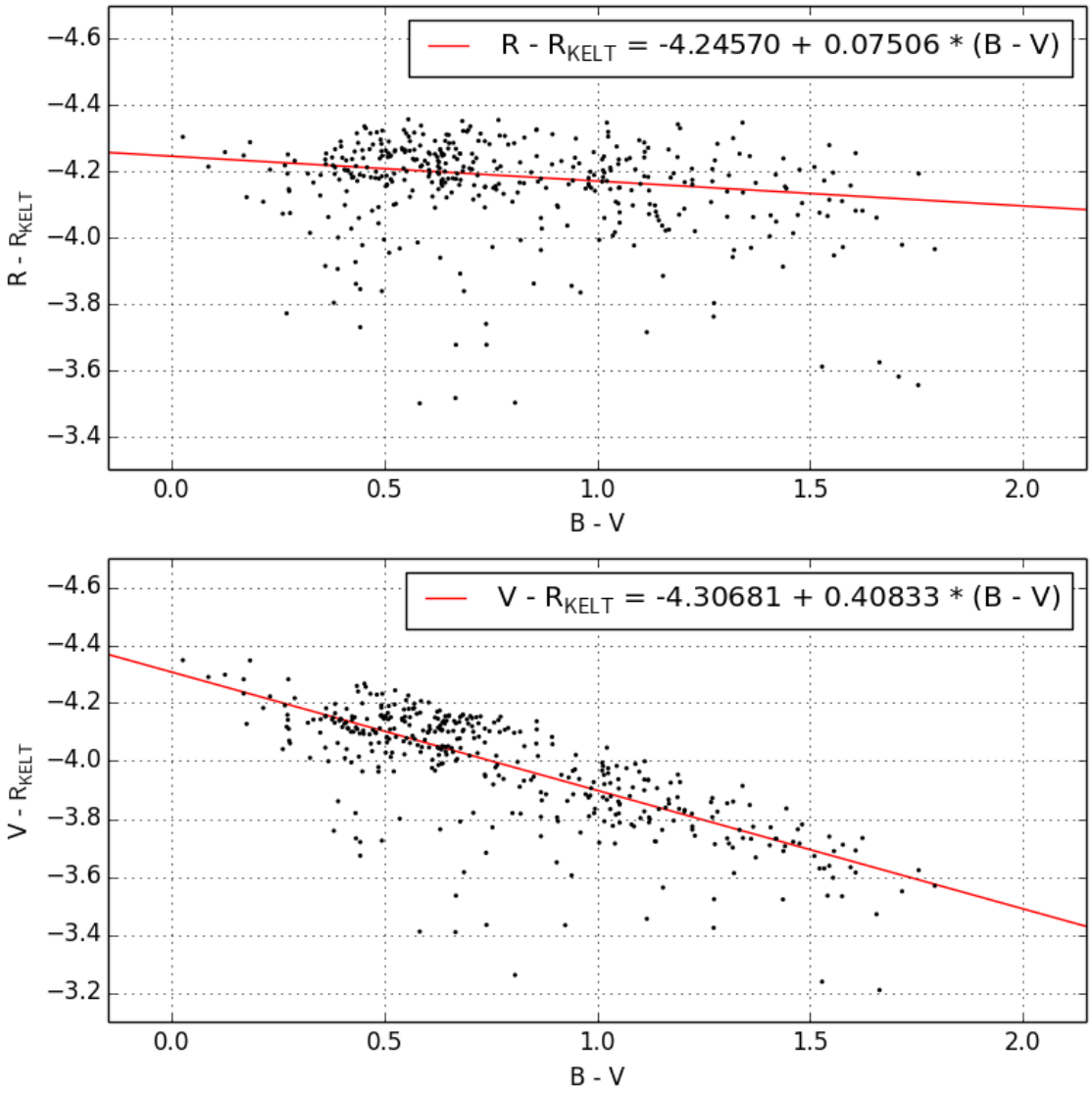

Figure 3.2: Relationships between the KELT-North instrumental system and Johnson V and R magnitudes (see the text).

a count rate in the KELT system of $\sim 3.328 \times 10^9$ ADU s^{-1}. Multiplying by the effective width of the KELT bandpass (≈ 3180 Å), we obtain an integrated A0V star *R*-band flux of $\sim 5.565 \times 10^{-6}$ erg s^{-1} cm^{-2}. Thus a count rate of 1 ADU s^{-1} corresponds to a total flux in the KELT system of 1.672×10^{-15} erg s^{-1} cm^{-2}.

Finally, we adopt a nominal distance to M82 of $d = 3.5$ Mpc [Dalcanton et al., 2009]. Thus, we obtain a final empirical relation between the KELT observed count rate and the total emitted flux at the source of 1.672×10^{-15} erg s^{-1} cm^{-2} $\times 4\pi d^2$ erg s^{-1} = 2.451×10^{36} erg s^{-1} = 1 ADU s^{-1}.

In summary, 1 ADU s^{-1} in the KELT system corresponds to 2.451×10^{36} erg s^{-1} at the source (not including any effects of extinction).

3.3 Results

The full KELT-N light curve of SN 2014J is shown in Figure 3.3. To our knowledge, this is the most complete, high cadence light curve of this SN spanning the entire event yet reported. In this section, we report the results of analyzing the features of the light curve, specifically the time of initial explosion, short-timescale variability, the peak brightness time, the secondary bump, and the late-time plateau.

3.3.1 Time of initial explosion

The KELT-N light curve covering the explosion time of SN 2014J, along with the intermediate Palomar Transient Factory (iPTF) narrow-band data is analysed in an accompanying paper [Goobar et al., 2014b]. The extrapolation needed to determine the onset of the optical light from the supernova is model-dependent, since it takes into account the possibility that the early emission has contributions besides the radioactive decay of ^{56}Ni, e.g, the effect of shock-heated material of the progenitor, a donor star or the circumstellar medium. Furthermore, radioactivity arising in the outer parts of the exploding start could produce a different signature and light curve function to be fitted to the data to obtain T_0.

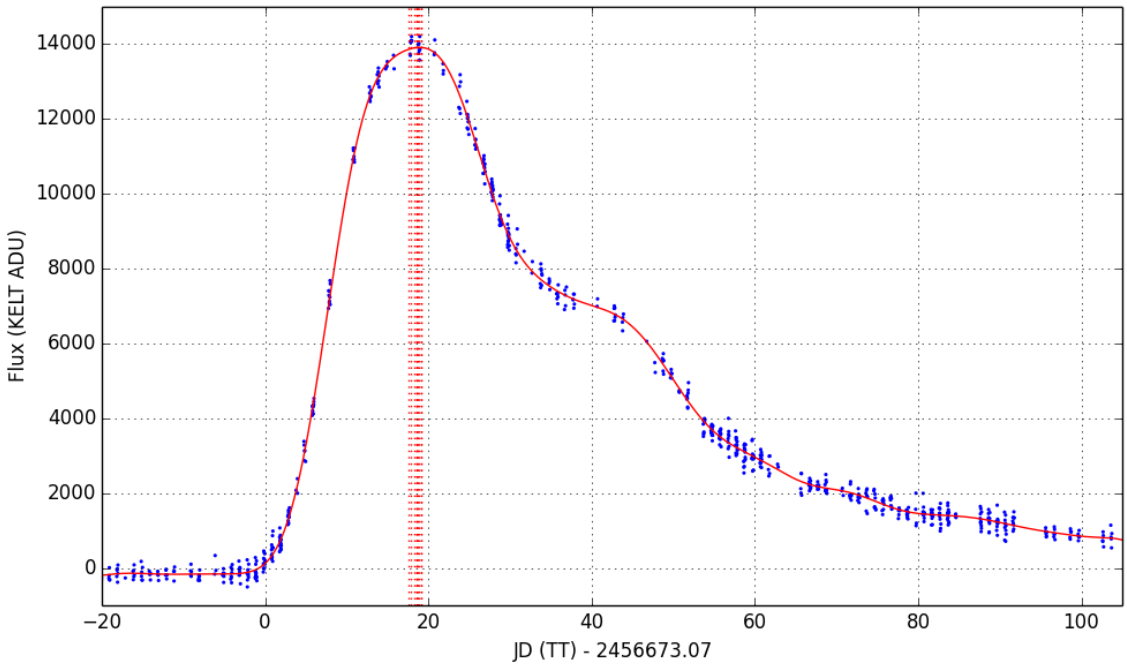

Figure 3.3: KELT light curve of SN 2014J (western data). Also shown is the range of peak time values (vertical lines) determined from best-fit empirical Fourier models (solid curve; see the text).

When all the considered alternatives are included, we concur with the best fit of Zheng et al. [2014]: Jan 14.75 UT, with a systematic uncertainty of ± 0.3 d, due to model dependence. We refer to Goobar et al. [2014b] for details.

3.3.2 Time of maximum light and total rise time

We investigate the time of maximum light by modeling the KELT-N light curve empirically using Fourier series and then extracting the time at the peak of the Fourier model (Figure 3.3). We emphasize that this Fourier representation is not physical and does not map on to physical parameters as are often used in detailed SN light curve models. Our intent is to characterize this important property of the light curve, the peak time, in terms of pure light curve shape parameters.

Our Fourier model is a combination of linear polynomial and Fourier terms. The polynomial is effectively a boundary condition, required because the initial and final fluxes are

not equal. The Fourier series representation is:

$$F(t,N) = a + bt + \sum_{n=1}^{N} c_i \sin(2\pi nt\,/\,\mathrm{T}) + d_i \cos(2\pi nt\,/\,\mathrm{T})$$

where T is the duration of the modeled segment.

We performed this Fourier fitting to the western data using a variety of Fourier terms, ranging from 5–14, and we adopt the spread of model light curve maxima (represented by vertical lines in Fig. 3.3) as indicative of the systematic uncertainty in the peak time. Using the ensemble of Fourier series fits to the data, we find that peak flux occurs at 2456691.12 $\pm$0.48 ($\mathrm{JD_{TT}}$).

Putting together our updated estimate of the initial explosion time with the updated estimate of the peak time, we can obtain an estimate of the total combined rise time for SN2014J in the KELT-N filter to be 18.6 ± 0.6 d.

3.3.3 Secondary bump

We observe a secondary "bump" in the SN 2014J light curve approximately 40 days following the initial explosion and approximately 20 days after the peak brightness. To objectively quantify the precise time of the secondary bump, we utilized our empirical Fourier representation of the light curve to locate the time when the model slope is closest to zero. Figure 3.4 illustrates this approach graphically. From this analysis, we locate the time of the secondary bump at 21.16 d after the first peak.

Such secondary bumps are a common feature of SNe at near-IR wavelengths and the red end of the optical spectrum. Figure 3.5 shows the KELT-N photometry along with the *R*-band data of SN 2011fe from Munari et al. [2013] and the synthetic model photometry based on the empirical SNIa SED of Hsiao et al. [2007], where we show both the predictions from the integration of the SED over the KELT-N transmission function with and without the additional effect of reddening in M82 and in the Milky-Way. For the latter we

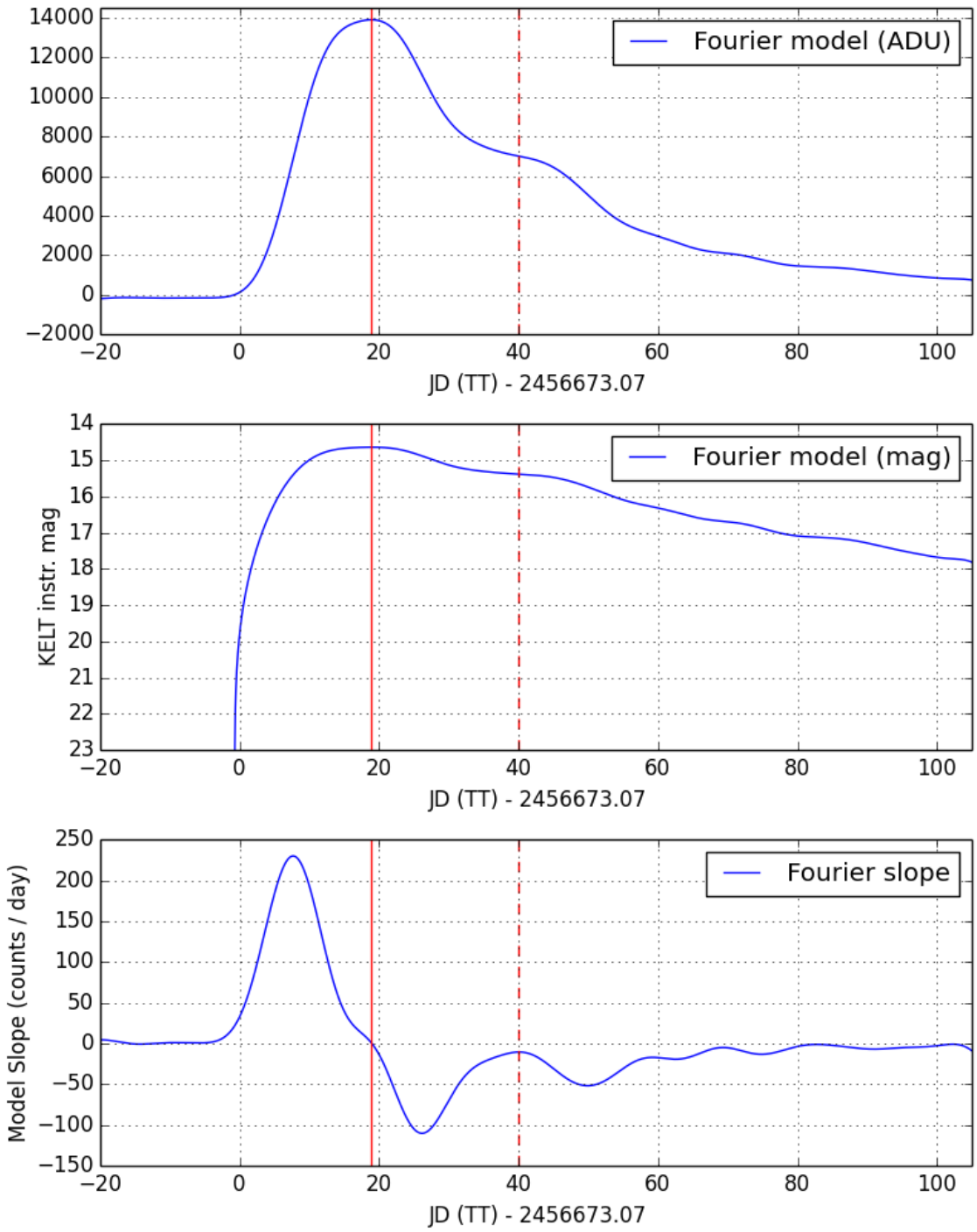

Figure 3.4: Fourier representation of the light curve used to quantify the time of the secondary bump (see the text). (Top) Fourier representation of the light curve in flux units. (Middle) Same as top but in magnitudes. (Bottom) Slope in flux per unit time. In each panel, the time of primary peak is represented by the solid vertical line (corresponding to the peak in the top and middle panels), and the time of secondary bump is represented by the dashed vertical line (corresponding to the peak in the bottom panel).

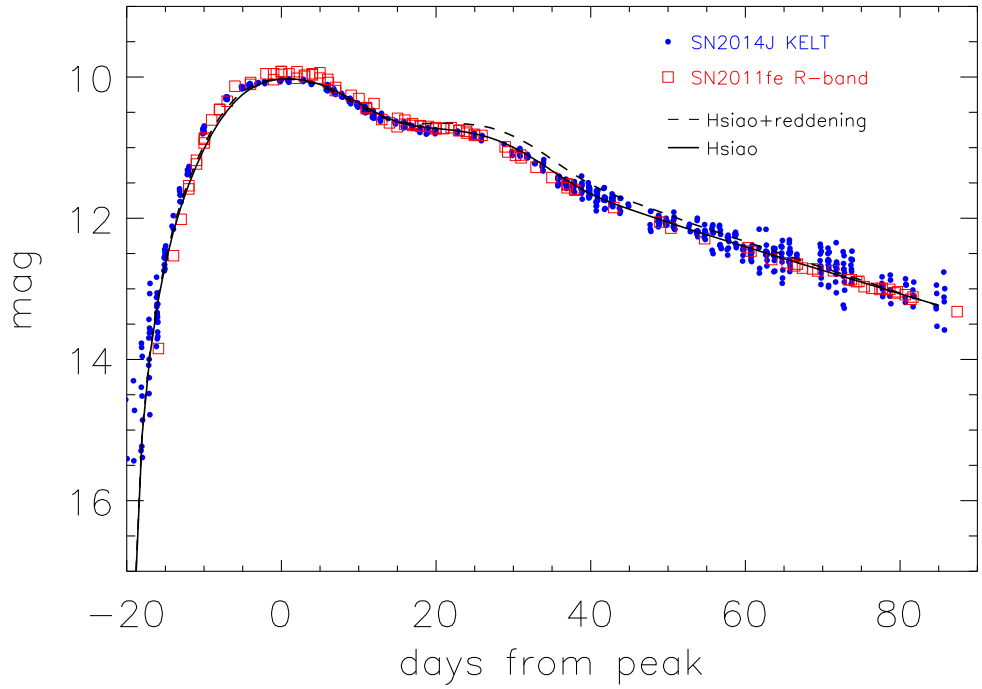

Figure 3.5: The KELT-N light curve of SN 2014J (blue circles) is shown with the *R*-band data of SN 2011fe from [Munari et al., 2013] (red squares) and the synthetic model photometry (solid line) based on the empirical SNIa SED of Hsiao et al. [2007]. The dashed line shows the expectation from the model SED once the effect of reddening is taken into account, i.e., including the effect of change of the effective wavelength. Note that the magnitudes from SN 2011fe are plotted exactly as tabulated in [Munari et al., 2013], i.e., without any adjustment for "stretch" or in the vertical axis. The synthetic models based on Hsiao et al. [2007] have been shifted to match the peak brightness of SN 2014J.

assume a reddening wavelength dependece as parameterized in Fitzpatrick [1999], using the best-fit extintion parameters in Amanullah et al. [2014].

The good match to the template lightcurve reinforces the conclusion that SN 2014J belongs to the class of core normal SNe Ia, although we note that the match is better when the reddening correction is *not* included, especially around the secondary maximum, a somewhat unexpected result. The differences may reflect a possible inaccuracy in the KELT system transmission curve, the calibration using stellar colors, or simply intrinsic differences among SNe Ia.

3.3.4 Short-Timescale Light Variations

Because of the fortuitously high cadence of observations achieved for the SN 2014J observations from pre- to post-explosion, the KELT-N light curve affords the opportunity to explore the degree of "smoothness" of the light curve as a function of time. This in turn can provide evidence for, or limits on, short-lived isotopes or inhomogeneities in the explosion or the medium surrounding it.

We characterize the intrinsic short-timescale variations of the light curve by measuring the r.m.s. of the light curve in several ways. First, we model the light curve as a whole using a high-order Fourier series representation, and measure the r.m.s. scatter relative to this fit. Note that the Fourier representation is not physical, rather it is a convenient way to empirically represent the overall light curve and isolate the short-timescale variations. In this way, we measure an overall r.m.s. of 5.1%. Near peak SN brightness, the r.m.s. scatter decreases to 1.49%. This r.m.s. is very nearly equal to the expected instrumental precision.

In addition, we have measured the r.m.s. variations on a night-to-night basis in order to explore whether there may be changes in the short timescale variations as the supernova progressed. To do this, on each night possessing at least 3 measurements, we fit a linear trend and then measure the r.m.s. of the measurements on that night relative to the trend line. Figure 3.6 shows these nightly r.m.s. measurements as a function of time. Based on these data, we do not observe statistically significant short-timescale variations on most nights, and therefore we do not observe statistically significant trends in the short timescale variations over time. The data do permit us to place an upper limit on the short timescale variations of 4.47% (3σ) in the time near and shortly following peak brightness.

In Fig. 3.6 we represent these r.m.s. variations on a night-by-night basis. In addition, since as mentioned above these variations are not significantly larger than the instrumental limit, we can use the empirical conversion beween flux in the KELT system to emitted flux at the source (see Sec. 2.6) to represent these measured nightly variability limits as limits on the amount of intrinsic variation at the source in erg s^{-1}. On this basis, we can set a 3σ

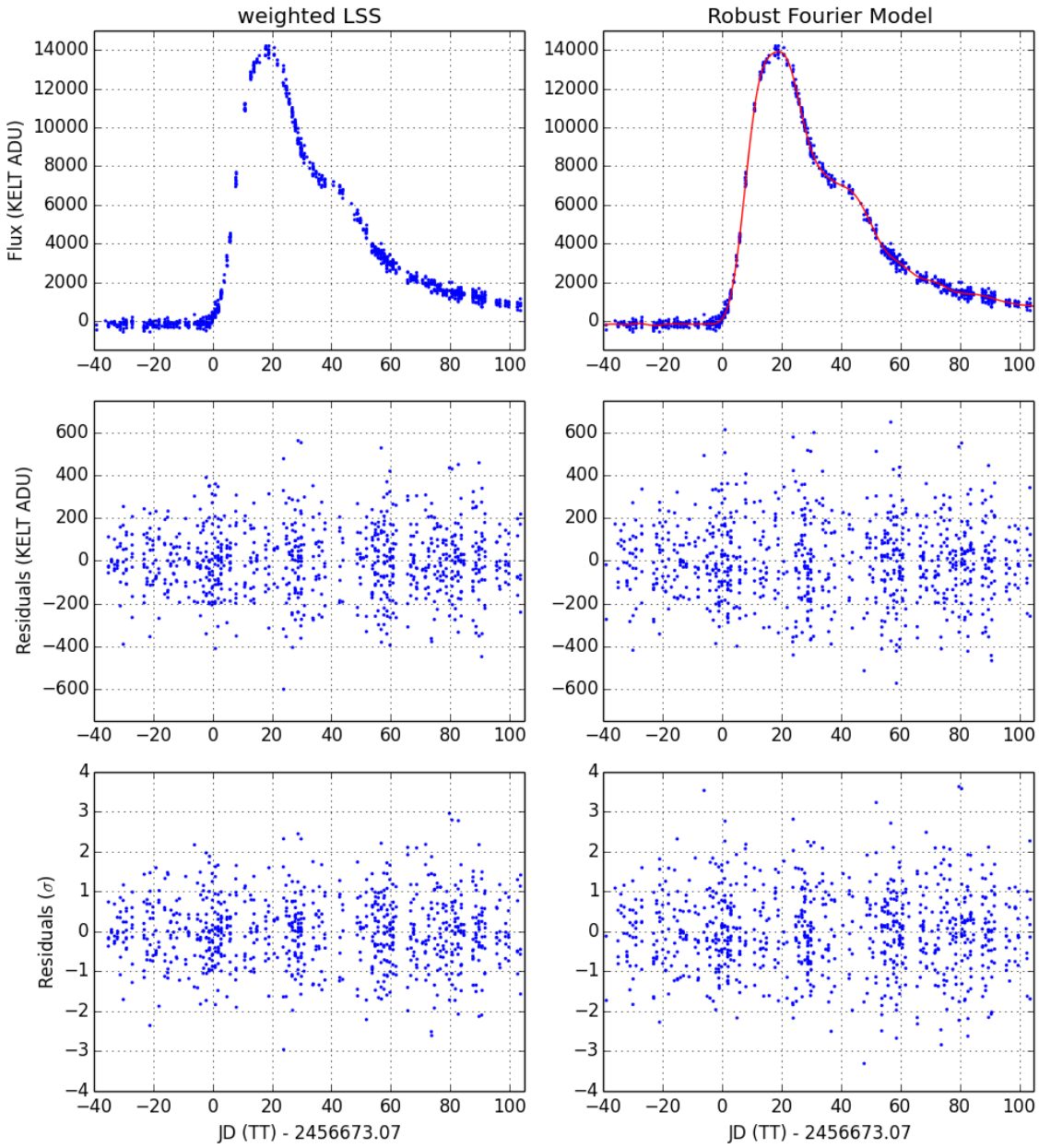

Figure 3.6: Comparison of light curve intra-night scatter using two different fitting methods. Within each night with three or more data points, we fit a straight line to all data points. The top row depicts the SN 2014J (west) light curve. The middle row shows the raw residuals in ADU (data points with the straight line fit subtracted). In the bottom row, residuals are divided by the uncertainties. Each column uses a different fitting method. Left uses weighted least-squares and right uses scatter about the empirical Fourier model fit. See the text.

limit of 3.34×10^{36} erg s^{-1} for the variations at the source at peak brightness, and similarly a 3σ limit of 8.7×10^{36} erg s^{-1} for the variations over the entire set of KELT observations.

3.4 Conclusions

We have reported a complete light curve of the bright M82 SN 2014J observed with high photometric cadence from before the explosion, through the early rise and peak light, and through the secondary bump and beyond to $\sim$100 d past peak brightness. The KELT light curve confirms that SN 2014J is a nearby replica of the SNe Ia used for precision distance estimates in cosmology. In Goobar et al. [2014b] we examined the first hours after the explosion to conclude that there is evidence for sources of luminosity in the very early light curve that would indicate either shock-heating of the SN ejecta, interaction with circumstellar matter or a companion star, or the presence of radiactive elements near the surface of the exploding star.

In this work we have extended the study to the entire KELT dataset. We have, for the first time, performed a study of the temporal evolution of a SNIa that includes the very short timescales of just a few minutes, corresponding to physical length scales $\lesssim 10 R_\odot$ of the expanding SN ejecta. We find that any perturbation to the diffuse light emission is smaller than 8.7×10^{36} erg s^{-1} for the variations over the entire KELT dataset, starting well before the explosion. The implications, both with regard to the potential presence of short-lived radioactive material near the surface of the progenitor, and/or the small scale structure of the circumstellar medium, will have to be explored with detailed modeling, currently not available. Thus, the KELT dataset provides new observational opportunities for the theoretical understanding of Type Ia supernovae.

Chapter 4

KELT-19Ab: a P$\sim$4.6 Day Hot Jupiter Transiting a Likely Am Star with a Distant Stellar Companion

4.1 Introduction

The Kilodegree Extremely Little Telescope (KELT; Pepper et al. 2003, 2007, 2012) survey was originally designed to discover transiting planets orbiting bright ($8 \leq V_{\rm mag} \leq 11$) host stars. The scientific value and strategy behind that approach was described in detail in the introduction of the recent discovery of KELT-20b [Lund et al., 2017][1]. In short, these bright systems are the most amenable to detailed follow-up characterization (i.e., transit spectroscopy, secondary eclipse spectroscopy, phase curve measurements, etc., Winn et al. 2010). Because the KELT project did not actively start to vet candidates until 2011, many of the initial transit candidates had already been discovered by other collaborations (e.g., Alonso et al. 2004, McCullough et al. 2006, Bakos et al. 2007, Collier Cameron et al. 2007b).

This fact, combined with a few additional, coincidental, and nearly-simultaneous occurrences, such as the confirmation of WASP-33b [Collier Cameron et al., 2010b] via Doppler tomography (see §4.2.4.4 for an overview of this technique), our somewhat fortuitous discovery of KELT-1b [Siverd et al., 2012], and the 'late entry' of KELT into the field of exoplanet discovery via transits, led us to pursue the discovery of transiting planets around hotter stars. This strategy has ultimately proven quite successful. In retrospect, the pursuit of hot stars was well-suited to the survey, both because KELT observes a larger fraction of hot stars than other ground-based transit surveys (due to Malmquist bias, see Bieryla et al. 2015), but also because the reduction pipeline of the primary follow-up radial velocity vetting resource used by KELT, the Tillinghast Reflector Echelle Spectrograph (TRES)

[1] See also Talens et al. [2017b] for the simultaneous discovery of the same planet, MASCARA-2b.

on the 1.5 m telescope at the Fred Lawrence Whipple Observatory, Mount Hopkins, Arizona, USA, was actively optimized to measure radial velocities of hot, rapidly-rotating stars [Latham et al., 2009].

To date, this strategy of targeting hot stars has led to the discovery of four planets transiting A stars by the KELT survey: KELT-17b [Zhou et al., 2016b], KELT-9b [Gaudi et al., 2017a], KELT-20b/MASCARA-2b [Lund et al., 2017, Talens et al., 2017b], and KELT-19Ab, the planet announced here. Additionally, there are four planets known to transit A stars discovered by other collaborations: WASP-33b [Collier Cameron et al., 2010b], Kepler-13Ab [Shporer et al., 2011], HAT-P-57b [Hartman et al., 2015], and MASCARA-1b [Talens et al., 2017a].

As discussed in previous KELT planet discovery papers, rapidly rotating, hot stars above the Kraft break [Kraft, 1967] pose unique challenges but provide unique opportunities. Transiting planets orbiting these stars are difficult to confirm via Doppler reflex motion, but on the other hand are amenable to Doppler tomography due to the large $v \sin I_*$ of their hosts.

It is also the case that A stars have a remarkable diversity in their properties, partially due to the fact that their outer envelopes are primarily radiative, but exhibit extremely thin helium and hydrogen convective layers at the very outer edges of their atmospheres. In particular, the thin surface convection zones and very low mass loss rates of A stars lead to very efficient gravitational settling of some elements, similar to (although not as extreme as) the settling exhibited in white dwarfs. This results in weaker spectral lines of those elements relative to what would be expected of a star of similar temperature, and not indicative of an actual global underabundance of those elements. Similarly, because the convective zones are so thin, partially ionized elements with large radiative cross sections below the convective zone can exhibit radiative levitation. This may lead to stronger lines which may be interpreted as large selective overabundances in certain elements (see, e.g., Richer et al. 2000). Indeed, it is even possible to have an element experience both gravitational settling

and radiative levitation in different layers, creating a zone within an A star where that element is highly concentrated. In the case of iron, this effect may be severe enough to induce convective mixing that can impact surface abundances [Richard et al., 2001].

In general, thinner surface convection zones that are lower in density experience gravitational settling at a faster rate, and are more susceptible to radiative levitation. In normal A stars, there are thin hydrogen and helium ionization zones that are very close to each other, which through overshoot behave as a single deeper mixed layer. However, if the helium ionization zone is driven much deeper and no longer in causal contact with the hydrogen ionization zone, even more extreme abundance changes may be apparent, since the hydrogen ionization zone by itself is isolated and very shallow.

The net result is that determining the global metal abundances for A stars can be extremely difficult. Abundances determined by atmospheric spectroscopy may have very little to do with the global metallic abundance of the star. A particularly notable example is the metallic-line Am stars [Titus and Morgan, 1940], which, although they have hydrogen lines consistent with the effective temperatures of late A stars, also have metallic lines of heavier elements with strengths expected for cooler F stars, and lines of lighter elements consistent with hotter A stars. These Am stars are generally more slowly rotating [Abt and Morrell, 1995] than chemically normal stars with the same effective temperatures, likely due to a competition between elemental segregation and rotational mixing. The net result is that surface abundance anomalies can be enhanced in some elements and suppressed in others for Am stars [Abt and Morrell, 1995]. Empirically, stars with rotational speeds above ~ 150 km s^{-1} are chemically "normal" and it appears that mixing overcomes the settling described above. Virtually all slower rotators (including KELT-19A) are measured to be chemically peculiar, although there may well be exceptions. For example, a very young slow rotator might not yet have had time to develop unusual abundance patterns. Empirically, most slowly rotating Am stars are also in binaries [Abt and Levy, 1985], as is the case for KELT-19A (see §4.2.3 and §4.2.4.3). This may be due to tidal braking of the

A star, although in the case of KELT-19, the stellar companion is too distant for such tidal braking to be effective.

4.2 Discovery and Follow-Up Observations

We provide a brief summary of the KELT survey data reduction process and present the results in §4.2.1. §4.2.2 presents our ground-based time-series follow-up photometric observations, §4.2.3 presents our high contrast adaptive optics imaging, and §4.2.4 presents our spectroscopic follow-up observations.

4.2.1 KELT-North Observations and Photometry

KELT-19Ab is located in a field that is monitored by both KELT telescopes, centered on $\alpha = 07^h\ 39^m\ 36^s$, $\delta = +03^\circ\ 00'\ 00''$ (J2000). This field is labeled internally as KELT-South field 06 (KS06) and KELT-North field 14 (KN14). The reduction and candidate selection process for KELT-South and KELT-North are described in detail in Kuhn et al. [2016] and Siverd et al. [2012], respectively. From our analysis of 2636 images from KS06 (UT 2010 March 02 to 2013 May 10) and 2092 images from KN14 (UT 2011 October 11 to UT 2013 March 26), KJ06C009789 (KELT-19Ab) was identified as a top candidate. Figure 4.1 shows the combined KELT-South and KELT-North light curve (top), the KELT-South light curve only (middle), and the KELT-North light curve (bottom) for KELT-19Ab. KELT-19 (BD+07 1721) is located at $\alpha = 07^h\ 26^m\ 02\overset{s}{.}2895$, $\delta = +07^\circ\ 36'\ 56\overset{''}{.}834$ (J2000). This is the second planet discovered through a combination of KELT-South and KELT-North observations, KELT-17b being the first one [Zhou et al., 2016a].

4.2.2 Photometric Time-series Follow-up

The KELT collaboration includes a world-wide team of ground-based follow-up observers known as the KELT Follow-Up Network (KELT-FUN). KELT-FUN currently in-

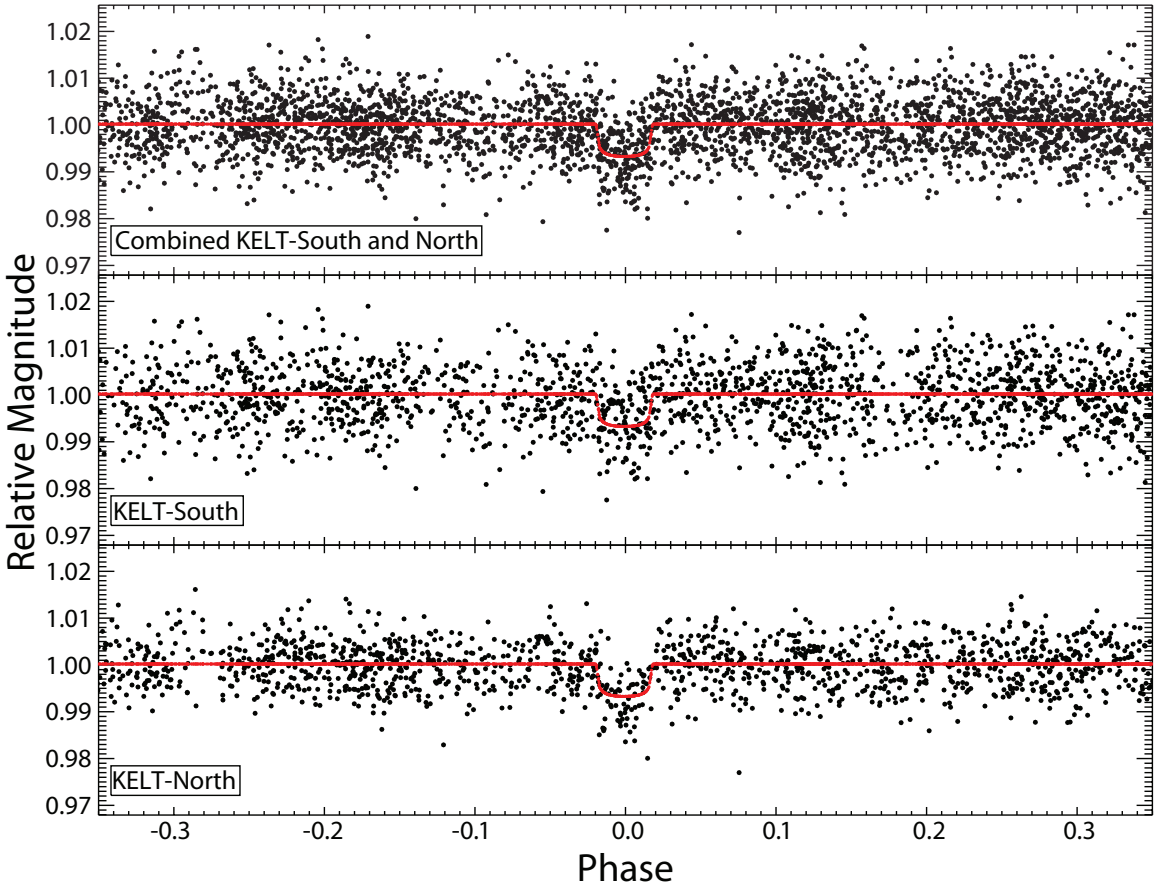

Figure 4.1: The combined KELT-South and KELT-North light curve (top), the KELT-South light curve only (middle), and the KELT-North discovery light curve (bottom) for KELT-19Ab. Each has been phase-folded to the discovery period of 4.6117449 days. The red line corresponds to an EXOFAST model of the combined light curve. (Supplemental data for this figure are available in the online journal.)

cludes members from $\approx$ 60 institutions. The KELT-FUN team acquired follow-up time-series photometry of KELT-19Ab transits to better determine the system parameters and to check for transit false positives. We used the `Tapir` software package [Jensen, 2013] to schedule follow-up observations. We obtained six full and three partial transits in multiple bandpasses from g to z between February 2015 and December 2016. Figure 4.2 shows all the transit follow-up light curves assembled. A summary of the follow-up photometric observations is shown in Table 4.1. We find consistent $R_P/R_\star$ ratios in all light curves across the optical bands, helping to rule out false positives due to blended eclipsing binaries. Figure 4.3 shows all transit followup light curves from Figure 4.2 combined and binned in 5 minute intervals. This combined and binned light curve is not used for analysis, but rather to show the best combined behavior of the transit.

All photometric follow-up observations were reduced with the `AstroImageJ` (`AIJ`) software package[2] [Collins et al., 2017]. We were careful to ensure that all observatory computers were referenced either through a network connection to a stratum 1 timing source or to a GPS stratum 1 timing source, and that all quoted mid-exposure times were properly reported in barycentric Julian dates at mid-exposure (BJD_{TDB}; Eastman et al. 2010).

4.2.2.1 KeplerCam

We observed an i-band transit ingress from KeplerCam on the 1.2 m telescope at the Fred Lawrence Whipple Observatory (FLWO) on UT 2015 February 20. KeplerCam has a single 4K $\times$ 4K Fairchild CCD 486 with an image scale of $0\farcs366$ pixel^{-1} and a field of view of $23\farcm1 \times 23\farcm1$.

[2] http://www.astro.louisville.edu/software/astroimagej/

4.2.2.2 WCO

We observed an *r*-band transit egress from Westminster College Observatory (WCO) on UT 2015 March 06. The observations were conducted from a 0.35 m f/11 Celestron C14 Schmidt-Cassegrain telescope equipped with an SBIG STL-6303E CCD with a 3K $\times$ 2K array of 9 μm pixels. The resulting images have a $24' \times 16'$ field of view and $1\farcs4$ pixel^{-1} image scale at 3×3 pixel binning.

4.2.2.3 Salerno

We observed an *R*-band transit ingress on UT 2015 March 19 from the Salerno University Observatory in Fisciano Salerno, Italy. The observing setup consists of a 0.35 m Celestron C14 SCT and an SBIG ST2000XM 1600×1200 CCD, yielding an image scale of $0\farcs54$ pixel^{-1}.

4.2.2.4 MINERVA

We observed a full transit simultaneously in the Sloan *r*-, *i*-, and *z*-bands using three of the MINERVA Project telescopes [Swift et al., 2015] on the night of UT 2016 January 18. MINERVA uses four 0.7 m PlaneWave CDK-700 telescopes that are located on Mt. Hopkins, AZ, at FLWO. While the four telescopes are normally used to feed a single spectrograph, we used three MINERVA telescopes in their photometric imaging mode for the KELT-19 observations. The telescopes were equipped with Andor iKON-L 2048×2048 cameras, which gave a field of view of $20\farcm9 \times 20\farcm9$ and a plate scale of $0\farcs6$ pixel^{-1}. The MINERVA telescope conducting the *r*-band observations experienced a $2\farcm6$ tracking jump during the time of egress. The resulting change in the position of the field on the detector produces a relatively large change in the baseline level of the light curve just after the beginning of egress. Furthermore, because of imperfect flat-field images, the baseline offset differs by $\sim \pm 1$ percent depending on the set of comp stars selected. The different baseline

offsets produce transit center times that differ by $\sim \pm 8$ minutes, even with detrending parameters included in the model to attempt to compensate for the baseline offset. Because of the unreliable detrending results, and the fact that we simultaneously observed four additional light curves on UT 2016 January 18, the *r*-band light curve is not included in the analysis to avoid the potential of improperly biasing the linear ephemeris derived from our global modelling effort (see §4.3.4.5).

4.2.2.5 MVRC

We observed a full transit from the Manner-Vanderbilt Ritchey-Chrétien (MVRC) telescope located at the Mt. Lemmon summit of Steward Observatory, AZ, on UT 2016 January 18. Exposures were taken in alternating *g*- and *i*-band filters yielding pseudo-simultaneous observations in the two filters. The observations employed a 0.6 m f/8 RC Optical Systems Ritchey-Chrétien telescope and an SBIG STX-16803 CCD with a 4K $\times$ 4K array of 9 μm pixels, yielding a $26.6' \times 26.6'$ field of view and $0\farcs39$ pixel^{-1} image scale.

4.2.2.6 CROW

We observed a full *I*-band transit from Canelas Robotic Observatory (CROW) in Portalegre, Portugal on UT 2016 December 05. The observatory is equipped with a 0.3 m Schmidt-Cassegrain telescope and a KAF-3200E CCD, having a $30' \times 20'$ field of view and a pixel scale of $0\farcs84$ pixel^{-1}.

4.2.3 High-Contrast Imaging

KELT-19 was observed on the night of UT 2016 December 18 at Palomar Observatory with the 200-inch Hale Telescope using the near-infrared adaptive optics (AO) system P3K and the infrared camera PHARO [Hayward et al., 2001]. PHARO has a pixel scale of $0\farcs025$ pixel^{-1} and a full field of view of approximately $25''$. The data were obtained

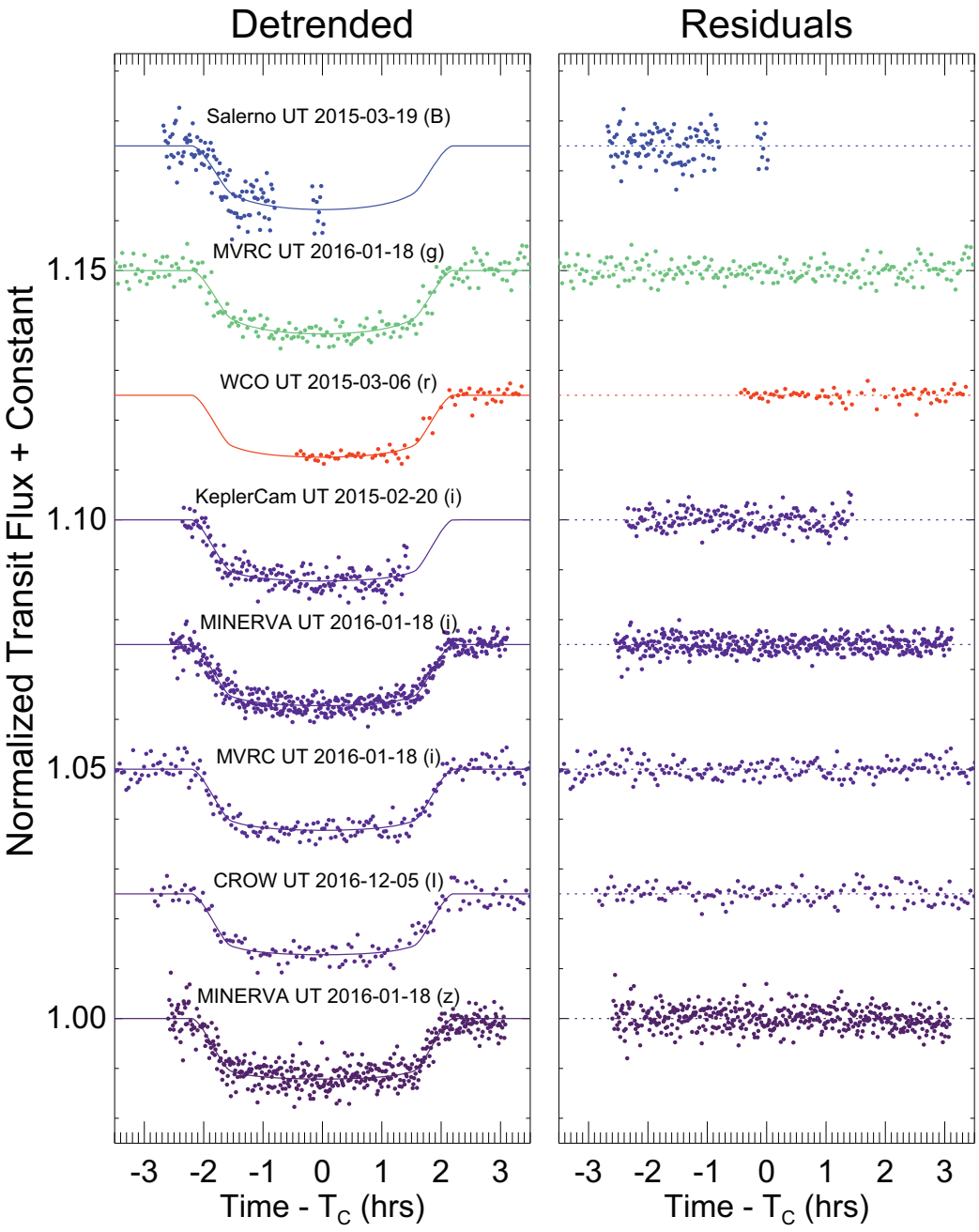

Figure 4.2: Follow-up transit photometry of KELT-19. *Left Panel:* Detrended transit light curves arbitrarily shifted on the vertical axis for clarity. The overplotted solid lines are the best fit transit model from the adopted global fit documented in Table 4.5. *Right Panel:* The transit model residuals. The labels are as follows: Salerno=Salerno University Observatory 0.35 m telescope; MVRC=Manner-Vanderbilt 0.6 m RCOS Telescope; WCO=Westminster College Observatory 0.35 m telescope; KeplerCam=1.2 m telescope at FLWO; MINERVA=MINiature Exoplanet Radial Velocity Array of 0.7 m telescopes; CROW=Canela's Robotic Observatory 0.3 m LX200 Telescope. (Supplemental data for this figure are available in the online journal.)

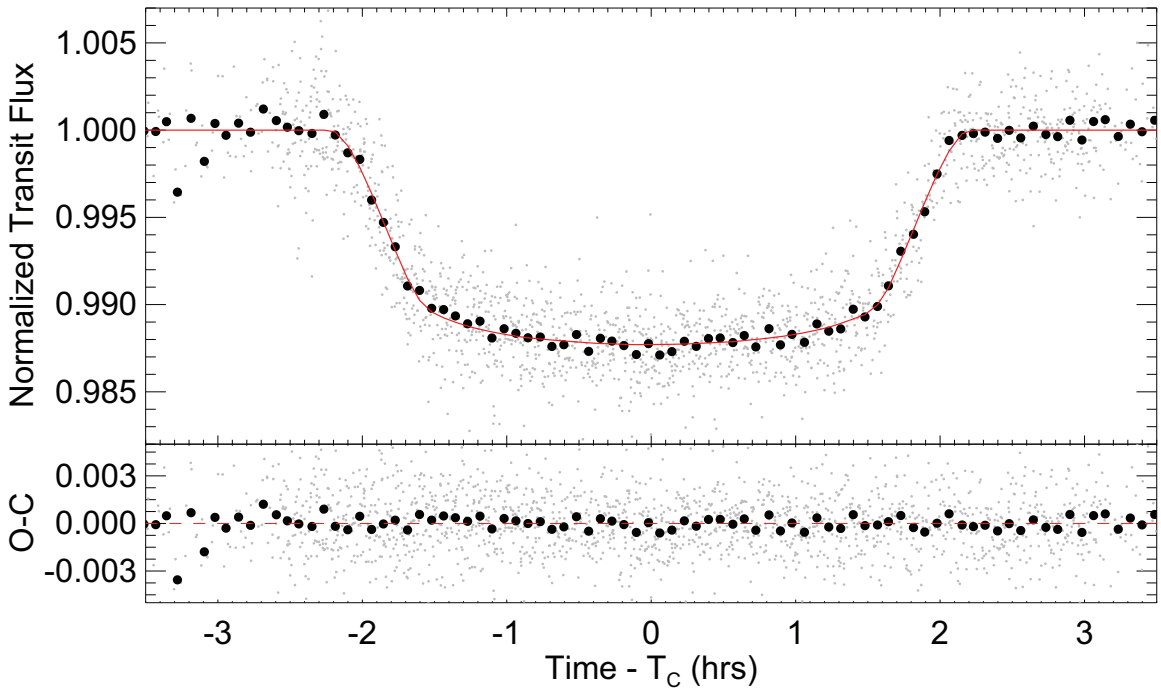

Figure 4.3: All detrended follow-up transits combined (small light-gray points) and binned in 5 minute intervals (large black points) and overplotted with the best fit global model (solid red line). The model shows the average limb darkening weighted by the number of transits in each band. The model residuals are shown in the bottom panel. The binned light curve data are not used in the analysis and are presented here to illustrate the overall statistical power of the follow-up photometry.

Table 4.1: Summary of Photometric Observations

Telescope	UT Date	# Obs	Filter	Cyc[a] (sec)	RMS[b] (10^{-3})	PNR[c] ($\frac{10^{-3}}{min.}$)	Error[d] Scale	Detrend Data
KeplerCam	2015-02-20	185	i	74	1.9	2.1	0.944	AM
WCO	2015-03-06	67	r	220	1.9	3.6	1.046	TM
Salerno	2015-03-19	110	B	68	3.1	3.3	1.429	AM
MVRC	2016-01-18	236	g	53	2.2	2.1	2.791	AM,SK
MVRC	2016-01-18	236	i	83	1.8	2.1	2.435	AM
MINERVA	2016-01-18	446	i	46	1.5	1.3	1.874	AM,FW
MINERVA	2016-01-18	444	z	46	2.1	1.8	1.774	AM
CROW	2016-12-05	128	I	186	1.7	3.0	1.827	MF,FW

Notes. See Figure 4.2 for a description of the telescope naming convention; AM=air mass; TM=time; SK=sky background; FW=average FWHM in image; MF=baseline offset at meridian flip.

[a] Cycle time in seconds, calculated as the mean of exposure time plus dead time during periods of back-to-back exposures.

[b] RMS of residuals from the best fit model in units of 10^{-3}.

[c] Photometric noise rate in units of 10^{-3} minute^{-1}, calculated as RMS/$\sqrt{\Gamma}$, where RMS is the scatter in the light curve residuals and Γ is the mean number of cycles (exposure time and dead time) per minute during periods of back-to-back exposures (adapted from Fulton et al. 2011).

[d] Error scaling factor determined by `MULTIFAST` (see §4.3.4).

with a narrow-band $Br\text{-}\gamma$ filter ($\lambda_o = 2.18; \Delta\lambda = 0.03\,\mu$m) and a standard J-band filter ($\lambda_o = 1.246; \Delta\lambda = 0.162\,\mu$m).

The AO data were obtained in a 5-point quincunx dither pattern with each dither position separated by $4''$. Each dither position is observed 3 times, each offset from the previous image by $0\farcs5$ for a total of 15 frames; the integration time per frame was 17 seconds in both the $Br\text{-}\gamma$ and J filters. We use the dithered images to remove sky background and dark current, and then align, flat-field, and stack the individual images. The PHARO AO data have a resolution of $0\farcs11$ and $0\farcs25$ (FWHM) in the $Br\text{-}\gamma$ and J filters, respectively.

The sensitivities of the final combined AO image were determined by injecting simulated sources azimuthally around KELT-19A every 45° at separations of integer multiples of the central source's FWHM [Furlan et al., 2017]. The brightness of each injected source was scaled until standard aperture photometry detected it with 5σ significance. The resulting brightness of the injected sources relative to KELT-19A set the contrast limits at that injection location. The 5σ limit at each separation was determined from the average of all of the determined limits at that separation. The contrast sensitivity curve shown in Figure 4.4 represents the 5σ limits of the imaging data in Δmagnitude versus angular separation in arcseconds. The slight decrease in sensitivity near $1'$ is caused by an increase in the relative brightness of the diffraction spikes in comparison to the smoothly declining point spread function of the target.

For KELT-19, a nearby stellar companion was detected in both the $Br\text{-}\gamma$ and J filters. The presence of the blended companion must be taken into account to obtain the correct transit depth and planetary radius (e.g. Ciardi et al. 2015). The companion separation was measured from the $Br\text{-}\gamma$ image and found to be $\Delta\alpha = 0.32'' \pm 0.02''$ and $\Delta\delta = 0.55'' \pm 0.02''$, which is a projected separation of $0.64'' \pm 0.03''$ at a position angle of 30.2 ± 2.5 degrees. At a distance of 255 ± 15 pc (see §4.3.1), the companion has a projected separation from the primary star of ≈ 160 AU. The positional offset uncertainties between the two stars are based upon the uncertainties in the positional fit to the centroids of the point spread

functions of the stars and is approximately 0.1 of a pixel corresponding to 2.5 mas. No distortion map was applied to the images; however, the optical distortion is 0.4% or less in the narrow camera mode for PHARO [Hayward et al., 2001].

The stars have blended 2MASS magnitudes of $J = 9.343 \pm 0.026$ mag and $K_s = 9.196 \pm 0.023$ mag. The stars have measured magnitude differences of $\Delta J = 2.50 \pm 0.06$ mag and $\Delta K_s = 2.045 \pm 0.03$ mag; the J-band differential measurement is less certain because of the poor AO correction in that filter on the night of the observations. Br-γ has a central wavelength that is sufficiently close to Ks to enable the deblending of the 2MASS magnitudes into the two components. The primary star has deblended (real) apparent magni-

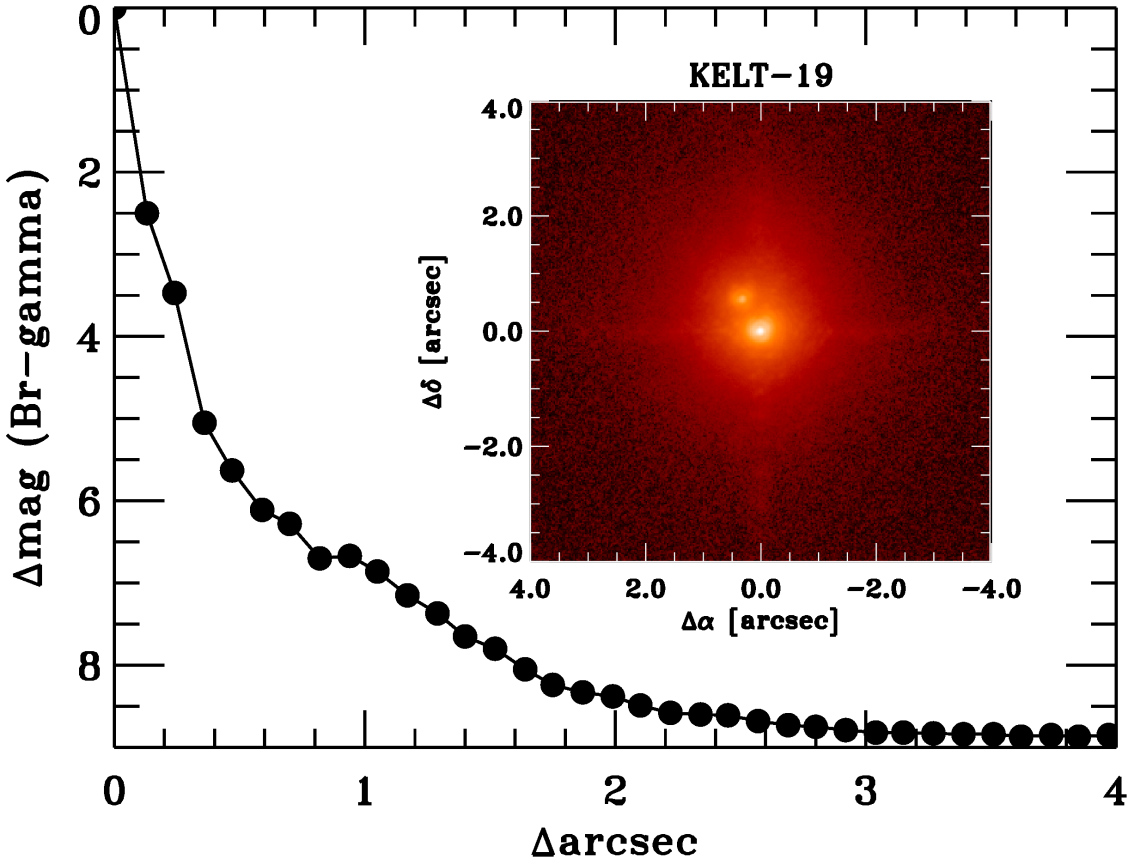

Figure 4.4: Contrast sensitivity and inset image of KELT-19 in Br-γ as observed with the Palomar Observatory Hale Telescope adaptive optics system; the secondary companion is clearly detected. The 5σ contrast limit in Δmagnitude is plotted against angular separation in arcseconds. The slight decrease in sensitivity near $1''$ is caused by an increase in the relative brightness of the diffraction spikes in comparison to the smoothly declining point spread function of the target.

tudes of $J_1 = 9.45 \pm 0.03$ mag and $Ks_1 = 9.35 \pm 0.02$ mag, corresponding to a color of $(J - K_s)_1 = 0.10 \pm 0.04$ mag; the companion star has deblended (real) apparent magnitudes of $J_2 = 11.95 \pm 0.06$ mag and $Ks_2 = 11.40 \pm 0.03$ mag, corresponding to a color $(J - K_s)_2 = 0.55 \pm 0.07$ mag. The uncertainties in the stellar colors are dominated by the uncertainty in the *J-band* measurement. Using the Casagrande et al. [2010] relations, the colors give $T_{\rm eff} = 7190^{+270}_{-250}$ K for the primary and $T_{\rm eff} = 5030^{+260}_{-240}$ K for the companion, which are consistent with the effective temperatures derived from the SED analysis in §4.3.1 and the spectral analysis in §4.2.4.5.

4.2.4 Spectroscopic Follow-up

4.2.4.1 TRES at FLWO

To constrain the planet mass and enable eventual Doppler tomographic (DT) detection of KELT-19Ab, we obtained a total of 60 spectroscopic observations of the host star with the Tillinghast Reflector Echelle Spectrograph (TRES) on the 1.5 m telescope at the Fred Lawrence Whipple Observatory, Arizona, USA. Each spectrum delivered by TRES has a spectral resolution of $\lambda/\Delta\lambda = 44000$ over the wavelength range of $3900 - 9100$ Å in 51 échelle orders. A total of 7 observations were obtained during the out-of-transit portions of the planet's orbit to constrain its mass (§4.2.4.3). Two spectroscopic transits were observed, on 2016-02-24 and 2016-11-08, for the Doppler tomographic analysis. The observations on 2016-02-24 were plagued by bad weather, and were discarded. The transit sequence obtained on 2016-11-08, totaling 24 spectra, successfully revealed the planetary transit, and were used in the analysis described in §4.2.4.4.

4.2.4.2 HJST at McDonald

To provide additional constraints on the planet mass, we obtained 14 spectra of KELT-19 covering the entire orbital phase with the 2.7 m Harlan J. Smith Telescope (HJST) at

McDonald Observatory and the Robert G. Tull Coudé spectrograph [Tull et al., 1995] in its TS23 configuration. This is a cross-dispersed échelle spectrograph with a resolving power of $R = 60,000$ and coverage from 3570 to 10200 Å (complete below 5691 Å) over 58 orders. The first two spectra (from 2016 October) have exposure lengths of ~ 375 seconds, while the last twelve (from 2016 December) have 1200 second exposure lengths.

4.2.4.3 Radial Velocities

The nearby stellar companion (see §4.2.3) is blended with the primary in our spectroscopic observations. Because of the resulting composite spectra, our radial velocity analysis is somewhat modified from previous KELT papers. For each observation, we derived a line broadening kernel via a least-squares deconvolution [following Donati et al., 1997, Collier Cameron et al., 2010b], from which both spectroscopic components can be identified (Figure 4.5). To derive radial velocities and rotational broadening parameters, we fit for the two spectroscopic components simultaneously across all available out-of-transit spectra, allowing for independent radial velocities of the two components, whilst requiring all observations to have the same velocity broadening parameters. The TRES and HJST observations were fit independently, since they are subjected to different instrumental broadening, and the broadening profiles were derived from different spectral wavelength regions.

From the simultaneous fit, we find that the out-of-transit broadening profile can best be described by a rapidly rotating primary star and a faint, slowly rotating, secondary star. The primary component has a rotational broadening velocity of $v \sin I_* = 84.1 \pm 2.1\,\mathrm{km\ s^{-1}}$ and a combined macro- and microturbulent broadening of $3.4 \pm 2.0\,\mathrm{km\ s^{-1}}$. The effect of instrumental broadening is taken into account separately in the global modelling. The secondary component has a line broadening velocity of $8.23 \pm 0.11\,\mathrm{km\ s^{-1}}$, which includes the influence of instrumental ($6.8\,\mathrm{km\ s^{-1}}$), rotational, and turbulent sources. We find a flux ratio of $F_\mathrm{B}/F_\mathrm{A} = 0.0270 \pm 0.0034$ to the total light of the system over the wavelength

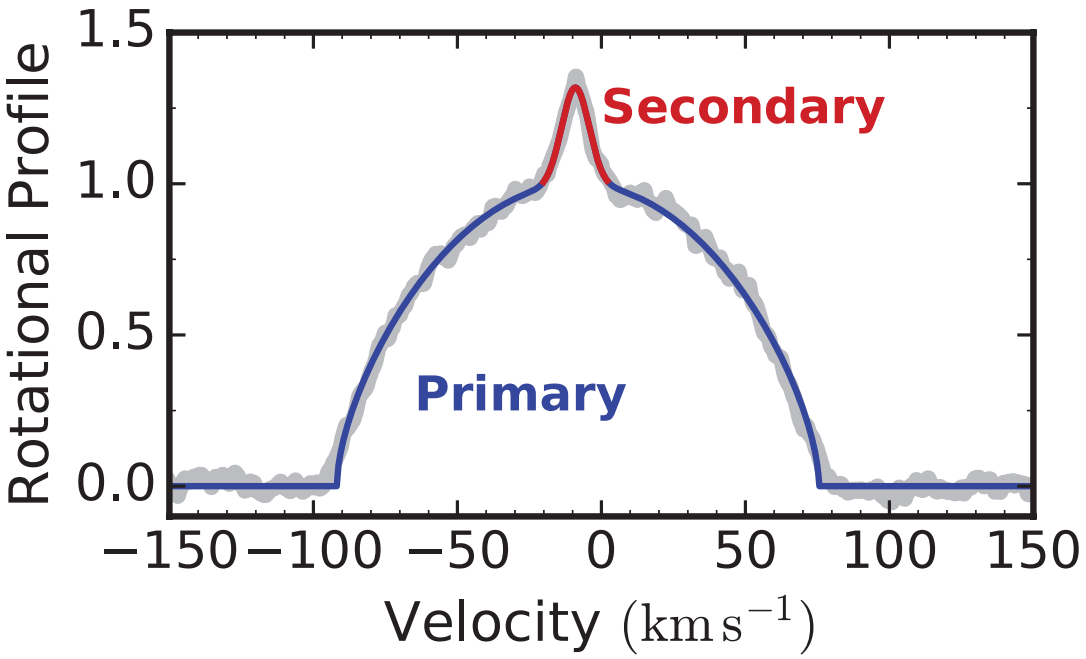

Figure 4.5: An example broadening kernel of KELT-19 (gray line), as observed by TRES, showing the spectroscopic binary nature of the system. We fit both spectroscopic components simultaneously to obtain the radial velocities of both stellar components; the best fit profiles for the primary and companion are shown in blue and red, respectively.

range 5200 ± 150 Å. This flux ratio is consistent with the AO observations of the spatially separated companion, and with the interpretation that the secondary companion is a G-dwarf associated with the system (§4.3.1).

We estimate the absolute center of mass radial velocity for KELT-19 from the Mg b region of our TRES spectra. We examined the mean of (1) all velocities, (2) the out-of-transit velocities, and (3) the high SNR velocities and concluded that the best nominal value and uncertainty representing the absolute radial velocity of the KELT-19 system is $-7.9 \pm 0.5\,\mathrm{km\ s^{-1}}$. The absolute RV was then adjusted to the International Astronomical Union (IAU) Radial Velocity Standard Star system via a correction of $-0.62\,\mathrm{km\ s^{-1}}$ resulting in a final value of $\mathrm{RV_{IAU}} = -8.5 \pm 0.5\,\mathrm{km\ s^{-1}}$. The correction primarily adjusts for the gravitational red-shift, which is not included in the library of synthetic template spectra.

The TRES and HJST out-of-transit velocities are shown in Figure 4.6, and presented in

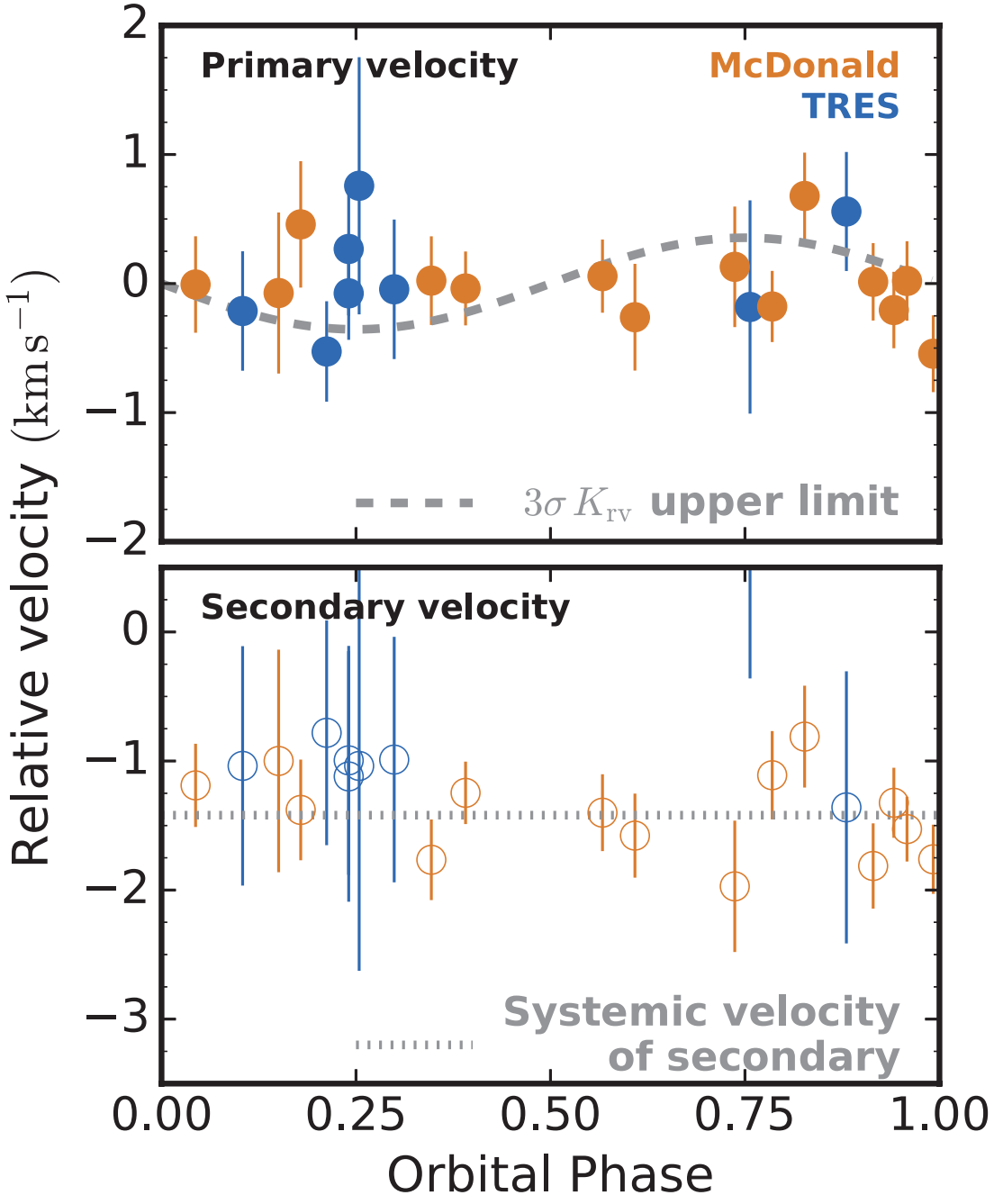

Figure 4.6: Radial velocities of the two stellar components in the KELT-19 system, phase folded to the transit period. We can place a 3σ upper limit on the radial velocity semi-amplitude K of $0.35\,\mathrm{km\,s^{-1}}$, confirming that the transiting companion is of planetary mass. The velocity of the stellar companion is constrained to be $< 2.31\,\mathrm{km\,s^{-1}}$ at 1σ, and $< 7.50\,\mathrm{km\,s^{-1}}$ at 3σ. The systemic velocity of the companion is similar to that of the primary, consistent with the interpretation that they are physically associated. The primary velocities are plotted in the top panel, secondary velocities in the bottom panel. The systemic velocity of the primary has been subtracted for all measurements. The TRES velocities are plotted in blue, McDonald in orange.

Table 4.2. As discussed in §4.3.4, the radial velocity semi-amplitude of the primary can be constrained to be $< 0.35\,\mathrm{km\ s^{-1}}$, confirming that the transiting companion is of planetary mass. We also confirmed that the velocity of the stellar companion is not varying, and is constrained to be $< 2.31\,\mathrm{km\ s^{-1}}$ at 1σ, and $< 7.50\,\mathrm{km\ s^{-1}}$ at 3σ. We note that the biggest hurdle to obtaining precise radial velocities for KELT-19A is its rapid rotational velocity. In comparison, we often reach $\sim 10\,\mathrm{m\ s^{-1}}$ precision for slowly rotating non-active stars with TRES [Quinn et al., 2014]. The systemic velocity of the primary ($-8.5 \pm 0.5\,\mathrm{km\ s^{-1}}$) is consistent with that of the companion ($-9.4 \pm 1.0\,\mathrm{km\ s^{-1}}$), which we interpret as KELT-19A and KELT-19B being bound. Assuming a $0.5\,\mathrm{M_\odot}$ bound companion in a circular, nearly edge-on orbit with radius 160 AU, KELT-19B would cause a maximum acceleration of KELT-19A (at conjunction or opposition) of $\sim 4\,\mathrm{m\ s^{-1}\ yr^{-1}}$. Given the current relatively low RV precision due to the rapid rotation of the primary, it is not surprising that an RV trend is not detected in the current data, and furthermore would not be detected for the foreseeable future. However, under the same assumptions, KELT-19A would cause a maximum acceleration of KELT-19B of $\sim 12\,\mathrm{m\ s^{-1}\ yr^{-1}}$, which might be detectable after several years with radial velocity instruments that can achieve precisions of a few $\mathrm{m\ s^{-1}}$ for a J = 12 mag star, given the relatively low $v \sin I_*$ of $\sim 4\,\mathrm{km\ s^{-1}}$ of the secondary.

4.2.4.4 Doppler Tomographic Observations

As a star rotates, one hemisphere moves toward the observer relative to the integrated stellar radial velocity, which produces light with a blue-shifted spectrum. The other hemisphere moves away from the observer, producing light with a red-shifted spectrum. In total, this produces rotationally broadened spectral lines. As a planet transits a star, differing blue- and/or red-shifted stellar spectral components are obscured by the shadow of the planet on the star. The planet shadow thus produces a spectral line profile distortion that varies in velocity space (except for the case of a polar orbit) as the transit progresses from ingress to egress. The measurement of the motion of the distortion can be modeled to

reveal the system's spin-orbit misalignment, λ, and the impact parameter, b, of the planet's orbit relative to the stellar disk. See Johnson et al. [2014] for a more technical description.

To confirm that a transiting companion is indeed orbiting the primary star in the KELT-19 system, and to measure the projected spin-orbit angle and impact parameter of the planetary orbit, we performed a Doppler tomographic analysis of the spectroscopic transit observed by TRES on 2016-11-08. Line broadening profiles were derived for each observation via a least-squares deconvolution analysis [following Donati et al., 1997, Collier Cameron et al., 2010b, Zhou et al., 2016a]. A master broadening profile was calculated by combining the out-of-transit profiles. Each observation was then subtracted from the master broadening profile, revealing the spectroscopic shadow of the transiting planet, as shown in Figure 4.7. The Doppler tomographic signal was modelled as per Gaudi et al. [2017a]. Limb darkening parameters were adopted from Claret [2004] for the photometric V band, similar to the wavelength region from which the broadening profiles were derived.

4.2.4.5 Stellar Parameters from Spectra

Because the spectrum of KELT-19A includes the light from KELT-19B (see §4.2.4.3 and §4.2.3), standard spectral synthesis or fitting techniques that ignore the influence of the secondary on the primary line profiles may be susceptible to systematic bias. We therefore applied a two-dimensional cross-correlation analysis [TODCOR; Zucker and Mazeh, 1994] using pairs of synthetic spectra to identify the stellar parameters that provided the best fit to the observed composite spectra. For this analysis we used the TRES spectra of KELT-19 and the CfA library of synthetic spectra, which were generated by John Laird using Kurucz model atmospheres [Kurucz, 1992] and a linelist compiled by Jon Morse. The synthetic grid covers the wavelength range 5050–5350 Å, and has spacing of 250 K in $T_{\rm eff}$ and 0.5 dex spacing in $\log g_\star$ and $[{\rm m/H}]$. We note that this latter parameter is a scaled solar bulk metallicity, rather than the iron abundance, $[{\rm Fe/H}]$. It is generally a reasonable assumption that the two quantities are similar, but it might not be the case for stars exhibiting peculiar

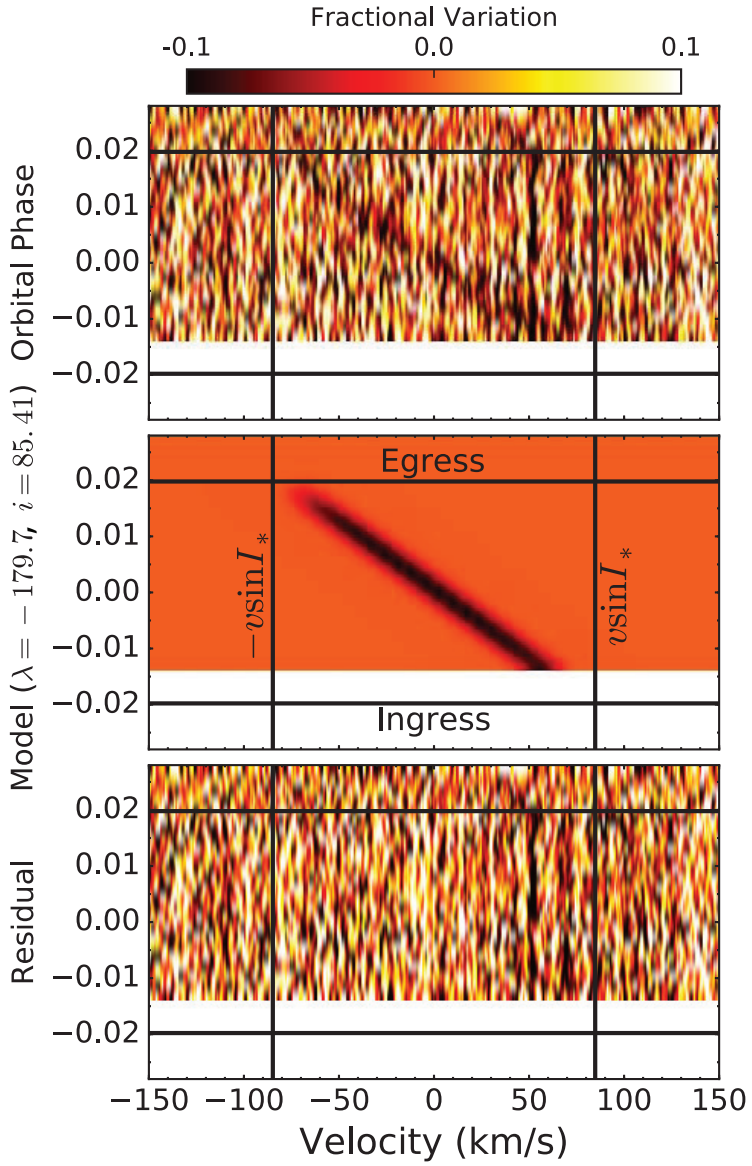

Figure 4.7: Doppler tomographic line profile plot. The top panel shows the spectroscopic data, the middle panel shows the derived model, and the bottom panel shows the residuals. In each panel, the vertical lines denote the width of the convolution kernel (i.e., $\pm v \sin I_*$), and the horizontal lines show the duration of the transit. Time increases from bottom to top. Each color-scale row indicates the deviation of the line profile at that time from the out-of-transit line profile, with dark regions of the plot indicating regions of the in-transit line profile that are shallower with respect to the out-of-transit line profile. The Doppler tomographic signal implies a retrograde orbit for the planet, as the line profile perturbation moves from the red wing of the line profile across to the blue wing. The planet moves in a corresponding manner during the transit, from obscuring the red-shifted hemisphere of the star across to the blue-shifted hemisphere.

abundances (like many A stars). Throughout the paper we do use [m/H] and [Fe/H] interchangeably, but because we neither derive nor impose strong constraints on the metallicity, we expect that any differences between the two quantities will have negligible effects on our results.

We ran TODCOR on all combinations of templates in the (6-dimensional) parameter space spanning temperatures $6000 \leq T_{\rm eff,A} \leq 8500$ K and $3750 \leq T_{\rm eff,B} \leq 6750$ K, surface gravities $3.0 \leq \log g_\star \leq 5.0$, and metallicities -1.5 dex $\leq$ [m/H] $\leq +0.5$ dex for both stars. We allowed the primary and secondary metallicities to be fit independently because even if the two stars formed together, many A stars display peculiar photospheric metallicities. The mean TODCOR correlation coefficient from each of these $\sim$37000 template pairs defines a 6-D surface (the axes corresponding to the 6 stellar parameters), on which we interpolate to the peak and adopt the corresponding stellar parameters. The result comes with several caveats. Derived spectroscopic stellar parameters are highly covariant — temperatures, metallicities, and gravities can be altered simultaneously to obtain very similar spectra over relatively large ranges of parameter space — so this degeneracy must be broken with independent constraints. In our case, we have derived the primary surface gravity ($\log g_\star = 4.127$) from constraints on the stellar density, mass, and radius as part of the global system fit (see §4.3.4). Because $\log g_\star$ is determined so precisely, even a 3-σ error in this value has minimal effect on the other parameters. As a result, we fix it in the TODCOR analysis for simplicity. Additionally, the secondary spectrum possesses a very low signal-to-noise ratio, so its parameters are poorly constrained by the spectra alone. Instead, we require it to be a main sequence companion $\log g_\star \sim 4.5$, with a temperature of 5200 K (as derived in our initial SED analysis; §4.3.1). We note that the projected rotational velocities, $v \sin I_*$, are nearly orthogonal to the other parameters, so we fixed these to simplify the analysis and reduce computation time: the primary $v \sin I_*$ was set to 84.1 km s^{-1} (see §4.2.4.3), while the secondary $v \sin I_*$ was estimated to be $\sim$2 km s^{-1} via an empirical gyrochronology relation [Mamajek and Hillenbrand, 2008] and the age and colors derived

from the initial SED and isochrone analysis.

Under these constraints, we find the following parameters: $T_{\rm eff,A} = 7505 \pm 104$ K; $[{\rm m/H}]_{\rm A} = +0.24 \pm 0.16$; $[{\rm m/H}]_{\rm B} = -0.26 \pm 0.35$. The reported errors include contributions from both formal and correlated errors. It is interesting to note that the primary metallicity is 0.5 dex higher than that of the secondary, albeit at low confidence because of the noisy secondary spectrum. We would expect to observe this difference if the primary is an Am star, a possibility we explore in §4.2.4.6. Given the uncertainty in the metallicities — and the possibility that the photospheric spectrum of the primary is not representative of its true metallicity — we choose to adopt a broad metallicity prior appropriate for the solar neighborhood ($[{\rm Fe/H}] = 0.0 \pm 0.5$ dex) in our subsequent global modeling. The main result of the TODCOR analysis, then, is a spectroscopic temperature for the primary of $T_{\rm eff} = 7505 \pm 104$ K.

4.2.4.6 KELT-19A is likely an Am star

As noted in the introduction, KELT-19A has a peculiar abundance pattern that is indicative of it belonging to the class of metallic-line A stars (Am stars). The hallmark of such stars is that they have some stronger metallic lines (such as strontium) than are expected for stars of their effective temperatures (as measured by their, e.g., Hα line), but weaker lines in others, such as calcium, than expected for the same metallicity and effective temperature. In other words, the star does not appear to have a consistent metallicity given its effective temperature.

This leads to a classical definition of Am stars, which notes that the spectral type one deduces depends on the feature used for typing. Because A stars in general have metallic lines that increase in strength toward later type, a spectral type based on some metal lines that show enhancement will lead to a spectral type for an Am star that is "too late" compared to the Balmer line spectral type. Similarly, because A stars have Ca II K lines that increase in strength toward later type, the calcium deficiency for Am stars will lead to a

calcium spectral type that is "too early". Thus a classical definition of Am stars is a range of spectral types from these methods of at least 5 subtypes. This is demonstrated in the spectrum of KELT-19A in Figures 4.8 and 4.9.

In Figure 4.8, the top panel shows iron lines, bottom left shows Hα, and bottom right shows the Ca II K line. In each panel, the black line is the observed KELT-19A spectrum, and the thin colored lines are three PHOENIX model atmospheres. Each has KELT-19A's estimated $\log g_\star$, $v \sin I_*$ and [Fe/H]=+0.5. The blue-green dotted, purple dashed, and yellow dash-dotted lines correspond to 7000, 7500, and 8000 K, respectively[3]. One can see that the 7000 K model (blue-green dotted line) is most appropriate for the metal lines, whereas the Hα is most consistent with our adopted temperature ($\sim$7500 K; purple dashed line), and the Ca II K line profile is most consistent with a hotter star (8000 K; yellow dash-dotted line). We also note that solar metallicity PHOENIX models all yield Fe II lines that are too weak at any temperature, which provides additional evidence that the photospheric metallicity is enhanced, as hinted at in the TODCOR analysis of §4.2.4.5.

To provide a more detailed spectral type for KELT-19, we compare its spectrum to a sequence of observed spectra ranging from A3V to F3V. All of these spectra were observed by TRES and reduced in the same way as KELT-19, which minimizes systematic bias, e.g. due to continuum normalization. Because each star has a different projected rotational line broadening, we measure it for each star and convolve the normalized spectrum with a Gaussian with a width appropriate to produce a total broadening (rotational, instrumental, and artificial) of 100 km s^{-1}. We compare KELT-19 to the spectral sequence and identify the spectral types that provide the best match to the Ca II K, Hα, and metal lines of KELT-19, and we illustrate this in Figure 4.9. While the Sr II line does not show any obvious enhancement, as might be expected for an Am star, this is not entirely surprising: the abundance anomalies in Am stars are negatively correlated with rotation so that those rotating as rapidly as KELT-19 are less anomalous; and the relatively rapid rotation of KELT-19

[3]None of these are fits; they are merely overplotted for illustration.

results in the Sr II line blending with at least three other lines of similar strength, so that the strength of any anomaly is diluted. Nevertheless, the other features in the spectrum are consistent with an Am star. An A5V star is an excellent match for the Ca II K line, an A7V star for the Hα profile, and an F2V star is the best match for the strength of the metal lines, resulting in a range of spectral types of $\sim$A5 to $\sim$F2. We therefore conclude that KELT-19A meets the classical definition of an Am star, with a spectral type of "Am kA5 hA7 mF2 V."

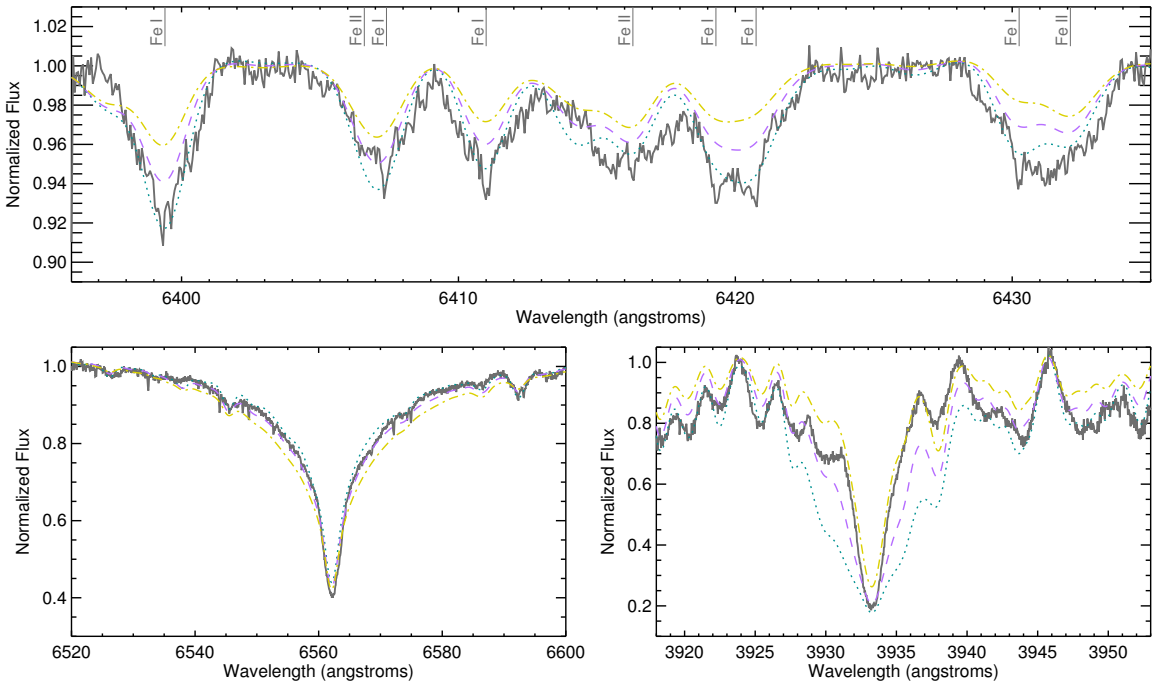

Figure 4.8: The spectrum of KELT-19A (gray solid line) and three PHOENIX model atmospheres [colored lines; Husser et al., 2013], overplotted for illustration (i.e., not fit to the data). All models were generated with $\log g_\star = 4.124$ (cgs) and $[\mathrm{Fe/H}] = +0.5$ and were broadened to 84.8 km s^{-1} rotation, but have temperatures of 7000 K (blue-green dotted), 7500 K (purple dashed), and 8000 K (yellow dash-dotted). *Bottom left:* The Hα profile is consistent with a 7500 K atmosphere, like we find in the spectroscopy and the global fit. *Top:* Iron lines are enhanced, and therefore more consistent with a cooler (7000 K) atmosphere. *Bottom right:* The Ca II K line is weaker than expected, with a profile similar to that of the 8000 K atmosphere. A spectral type that is "too late" in metals and a Ca II K spectral type that is "too early" for the Balmer line spectral type is a hallmark of Am stars because of their photospheric metal enhancement and calcium deficiency.

Table 4.2: Radial Velocity Measurements of KELT-19

BJD_{TDB}	Primary RV ($m\,s^{-1}$)	Primary σ_{RV} [a] ($m\,s^{-1}$)	Secondary RV ($m\,s^{-1}$)	Secondary σ_{RV} [a] ($m\,s^{-1}$)
TRES				
2457118.717801	-8322	677	-6315	2185
2457323.926960	-7382	817	-9178	1588
2457704.974522	-7582	378	-9499	1054
2457706.006779	-8353	379	-9178	928
2457706.905449	-8185	443	-9129	951
2457715.859122	-7872	422	-9260	971
2457761.845292	-8667	319	-8922	871
McDonald				
2457685.865924	-7126	413	-9227	509
2457687.904483	-6797	434	-8635	391
2457732.803281	-7243	266	-9069	330
2457732.925982	-7461	262	-8580	271
2457733.004039	-7236	273	-8784	251
2457733.890461	-7329	552	-8256	862
2457734.795794	-7234	304	-9021	312
2457734.998676	-7294	253	-8503	241
2457735.810347	-7199	251	-8656	298
2457736.002794	-7517	366	-8834	326
2457736.816475	-7434	244	-8366	342
2457737.008672	-6577	297	-8067	395
2457737.771236	-7800	263	-9017	268
2457738.009789	-7263	331	-8445	322

Note. Because of the rapidly rotating host star, we were unable to derive bisector spans.

[1] RV errors before being scaled by `MULTIFAST`.

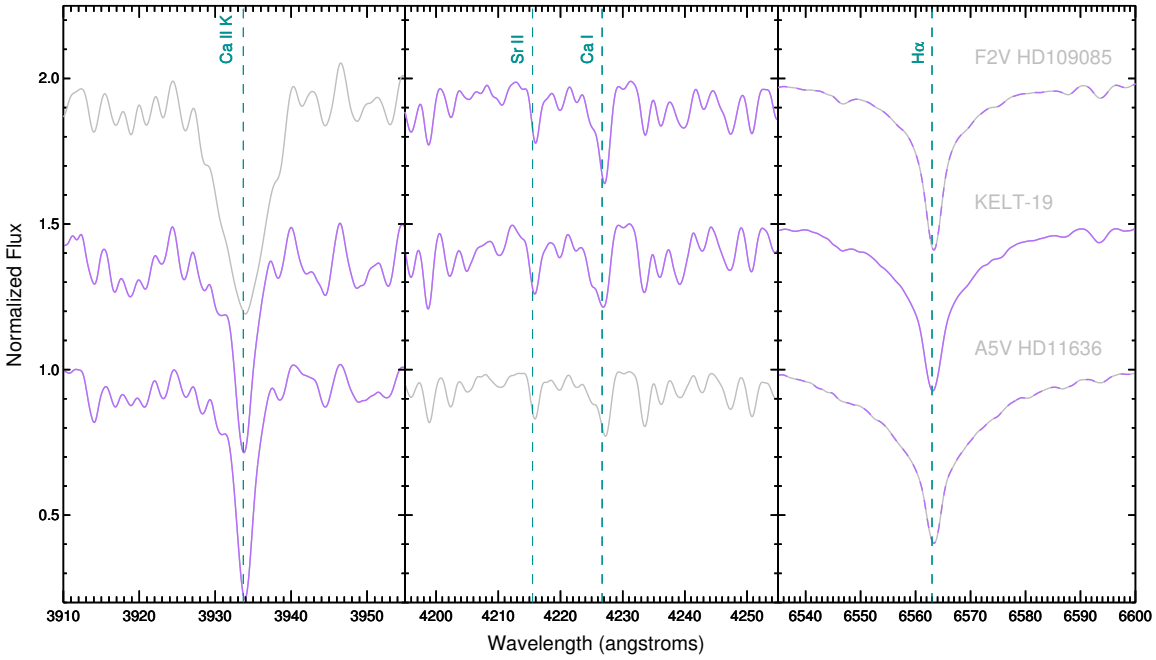

Figure 4.9: The spectrum of KELT-19 (middle row, purple) and two spectral standard stars – F2V HD109085 (top) and A5V HD11636 (bottom). All spectra were obtained by TRES and broadened so that the total broadening (combined rotational, instrumental and artificial) is 100 km s^{-1}. Each panel shows a feature or features important for determining spectral type, and we color the matching spectrum purple to indicate a match (or dashed purple to indicate a partial match). The Ca II K profile (left) of KELT-19 is an excellent match for that of the A5V star. The Hα profile (right) is broader than the F2V, narrower than the A5V, and matches well to an A7V spectrum (not pictured). The strength of the metal lines (middle) match the F2V spectrum, with the exception of Ca I, which is much weaker in KELT-19. Sr II, which is expected to be enhanced in Am stars, does not appear significantly stronger in KELT-19, but it is blended with many other lines because of the star's rapid rotation.

4.3 Host Star Properties

Table 4.3 lists various properties and measurements of KELT-19 collected from the literature and derived in this work. The data from the literature include *BV* and *gri* photometry from Henden et al. [2015], optical fluxes in the B_T and V_T passbands from the Tycho-2 catalog [Høg et al., 2000], near-infrared (IR) fluxes in the *J*, *H* and K_S passbands from the 2MASS Point Source Catalog [Cutri et al., 2003b, Skrutskie et al., 2006], near- and mid-IR fluxes in four WISE passbands [Wright et al., 2010, Cutri and et al., 2012a], and distance and proper motions from Gaia [Gaia Collaboration et al., 2016].

Table 4.3: Literature Properties for KELT-19

Other Names	BD+07 1721 TYC 764-1494-1	2MASS J07260228+0736569 TIC 425206121	
Parameter	Description	Value	Ref.
α_{J2000} ...	Right Ascension (RA)	$07^h26^m02^s.2895$	1
δ_{J2000} ...	Declination (Dec)	$+07°36'56''.834$	1
B_T	Tycho B_T mag.	10.273 ± 0.036	2
V_T	Tycho V_T mag.	9.899 ± 0.035	2
B	APASS Johnson B mag.	10.201 ± 0.030	3
V	APASS Johnson V mag.	9.885 ± 0.040	3
g'	APASS Sloan g' mag.	10.163 ± 0.120	3
r'	APASS Sloan r' mag.	9.872 ± 0.050	3
i'	APASS Sloan i' mag.	9.878 ± 0.040	3
J	2MASS J mag.	9.343 ± 0.030	4
H	2MASS H mag.	9.237 ± 0.020	4
K	2MASS K mag.	9.196 ± 0.020	4
WISE1 ..	*WISE1* mag.	9.138 ± 0.022	5
WISE2 ..	*WISE2* mag.	9.156 ± 0.020	5
WISE3 ..	*WISE3* mag.	9.132 ± 0.035	5
WISE4 ..	*WISE4* mag.	≥ 8.089	5
μ_α	Gaia DR1 proper motion ..... in RA (mas yr^{-1})	-3.706 ± 1.126	6
μ_δ	Gaia DR1 proper motion ..... in DEC (mas yr^{-1})	-1.303 ± 1.226	6
RV	Systemic radial ..... velocity (km s^{-1})	-8.5 ± 0.5	§4.2.4.3
$v \sin i_\star$ ...	Stellar rotational ..... velocity (km s^{-1})	84.8 ± 2.0	§4.3.4.4
Sp. Type$_A$.	Primary Star Sp. Type	A8V	§4.2.4.5
Sp. Type$_B$.	Secondary Star Sp. Type	G9V–K1V	§4.2.4.5
Age	Age (Gyr)	1.1 ± 0.1	§4.3.2
Π	Gaia Parallax (mas)	3.60 ± 0.72	6†
$d_{\star Gaia}$ ...	Gaia-inferred dist. (pc)	278^{+69}_{-47}	6†
$d_{\star SED}$ ...	SED-inferred dist. (pc)	255 ± 15	§4.3.1
A_V	Visual extinction (mag)	0.03 ± 0.03	§4.3.1
U^*	Space motion (km s^{-1})	14.6 ± 0.9	§4.3.3
V	Space motion (km s^{-1})	17.6 ± 1.3	§4.3.3
W	Space motion (km s^{-1})	0.2 ± 1.4	§4.3.3

NOTES: References are: [1]van Leeuwen [2007],[2]Høg et al. [2000], [3]Henden et al. [2015], [4]Cutri et al. [2003b], [5]Cutri and et al. [2013], [6]Gaia Collaboration et al. [2016] Gaia DR1 http://gea.esac.esa.int/archive/
†Gaia parallax after correcting for the systematic offset of -0.18 mas for an ecliptic latitude of $-14°$ as described in Stassun and Torres [2016].

4.3.1 SED Analysis

We performed a fit to the broadband spectral energy distribution (SED) of KELT-19 in order to obtain constraints on stellar parameters for use in the global system fit. We assembled the available broadband photometry from extant catalogs, with measurements spanning over the wavelength range 0.4–22 μm (see Figure 4.10 and Table 4.3).

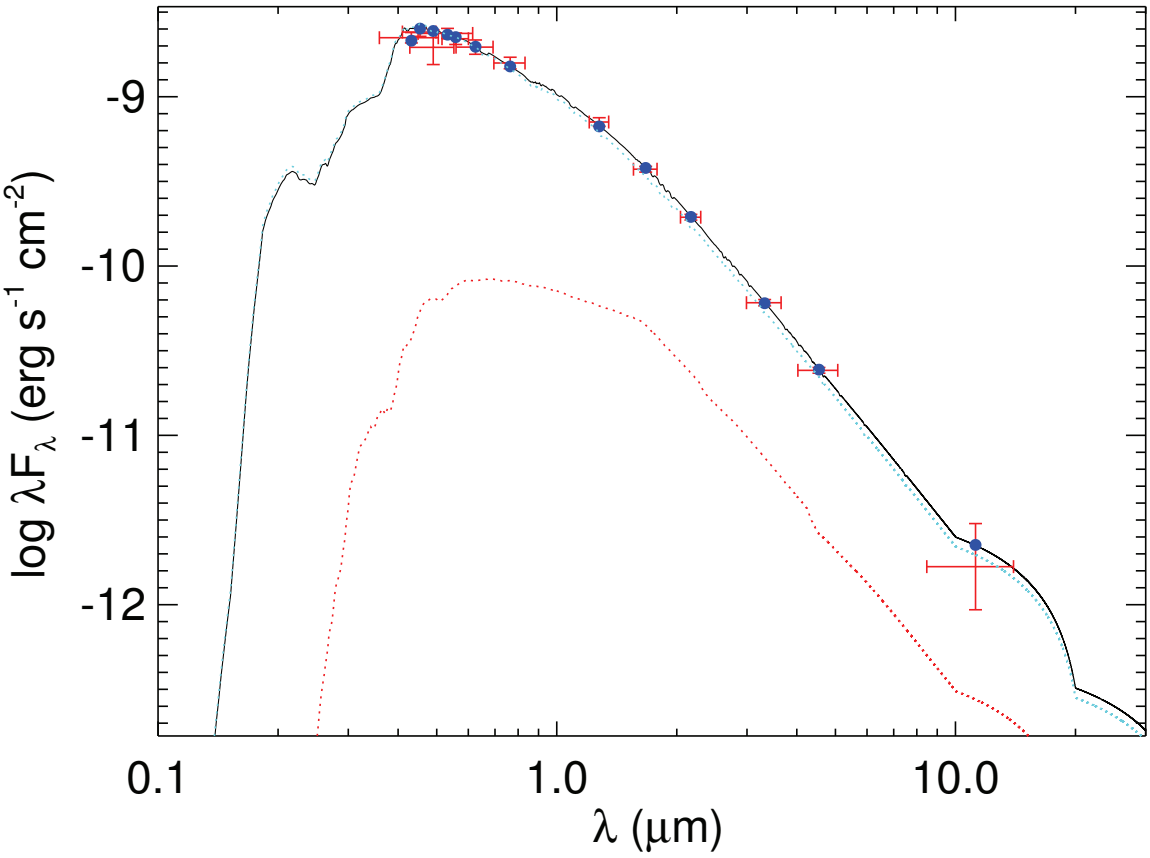

Figure 4.10: KELT-19 two-component spectral energy distribution (SED). Crosses represent the measured fluxes of the two unresolved stars, with vertical bars representing the measurement uncertainties and the horizontal bars representing the width of the bandpass. The blue dots are the predicted passband-integrated fluxes of the best-fit theoretical SED corresponding to our observed photometric bands. The black solid, blue dotted, and red dotted curves represent the best-fit two-component, KELT-19A, and KELT-19B stellar atmospheres, respectively, from Kurucz [1992] (see the text).

For the fitting, we used the stellar atmosphere models of Kurucz [1992], where the free parameters are the effective temperature ($T_{\rm eff}$), the extinction (A_V), and the distance

($d_\star$). In principle, the atmosphere models also depend on metallicity ([Fe/H]) and surface gravity ($\log g_\star$), however we do not have strong independent constraints on these, and in any event they are of secondary importance to $T_{\rm eff}$ and A_V. Thus we assumed a main-sequence $\log g_\star \approx 4.0$ and a solar [Fe/H]. For A_V, we restricted the maximum permitted value to be that of the full line-of-sight extinction from the dust maps of Schlegel et al. [1998]. We also ran the fit with [Fe/H]= +0.5 and the result was not significantly different than the solar metallicity result.

Importantly, the high-resolution imaging (see §4.2.3) revealed another faint star, sufficiently close to KELT-19 that it can be assumed to contaminate the broadband photometry. Therefore, we performed the fit with two components, assuming (for the purposes of the fit) the same A_V and $d_\star$ for both, and we adopted as additional constraints the flux ratios determined from the adaptive optics imaging and from the spectroscopic analysis: $F_{\rm B}/F_{\rm A} = 0.0270 \pm 0.0034$ in the range 5200 ± 150 Å, $\Delta J = 2.50 \pm 0.06$, and $\Delta K_S = 2.045 \pm 0.030$. This introduces one additional fit parameter, namely, the ratio of stellar radii ($R_{\rm B}/R_{\rm A}$) that effectively sets the relative bolometric fluxes of the two stars.

The best fit model shown in Figure 4.10 has a reduced χ^2 of 0.66. We find $A_{\rm V} = 0.03 \pm 0.03$, $T_{\rm effA} = 7500 \pm 200$ K, $T_{\rm effB} = 5200 \pm 100$ K, $d_\star = 255 \pm 15$ pc, and $R_2/R_1 = 0.46 \pm 0.03$. We note that the quoted statistical uncertainties on $A_{\rm V}$ and $T_{\rm eff}$ are likely to be slightly underestimated because we have not accounted for the uncertainty in $\log g_\star$ or [Fe/H]. We also note, however, that the inferred $d_\star$ obtained here is fully consistent with that from the *Gaia* parallax [after correction for the systematic offset of -0.18 mas determined by Stassun and Torres, 2016], and moreover the inferred properties of the secondary star are consistent with those of the observed secondary spectrum (see §4.2.4).

The two-component SED fit also permits determination of the amount of contaminating flux from the companion in the observed transit at each wavelength. This is accounted for in the global solution as discussed in §4.3.4.

4.3.2 Stellar Models and Age

With $T_{\rm eff}$ from the SED analysis, and with an estimated $\log g_\star$ and $M_\star$ from the global analysis (see below), we can place KELT-19A in the Kiel diagram for comparison with theoretical stellar evolutionary models (Fig. 4.11). The estimated system age using the final global fit parameters is ≈1.1 Gyr, with an approximate uncertainty of order 0.1 Gyr. The KELT-19 system is more than halfway through its main-sequence lifetime but is at a stage of evolution well before the "blue hook" transition to the subgiant and eventual red giant evolutionary phases.

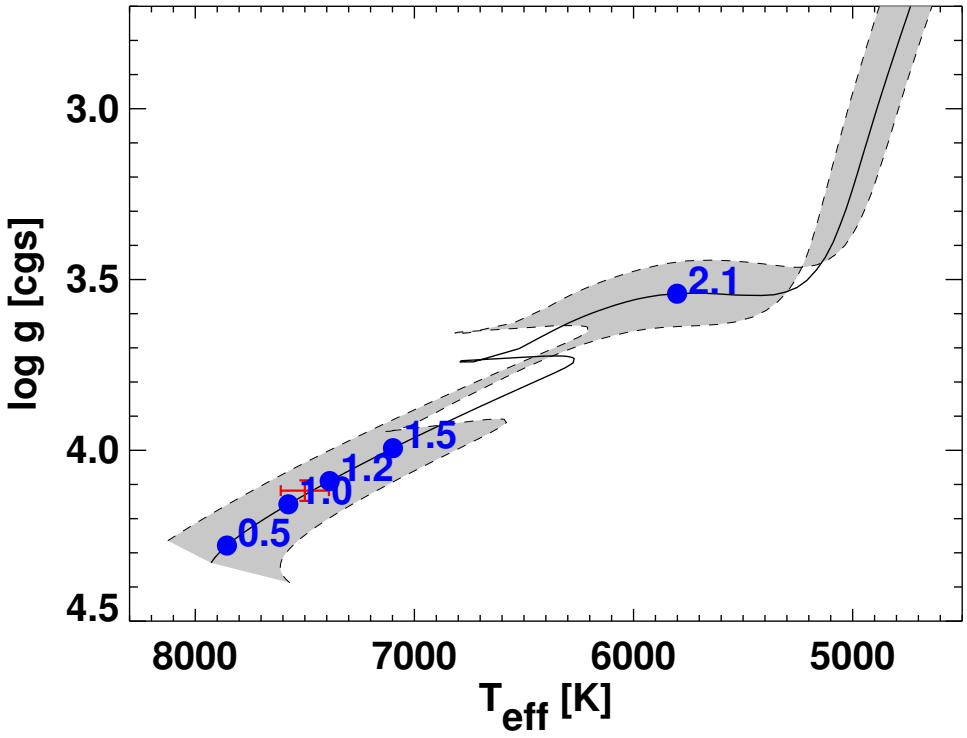

Figure 4.11: Evolution of the KELT-19A system in the Kiel diagram. The red cross represents the KELT-19A parameters from the final global fit. The black curve represents the theoretical evolutionary track for a star with the mass and metallicity of KELT-19A, and the grey swath represents the uncertainty on that track based on the uncertainties in mass and metallicity. Nominal ages in Gyr are shown as blue dots.

4.3.3 UVW Space Motion

We determine the three-dimensional space velocity of KELT-19 in the usual (U,V,W) coordinates in order to determine the Galactic population to which it belongs. We used a modification of the IDL routine `GAL_UVW`, which is itself based on the method of Johnson and Soderblom [1987]. We adopt the Gaia proper motions as listed in Table 4.3, the SED-inferred distance 255 ± 15 pc, and the absolute radial velocity as determined from TRES spectroscopy of -8.5 ± 0.5 km s^{-1}. We find that KELT-19 has U,V,W space motion of $(U,V,W) = (14.6 \pm 0.9, 17.6 \pm 1.3, 0.2 \pm 1.4)$ km s^{-1}, in a coordinate system where positive U is in the direction of the Galactic center, and using the Coşkunoğlu et al. [2011b] determination of the solar motion with respect to the local standard of rest. These values yield a 99.2% probability that the KELT-19 binary system is in the thin disk, according to the classification scheme of Bensby et al. [2003], as expected for its age and spectral type.

4.3.4 Global System Fit

We determined the physical and orbital parameters of the KELT-19A system by jointly fitting 8 transit light curves, 7 TRES and 14 HJST out-of-transit RVs, and a TRES Doppler tomographic data set (see §4.2.4). To perform the global fit, we used `MULTI-EXOFAST` (`MULTIFAST` hereafter), which is a custom version of the public `EXOFAST` software package [Eastman et al., 2013]. `MULTIFAST` first performs an `AMOEBA` [Nelder and Mead, 1965] best fit to each of the RV and light curve data sets individually to determine uncertainty scaling factors. The uncertainties are scaled such that the probability that the χ^2 for a data set is larger than the value we achieved, $P\left(>\chi^2\right)$, is 0.5, to ensure the resulting parameter uncertainties are roughly accurate. The resulting RV uncertainty scaling factors are 1.22 and 1.13 for the TRES and HJST velocities, respectively. The uncertainties of the DT observations were scaled by 1.0. Finally, `MULTIFAST` performs a joint `AMOEBA` model fit to all of the datasets and executes a Markov Chain Monte Carlo (MCMC), starting at

the global best fit values, to determine the median and 68% confidence intervals for each of the physical and orbital parameters. MULTIFAST provides the option to include the Yonsei-Yale (YY) stellar model constraints [Demarque et al., 2004a] or the Torres empirical constraints [Torres et al., 2010] to break the well-known degeneracy between $M_\star$ and $R_\star$ for single-lined spectroscopic eclipsing systems. Siverd et al. [2012] provides a more detailed description of MULTIFAST, except the Doppler tomographic model is described in Gaudi et al. [2017a].

4.3.4.1 Light Curve Detrending and Deblending

We use AIJ to determine the best detrending parameter data sets to include in the MULTIFAST global model by finding the AMOEBA best fit of a Mandel and Agol [2002] exoplanet transit model to the transit photometry plus linear combination(s) of detrending data set(s). Up to two detrending data sets were selected per light curve based on the largest reductions in the Bayesian Information Criterion (BIC) calculated by AIJ from the model fits with and without the detrending data set included. A detrending data set was not included unless it reduced the BIC by > 2.0, resulting in some light curves with only one detrending data set. The final detrending data sets we chose for each light curve are listed in Table 4.1. It is important to emphasize that the AIJ-extracted raw differential light curves (i.e. not detrended) and the detrending data sets were inputs to MULTIFAST and were simultaneously fitted as a part of the global models.

As discussed in §4.2.3 and §4.2.4.3, KELT-19A has a bound stellar secondary companion at a projected separation of $0\farcs64$. Because the secondary is blended in all follow-up photometry apertures, the flux from the secondary must be taken into account to obtain the correct transit depth and planetary radius (e.g. Ciardi et al. 2015). As discussed in §4.3.1, the two-component SED fit permits determination of the amount of contaminating flux from the companion in the observed transit at each wavelength. The determined blend factors, $F2/F1$, for all of the follow-up photometry filter bands are shown in Table 4.4. The

Table 4.4: Flux Contamination From SED Fit

Band	F_B/F_A
5200 ± 150 Å	0.02782
U	0.02412
B	0.03389
V	0.03710
R	0.04619
I	0.04693
Sloan g'	0.03961
Sloan r'	0.04469
Sloan i'	0.04867
Sloan z'	0.05261

blend factors for each filter band were included in MULTIFAST as fixed values to adjust the transit depth in each filter to account for the blend.

4.3.4.2 Gaussian and Uniform Priors

We included Gaussian priors on the reference transit center time, T_0, and orbital period, P. To determine the prior values for the final global fits, we executed preliminary MULTIFAST global fits, including a TTV parameter in the model for each light curve to allow the transit center time to vary from a linear ephemeris, and used priors $T_0 = 2457055.276 \pm 0.013$ $\mathrm{BJD_{TDB}}$ and $P = 4.611758 \pm 0.000053$ d derived from the KELT data. For these preliminary fits, we included the 8 primary transit light curves and the DT data. We chose to include a circular orbit constraint and fixed the RV slope to zero for the model fits. The preliminary YY-constrained model fit resulted in a TTV-based linear ephemeris $T_0 = 2457281.249522 \pm 0.000359$ $\mathrm{BJD_{TDB}}$ and $P = 4.6117091 \pm 0.0000089$ d. These values were used as Gaussian priors in the final YY-constrained global model fit. The preliminary Torres-constrained model fit resulted in a TTV-based linear ephemeris $T_0 = 2457285.861243 \pm 0.000355$ $\mathrm{BJD_{TDB}}$ and $P = 4.6117094 \pm 0.0000090$ d. These values were used as Gaussian priors in the final Torres-based global model fit. Since the KELT- and TTV-based ephemerides are generally derived from independent data, we prop-

agate forward the precise TTV-based ephemerides without concern for double-counting data.

We also included Gaussian priors on the stellar parameters $T_{\rm eff} = 7505 \pm 104$ K and $[{\rm Fe/H}] = 0.0 \pm 0.5$ from the SED analysis in §4.3.1 and the stellar parameter analysis in §4.2.4.5 and $v \sin I_\star = 84.1 \pm 2.1$ km s^{-1} and macroturbulent broadening of 3.4 ± 2.0 km s^{-1} from the out-of-transit broadening profile. A prior was not imposed on $\log g_\star$, since the value derived from the light curve-based stellar density and our stellar radius constraints is expected to be more accurate than the spectroscopic (e.g. Mortier et al. 2013, 2014) or SED-based $\log g_\star$.

We limited the range of certain parameters by including bounded uniform priors. We restricted the RV semi-amplitude to $K > 1.0$ m s^{-1}. To prevent problems when interpolating values from the limb darkening tables, we restricted the stellar parameters to $3500 \leq T_{\rm eff} < 20{,}000$ K, $-2.0 \leq [{\rm Fe/H}] < 1.0$, and $2.0 \leq \log g_\star < 5.0$. We inspected the corresponding posterior parameter distributions to ensure that there was no significant likelihood near the uniform prior boundaries.

4.3.4.3 Global Model Configurations

We examine the results of two global model configurations to explore the effects of YY-constrained and Torres-constrained global model fits on parameter posterior distributions. Since no RV orbit is detected, we force both models to have a circular orbit and an RV slope of zero. Since the Gaia distance error is greater than 10%, we do not impose an empirical stellar radius constraint.

4.3.4.4 Global Model Results

We adopt the posterior median parameter values and uncertainties produced by the YY-constrained fit as the fiducial global model and compare them to the results from the Torres-constrained global model. The posterior median parameter values and 68% confidence

intervals for both final global models are shown in Table 4.5. The KELT-19Ab fiducial model indicates the system has a host star with mass $M_\star = 1.62\,M_\odot$, radius $R_\star = 1.830\,R_\odot$, and effective temperature $T_{\rm eff} = 7,500$ K, and a planet with $T_{\rm eq} = 1935$ K, and radius $R_P = 1.891\,R_J$. Because an RV orbit is not detected, we state 3σ upper limits on all of the planet mass related posterior parameter values. KELT-19Ab's planet mass is constrained to be $< 4.07 M_J$ with 3σ significance.

In summary, we find that the YY and Torres stellar constraints result in system parameters that are well within 1σ.

4.3.4.5 Transit Timing Variation Results

We derive a precise linear ephemeris from the transit timing data by fitting a straight line to all inferred transit center times. These times are listed in Table 4.6 and plotted in Figure 4.12. We find a best fit linear ephemeris of $T_0 = 2457281.249537 \pm 0.000362$ BJD_{TDB}, $P_{\rm Transits} = 4.6117091 \pm 9.0 \times 10^{-6}$ d, with a χ^2 of 20.9 and 6 degrees of freedom, resulting in $\chi^2_r = 3.5$. While the χ^2_r is larger than one might expect, this is often the case in ground-based TTV studies, likely due to systematics in the transit data. Even so, all of the timing deviations are less than 3σ from the linear ephemeris. Furthermore, note that the TTVs of the four simultaneous transit observations on epoch 27 range from $\sim -2\sigma$ to $+3\sigma$, indicating that the TTVs are likely due to light curve systematics. We therefore conclude that there is no convincing evidence for TTVs in the KELT-19Ab system. However, due to the limited number of full light curves included in this study, we suggest further transit observations of KELT-19Ab before ruling out TTVs.

4.4 False Positive Analysis

Despite the lack of a definitive measurement of the companion mass, we are confident that this system is truly a hot Jupiter transiting a late A star. The evidence for this comes from several sources which we will briefly review. However, we invite the reader

Table 4.5: Global fit posterior parameter values for the KELT-19Ab system

Parameter	Units	YY Circular (adopted) 68% Confidence (99.7% Upper Limit)	Torres Circular 68% Confidence (99.7% Upper Limit)
Stellar Parameters:			
M_*	Mass ($M_\odot$)	$1.62^{+0.25}_{-0.20}$	$1.64^{+0.19}_{-0.15}$
R_*	Radius ($R_\odot$)	1.830 ± 0.099	$1.832^{+0.086}_{-0.080}$
L_*	Luminosity ($L_\odot$)	$9.5^{+1.2}_{-1.1}$	$9.5^{+1.1}_{-1.0}$
ρ_*	Density (cgs)	$0.376^{+0.031}_{-0.027}$	$0.378^{+0.031}_{-0.027}$
$\log g_*$	Surface gravity (cgs)	4.127 ± 0.029	4.129 ± 0.026
$T_{\rm eff}$	Effective temperature (K)	7500 ± 110	7500 ± 110
[Fe/H]	Metallicity	-0.12 ± 0.51	$-0.12^{+0.58}_{-0.34}$
$v \sin I_*$	Rotational velocity (m/s)	84800 ± 2000	84800 ± 2100
NRLW	Non-rotating line width (m/s)	3100 ± 1800	3100 ± 1800
Planetary Parameters:			
M_P	Mass (M_J)	(< 4.07)	(< 4.15)
R_P	Radius (R_J)	1.91 ± 0.11	$1.909^{+0.06}_{-0.091}$
ρ_P	Density (cgs)	(< 0.744)	(< 0.739)
$\log g_P$	Surface gravity (cgs)	(< 3.44)	$(< 3.44))$
T_{eq}	Equilibrium temperature (K)	1935 ± 38	1934 ± 37
Θ	Safronov number	$0.0083^{+0.039}_{-0.0071}$	$0.0083^{+0.039}_{-0.0070}$
$\langle F \rangle$	Incident flux (10^9 erg s^{-1} cm^{-2})	3.18 ± 0.25	3.18 ± 0.25
Orbital Parameters:			
T_{C_0}	Reference time of transit from TTVs (BJD_{TDB})	$2457281.249537 \pm 0.000361$	$2457281.249520 \pm 0.000359$
T_{S_0}	Reference time of secondary eclipse (BJD_{TDB})	$2457278.94367 \pm 0.00036$	$2457283.55539 \pm 0.00035$
P	Period from TTVs (days)	4.6117093 ± 0.0000088	4.6117093 ± 0.0000089
a	Semi-major axis (AU)	$0.0637^{+0.0031}_{-0.0027}$	$0.0640^{+0.0024}_{-0.0020}$
λ	Spin-orbit alignment (degrees)	$-179.7^{+3.7}_{-3.8}$	-179.9 ± -3.8
RV Parameters:			
K	RV semi-amplitude (m/s)	(< 352)	(< 355)
$M_P \sin i$	Minimum mass (M_J)	(< 4.05)	(< 4.14)
M_P/M_*	Mass ratio	(< 0.00237)	(< 0.00236)
u	RM linear limb darkening	$0.5440^{+0.014}_{-0.0059}$	$0.5460^{+0.017}_{-0.0076}$
$\gamma_{McDonald}$	m/s	-7256 ± 90	-7258 ± 90
γ_{TRES}	m/s	-8150 ± 180	-8150 ± 180
Primary Transit Parameters:			
R_P/R_*	Radius of the planet in stellar radii	0.10713 ± 0.00092	0.10709 ± 0.00093
a/R_*	Semi-major axis in stellar radii	$7.50^{+0.20}_{-0.18}$	7.52 ± 0.20
i	Inclination (degrees)	$85.41^{+0.34}_{-0.31}$	$85.34^{+0.35}_{-0.32}$
b	Impact parameter	$0.601^{+0.026}_{-0.030}$	$0.599^{+0.026}_{-0.031}$
δ	Transit depth	0.01148 ± 0.00020	0.01147 ± 0.00020
T_{FWHM}	FWHM duration (days)	0.15645 ± 0.00075	0.15650 ± 0.00076
τ	Ingress/egress duration (days)	0.0266 ± 0.0016	0.0265 ± 0.0016
T_{14}	Total duration (days)	0.1831 ± 0.0015	0.1830 ± 0.0015
P_T	A priori non-grazing transit probability	0.1190 ± 0.0030	0.1188 ± 0.0030
$P_{T,G}$	A priori transit probability	$0.1476^{+0.0037}_{-0.0039}$	$0.1473^{+0.0038}_{-0.0039}$
u_{1B}	Linear Limb-darkening	$0.3798^{+0.018}_{-0.0092}$	$0.382^{+0.022}_{-0.011}$
u_{2B}	Quadratic Limb-darkening	$0.3483^{+0.0071}_{-0.011}$	$0.3487^{+0.0064}_{-0.012}$
u_{1I}	Linear Limb-darkening	$0.139^{+0.034}_{-0.011}$	$0.139^{+0.040}_{-0.011}$
u_{2I}	Quadratic Limb-darkening	$0.319^{+0.018}_{-0.031}$	$0.319^{+0.021}_{-0.034}$
$u_{1Sloang}$	Linear Limb-darkening	$0.3500^{+0.022}_{-0.0082}$	$0.3513^{+0.026}_{-0.0089}$
$u_{2Sloang}$	Quadratic Limb-darkening	$0.344^{+0.012}_{-0.015}$	$0.344^{+0.013}_{-0.016}$
$u_{1Sloani}$	Linear Limb-darkening	$0.1558^{+0.037}_{-0.0100}$	$0.156^{+0.043}_{-0.010}$
$u_{2Sloani}$	Quadratic Limb-darkening	$0.324^{+0.018}_{-0.032}$	$0.324^{+0.021}_{-0.036}$
$u_{1Sloanr}$	Linear Limb-darkening	$0.2221^{+0.036}_{-0.0066}$	$0.2221^{+0.042}_{-0.0061}$
$u_{2Sloanr}$	Quadratic Limb-darkening	$0.347^{+0.014}_{-0.030}$	$0.347^{+0.016}_{-0.034}$
$u_{1Sloanz}$	Linear Limb-darkening	$0.109^{+0.026}_{-0.013}$	$0.109^{+0.030}_{-0.013}$
$u_{2Sloanz}$	Quadratic Limb-darkening	$0.311^{+0.018}_{-0.025}$	$0.311^{+0.021}_{-0.027}$

Table 4.6: Transit times for KELT-19Ab.

Epoch	T_C (BJD$_{\rm TDB}$)	σ_{T_C} (s)	O-C (s)	O-C (σ_{T_C})	Telescope
-45	2457073.723660	90	89.10	0.98	KeplerCam
-42	2457087.554255	122	-302.48	-2.48	WCO
-39	2457101.393149	163	22.97	0.14	Salerno
27	2457405.764653	45	-88.84	-1.97	MINERVA
27	2457405.766335	59	56.49	0.96	MINERVA
27	2457405.768490	86	242.68	2.80	MVRC
27	2457405.766362	71	58.82	0.82	MVRC
97	2457728.584553	90	-65.88	-0.73	CROW

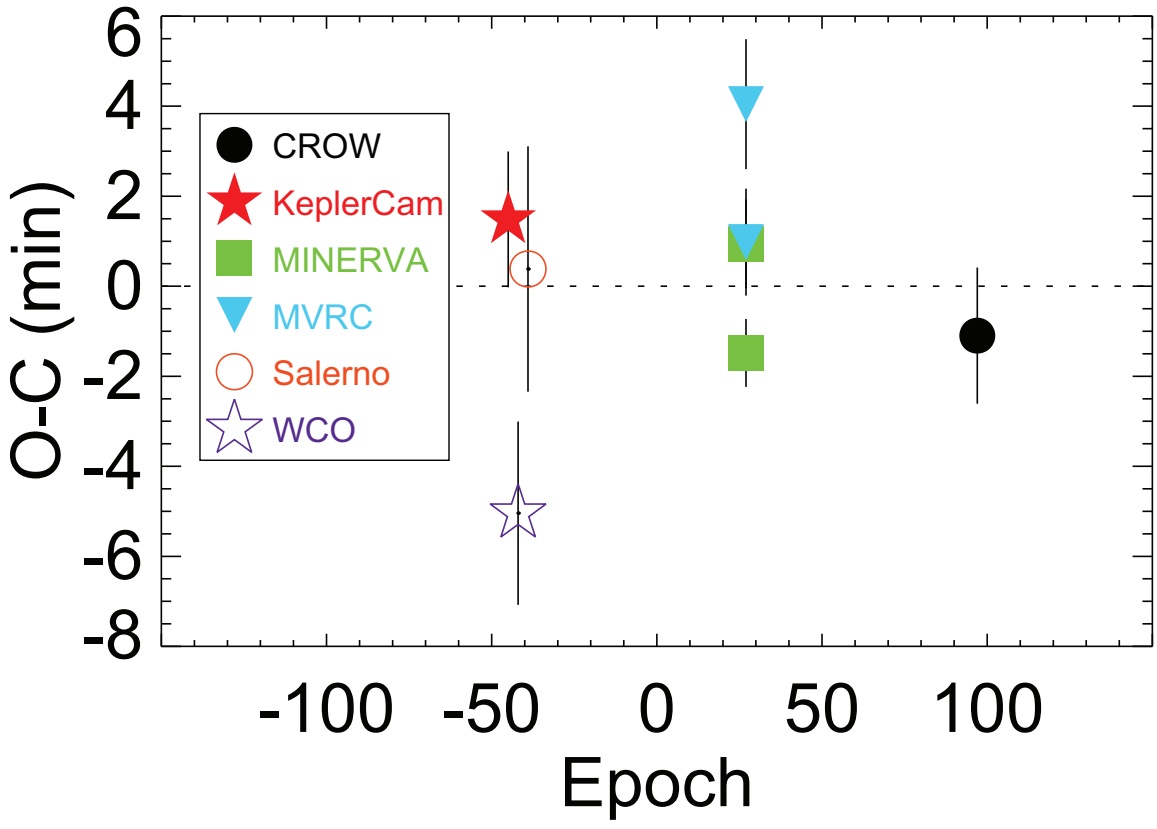

Figure 4.12: KELT-19Ab transit timing variations. All of the timing deviations are less than 3σ from the linear ephemeris. The transit center times of the four transits on epoch 27 range from $\sim -2\sigma$ to $+3\sigma$, indicating that the TTVs are likely due to light curve systematics rather than astrophysical influences.

to review papers by Bieryla et al. [2015], Zhou et al. [2016a,b], and Hartman et al. [2015] for a more detailed explanation. The basic point is that the radial velocity measurements, while not sufficiently precise to measure the mass of the transiting companion, do indicate that it is not a brown dwarf or a low-mass star, if it is indeed transiting the primary A star. On the other hand, we are confident that the companion is transiting the primary A star (rather than, say, the later spectral-type bound companion), because we see a Doppler tomographic signal with the expected amplitude, duration, and impact parameter inferred from the follow-up light curves. Of course, the first system to have been validated in this way was WASP-33b [Collier Cameron et al., 2010b].

The Doppler tomographic observation eliminates the possibility of a blended eclipsing binary causing the transit signal. Even though the line profile derived from the least-squares deconvolution shows a spectroscopic companion blended with KELT-19A, the spectroscopic transit is seen crossing nearly the entirety of the rapidly rotating primary star's line profile (the TRES DT observations did not cover ingress), confirming that the planet is indeed orbiting KELT-19A. The summed flux underneath the Doppler tomographic shadow and the distance of closest approach of the shadow from the zero velocity at the center of the predicted transit time is consistent with both the photometric transit depth and impact parameter, suggesting that the photometric transit is not diluted by background stars, and is fully consistent with the spectroscopic transit.

Adaptive optics observations (§4.2.3) also show a nearby companion consistent in relative brightness with the TRES companion's relative brightness, but no other stars brighter than $\Delta Br\text{-}\gamma < 6$ with separation $> 0.6''$ from KELT-19A at 5σ significance. Furthermore, the deblended follow-up observation transit depths are consistent across the optical and infrared bands as indicated in Figure 4.2.

Finally, the planetary nature of KELT-19Ab is confirmed by the TRES and HJST radial velocity measurements, which constrain the mass of the companion to be $\lesssim 4.1\,M_J$ at 3σ significance. This eliminates the possibility that the transiting companion is a stellar or

brown-dwarf-mass object.

Thus we conclude that all the available evidence suggests that the most plausible interpretation is that KELT-19Ab is a Jupiter-size planet transiting the late A-star TYC 764-1494-1 with a retrograde projected spin-orbit alignment (see §4.2.4.4 and §4.5.1), and with a late G or early K bound companion with a projected separation of ≈ 160 AU.

We do note, however, that this was a particularly complicated case; one that may have easily been rejected as a false positive based simply on the double-lined nature of the line profiles (see Figure 4.5). KELT-19Ab therefore provides an important object lesson: transiting planets can indeed be found and definitively confirmed in initially unresolved binary systems. Indeed, such systems may provide important constraints on the emplacement of hot Jupiters, as the outer bound stellar companion can easily be responsible for Kozai-Lidov oscillations and so emplacement of hot Jupiters [Kozai, 1962, Lidov, 1962].

4.5 Discussion

Figure 4.13 shows host star effective temperature versus V-band magnitude for known transiting planets. Within $T_{\rm eff}$uncertainties, KELT-19A joins KELT-17, WASP-33, HAT-P-57, and MASCARA-1 as having the third highest $T_{\rm eff}$of all known transiting hot Jupiter host stars. With a host star luminosity of $\sim 9.5\,L_{\odot}$ and an orbital period of ~ 4.6 days, the planet has a high equilibrium temperature of $T_{\rm eq} \sim 2000$ K, assuming zero albedo and perfect heat redistribution. With a V-band magnitude of 9.9, a high equilibrium temperature, and a likely large scale height, it is an excellent target for detailed follow-up and characterization. Because KELT-19A is an A star, the planet receives a higher amount of high-energy radiation than the majority of known transiting planet systems, which may lead to significant atmospheric ablation [Murray-Clay et al., 2009].

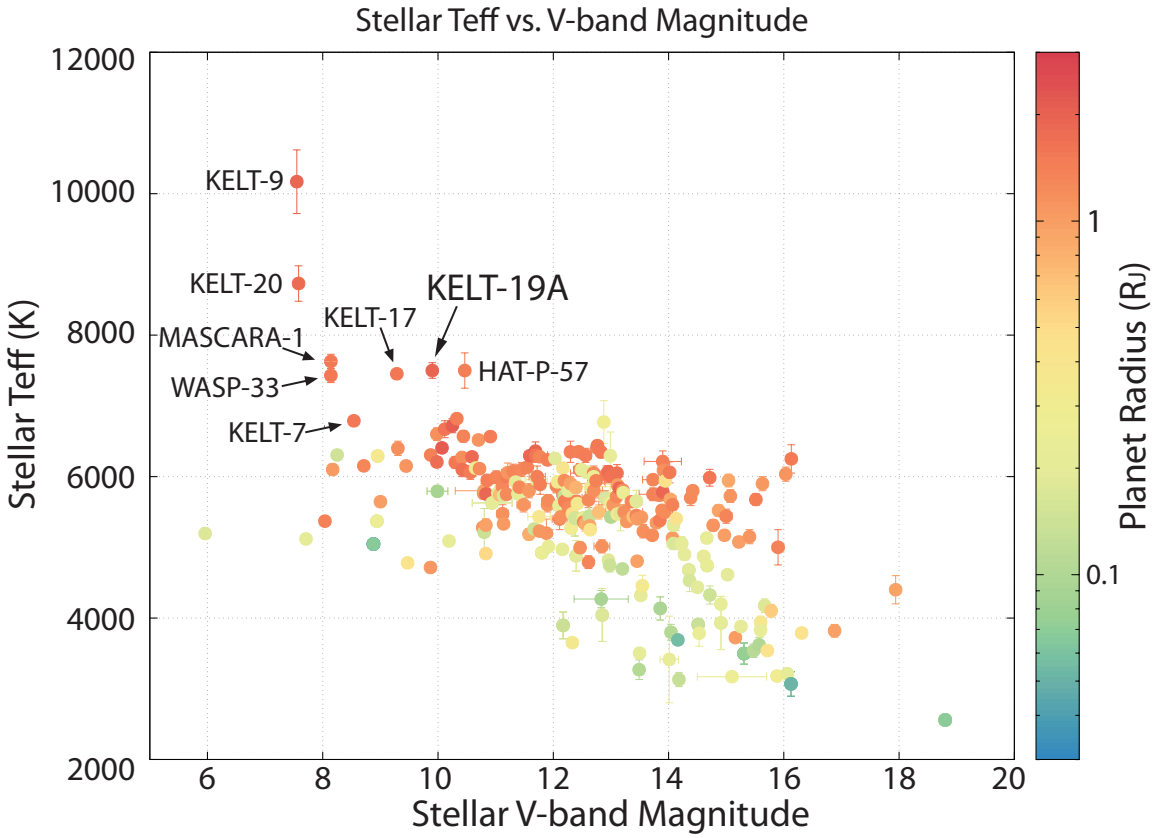

Figure 4.13: The population of transiting exoplanets based on the host star's V-band magnitude and effective temperature ($T_{\rm eff}$), with colors indicating the radius of the planet in R_J. Within $T_{\rm eff}$ uncertainties, KELT-19A joins KELT-17, HAT-P-57, and WASP-33 as having the third highest $T_{\rm eff}$ of all known transiting hot Jupiter host stars. These data, except KELT-19A and KELT-20, were extracted from the NASA Exoplanet Database (https://exoplanetarchive.ipac.caltech.edu).

4.5.1 Spin-Orbit Misalignment

Although we have measured the sky-projected spin-orbit misalignment λ, we cannot measure the full three-dimensional spin-orbit misalignment ψ because we do not know the inclination angle of the stellar rotation axis with respect to the line of sight, I_*. We can, however, set limits upon ψ. First, we follow Iorio [2011] and limit I_*, and therefore ψ, by requiring that KELT-19A must rotate at less than break-up velocity. Doing so, we find that, at 1σ confidence, $19.7^\circ < I_* < 160.0^\circ$ and $105^\circ < \psi < 180^\circ$. We can, however, use the possible Am star nature of KELT-19A to set somewhat stricter limits upon I_* and ψ. Although physically KELT-19A must have an equatorial rotation velocity of $v_{\rm eq} < 250\,{\rm km\ s^{-1}}$ to avoid break-up, empirically Am stars are not observed to have rotation velocities of greater than $\sim 150\,{\rm km\ s^{-1}}$. If we instead require that KELT-19A have $v_{\rm eq} < 150\,{\rm km\ s^{-1}}$, we obtain limits of $33.5^\circ < I_* < 146.5^\circ$ and $119^\circ < \psi < 180^\circ$.

KELT-19Ab continues the trend of hot Jupiters around A stars to have a wide range of sky-projected spin-orbit misalignments. Of the eight A-star-hosted hot Jupiters with measured spin-orbit misalignments to date, one is on a prograde, well-aligned orbit [KELT-20b/MASCARA-2b: Lund et al., 2017, Talens et al., 2017b]; two have misaligned prograde orbits [Kepler-13Ab and MASCARA-1b: Johnson et al., 2014, Talens et al., 2017a]; one is in a prograde orbit with an unclear degree of misalignment [HAT-P-57b: Hartman et al., 2015]; one is on a near-polar orbit [KELT-9b: Gaudi et al., 2017a]; two are on misaligned retrograde orbits [WASP-33b and KELT-17b: Collier Cameron et al., 2010b, Zhou et al., 2016a]; and, now, KELT-19Ab is on a near-antialigned retrograde orbit. Qualitatively, the distribution of A-star hot Jupiter spin-orbit misalignments appears consistent with isotropic, but detailed investigation of this distribution will require a larger sample of planets.

4.5.2 Tidal Evolution and Irradiation History

Following Penev et al. [2014], we model the orbital evolution of KELT-19Ab due to the dissipation of the tides raised by the planet on the the host star under the assumption of a constant phase lag. The starting configuration of the system was tuned to reproduce the presently observed system parameters (Table 4.5) at the assumed system age of 1.1 Gyr (see §4.3.2). The evolution model includes the effects of the changing stellar radius and luminosity following the YY circular stellar model with mass and metallicity as given in Table 4.5. No effects of the stellar rotation have been included in the calculation, since the star is observed to counter-rotate with respect to the orbit. In a retrograde configuration, tidal coupling always acts to remove energy and angular momentum from the planet, and as a result under the assumption of a constant phase lag, the evolution is indistinguishable from that of a non-rotating host star.

Orbital and stellar irradiation evolutions are shown in Figure 4.14 for a range of stellar tidal quality factors ($Q'_* = 10^5, 10^6, \text{and } 10^7$), where Q'^{-1}_* is the product of the tidal phase lag and the Love number. We find that the insolation received by the planet is well above the empirical inflation irradiation threshold of $\sim 2 \times 10^8$ erg s^{-1} cm^{-2} [Demory and Seager, 2011] for the entire main-sequence existence of the star (bottom panel of Figure 4.14).

We consider a wide range of Q'_* because of the wide range of proposed mechanisms for tidal dissipation in current theoretical models and the conflicting observational constraints backing those models, especially for stars that may have surface convective zones (see the review by Ogilvie 2014 and references therein). Furthermore, because the dependence on stellar mass and tidal frequency is different for the different proposed mechanisms, we make the simplifying assumption that Q'_* remains constant over the life of the star. However, with multi-year baselines, it may be possible in the future to empirically constrain the lower limit on Q'_* for KELT-19Ab via precise measurements of the orbital period time decay (cf. Hoyer et al. 2016).

Finally, note that this model does not account in any way for the larger-distance Type II

or scattering-induced migration that KELT-19Ab and other hot Jupiters likely undergo. It considers only the close-in migration due to tidal friction alone.

4.6 Conclusion

KELT-19 consists of a hierarchical triple system of an Am star that is being transited by a $P \sim 4.6$ day hot Jupiter with a mass of $\lesssim 4$ M_J. The planet is highly inflated and highly irradiated, with a radius of $\simeq 2$ R_J, and an equilibrium temperature of $T_{eq} \sim 2000$K. It is also on a retrograde orbit with projected spin-orbit alignment of $\lambda \sim -180$ degrees. Finally, the primary A star (KELT-19A) and hot Jupiter (KELT-19Ab) are orbited by an outer bound stellar G9V/K1V companion (KELT-19B) with a projected separation of ~ 160 AU.

In many ways, KELT-19 is one of the most unusual transiting hot Jupiter systems yet discovered. Firstly, the primary star (KELT-19A) and planet host is an Am (metallic line-enhanced) star. To the best of our knowledge, this is the only such star known to host a transiting hot Jupiter[4]. As is the case for other Am stars, KELT-19A rotates slowly compared to stars of similar effective temperature. Although the presence of a nearby stellar companion is usually invoked to explain both the slower rotation and peculiar abundance patterns of Am stars, the stellar companion KELT-19B seems too distant to cause significant tidal braking. Furthermore, the planetary companion (KELT-19Ab) is likely too low mass to sufficiently slow the rotation of its host star, KELT-19A [Matsumura et al., 2010]. Thus, we believe that the slow rotation of KELT-19A is either primordial or was induced by a more efficient tidal braking mechanism than expected.

Finally, we note that the confirmation of KELT-19Ab provides an important object lesson for future transit surveys. The initial line-spread function exhibited two peaks: a broad peak due to the rapidly rotating A star, and a narrower peak due to the more slow-rotating (but bound) blended late G/early K companion. Without careful analysis, such multiple-

[4]However, see Grenier et al. 1999, who suggest that WASP-33 may be an Am star, although Collier Cameron et al. 2010b note that "No obvious Am characteristics are visible in this spectrum other than slightly weak Ca II H&K lines"

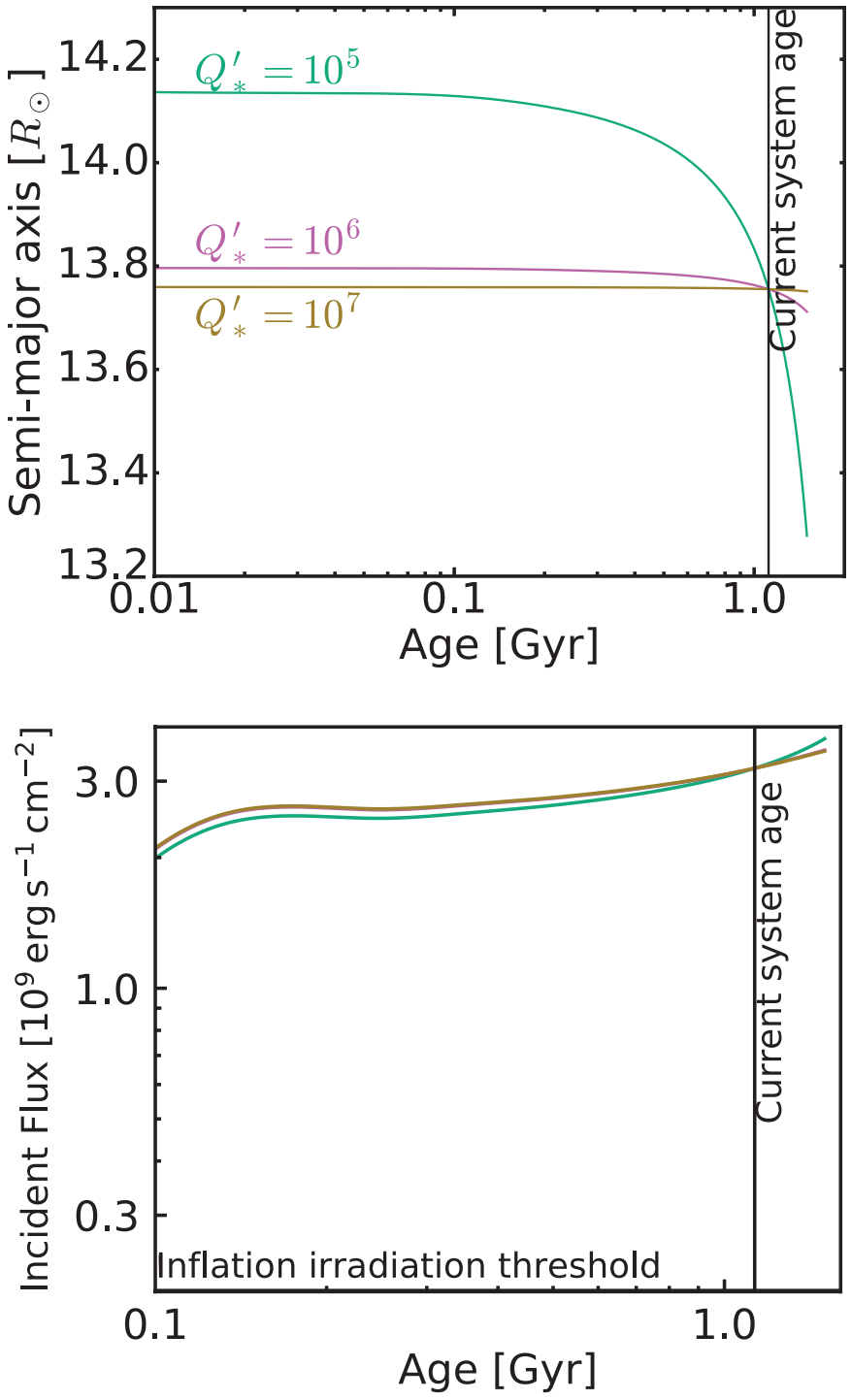

Figure 4.14: (Top) The orbital semi-major axis history of KELT-19Ab modeled for a range of stellar tidal quality factors, Q'_*, where Q'^{-1}_* is the product of the tidal phase lag and the Love number. The black vertical line marks the current system age of 1.1 Gyr. (Bottom) The irradiation history of KELT-19Ab modeled for a range of stellar tidal quality factors. The black horizontal line nearly coincident with the x-axis marks the inflation irradiation threshold of $\approx 2 \times 10^8$ erg s^{-1} cm^{-2} [Demory and Seager, 2011].

star systems may be spuriously rejected as false positives. Generally, we suggest that multi-lined systems not be immediately discarded unless the line of the blended secondary shows relative motion that is consistent with the photometric ephemeris of the transit event, in which case the secondary is likely one component of a eclipsing binary, whose eclipses are being diluted by the primary. In this case, our analysis revealed the presence of a genuine transiting hot Jupiter orbiting an A-type star in a hierarchical triple system.

Chapter 5

Catalog-Driven Extraction: a New Paradigm for Improved Performance from the KELT Transit Survey

5.1 Introduction

Wide-field photometric surveys are an efficient tool for transiting exoplanet detection but their execution poses significant data management and processing challenges. The choice of methods used to meet these challenges can have profound impact on the success of the project. The ideal course of action is generally not known in advance and significant changes to infrastructure and methods may occasionally be warranted in order to maintain high scientific output.

The KELT survey telescope (an f/1.9 Mamiya camera lens with 42mm aperture) provides an extremely wide field of view ($26^\circ \times 26^\circ$) but with coarse resolution (23/pix). Further, this lens introduces significant, spatially-varying optical aberrations that complicate photometry and increase the degree of blending among nearby sources (depending on the CCD location, a single stellar FWHM may subtend nearly a square arcminute).

The first version of the KELT data reduction pipeline (described briefly in §2.2.2) made careful use of existing and modified difference imaging tools and led to the discovery of over 20 new, bright transiting exoplanets. However, this initial success entailed some significant compromises. In particular, our methods often introduced large errors in average star flux measurements and corresponding changes (usually reductions) in apparent transit depth, especially often in crowded fields. This fundamental uncertainty in transit depth in our discovery data required us to invest significant effort and telescope time in photometric follow-up observations of transits to both confirm the source and depth of the detected signal which might not otherwise be necessary. In addition, these biases in KELT light curves preclude their use in statistical assessment of stellar and exoplanetary parameters.

Not surprisingly, these properties render KELT light curve data less useful (at times unsuitable) for a variety of ancillary science tasks which is a barrier to sharing our data with the community.

Catalog-Driven Extraction (CDE) is a set of key changes to methods of KELT data storage, handling, and reduction designed to improve the photometric accuracy of KELT data products and simplify the candidate identification process. These new methods build upon our existing infrastructure to the greatest extent possible while still addressing the most pressing shortcomings of our legacy system.

This chapter is organized as follows. Section 5.2 provides a short primer on difference imaging photometry techniques and how they are used in the KELT pipeline. Section 5.3 follows with an overview of several significant shortcomings of the legacy pipeline and candidate selection system and how those issues impact the KELT transit survey. Section 5.4 describes what Catalog-Driven Extraction entails and why it resolves or improves the main issues identified. Section 5.5 describes the processes of light curve extraction, quality control, post-processing and detrending, followed by construction of the CDE multi-extension FITS data products. Section 5.5.4 then describes the structure and contents of the new data product. Section 5.6 then discusses initial results with the first set of CDE light curves produced, illustrating in particular the improved blend detection ability provided. Lastly, Section 5.7 summarizes the results obtained and provides some thoughts on future direction.

5.2 KELT Photometry and Difference Imaging Primer

In Astronomy, photometry is the process of measuring the amount of light received from distant sources. Today, these data are often in the form of digital images obtained by a Charge-Coupled Device (CCD) connected to a telescope and stored on a computer. Each image usually records light from many different objects. When numerous images are obtained of the same location on the sky, the brightness measurements form time series

often referred to as "light curves."

Different digital photometry techniques exist to accommodate the wide range of science objectives and data collection methods but nearly all of them share the same core steps of source identification and brightness measurement. Source identification entails determining where the targets of interest lie in the images and how large they are (which pixels to add). Brightness measurement then involves estimating and removing background and then adding up what remains at the specified locations.

Image content often influences the choice of technique applied. With its $26\,\mathrm{deg} \times 26\,\mathrm{deg}$ field-of-view and $23''$ pixels, KELT operates in the "crowded" regime meaning essentially that the density of sources is high enough that object separation and background estimation can become difficult. Difference imaging techniques have proven very adept at high-quality light curve production in the crowded-field regime [see e.g., Alard and Lupton, 1998, Alard, 2000, Bramich, 2008, Miller et al., 2008] and thus comprise a core element of the KELT data reduction system.

The difference imaging software measures the flux *difference* between pairs of aligned frames; per common practice, KELT produces a high-SNR "reference image" by median combination of numerous high-quality, aligned images. This image is often analyzed in order to produce an object list (consisting of X,Y pixel position, measured brightness, and an output file name for each object) describing the sources and locations of photometric interest. Though apparently simple, the object list has a very significant influence on the results of the difference imaging process and its importance is difficult to overstate.

The above reference image is also then subtracted from each original image in the data set (referred to below as the "target" images) to produce difference images on which the brightness changes are measured. The subtraction and brightness measurement processes are closely related and proceed as follows in the KELT pipeline:

1. For each target image in the data set, one solves for the convolution kernel that most closely warps the reference image to that target image. This warping typically in-

volves a shape match (i.e., a change in PSF), a flux scaling adjustment to accommodate changes in transparency, air mass, etc. A background adjustment (e.g., a constant value or low-order polynomial model) may also be included in this procedure. The fitted kernel may be spatially variability. Due to the high degree of PSF variability, each KELT image is broken into 25 smaller sub-frames that are individually processed.

2. The convolved reference image is subtracted from the target image to produce a difference. If successful, the difference image will have a PSF similar to the target frame.

3. Residual sky background on the difference image is estimated using a low-pass median filter and then subtracted away.

4. Flux differences are measured on the resulting difference image by repeating the following process for each source on the object list:

   (a) A high-quality PSF is estimated, usually by stacking stars found on the reference image near this location.

   (b) This PSF is convolved using the kernel derived earlier in order to match the appearance of stars in the difference image.

   (c) The convolved PSF is then used to weight the pixels in a photometric aperture according to the expected star shape at that position. This weighting procedure decreases the contamination by neighbors and minimizes the impact of artifacts such as dead or hot pixels.

The above procedure results in a set of flux differences for each listed object from each image processed. As a final step, the measured reference frame brightness (which was effectively removed in the image subtraction step noted above) is added back to the flux differences to produce a time series of flux measurements suitable for further analysis.

5.3 Legacy System Shortcomings

The initial version of the KELT data reduction pipeline (§2.2.2 and the associated candidate selection infrastructure have successfully carried the KELT transit survey to over 25 exoplanet discoveries. As the survey has grown to produce more data covering more of the sky, some of the early design decisions have turned into limitations. Their origins and lasting impacts are described below.

5.3.1 Difficulty in Exploiting Overlapping Fields

For the first several years after beginning operation and before the southern telescope became operational, the KELT transit survey focused on observing the $\sim 40\%$ of the sky directly overhead using observing fields centered at Declination of $\sim 31^{\circ}$ (matching the Winer Observatory site latitude). Chosen with mostly sensible spacing, there was relatively little overlap between adjacent fields in part due to the relatively low Declination. Each observed survey field was handled in isolation and no provision was made to allow combination of data from different fields. For expediency, the candidate selection process itself became tied to observed fields. This simplifies the task of producing detailed web pages in large quantities and allows users to explore the data in detail but also cemented assumptions that make the system less flexible.

As the KELT survey has progressed, more and more new fields have been added to the target list. Especially due to the addition of fields at higher Declinations, the amount of overlap between neighboring fields has grown significantly (see Figure 5.1). The existence of 3-way and 5-way field overlaps seen in the modern KELT survey footprint offer unique opportunities to discover planets with smaller radii or longer orbital periods than would otherwise be possible. The legacy candidate vetting system and its deep connection to the observed field concept makes it difficult to exploit these data troves.

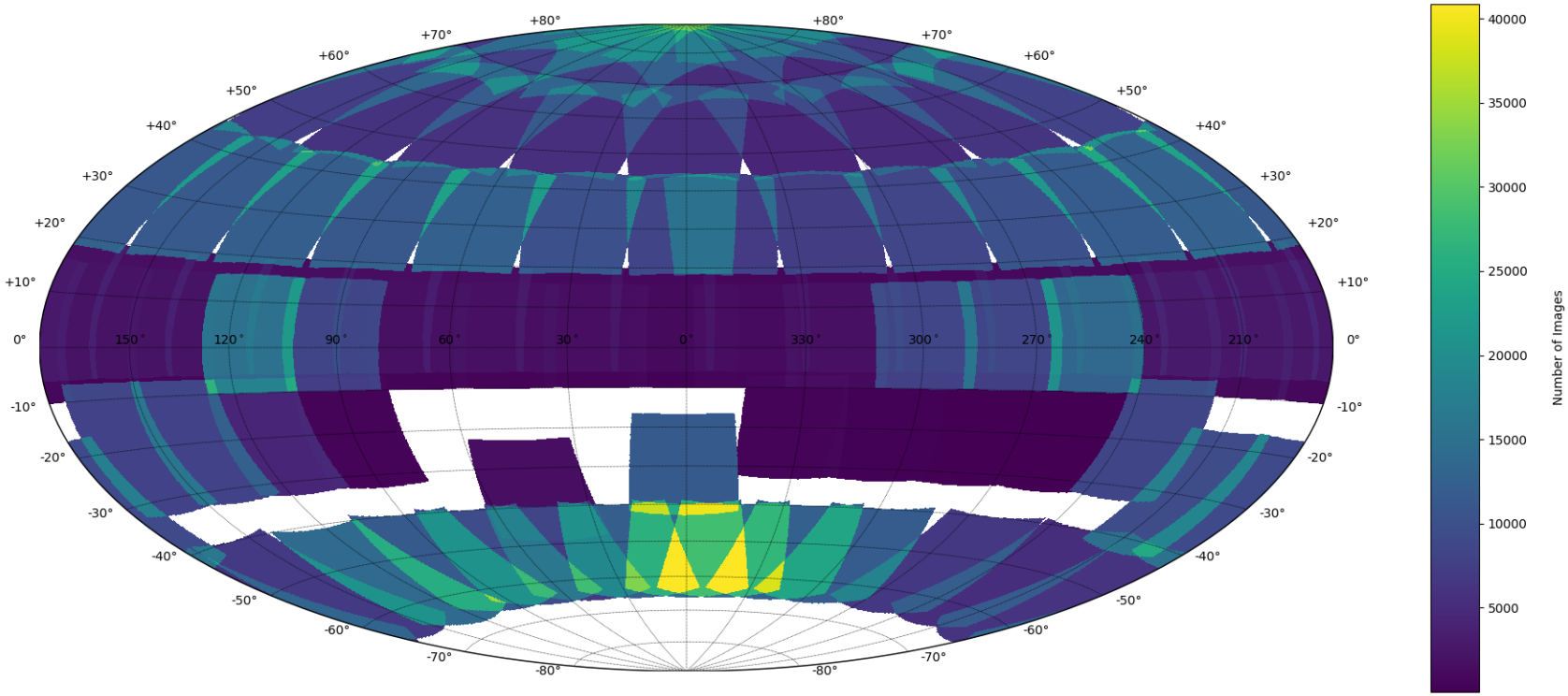

Figure 5.1: Full-sky map of KELT survey coverage showing the number of high-quality images collected as a function of R.A. and Dec. The use of a large ($26^\circ \times 26^\circ$), square field of view creates many areas of partial overlap between adjacent fields that become increasingly common near the celestial poles. While this presents an opportunity to enrich light curves, the need to combine data sets and heterogeneity of results pose extra technical challenges for data reduction and candidate selection.

5.3.2 Object List Problems: Missing Stars and Erroneous Depths

As noted in §5.2, the object list plays a critical role in the photometry process for difference imaging. The legacy pipeline identifies stars on the reference frame for extraction using a the PSF photometry program DAOPHOT [Stetson, 1987, 1990]. With careful use, this software does a good job of finding most stars on the frame but is ultimately stymied by the extreme and inevitable crowding encountered with $23''$ pixel^{-1}image scale of the KELT survey telescope. This ultimately leads to systematic errors in depth measurement.

5.3.2.1 Crowding-Induced Photometry Errors

For the purposes of object list creation, crowding is the condition where the proximity of sources to one another leads to errors in measurement of the brightness and/or position of the stars involved. When adjacent stars have grossly different brightness, the fainter object may not be detected (even after PSF fitting and subtraction) due to the increased statistical noise on the affected pixels. In this instance, the fainter object is missing from the object list and no light curve will be produced. The brighter object is also affected; the light from the fainter star is inappropriately included in the measurement leading to slight overestimates of brightness and slight errors in position.

A similar issue can occur between two stars of similar brightness in close proximity. Often such pairs are detected as a single source. This generally leads to a grossly incorrect brightness measurement and often also entails a poor position measurement midway between the stars. Note that in this case the total light in the area may be measured correctly but is then incorrectly ascribed to a single source. The density of stars increases rapidly as fainter sources are considered (the number of detectable stars increases $\sim$5-fold for each magnitude increase of detection threshold), leading to increased frequency and severity of object list measurement errors for fainter objects.

Systematic errors in either position or brightness operate differently but ultimately both

lead to the same underestimation of eclipse depths and other signals. The observed relative amplitude of variation (measured using magnitude units or relative fluxes) relates to the difference fluxes and object list photometry in a straightforward fashion:

$$\text{amplitude} = \frac{\text{diff} - \text{flux amplitude}}{\text{object list brightness}} \tag{5.1}$$

Errors in position cause photometric apertures to be offset relative to the true location of the variable source. This offset leads to a loss of flux due to missing the aperture. The signal loss may be greatly exacerbated in the weighted aperture case depending on the shape of the PSF at that location. This signal loss (a reduction in the numerator of Eq.5.1) combines with an accurate (or worse, overestimated) object list brightness to reduce the apparent amplitude of the final result.

Gross errors in object list brightness have the same effect through the opposite channel. The aperture may be sited correctly leading to a full intensity difference flux measurement but the overestimated brightness that it combines with leads to a shallower amplitude in the finished product. In fact, the correct amplitude of a variable is only observed if the object list brightness corresponds exclusively to the source of the signal. This is likely not achievable under extremely crowded conditions.

5.3.2.2 Systematic Depth Errors in Practice

Systematic depth errors produced in this fashion lead to both false negatives and false positives. False negatives occur when the depth of an otherwise viable candidate is reduced below the detection threshold. False positives occur when deep eclipse events are reduced in amplitude and mimic planetary transit events. The latter often result in wasted follow-up telescope time before they are identified.

The case of KS13C036752 is an illustrative example. This candidate was identified in KELT-South field 13. With an apparent TFA-detrended depth of $\sim 1.5\%$ and undetrended

depth of $\sim 3\%$, this object was selected as a potential planet candidate and scheduled for photometric follow-up. Upon inspection with a larger telescope that resolves the star from its neighbors, a depth of nearly 8% was observed with KeplerCam (see Figure 5.2). Had we observed the larger depth in KELT data during the selection process, this object would have been set aside as an obvious eclipsing binary.

As noted above, the blending of numerous close sources causes this systematic error. Figure 5.3 illustrates how this appears in practice with two images of matched position and extent. The image on the left is a $15' \times 15'$ cutout from the KELT-South reference frame centered on the aforementioned candidate. The image on the right is an image from the Digitized Sky Survey (DSS) with the same center and angular extent. While numerous stars are visible in the KELT image, there is no sense of the hundreds of distinct sources plainly visible in the DSS image. Importantly, there is no way (using KELT data alone) to identify the neighbors near the candidate which contribute a significant amount of flux within what appears to be the same PSF.

The synthetic KELT magnitude estimates from the CDE pipeline illustrate the origin of this depth error. The legacy KELT pipeline found an instrumental magnitude for KS13C036752 of 13.94 using PSF photometry on the reference frame. The synthetic photometry method (discussed in §5.4.3), however, produces an instrumental magnitude of 14.74. This 0.8 mag difference corresponds to a flux ratio of 2.09 and, within measurement uncertainties, accounts for the significant depth discrepancy between KELT and follow-up photometry.

5.4 Catalog-Driven Extraction

The Catalog-Driven Extraction paradigm was conceived as a single solution in response to the several aforementioned problems identified over the course of the KELT survey. It is a set of modifications to both processing methods and the pipeline output products themselves that together resolve several of the long-standing issues. It further accomplishes

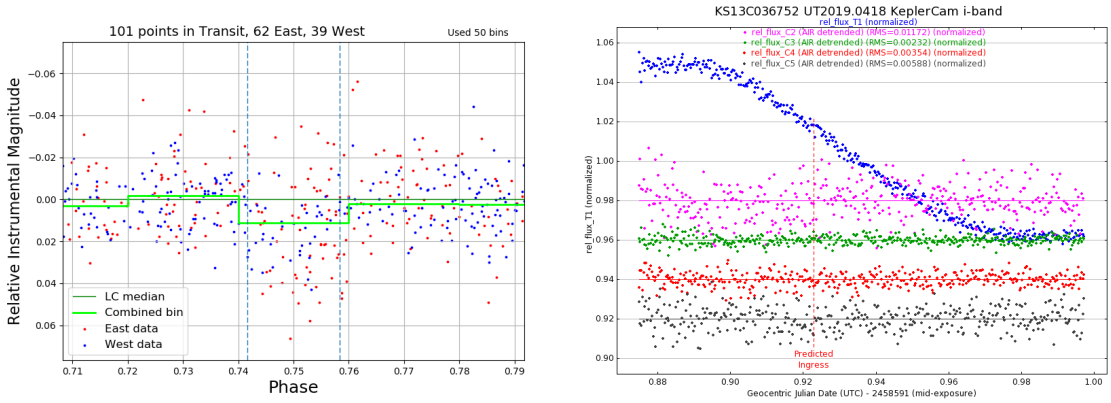

Figure 5.2: Comparison of KELT light curve (left) eclipse depth with results obtained in follow-up with KeplerCam (right). With TFA detrending applied, the KELT light curve exhibits a transit-like feature with a depth of $\sim 1.5\%$. Raw data (without TFA detrending; not shown) exhibit $\sim 3\%$ depth. Although larger, even undetrended data fall significantly short of conveying the true eclipse depth which is found to be $\sim 8\%$.

this in a way that builds upon the existing KELT data processing pipeline, avoiding the need to completely rebuild significant amounts of software from scratch. Most importantly, these changes were conceived in a way that will retain compatibility with the significant candidate selection and web infrastructure developed previously. A brief overview follows below follows by details regarding the specific components.

5.4.1 CDE Process Overview

The core element of Catalog-Driven Extraction is the creation of new object lists based on external catalogs. As noted previously, errors in object list positions and magnitudes lead directly to systematic underestimations of eclipse and transit depths. These, in turn, lead to significant wasted effort both vetting candidates and in photometric follow-up.

Due to the severity of crowding, it is unlikely that measurements extracted directly from KELT images will ever be able to overcome these hurdles. Instead, CDE begins creating a KELT Target Catalog of sources selected from the UCAC4 catalog [Zacharias et al., 2013] for which KELT light curves are desired. These objects were selected based on magnitude range and the availability of numerous photometric measurements in a variety of

bandpasses. Object lists for difference imaging are then created for each of the KELT-North and -South fields by drawing from this KTC.

Every components of the new CDE object lists are drawn from UCAC4 using data from KELT. Object positions are obtained from sky coordinates using the high-quality coordinate solutions available in the KELT reference images. To simplify record-keeping and eliminate the need for object cross-matching, we adopt file names based on UCAC4 identifiers. Importantly, this choice allows us to identify light curves of the same object in different fields using file names alone, eliminating cumbersome steps data reduction and candidate selection. Finally, we apply approximate SED fitting techniques to the UCAC4 multi-bandpass magnitudes to infer object brightness in the KELT system directly. Since the UCAC4 measurements are resolved, we need not worry about gross errors due to the

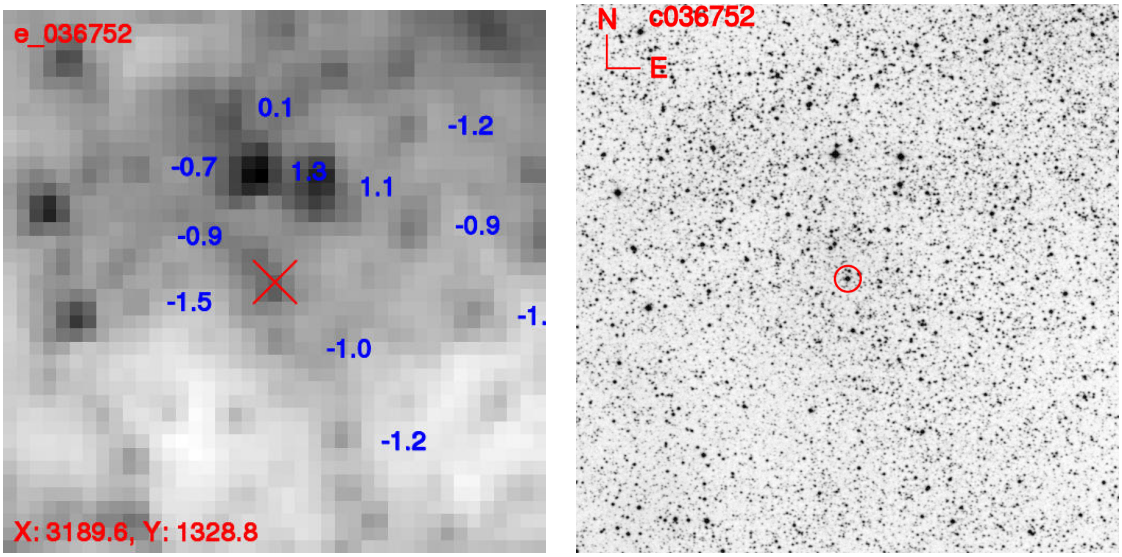

Figure 5.3: Comparison of image resolutions of KELT-South (left) and the Digitized Sky Survey (right). Both images are centered on KELT exoplanet candidate KS13C036752 (TYC 5114-0149-1) and have $15' \times 15'$ FOV. This object was identified as a promising exoplanet candidate based on its KELT light curve which exhibited a 1.5% transit in TFA-detrended data and a $\sim$ 3% depth transit in raw data. However, photometric follow-up of this event revealed a significantly deeper event of $\sim$8% depth. The discrepancy is due to crowding. The presence of multiple stars within the same pixel led to an overestimation of reference flux and erroneous reduction of eclipse depth. Had the true depth been known directly from KELT photometry, this object would not have been selected for additional follow-up. This is a common occurrence due to the KELT pixel scale but will be addressed through the use of external catalogs that resolve the stars of interest.

presence of numerous stars within individual pixels. Fluxes estimated in this way much more accurately reflect those of real stars in the field, promising a significant improvement of systematic light curve errors.

With new object lists in place, photometry is then re-extracted from the existing difference images to make new light curves. No reprocessing of image-level data is required. An overview of the CDE pipeline and how it relates to the legacy pipeline is provided in Figure 5.4. The technical details of this process are discussed in detail in the following sections.

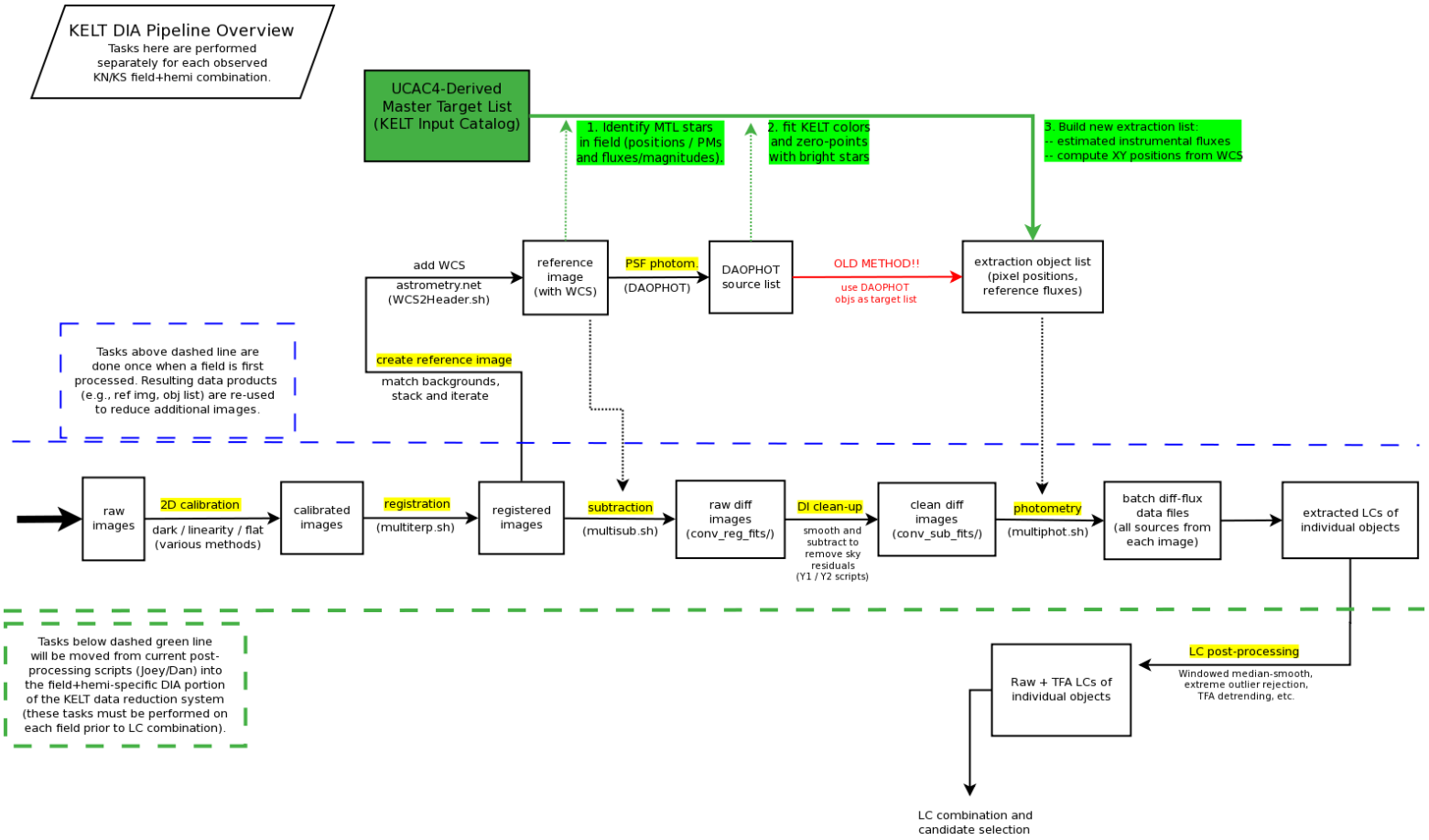

Figure 5.4: Flowchart outlining the various steps of the KELT difference imaging data reduction pipeline. New tasks associated with Catalog Driven Extraction (CDE) are highlighted in green near the top of the chart. The CDE enhancement builds upon the existing pipeline in a way that minimizes the need to reprocess data. A new, much-expanded object list is produced for each observed field by selecting sources from UCAC4 brighter than a limiting magnitude ($V \lesssim 14$). The final (photometry) stage of the pipeline is then re-executed using this expanded list. This structure avoids the need to repeat the image registration, convolution, and subtraction steps.

5.4.2 KELT Target Catalog: UCAC4 Source Selection

Light curves extracted by the CDE procedure are selected in advance from the UCAC4 catalog [Zacharias et al., 2012, 2013] and compiled into a master listed called the KELT Target Catalog (KTC). The choice of UCAC4 was motivated by two primary factors. Firstly, UCAC4 offers reliable positions and proper motions as well as high completeness over the magnitude range of interest to KELT and CDE ($7 \lesssim V \lesssim 14$). This helps both ensuring that bright, valuable targets are included and that potential background contaminants can be identified. Secondly, UCAC4 also provides optical ($BVgri$ photometry from APASS DR6 or $B_T V_T$ from Tycho-2; Høg et al. 2000) and NIR (JHK from 2MASS; Skrutskie et al. 2006) magnitudes for nearly all sources in this magnitude range. Critically, these bandpasses bracket that of the KELT telescope and provide a means by which we can estimate the KELT instrumental flux.

Selection criteria from UCAC4 include:

- source must include a position and proper motion
- source has UCAC4 model magnitude $fmag \leq 14$
- source includes at least two of five APASS $BVgri$ or Tycho-2 $B_T V_T$ measurements

These criteria yield a set of 12,842,065 sources distributed across the entire sky. A plot of star density as a function of sky position is shown in Figure 5.5. We store the resulting data set in CSV files for compatibility with multiple platforms. Following the UCAC4 convention, we separate objects into separate files by zone number (from 001 to 900) to expedite file look-up.

Once the KTC sources are identified, we perform an internal search for neighbors. Each KTC object is checked against the rest of the catalog and any objects found within $180''$are recorded as neighbors in an addendum to the KTC. The number and identifiers of all known neighbors are ultimately recorded in the FITS headers of CDE data products to assist in blend detection (discussed further in §5.5.4.1.

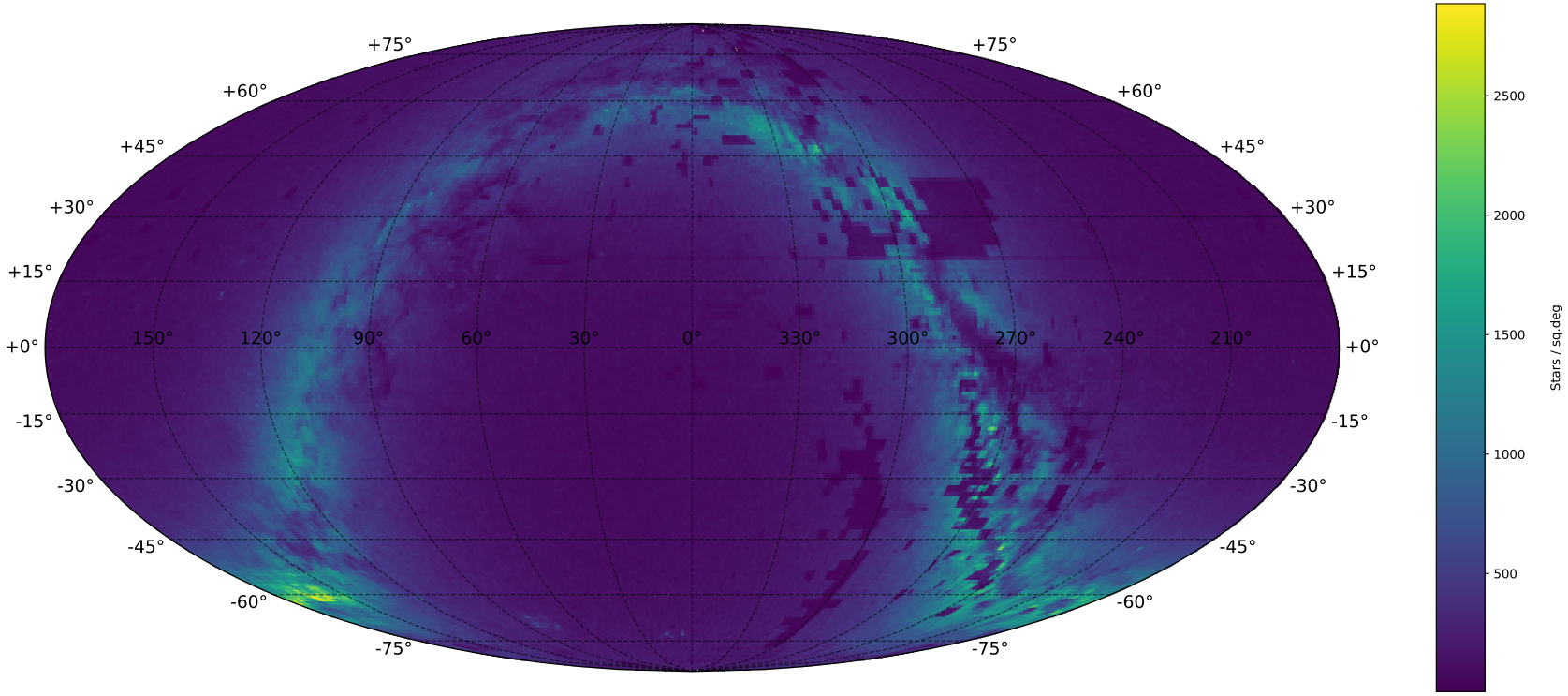

Figure 5.5: The spatial distribution of UCAC4 catalog sources selected for the KELT Target Catalog (KTC), displayed with an equal-area Mollweide projection. The primary inclusion criteria are (a) source brightness (keeping $V \lesssim 14$) and (b) the availability of reliable optical/NIR supplemental photometry (used to estimate KELT instrumental magnitude). More details about the selection process can be found in §5.4.2. The KELT instrumental magnitude estimation procedure is discussed in detail in §5.4.3.

5.4.3 Photometric Zero-Point and Synthetic KELT Magnitudes

The KELT photometric zero point varies between the two telescopes and from field to field for individual telescopes. The systematic North-South difference is mainly due to differences in the CCD (KELT-North and -South employ different CCD sensors). The bulk of this difference is caused by a factor of ~ 2 difference in gain that is not corrected prior to data reduction. Secondarily, differences in CCD quantum efficiency and linearity lead to slight differences in throughput between the two systems. Field-to-field variation arises primarily due to the differences in air mass and sky transparency (i.e., atmospheric extinction) in the reference image.

The zero-point is independently fit for each KELT reference image in order to account for these variations. First, KELT instrumental magnitudes are taken from the pre-existing (legacy pipeline) reference image photometry. Saturated stars and obvious blending cases are removed from this list to avoid biasing the zero point fit. The remaining objects are cross-matched to the UCAC4 catalog [Zacharias et al., 2013] from which we obtain comparison data. UCAC4 provides magnitudes in several bandpasses which bracket the KELT bandpass, including Johnson BV and SDSS gri from APASS plus 2MASS $JHK_{\rm s}$.

For each cross-matched object we select all $BVgriJHK_{\rm s}$ magnitudes with valid data and convert these magnitudes to flux densities in Jy (the effective wavelengths and zero-points used in this conversion are listed in Table 5.1). Objects with fewer than 3 bands provided by UCAC4 are excluded from the fitting process. For objects with at least 3 bands, we fit a 2nd-order polynomial to $\log(F_\nu$ / Jy) vs. $\log(\lambda_{eff}/\mu{\rm m})$ to establish an approximate spectral energy distribution (SED). We then convolve this best-fit polynomial with the assumed KELT response curve to derive a synthetic flux density and convert this (approximately) to the KELT instrumental magnitude scale assuming a zero point of 1.9×10^5 Jy. See Figure 5.6 for an example fit.

Synthetic magnitudes produced in this fashion are not observed to deviate systematically from measured values with $B-V$ or $J-K$ color. However, we do see a clear trend

Table 5.1: Photometric Zero-Points and Effective Wavelengths

Bandpass	$\lambda_{\rm eff}(\mu{\rm m})$	Zero Point (Jy)	Reference
Johnson B	0.4442	4260.00	1
Johnson V	0.5537	3640.28	1
SDSS g	0.4776	3630.78	2
SDSS r	0.6130	3630.78	2
SDSS i	0.7485	3630.78	2
2MASS J	1.239	1577.0	3
2MASS H	1.650	1050.0	3
2MASS $K_{\rm s}$	2.164	674.9	3

[1] Johnson zero-points adopted from Bessell [1979]
[2] SDSS zero-points adopted from Fukugita et al. [1996]
[3] 2MASS zero-points adopted from Cohen et al. [2003]

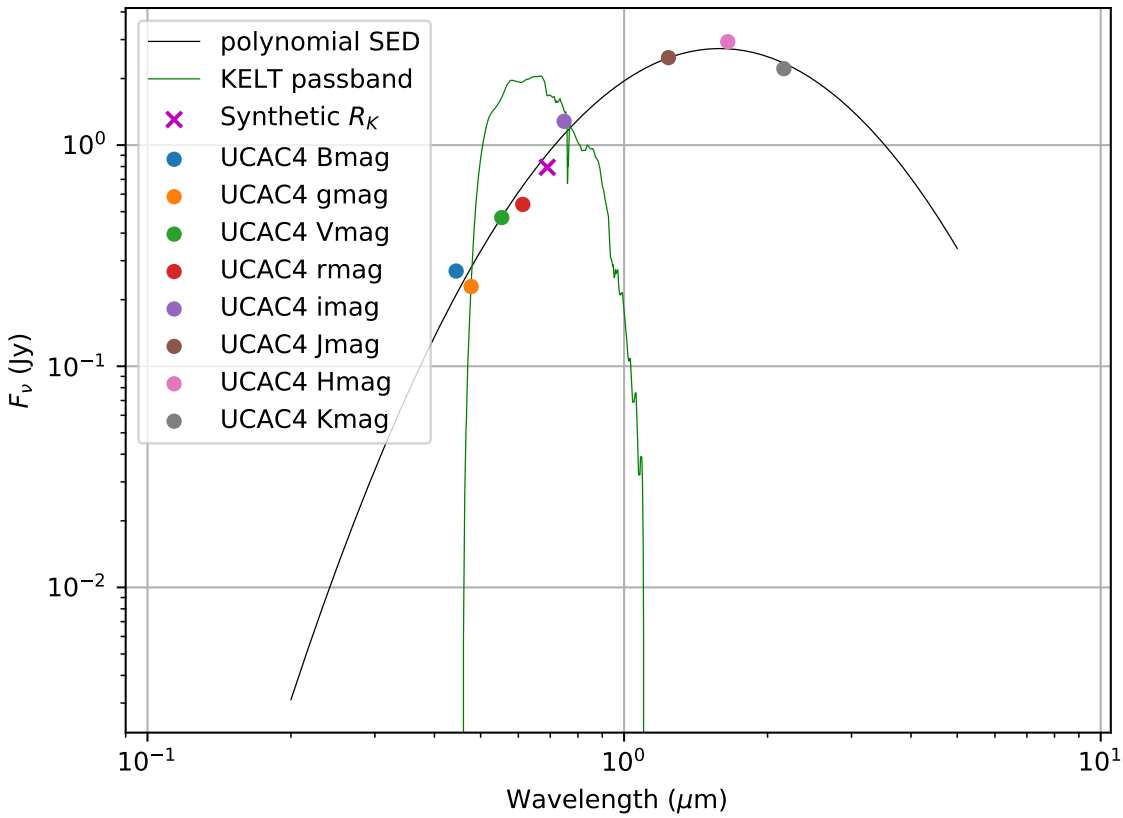

Figure 5.6: Polynomial SED fit and synthetic KELT flux density for a typical object. Each KELT synthetic flux measurement is produced by convolving the KELT bandpass (solid green line) with an approximate SED (solid black line) for each object. This SED is obtained by first converting UCAC4 $BVgriJHK_{\rm s}$ magnitudes to flux densities (see Table 5.1 for effective wavelengths and zero points) and fitting a 2nd-order polynomial to $\log(F_\nu$ / Jy) vs. $\log(\lambda_{eff}/\mu{\rm m})$. The filled circles indicate catalog flux densities in various bands. The magenta X illustrates the derived synthetic KELT flux.

with KELT instrumental magnitude (see Figure 5.7). The origin of this effect is not clear and may be due to an unknown detector systematic. We remove this trend and any remaining zero-point offset by performing a robust linear fit (Theil-Sen slope estimator; Theil 1950, Sen 1968 to $(R_{K,meas.} - R_{K,synth})$ vs. $R_{K,synth.}$. We restrict this fit to objects between the 2nd and 98th percentiles of KELT instrumental magnitude to minimize potential bias due to saturated or very faint objects. We further exclude data points where the measured and synthetic magnitudes differ by more than 0.5 (indicative of a significant photometry problem such as blending or a detector defect). An example of unadjusted measured-synthetic differences and the linear fit described is provided in the top panel of Figure 5.7.

The resulting adjusted synthetic magnitudes (e.g., bottom panel of Figure 5.7) agree fairly well with measurements on average but exhibit a scatter of roughly 5-10%. Although this is significantly less precise than the Poisson limit (especially for bright stars), we can be confident that these values are free of systematic blending effects for most objects. Importantly, the zero-point and trend correction established by this procedure can be used with fainter stars that cannot be reliably measured on the KELT reference image due to crowding and high background.

The fitting process described here has proven itself to be quite consistent through application to many KELT-North and -South fields. Although the two telescopes systematically differ in their zero-points by roughly 2 magnitudes due to hardware differences, both systems respond consistently to this fitting procedure. Figure 5.8 shows the linear fit to the instrumental offsets for all reference images and fields analyzed to date. This sample includes both east and west data for 22 different KELT-North imaging fields (44 reference frames total) as well as east and west data for each of 13 different KELT-South fields (26 reference images total). Some differences are expected to appear from field to field. Not all fields have equally good data quality for various reasons. Fields at different Declination will be obscured by differing amounts of air mass.

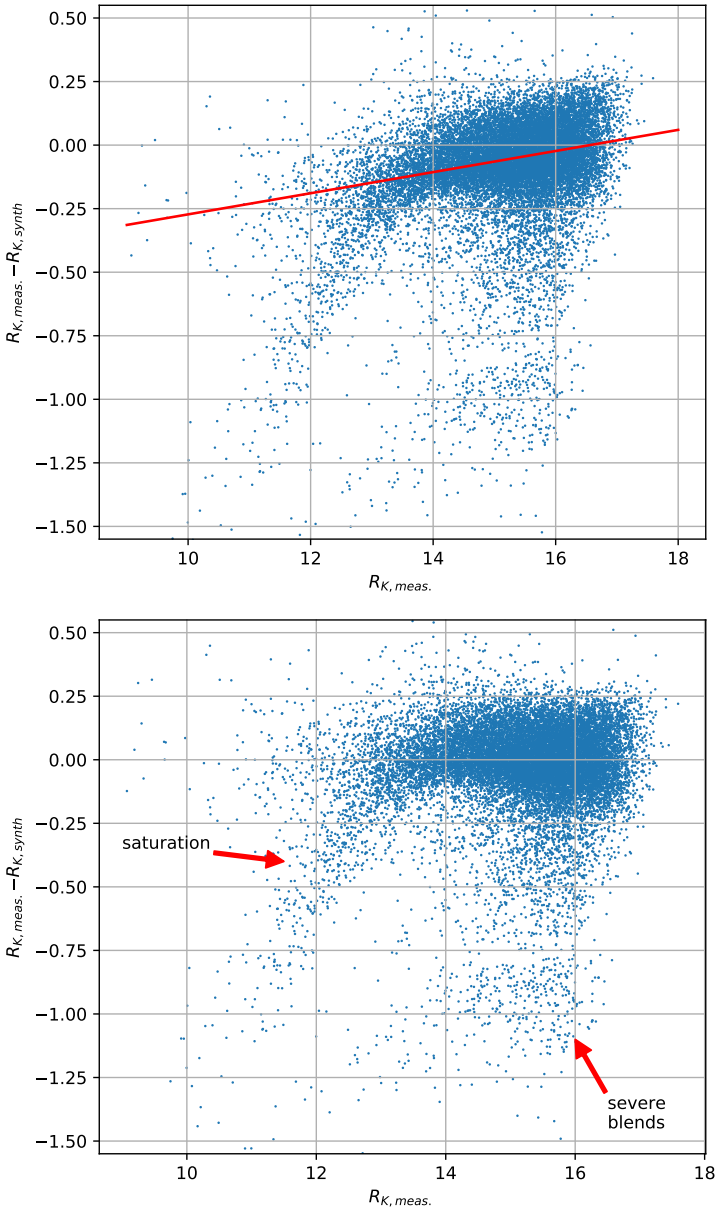

Figure 5.7: Calibration of KELT synthetic magnitudes for a single KELT field. The top panel shows the difference between measured and synthetic KELT instrumental magnitudes as a function of object brightness. A linear fit (solid red line) is used to remove the field-specific offset and trend. The bottom panel shows the same differences after this calibration. Two important classes of photometric error are annotated with red arrows: saturated stars and blended sources. In both cases we observe negative values of $R_{K,meas.} - R_{K,synth}$, indicating the synthetic flux is markedly lower than the measured value. In the case of extremely bright stars, this may indicate saturation in the UCAC4 catalog and motivates our reliance on measured fluxes for the brightest objects when available. Blending errors are caused by crowding that is not resolved by DAOPHOT and can lead to factor-of-several misestimation of measurement flux. Data shown are taken from field KN09E.

Importantly, since the observed KELT fields cover the full gamut of Declinations, not all fields will be observed at the same effective air mass. Especially given the large number of blue stars observed (a function partly of the brighter magnitudes on which KELT focuses), these systematic changes in air mass are expected to introduce not only an offset but perhaps also a slight color-dependence to the zero-point calibration. Seasonal differences in weather and observing conditions may also play a role though this has not been investigated. Despite these expected variations and a few isolated cases of fitting failure, the measured instrumental offsets seem to be fit with remarkable consistency.

It is difficult to overstate the significance of errors due to crowding. The part of parameter space corresponding to crowding errors is highlighted with a red arrow in the lower-right portion of Figure 5.7 (bottom panel). These errors are caused by the presence of multiple stars within the PSF that cannot be resolved on our detector. Reliance on the apparent flux at the position of these overlapping sources leads to large errors in reference flux estimation. For the KN09E data shown in Figure 5.7, errors as large as 1.25 mag (a factor of ~ 3 in flux) are apparent. When re-combined with difference flux measurements, an overestimated source flux causes a *decrease* in the observed amplitude of any variation (such as eclipse or transit depth). Further, since the KELT candidate selection relies on transit depth, these crowding errors ultimately introduce many extra false positives into the candidate vetting process, making the discovery process significantly less efficient. The external catalog-driven photometric estimates described here will eliminate these large amplitude mistakes and significantly reduce the amount of telescope time devoted to these mis-measured objects.

5.4.4 Building the CDE Object List

Once the effective photometric zero-point of a reference image is known, a source list – consisting of positions, magnitudes, and file names in the format needed for our pipeline – is generated from the KELT Target Catalog in a multi-step process. First, UCAC4 sources

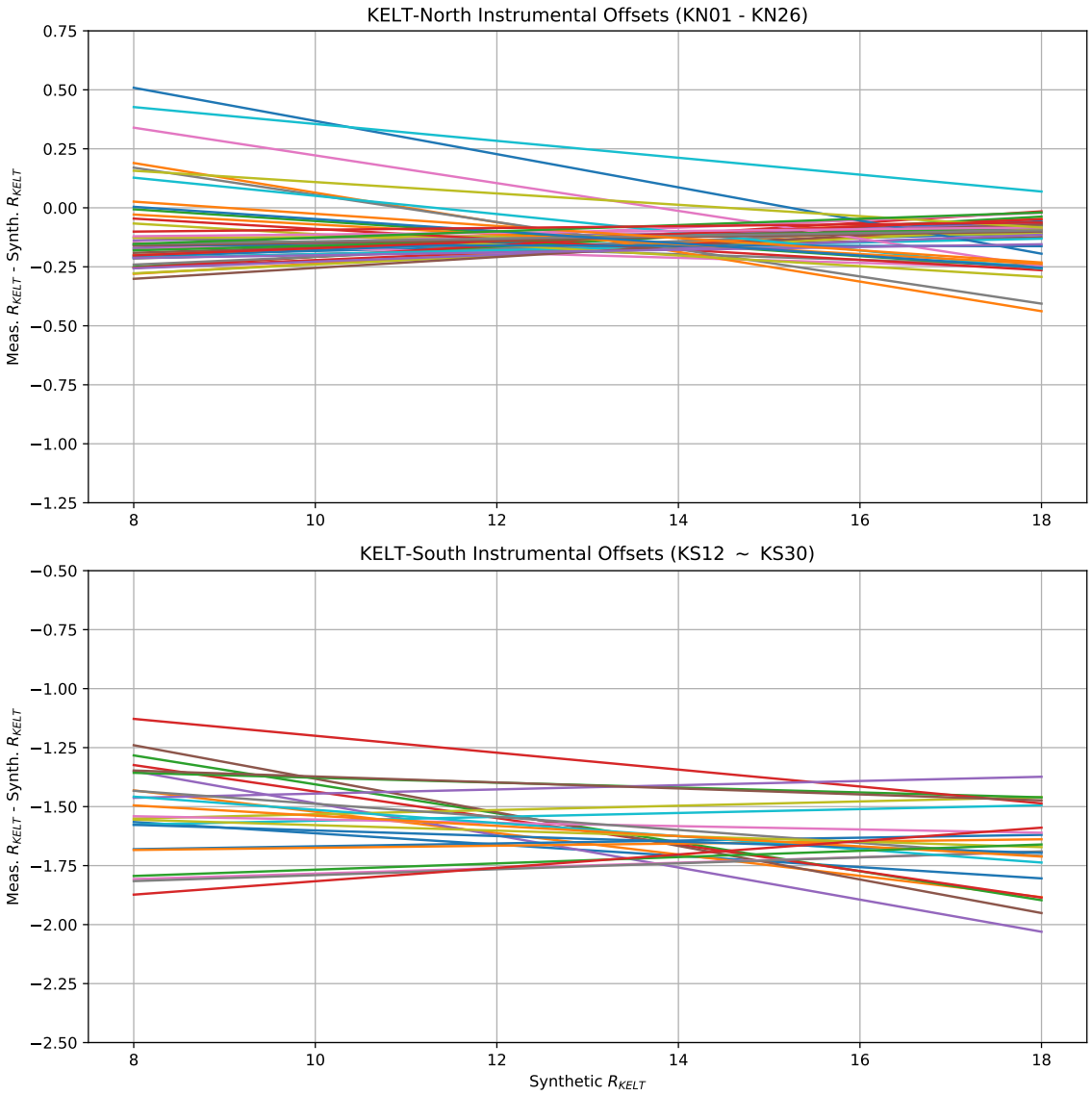

Figure 5.8: Comparison of fitted instrumental offsets for many different KELT fields. These linear fits illustrate the field-to-field deviations from the nominal zero-point for 70 different reference images from KELT-North and KELT-South, obtained in both east and west orientations. Note that there is a fixed difference between the North and South telescopes of roughly 2 mag owing to differences in camera hardware (primarily gain) which are not corrected before the difference imaging pipeline. Each line shown is a linear fit to (measured R_K - synthetic R_K) vs. synthetic R_K. We perform the fits using a variant of the robust Theil-Sen procedure (Theil 1950, Sen 1968) to measure slope and then use a median to establish the intercept. Field-to-field variations are clearly present but generally not severe. In practice, some variation is expected due to heterogeneous observing conditions. Figure 5.7 provides a closer look at a single field case to illustrate the nature of the measurement and why statistically robust methods are important.

in the vicinity of the field are selected from the KELT Target Catalog. The J2000 UCAC4 celestial coordinates of these nearby stars are converted to CCD pixel positions using the WCS embedded in the reference frame (also in J2000, obtained using Astrometry.net; Lang et al. [2010]). Our typical coordinate solution uncertainty translates to ~ 0.1 pixel ($\sim 2.3''$) which is sufficient for our needs. In fact, in most cases, these these WCS-derived pixel coordinates are both more accurate and more precise than what photometry routines would measure on the reference frame. The improved accuracy arises due to the higher resolution of UCAC4 at which our sources of interest are generally not blended and therefore largely free of systematic errors. The improved precision is owed to the high SNR of the bright stars used to solve for astrometry. The relatively low SNR of most stars limits the precision that can be measured directly from pixel data. Estimates of the typical centroid precision are developed with the help of a simple Gaussian model in Appendices A through C.

Using these pixel coordinates, objects residing near the image edges or atop artifacts where useful photometry will not be measured are discarded from the set. Such artifacts often occur when there is substantial pointing scatter among the images available to build a reference frame. One such case of a large border artifact and its pruned sources are presented in Figures 5.9 and 5.10. Border artifacts like this arise due to large pointing scatter among the images combined to build the reference image. The extra border is caused by the "filler" values that surround an image after registration. If the images are significantly misaligned, these filler sections may be hundreds of pixels across. By-eye examination of suspect sources is performed prior to ejection to avoid unnecessary data loss. Fortunately, severe cases such as those shown here are quite infrequent. Remaking the reference image from scratch in the future would likely yield more light curves and improved photometric precision.

Once the final set of objects is chosen, KELT magnitudes are estimated for the entire collection of objects using the nominal zero-point and the best-fit correction obtained previously. Finally, we eliminate the need to cross-match objects from fields by adopting

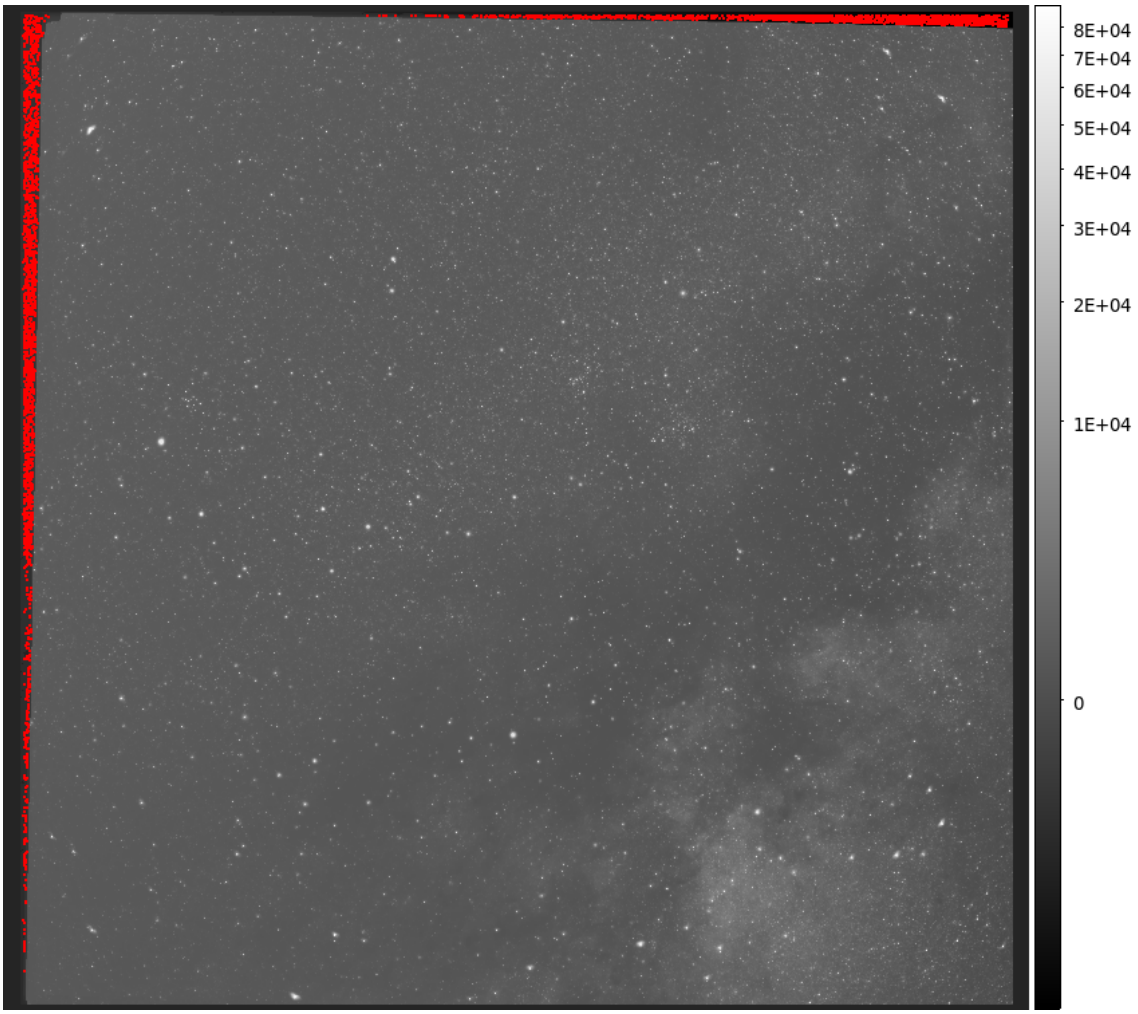

Figure 5.9: The KELT-South field 13 West reference image is shown above. The red circle annotations indicate sources that were discarded during object list creation for this field. The discarded objects are visible along the entire left edge of the reference frame and also near the upper-right corner. These objects were all correctly identified as on-frame but would not produce useful data when extracted. Figure 5.10 shows a zoomed-in view of the upper-left hand corner in order to better illustrate the nature of these artifacts. Blank regions near image edges often develop as a result of pointing scatter among images used to build the reference frame. All objects are verified with a by-eye inspection prior to discarding in order to avoid losing useful data.

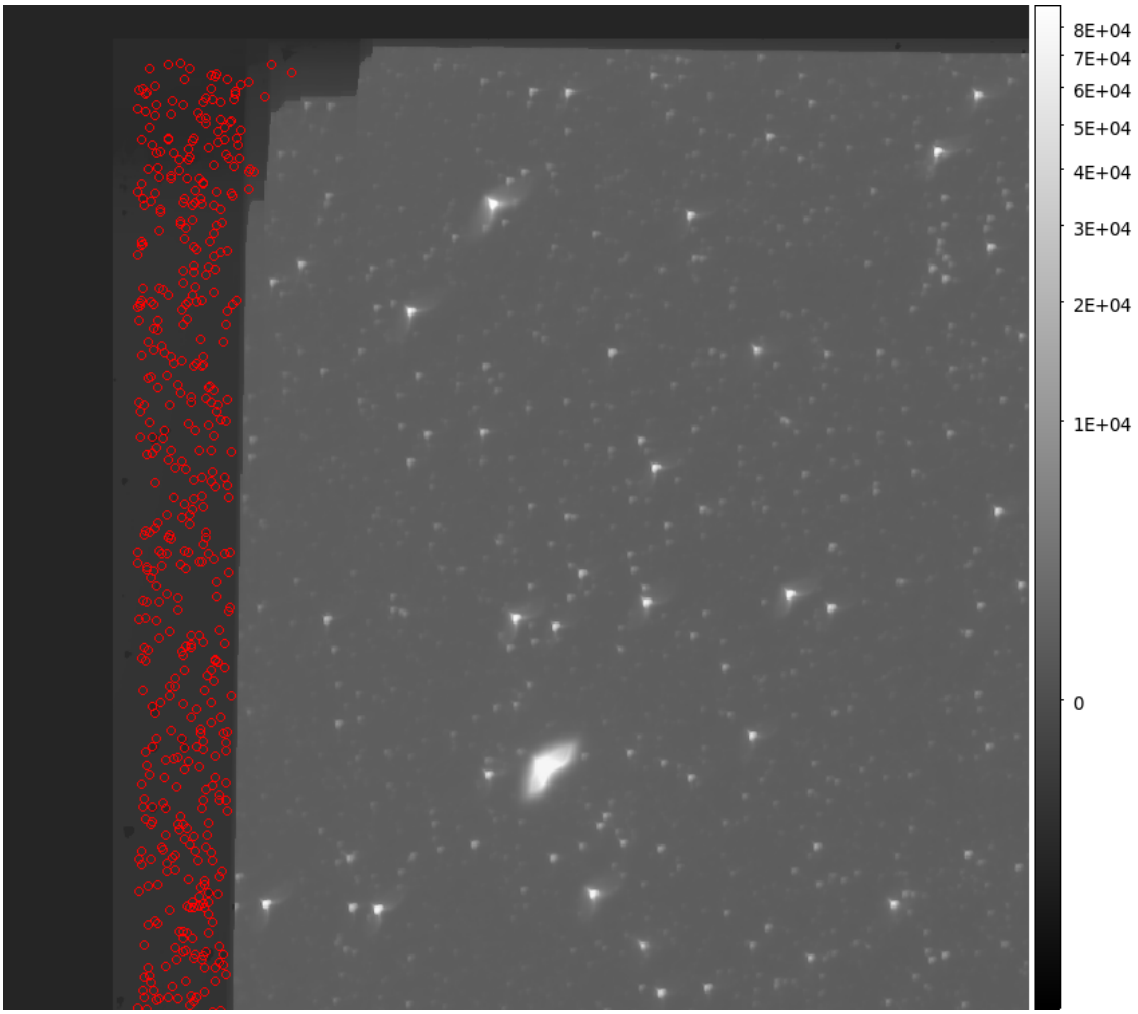

Figure 5.10: Zoomed-in view of the upper-left corner of the KELT-South field 13 West reference image. The red circle annotations indicate sources that were discarded during object list creation for this field. This close-up view helps illustrate the irregular nature of the edge artifacts. Blank regions near the image edges are usually a result of pointing scatter among the images used to build the reference frame. Such removals are confirmed with by-eye inspection prior to ejection in order to avoid unnecessary data loss. A full-frame view of this image can be seen in Figure 5.9.

file names based on the unique, 9-digit UCAC4 identifiers (i.e., `lc_123456789.dat`). Adopting this naming convention eliminates the need for east/west cross-matching within a field and for cross-matching by ID between adjacent fields in case of overlap. We later exploit this naming scheme to simplify the process of data product generation.

5.4.5 Decoupling Candidate Selection from Observing

CDE naturally resolves the overlapping field difficulties in two distinct ways. Firstly, the final CDE data product eliminates the need for multi-way cross matching. The output data products already contain light curves from all available fields in a single location. This eliminates much of the work that has been required in the past to exploit overlap regions for candidate selection. Secondly, the resulting set of CDE data products is fully separated from the KELT survey fields (the locations where the telescopes point) that have previously dominated the candidate selection process. Instead, CDE conceptually replaces these with new and convenient "candidate batches" within which candidate searches can be performed. A candidate batch should be a region on the sky deliberately chosen for its relevance to follow-up. For example, by dividing the sky into so-called "orange slices" (a thin wedge spanning $\sim$ 15 degrees of RA and all Declinations), effort can be focused on objects based on the prospects and/or urgency of follow-up. This region on the sky is populated with CDE light curve files and provided as input to our existing candidate vetting infrastructure. This satisfies the requirement that our vetting pertain to a contiguous area of sky but completely divorces that region from the pointings used for data collection. The existence of software to convert ASCII light curves that mimic the data format of legacy ASCII data products ensures compatibility between new data and existing software.

5.5 Light Curve Extraction and CDE Data Product Assembly

5.5.1 Difference Image Photometry and Initial Quality Control

Once the CDE object list has been produced, light curve extraction proceeds as normal using our ISIS-based software. Fluxes are measured on the difference images using a PSF-weighted aperture to minimize the effects of blending. The PSF used for weighted is measured on the reference frame and convolved using the kernel established in an earlier step to ensure that the size and shape is appropriate for the image in question. For computational efficiency, all fluxes measured from a single image are returned as a batch (data points are not written directly to light curves at this time).

Flux extraction is followed by one or more passes of quality assurance before unpacking data points into individual light curves. We do this by calculating a single statistic for each photometry file that compares the measured flux deviation to the expected photometric uncertainty. Specifically, for each photometry file j, we compute

$$S_j = \text{median}(|\Delta\text{flux}_i \,/\, \text{flux\_err}_i|), \tag{5.2}$$

where the i index refers to the many objects (fluxes) from a single image. Since the DIA process subtracts an average or median from each image, the formula above is similar to the median absolute deviation (MAD) and median absolute residual (MAR) scale estimates. Once all S_j are calculated, sub-par photometry results of all kinds tend to emerge as strong outliers which can be set aside. This simple procedure is able to identify a significant fraction of low-quality data points at relatively minimal computational expense. A purpose-built `BulkLCO` utility is currently used to make these measurements. However, future software versions can compute S_j as part of the flux extraction and record the result as metadata alongside the fluxes themselves to significantly reduce the computational burden of this test.

5.5.2 Raw Light Curve Generation

Assembly of science-grade light curves occurs in several stages, each of which has a significant effect on the data contained. A brief description of these stages follows below.

5.5.2.1 Extraction of Difference Fluxes

In this first stage, individual objects' light curves are extracted from the batch photometry files. This process amounts to a transposition of file structure: the few thousands of photometry files (one each per image) containing hundreds of thousands of data points are repackaged into hundreds of thousands of ASCII files (one each per object), each containing thousands of data points. In addition to JD (TT) time stamps, these files contain two sets of residual fluxes and uncertainties: one measured with a PSF-weighted aperture and one with unweighted aperture. The convolution kernel normalzation (essentially a transparency measurement) is also included for diagnostic purposes. These data are referred to hereafter as LCTYPE `FLUX`.

5.5.2.2 Conversion to Magnitudes and Quality Assessment

Each difference flux light curve is converted to a flux light curve (in ADU units) by adding the object-specific reference flux level. These flux-unit light curves are then immediately converted to instrumental magnitudes. Here, we adopt a zero-point where 1 ADU corresponds to 25th magnitude in instrumental units. Critically, this reintroduction of reference flux (needed to transform from the difference fluxes we actually measure to true fluxes we can use) is the origin of our systematic errors in amplitude. Adding an overestimated reference flux leads to a decrease in amplitude of any variability present when examined in relative units (it also gives the appearance of greater photometric precision than is actually obtained). As noted in §5.4.3, CDE alleviates this core problem by estimating KELT reference fluxes from resolved UCAC4 multi-band photometry.

After conversion to magnitude units, light curves are assessed for photometric performance and variability identification. A so-called "RMS plot" (such as those shown in Fig. E.1) that displays the measured light curve scatter as a function of source magnitude. Variable stars are easily spotted with scatter far exceeding that of other objects with similar brightness. A sudden decrease in precision with increasing brightness marks the onset of detector saturation.

Once stars exhibiting either high variability or detector saturation have been noted, we proceed with a second round of outlier detection. This second pass identifies outlying data points on an object-by-object basis *excluding* the variable or saturated sources identified above. In each light curve we perform a robust outlier check using the median and scaled MAD[1]. Magnitudes that differ from median by more than $4 \cdot \hat{\sigma}$ are considered outlying and the JDs of all such points are recorded. Once all light curves are analyzed, the occurrences of each outlier JD are tallied. Data points found to be discrepant in more than $\sim 5\%$ of light curves are stripped out of all light curves before proceeding. We designate these light curves as LCTYPE `LCS1`.

5.5.2.3 Windowed Median Smoothing

Long-term changes in light curves occur for a variety of reasons. In some cases there is true astrophysical variability that occurs over years. In other cases, systematic errors such as pointing changes may introduce variation on time scales of a year or longer. Without correction, this long-term variability introduces significant aliasing (especially near the diurnal sampling frequency) that can swamp the low-level astrophysical signals of transiting exoplanets.

In order to mitigate this effect, we remove long-term variation using a high-pass filter.

[1] We adopt the standard scaling $\hat{\sigma} = 1.4826 \cdot \mathrm{MAD}$ as our robust estimate of standard deviation since we expect our light curve scatter to have an approximately normal distribution. The scale factor 1.4826 is needed to account for the different cumulative distribution coverage of the two estimators; for any symmetric distribution, 50% of the distribution is enclosed by [-MAD, +MAD] whereas $[-\sigma, \sigma]$ covers $\sim 68.3\%$ of the standard normal distribution. See Rousseeuw and Croux [1993] for further discussion.

We reconstruct the long-term variation at each point i by taking the median of all data points within a 90-day window centered on JD_i:

$$\mathrm{window\_mag}_i = \mathrm{median}(\mathrm{mag}_j) \tag{5.3}$$

where $|\mathrm{mag}_j - \mathrm{mag}_i| < 45$ days. The median light curve magnitude is subtracted prior to this filtering operation so that the overall magnitude level is not changed. We designate these light curves as LCTYPE `LCS2`.

This process effectively removes long-term secular or seasonal variations due to a variety of sources, many of them related to systematic changes in the observing system (e.g., pointing changes due to telescope maintenance). However, it necessarily also eliminates real astrophysical variability on long timescales. As a result, these data are generally not suitable for study of long-term astrophysical phenomena.

5.5.2.4 Extrema Clipping

Sporadic strong outliers often persist in light curves despite the aforementioned steps. Often these are caused by short-lived insults that affect few stars. The origins of such events vary widely from astrophysical to environmental and detector-based. Extra-terrestrial examples (primarily brightenings) include meteors, bolides (explosions), and visible satellite trails near dawn or disk. Detector-based examples are due primarily to pixel defects; telescope pointing errors move hot and inactive pixels with respect to the stars leading to sudden brightness changes for unlucky objects. Environmental issues such as cosmic ray strikes similarly cause isolated brightness changes.

If present, strong outliers are often disruptive to statistical fitting routines. In particular, a small number of highly deviant data points may prevent the successful application of TFA detrending [Kovács et al., 2005]. To mitigate this effect, we apply a round of extremum clipping. This process is very similar to that described in §5.5.2.2. Light curves are pro-

cessed individually and scanned for outliers using robust methods. Data found to differ from median by more than $7\hat{sigma}$ are considered outlying and removed. We limit the number of points removed from each extreme that can be removed to prevent catastrophic removal of strong signals ($N = 5$ works well in practice). We designate these window-smoothed, clipped light curves LTYPE `LCS3`.

5.5.3 Light Curve Detrending with TFA

We use the Trend Filtering Algorithm (TFA; Kovács et al. 2005) to help identify and remove systematic errors from our photometric time series. We use the TFA implementation provided by the publicly available `VARTOOLS` program for this analysis [Hartman and Bakos, 2016].

The TFA algorithm first requires an input list of template light curves. Detrending entails modeling each target light curve as a linear combination of templates and then subtracting this best-fit model. Ideally the templates should sample a wide range of effects to be most useful (systematic errors not covered by the templates cannot be corrected). Since the nature of systematic effects may vary with detector position (in KELT, for instance, air mass often varies significantly across the field), choosing trends spread broadly across the field can be an effective way to proceed. To avoid overfitting, the number of trends should be small (up to a few percent) compared to the number of data points in a light curve.

TFA can require a significant amount of computation if not applied carefully. Per Kovács et al. [2005], most of the computational burden is incurred during setup before any corrections are performed. This setup entails creation and inversion of a large ($N_{\text{template}} \times N_{\text{template}}$) design matrix from the templates. With the filter constructed, correction of individual light curves is very fast. To avoid self-detrending, trend stars are prohibited within some exclusion radius of targets. When a "collision" occurs, a new filter matrix must be built with the modified trend set. Unfortunately, memory requirements generally prevent the storage of multiple matrices simultaneously, forcing the original to be discarded. As

Table 5.2: TFA Run-Time Performance Measurements

Template Stars	100	144
Filter setup (sec)	0.23517	0.71958
Detrend time (sec/obj)	0.00542	0.00942
Setup-to-detrend ratio	43.35977	76.40624

Linear fits to TFA run-time(number of light curves) provide direct estimates of filter setup time (intercept) and fitting/correcting time per light curve (slope).

a result, each collsion incurs the setup cost *twice*: once to build the restricted filter and a second time to rebuild the original filter after the interference is resolved. In this scheme, the order of light curves may have a significant effect on program run-time. The ordering of objects to detrend should reflect their placement relative to trend stars in order to minimize the number of filter reconstructions.

Motivated in large part by the desire to detrend the large sample of CDE light curves in the near future, we conducted a few simple speed tests to assess the importance of these choices. In these tests the *same* light curve was repeatedly detrended between 1 and 1000 times. Repeating the same object eliminates the chance of filter reconstruction and also mitigates the confounding effects of disk speed. Under these conditions, a linear fit to run-time versus job size separately determines the costs of filter setup (Y-intercept) and light curve correction (slope). Results of these tests are shown in Figure 5.11 and the fitted parameters are summarized in Table 5.2. We find that the filter setup time is $\sim$ 50x longer than the object detrending time. These results confirm the importance of careful task planning, particularly for very large light curve samples.

Motivated by these findings, we developed a new scheme for TFA detrending that allows all objects to be processed but avoids the need to rebuild the design matrix. This procedure ultimately detrends each star $\sim$ 4 times but finishes more quickly by eliminating target-trend collisions. We accomplish this by dividing the field into nested grid cells: an N x M outer grid (with N,M usually $\sim$ 10) that is further internally separated into a 2x2

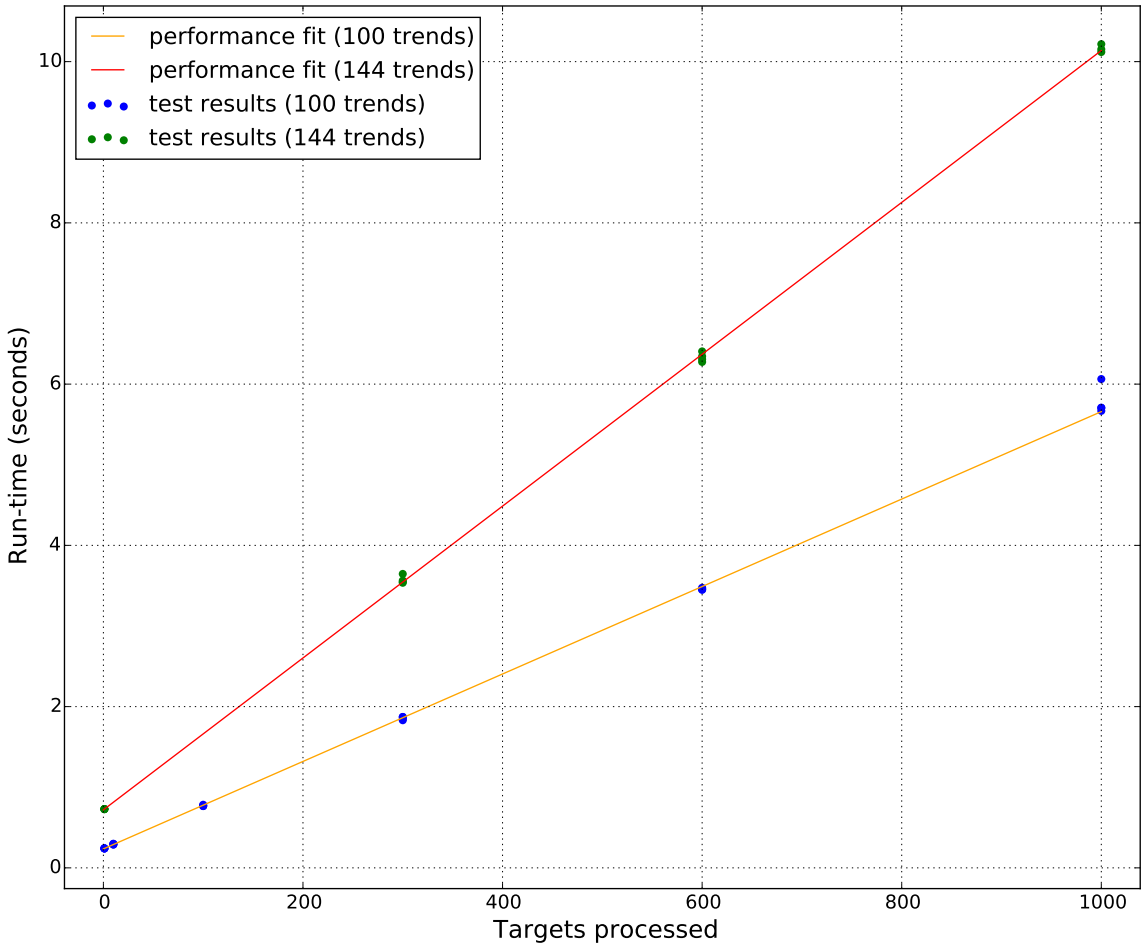

Figure 5.11: Measured program run-times for the VARTOOLS Trend Filtering Algorithm (TFA) implementation for varied workloads are shown above. Linear fits to data allow us to measure both the TFA setup time (intercept) and correction time per object (slope). Table 5.2 provides a summary of fitted parameters. We varied the number of detrended light curves from 1 to 1000 and repeated the procedure separately with trend sets of 100 stars (blue points and yellow line) and 144 stars (green points and red line). In particular, we find that filter setup time requires $\sim$ 50x longer than detrending, stressing the importance of careful task planning.

subgrid ("quadrants" hereafter). Internally we refer to these with labels LL, LR, UL, and UR. An illustration of this arrangement is given in Figure 5.12. Four independent trend lists (one for each quadrant) are produced by selecting one or more stars from the corresponding quadrant of every cell. When selected this way, all four trend lists are able to sample most of the field area with no risk of overlap. This scheme does create exclusion regions where trends cannot be selected but this is unlikely to be a problem for crowded fields. If necessary, decreasing the number of grid cells and increasing the stars drawn per quadrant can shrink the avoided areas without changing the number of trend stars.

We next produce four separate object lists, one for use with each of the trend sets. Each list is produced by starting with the complete original list and removing from it any objects that would collide with the chosen trend stars. Effectively, we exclude the objects responsible for performance loss. Note that the disjoint nature of the quadrants ensures that no target can be ejected from more than one list. In summary, most objects appear in all four target lists but a handful of sources only appear in three. We refer to each of the quadrant-specific cases (which light curves to process, which trend stars to use, and where to store results) as a work plan.

Once organized, all four work plans are executed. This results in four separate sets of detrended light curves with many objects in common. Final detrended outputs (corresponding to the entire original list of sources) are then produced by merging the corresponding outputs from the different work plans. The final detrended light curve (JD, magnitude, and mag uncertainty) is obtained by averaging the corresponding files from the separate work plans. We augment the averaged output with an additional σ_{TFA}column obtained by computing the element-wise standard deviation among the TFA-detrended magnitudes. This provides an empirical estimate of errors introduced by detrending: small σ_{TFA}values indicate good agreement and thus weak dependence on choice of trend stars. Large σ_{TFA}values signal discrepancy and warrant inspection.

The merged, TFA-detrended light curves produced at this stage are considered science-

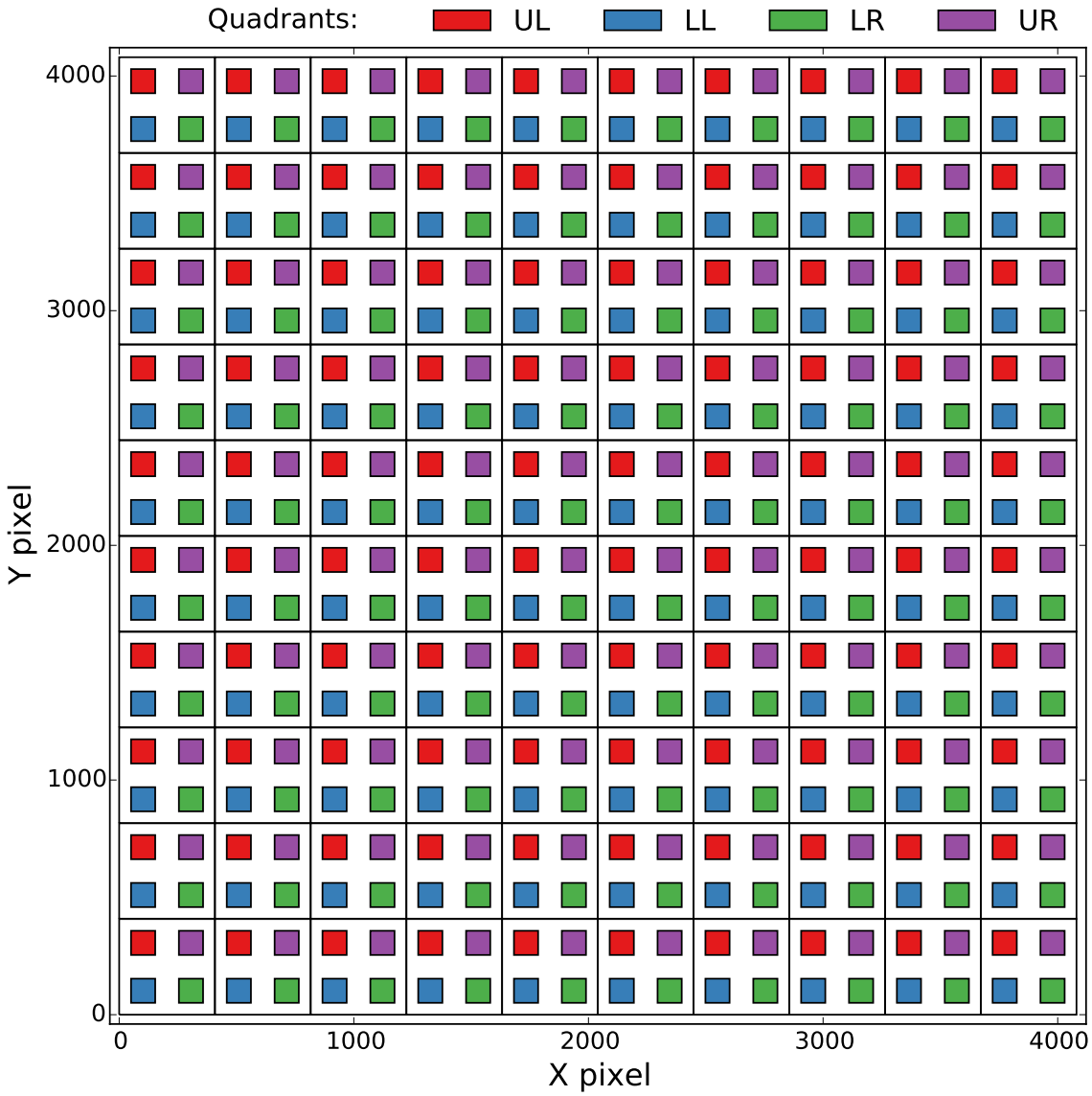

Figure 5.12: A schematic of the nested grid and quadrant arrangement for TFA trend star selection is shown above. The thin black lines above mark the edges of the larger grid cells into which the full image is divided. Each cell is then further divided 2x2 into four quadrants separated by gaps based on the TFA exclusion radius. We use this structure to create four work-plans (combinations of trend list and object list to be executed). For instance, the UL trend list contains one star from each of the red UL quadrants and the UL target list contains most of the original set but excludes those which will "collide" with the UL trend stars. The three other work-plans follow similarly. The spacing between quadrants ensures that no target star is excluded from more than one work-plan. All four work-plans are executed and the results are combined. Despite the 4-fold increase in detrendings, this process executes more quickly than normal due to collision prevention.

grade and ready for transiting exoplanet detection. We refer to these data as LCTYPE `MTFA`.

5.5.4 Combined CDE Data Products

Once light curves are extracted for all desired targets in all fields, a single CDE data file is produced for each object in the KELT Target Catalog for which light curves have been extracted (in *any* field). In order to allow a wide range of contents, we have opted for multi-extension FITS files. Each data file is named for the UCAC4 object identifier to which it corresponds. This naming convention simplifies the data-gathering process and also ensures uniqueness of the CDE FITS files.

Each multi-extension file contains several components. The first HDU is used to store useful target metadata to help interpret measurements and link this object to related data in other files. Subsequent extensions consist of binary tables containing time series photometry (light curves) in a variety of units and at several different reduction stages. A provision exists to additionally include reduction-specific data such as PSF thumbnails. A Python API provides a stable interface with which internal data can be accessed and manipulated. Example listings of data product file structure and header contents can be found in Appendix D. More detailed explanations of data contents by section are provided below.

5.5.4.1 Object Metadata

One of the key advantages of the multi-extension FITS format we use is the ability to store significant quantities of metadata with different scope. We dedicate the first FITS extension to storing object-specific metadata (primarily obtained from external catalogs) that apply to all other extensions within the file.

Astronomical metadata are obtained primarily from the UCAC4 catalog [Zacharias et al., 2012] upon which CDE data reduction is based. Essentially all data from the main UCAC4 catalog are stored. Most importantly, these data include J2000 positions and proper

motions, their epochs, and corresponding uncertainties. Brightness measurements in several bandpasses are provided including aperture and fitted UCAC4 magnitudes with errors, 2MASS JHK magnitudes, errors, and quality flags, plus APASS BVgri magnitudes and errors. Extended source and double star flags are also stored. In addition to the UCAC4-provided quantities, we also record the J-K and J-H colors as separate keywords for convenience. Additional derived quantities such as reduced proper motion may be added in the future.

The first extension also contains numerous identifiers to simplify connection to external resources. The unique UCAC4 and 2MASS identifiers are included for all objects. When available, the UCAC2 and Tycho-2 identifiers (using the UCAC4-provided cross-match) are also included. Finally, we also record information about the "neighborhood" of each star in order to expedite the identification of blends. This data currently consists of the number and UCAC4 identifiers of all KELT Target Catalog sources (for which a KELT light curve likely exists) within $180''$of the target. Separations and magnitude differences are anticipated in the future, likely in an entirely separate extension for added flexibility.

Lastly, we record the date and time of creation as well as version information for several software components involved in the data product assembly. These details are meant to simplify data management, assist in debugging and diagnostic work, and to facilitate automated upgrades in the future such as inclusion of metadata from additional sources.

5.5.4.2 Light Curve Extensions

Light curve data are stored as binary table extensions in the CDE data product. Light curve data are separated and stored according to three criteria: the observed KELT field (such as KN10, KN11, or KS13), by hemisphere (east or west), and also by LCTYPE (FLUX, LCS1, LCS2, or MTFA). In effect, each ASCII light curve file described in §5.5 is kept in its own extension. This design greatly simplifies and speeds up data access (only a single extension is retrieved and its size is kept small) at the cost of some slight duplication

(for example, the time stamps of the LCSx and MTFA LCTYPEs are a subset of those in FLUX).

Every light curve extension is named (using FITS keyword EXTNAME) according to its field, hemisphere, and LCTYPE with the latter separated by an underscore. Example EXTNAMEs include `KN10E_FLUX`, `KN11W_LCS2`, and `KS13E_MTFA`. All data access is expected to use these extension names in order to eliminate dependence on the internal file structure. Relevant metadata including X,Y coordinates, reference flux and magnitude, and other reduction-dependent quantities are stored in the header of each of these extensions.

Every LCTYPE will offer two time stamps: a mid-exposure Julian Date in Terrestrial Time in column JD_TT and a Barycentric Julian Date in Barycentric Dynamical Time in column BJD_TDB (see Eastman et al. 2010 for a review and comparisons of the various time systems and algorithms). The former are present in KELT FITS imaging data and useful for comparison to images when necessary. The latter is the standard for scientific analysis and is likely to be the most frequently used for astronomical work. By taking into account observatory location and individual object coordinates, the BJD correction implemented for use in CDE data products may be up to two minutes more accurate than what has previously been used for exoplanet searching.

Flux measurement columns vary among the different LCTYPEs. FLUX light curves include the following columns: *wflux* and *werr*, the PSF-weighted aperture difference flux and error produced by ISIS that KELT ultimately uses for science; *flux* and *err*, an unweighted flux and error that ISIS also produces; and *ksum*, the normalization of the convolution kernel used to produce the measurement. The weighted fluxes resist blend contamination without appreciable SNR reduction making them ideal for most science applications. However, for cases where aperture placement is imperfect (e.g., moving objects and high-proper motion sources) the unweighted measurements may perform better. Since the two measures are not equally sensitive to blending, A difference in amplitude between them is a good predictor of a blend. The kernel normalization reports the ratio of reference and

target frames and thus as a transparency indicator. Values significantly different from 1.0 indicate either poor conditions or an improperly made reference frame.

The LCS1, LCS2, LCS3 (if present), and MTFA light curves provide *mag* and *err* columns in KELT instrumental magnitudes. These provide the data currently used for KELT exoplanet searching, candidate selection, and most ancillary science. Other than the migration to FITS binary tables, they do not deviate from current standards and practices. In addition to the columns noted above, MTFA light curves also include a *tfasig* column for diagnostic purposes. This is the standard deviation in magnitudes obtained during the merger of TFA results described in §5.5.3.

5.5.4.3 Python API

A Python API has been written to simplify interaction with the CDE data products. This API provides easy-to-use functions that allow access to data without knowledge of the internal structure. A full listing of the source code is presented in Appendix D.3 for reference.

It offers the following methods to the user:

1. load_file() – The load_file method is used to specify a CDE FITS file on disk. If found to be valid, a list of the fields and light curve types is extracted from the extension names.

2. extract_ltype() – After a file is loaded, the extract_ltype method is called to extract and combine all data sets (east and west for all available fields) of a chosen LTYPE. The different data sets are level-matched on-the-fly by median subtraction in a way that preserves the average magnitude in output. Each data point in the extracted result includes the EXTNAME, field tag (e.g., KN10E), LCTYPE, and a unique integer as additional columns so that origination is preserved if necessary.

3. save_to_ascii() – This routine writes an extracted data table to a specified file on

disk in a format compatible with most existing KELT infrastructure. The number of columns preserved and the delimiter used are both adjustable as arguments.

The current version provides sufficient functionality to reproduce the ASCII light curve format used previously throughout the KELT project. By bridging this format gap, this API (or a similar one) minimizes the effort required to incorporate the new CDE data products and results they contain into the existing KELT planet discovery infrastructure.

5.6 CDE Data Products: Quality and Applications

KELT light curves have been produced for a large number of sources from the KELT-North and KELT-South fields KN10, KN11, KN16, and KS13 that were produced using the new CDE system described in this work. Since each field is observed in both an east and west orientation we have six large light curve sets available to work with. The KN10 and KN11 observing fields partially overlap, providing an opportunity to evaluate the consistency of results across the sky. Raw and TFA-detrended light curves were produced in both East and West orientations for each of the fields noted above. Photometric performance (i.e., precision) is evaluated by plotting RMSD mangnitude scatter versus mean source magnitude (a so-called "RMS plot"). Such plots were produced for all fields noted above (each in both East and West orientation) using both raw and TFA-detrended data. These RMS plots are provided for reference in Appendix E. In addition to the general photometric performance, numerous individual light curves have been examined to illustrate how CDE addresses the shortcomings of the legacy pipeline. Those object-specific reports follow below.

5.6.1 KS13C036752 Depth Revisited

In §5.3.2.2, KS13C036752 was introduced to illustrate the extreme light curve discrepancies caused in cases of severe blending. The CDE pipeline estimate for this star differs

from the legacy pipeline PSF photometry result by 0.8 mag (a factor of 2.09 in flux and light curve amplitude). When the CDE estimate is used to produce light curves, the larger depth is indeed exposed as hoped. In fact, the CDE light curve of KS13C036752 (Fig. 5.13) exhibits an eclipse depth of roughly 8% in close agreement with the follow-up measurement.

5.6.2 BLS Measurements of Known Exoplanets

As an independent check on the fitness of CDE-produced light curves for exoplanet discovery, we compared the results of BLS frequency searches on both legacy and CDE light curves. In particular, we aimed to learn whether the same transit signals are recovered, and, if yes, are there appreciable differences in either the detection SNRor derived parameters due to systematic differences in the data reduction methods. To perform this test, we identified four planets from the region of sky with CDE light curves available, including KELT-9b, KELT-12b, WASP-3b, and TrES-4b. The complete set of reported BLS parameters are reproduced in Table 5.3. In all four cases, we measure a significantly greater depth measurement using the CDE-based light curves compared to legacy data. That the depth increases in all cases itself is not extremely surprising; the prevention of underestimated eclipse and transit depths was in fact a driving concern in CDE development. The magnitude of the change, however, is surprisingly large. This may indicate that amplitude errors are more prevalent than thought in shallow light curves and may measurably blunt the transit detection ability in the current survey system.

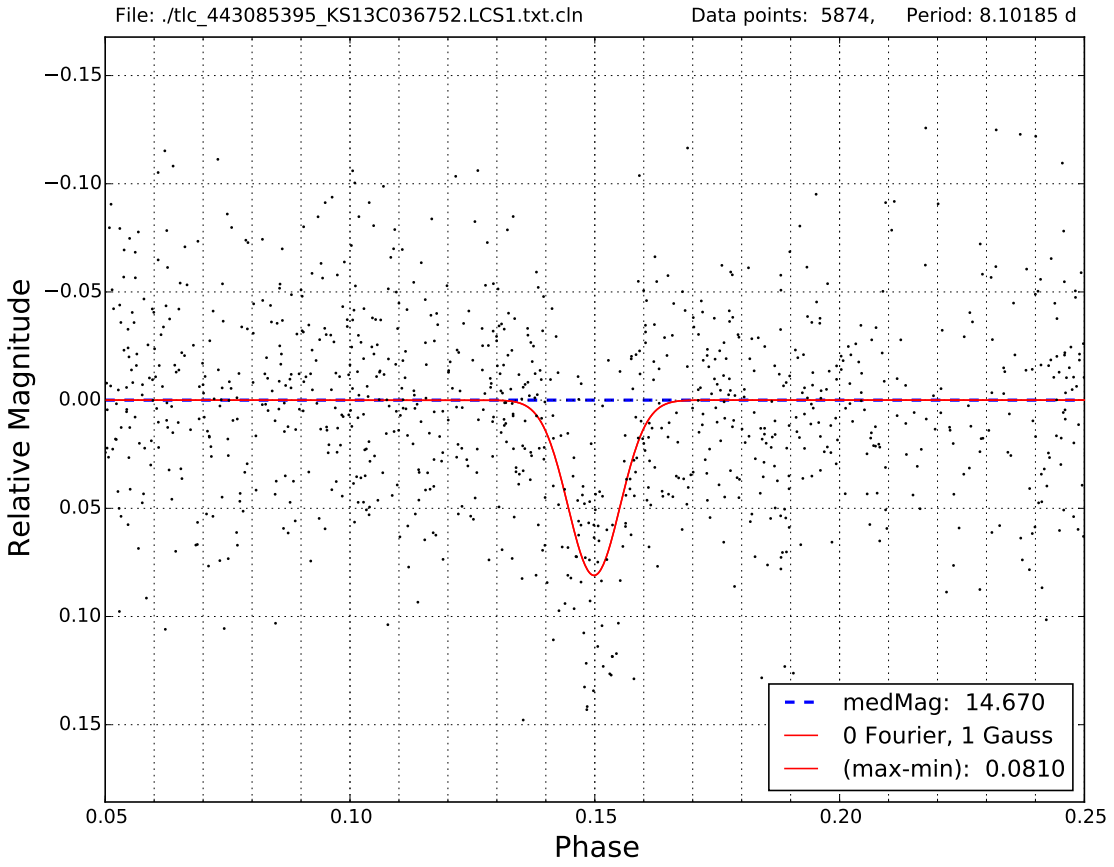

Figure 5.13: The CDE KELT light curve of KS13C036752 exhibits an eclipse depth of roughly 8%, remarkably close to the 8.5% depth obtained by follow-up observers (shown in Fig. 5.2). The black data points have been phased to the apparent orbital period of the eclipsing binary ($P \sim 8.10185$ days). A simple 3-parameter (midpoint, depth, and width) Gaussian model is fit to these phased data points to both help refine the orbital period and measure eclipse depth. The solid red curve shows the result of this iterative procedure. The depth and width (σ) of this Gaussian are 8.1% and 0.00751, respectively. This is a significant improvement over the legacy pipeline result which underestimates the eclipse depth by a factor of more than two.

Table 5.3: BLS Transit Parameters: Legacy vs. CDE Data

Parameter	Legacy BLS***	CDE BLS***	Published Value	Ref.
KELT-8b:				
Period(d)	3.2441312	3.2441269	3.24406	1
depth (ppt)	7.1	11.9	13.1	1
T_{14} (h)	2.08	2.08	3.466	1
KELT-12b:				
Period(d)	5.0315031	5.0316099	5.031623	2
depth (ppt)	3.5	4.3	6.0	2
T_{14}(h)	5.68	5.23	5.762	2
WASP-3b:				
Period(d)	1.8468212	1.8468165	1.846830	3
depth (ppt)	7.6	9.95	11.0	3
T_{14}(h)	2.36	2.66	2.77	3
TrES-4b:				
Period(d)	3.5538973	3.5539610	3.55392771	4
depth (ppt)	5.8	10.1	10.0	4
T_{14}(h)	2.36	2.66	3.65	4

*** The "Legacy BLS" and "CDE BLS" columns refer to the transit parameters reported by BLS when applied to data produced by the legacy pipeline and the CDE pipeline, respectively. Note that the same BLS routine is used in both cases.

[1] Fulton et al. [2015]
[2] Stevens et al. [2017]
[3] Pollacco et al. [2008]
[4] Daemgen et al. [2009]

5.6.3 Improvements in Blend Detection

CDE data products provide a new and important way to diagnose blends without resorting to on-sky observations. This new functionality is introduced by two separate factors: (1) the availability of difference flux light curves as part of the CDE data product and (2) the increased density of sources (and therefore apertures) on the sky. The combination of these two changes enables the detection of blends in many cases simply through comparison of light curves of neighboring objects.

To facilitate blend detection and neighbor identification, we identify relevant nearby objects from the KELT Target Catalog in advance for incorporation into CDE data products. The number of objects along with their UCAC4 identifiers stored alongside object-specific metadata in the first HDU of the CDE data product. This information has been included to facilitate light curve comparisons among neighbors without need for expensive look-ups or searches.

When difference flux measurements are available for numerous sources in close proximity on the sky, they can be readily checked to see if similar signals are present. When multiple objects are identified with the same apparent signal, determining which object (if any) is the true source of the variability is important. This true source (or at least the best option of objects available) is determined by finding the object with the largest difference flux amplitude. By its weighted nature, the difference fluxes encode in their amplitude the offset between the true source of signal and the aperture position. Figures 5.14 and 5.15 show the measured flux decrement of the true source and its neighbors as functions of sky position and radial separation, respectively. A breakout plot showing the eclipse itself along with the Gaussian fits used to measure the depth are provided in Figures 5.16, 5.17, and 5.18. Difference flux throughput is maximized when the aperture is centered as perfectly as possible. Exploiting this fact in reverse, the true source of the signal can be found by locating the object with the largest measured difference flux amplitude.

In some cases, individual light curves can be ruled out by virtue of unphysical flux

changes. For instance, if a flux decrement causes the total flux to become negative when the reference level is added in, that object is likely a blend. CDE data products include the reference flux level within the individual light curve data tables to facilitate this check.

5.7 Conclusion

Catalog-Driven Extraction is a collection of tools that together deliver significant increases in both light curve quantity and quality along with structural changes designed to maximize science output of both the core transit survey and ancillary work by the broader community.

The core exoplanet survey effort benefits in several ways. First and foremost, the use of external catalogs with reliable, resolved photometry enables the production of light curves free of significant systemat errors in depth or variability amplitude, cutting down on one of the main sources of false positives for the discovery effort. Further, the higher density of sources monitored on the sky translates into better ability to detect blends using KELT data alone, further avoiding wasted telescope time. Finally, the redesigned data structure for storange and dissemination structurally eliminates most of the barriers to exploiting the regions of overlapping fields with the greatest number of data points. For those areas, this new paradigm provides an easy and direct way to maximally exploit the detection ability of the KELT data.

These improvements will also benefit the broader astronomical community in immediate ways. To date, numerous scientific analyses have been blocked by the inability to produce light curves with truly believable amplitudes of variation. CDE addresses this defect by deriving critical information, including star positions and brightnesses, from external catalogs with reliable, resolved, and calibrated photometry. Combined, these features offer the potential to significantly increase the science output of the KELT survey.

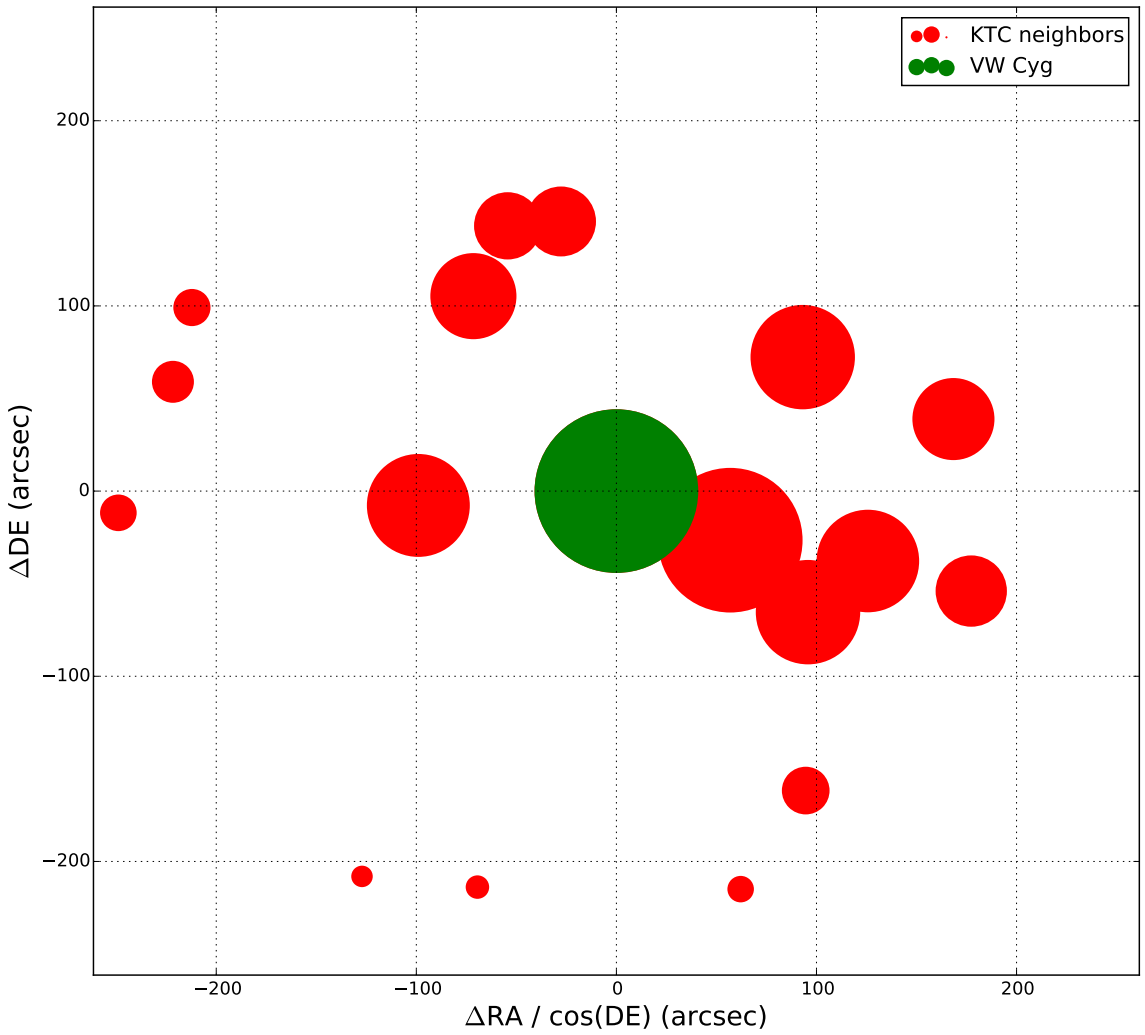

Figure 5.14: VW Cyg eclipse depth as measured in neighboring light curves as they appear on the sky. The large green spot indicates the position of the known variable. The red dots are other sources in the vicinity into which VW Cyg has blended. The size of points reflects the depth of eclipse seen in the difference fluxes of each object. This figure illustrates the centroid-like effect that can be achieved with numerous apertures in a single location when the raw difference flux data are examined. The larger number of objects extracted with CDE necessarily provides more apertures on the sky. While this will certainly result in more instances of blended light curves, the amount of signal recovered as a function of neighbor position provides a very useful measurement of the source of such signals. Implemented in practice, this effect can be used to identify a large fraction of blended sources without resorting to follow-up telescope observations.

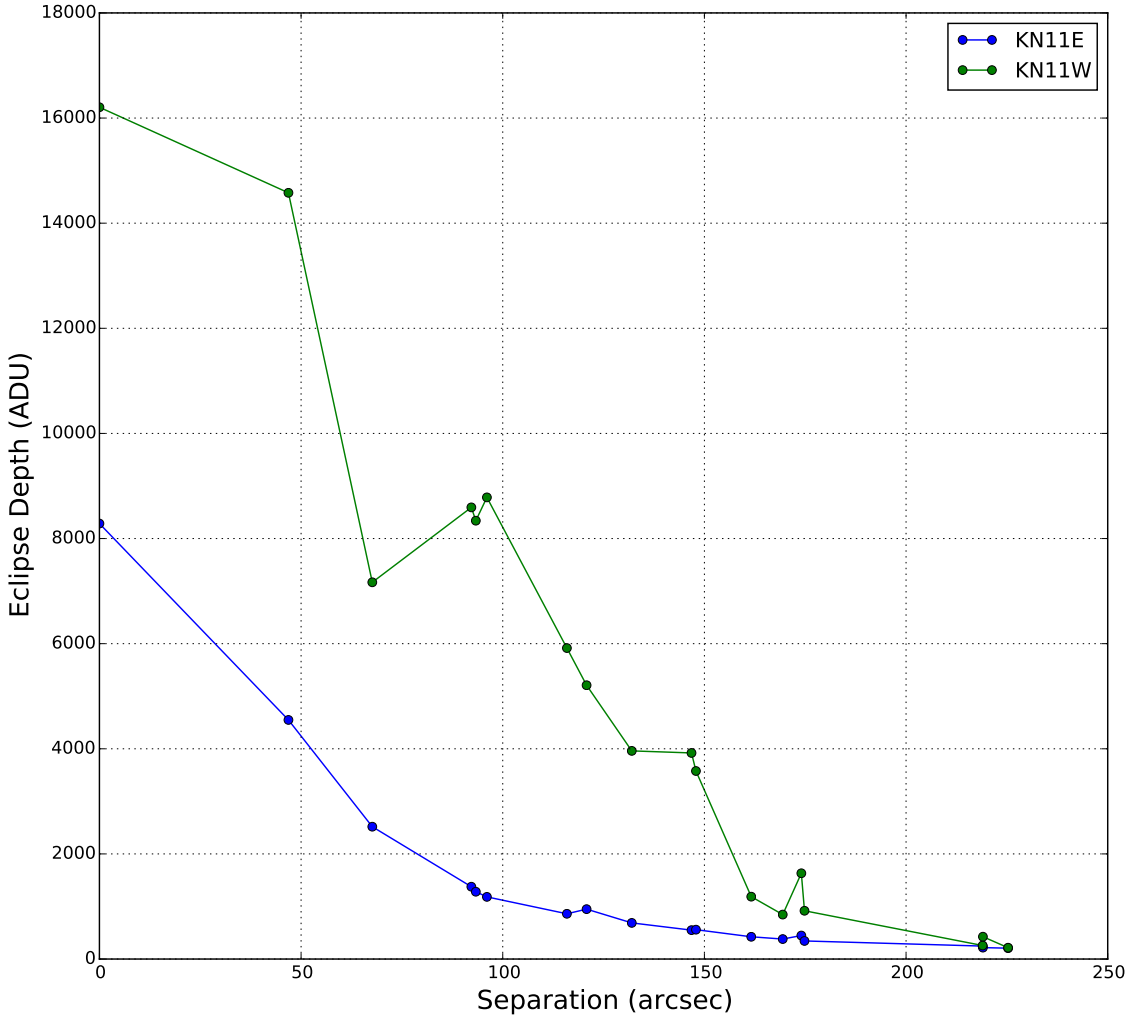

Figure 5.15: VW Cyg eclipse depth (blended into neighboring sources) is shown above as a function of angular separation from the true variable. Offset apertures collect less light than on-target apertures and the rate of signal decrease is fast. Exploiting this fact allows one to fairly easily select the best-placed aperture from among several options. The larger number of objects extracted using CDE necessarily entails greater density of apertures on the sky (and thus more blending instances). However, this phenomenon can be exploited to locate the true source of variability. In many cases, this larger number of blends encodes the true location of the varying source. In effect, the variation in measured diff-flux amplitude with position can be used to centroid the true source of the signal in question. In some cases, it may be possible to localize the signal source without having an aperture placed at the correct location.

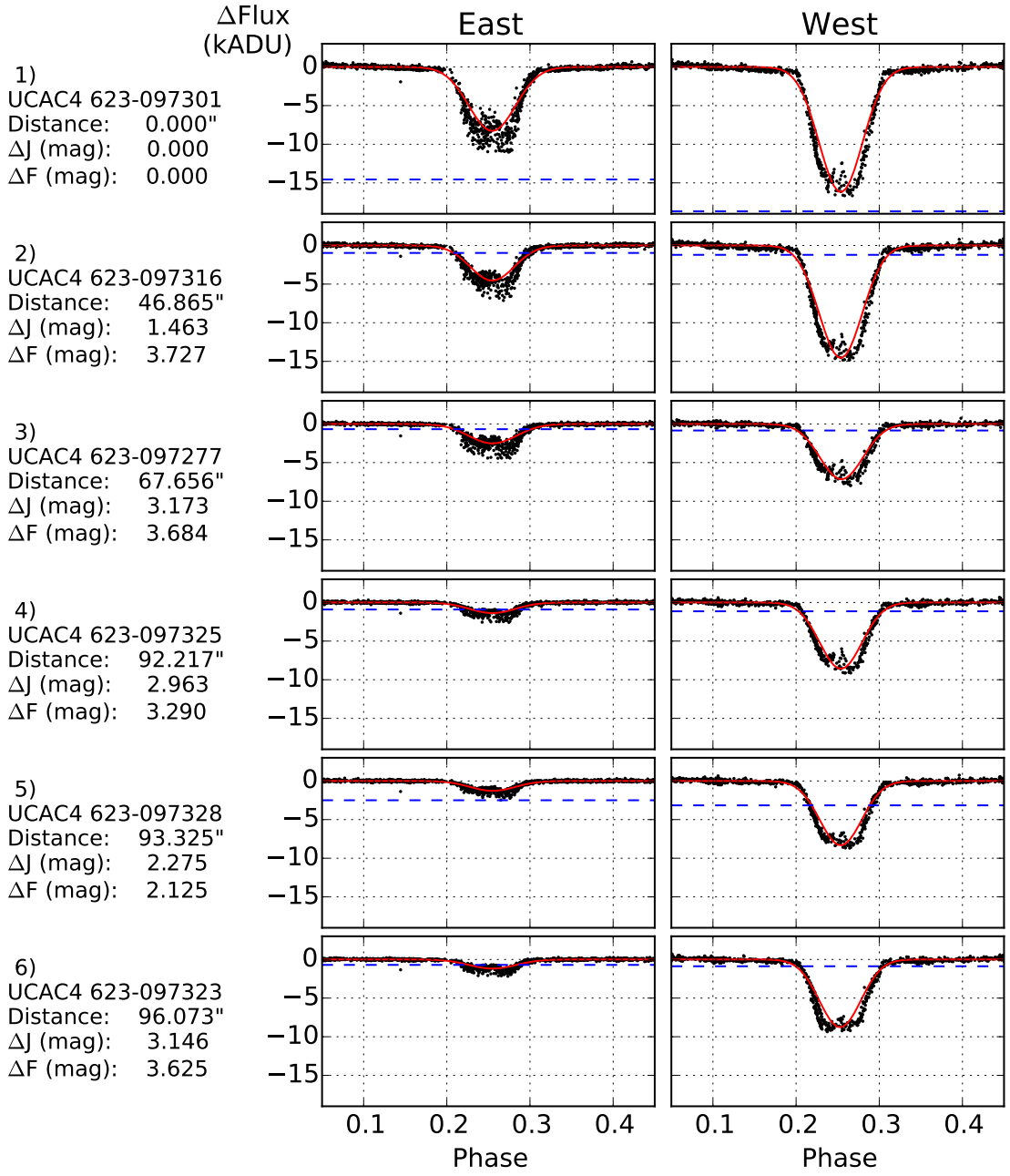

Figure 5.16: Eclipses in the VW Cyg neighborhood (1 of 3): objects 1-6. Panels above show flux decrements recorded in KN11 data for neighbors of the eclipsing binary star VW Cyg, sorted by distance from the (known) variable. Black points are KELT difference fluxes and the red line is a fitted Gaussian model used to estimate depth. Offset apertures record less flux change; this fact can be used to resolve blend scenarios. Dashed blue lines mark the maximum possible (100%) flux decrements for each panel; data below this are unphysical. If the signal source were unknown, this fact could be used to rule out stars as candidates. The "true" source is generally the object for which the strongest (physically allowed) signal is measured. **Above:** on this page, only the actual target (object 1, top line) is plausible as the source. All others show data below the blue line. Continued on next page.

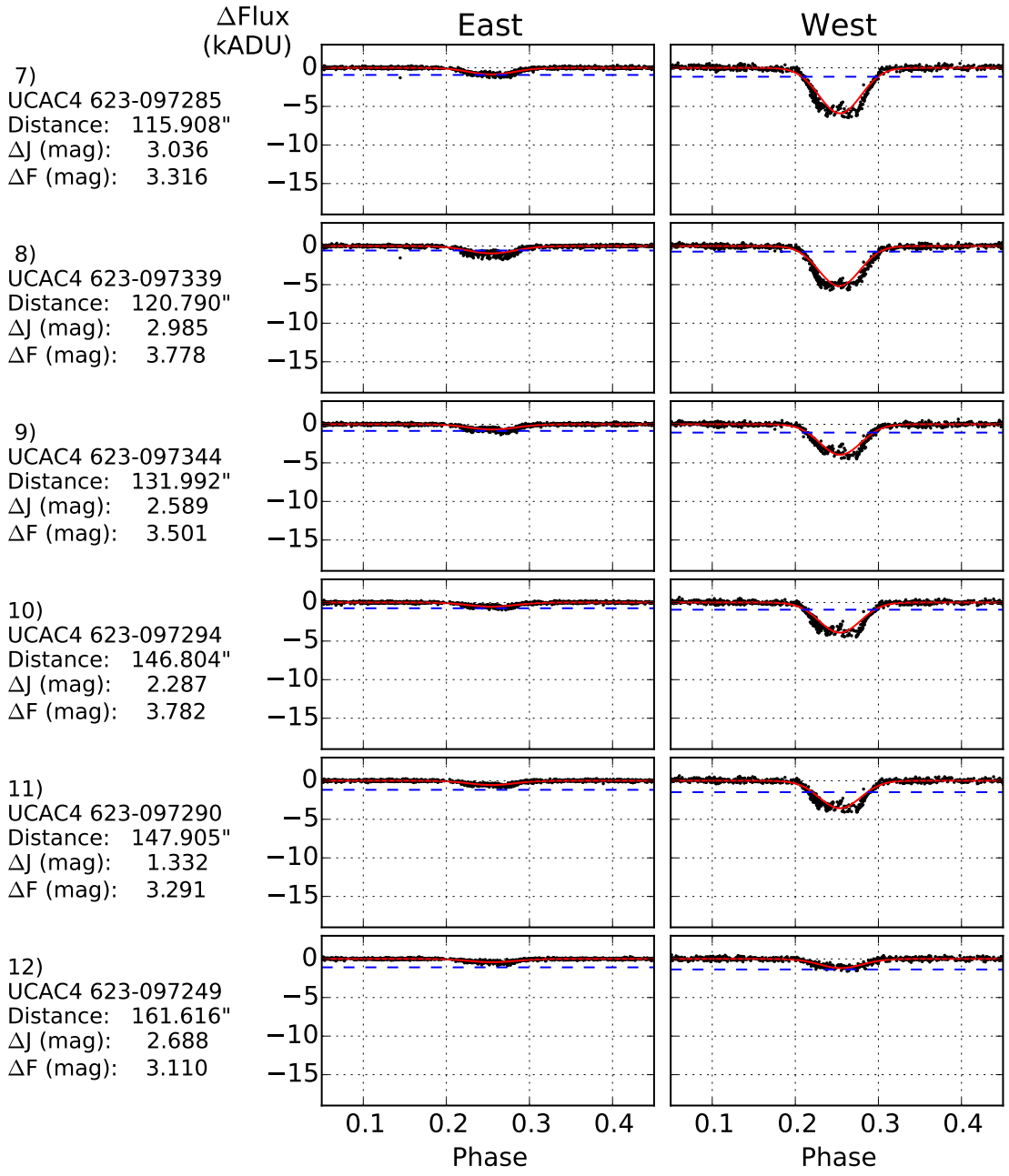

Figure 5.17: Eclipses in the VW Cyg neighborhood (2 of 3): objects 7-12. Panels above show flux decrements recorded in KN11 data for neighbors of the eclipsing binary star VW Cyg, sorted by distance from the (known) variable. Black points are KELT difference fluxes and the red line is a fitted Gaussian model used to estimate depth. Offset apertures record less flux change; this fact can be used to resolve blend scenarios. Dashed blue lines mark the maximum possible (100%) flux decrements for each panel; data below this are unphysical. If the signal source were unknown, this fact could be used to rule out stars as candidates. The "true" source is generally the object for which the strongest (physically allowed) signal is measured. **Above:** of these sources, only the last (object 12) is physically plausible. The other five would entail negative fluxes. Continued on next page.

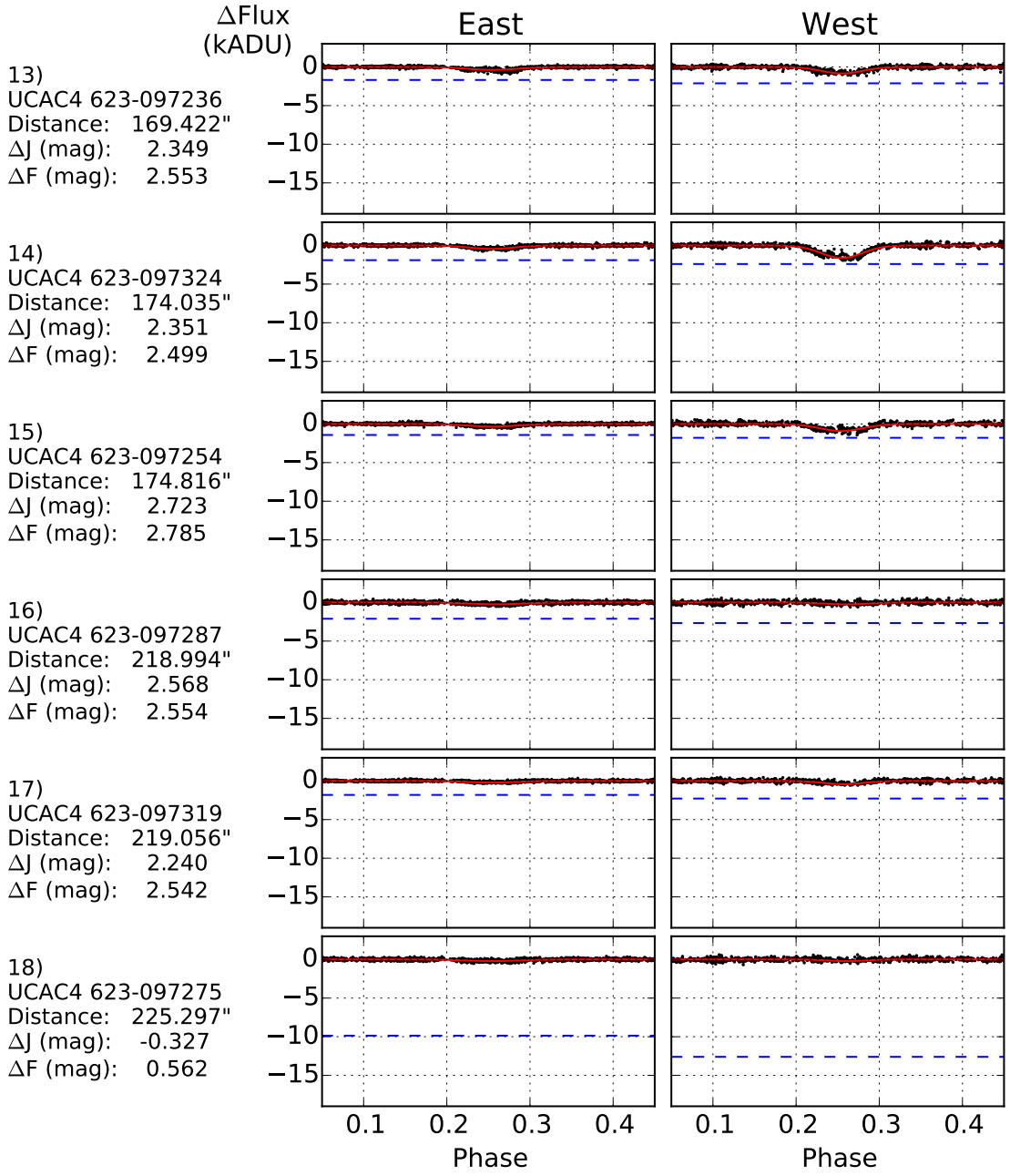

Figure 5.18: Eclipses in the VW Cyg neighborhood (3 of 3): objects 13-18. Panels above show flux decrements recorded in KN11 data for neighbors of the eclipsing binary star VW Cyg, sorted by distance from the (known) variable. Black points are KELT difference fluxes and the red line is a fitted Gaussian model used to estimate depth. Offset apertures record less flux change; this fact can be used to resolve blend scenarios. Dashed blue lines mark the maximum possible (100%) flux decrements for each panel; data below this are unphysical. If the signal source were unknown, this fact could be used to rule out stars as candidates. The "true" source is generally the object for which the strongest (physically allowed) signal is measured. **Above:** all six of these sources are plausible on the basis of depth (none entail negative fluxes) but none are plausible on the basis of signal strength.

Chapter 6

Conclusion

The KELT transit survey has discovered ~ 25 new transiting exoplanets in its 15 years of operation and remains poised to discover several more in the coming years. Per survey intent and design, many KELT discoveries, often by dint of the brightness of their host stars, provide excellent opportunities for unique and detailed follow-up studies that would not be possible with fainter systems. Several of these discoveries, such as a brown dwarf in orbit around a rapidly rotating F star (KELT-1b; Siverd et al. 2012) and a planet hotter than most stars (KELT-9b; Gaudi et al. 2017b), were genuinely unexpected and served to directly broaden our understanding of exoplanet demographics.

Partly due to the bright star focus and partly due to a late survey start, many KELT discoveries have featured hot and/or rapidly rotating host stars that have usually been overlooked by past radial velocity and transit surveys (e.g., Zhou et al. 2016b, Gaudi et al. 2017b, Lund et al. 2017, Johnson et al. 2018, Siverd et al. 2018). The KELT contribution to this hot-star niche has been particularly strong; fully half of the known exoplanets with host stars hotter than 7500 K have been discovered by KELT. Additional objects under study now are likely to increase this contribution further.

With high-cadence data of a very large number of targets, KELT has made numerous important contributions to fields outside its exoplanet focus. This unique survey coverage proved particularly useful in the case of SN2014J where high-cadence coverage during the early hours of the explosion led to a pair of papers and a first-ever ISM smoothness measurement [Siverd et al., 2015, Goobar et al., 2015]. Numerous investigations into variable stars have made use of KELT data (see e.g., Molnár et al. 2017, Labadie-Bartz et al. 2018, 2017) despite occasionally significant hurdles to interpretation due to the unusually coarse pixel scale and blending that ensues.

The recent development, testing, and deployment of Catalog-Driven Extraction (CDE) is now improving the prospects of KELT contributions to many areas of astronomy. CDE is a set of modifications to processing software and data management methods, including redesigned data products for data storage and dissemination, designed to alleviate or eliminate several limitations identified over the years of KELT operation. This new design structurally solves the persistent problem of linking together KELT light curves from different telescopes or fields and is poised to properly leverage the huge quantities of data in regions of the sky where fields overlap.

Further, rather than rely on KELT photometry alone, CDE uses external catalogs to select stars for photometric monitoring in a consistent and rigorous way ensuring that objects of interest are not lost and that the most critical measurements affecting the KELT difference imaging pipeline are free of egregious systematic errors. The net result of this work will be a significant increase in the number of light curves available from KELT along with a measurable improvement in data quality, making the data suitable for a wider array of scientific investigation, greatly increasing KELT science output potential in the long term.

Appendix A

FWHM and σ in a Gaussian Profile

The normal or Gaussian distribution probability density is defined as:

$$f(x) = \frac{1}{\sqrt{2\pi\sigma^2}} \exp\left(-\frac{(x-\mu)^2}{2\sigma^2}\right) \tag{A.1}$$

For convenience we choose a Gaussian profile with $\mu = 0$:

$$f(x) = \frac{1}{\sqrt{2\pi\sigma^2}} \exp\left(-\frac{x^2}{2\sigma^2}\right) \tag{A.2}$$

The Half Width at Half-Maximum (HWHM) is the distance from the profile center where height falls to half its central value. Mathematically, HWHM is the value of x that satisfies $f(x) = f(0)/2$.. Plugging this in to equation A.1 above and taking the natural logarithm of both sides, we find:

$$\exp\left(\frac{-\text{HWHM}^2}{2\sigma^2}\right) = 0.5 \;\rightarrow\; \frac{\text{HWHM}^2}{\sigma^2} = -2 \cdot \ln(0.5) = 2 \cdot \ln(2)$$

Taking the square-root of both sides leaves:

$$\text{HWHM} = \sigma \cdot \sqrt{2 \cdot \ln(2)} \tag{A.3}$$

The FWHM, defined as twice the HWHM, is then:

$$\boxed{\text{FWHM} = 2 \cdot \text{HWHM} = \sigma \cdot 2\sqrt{2 \cdot \ln(2)} = 2.35482 \cdot \sigma} \tag{A.4}$$

Appendix B

Integrated Flux under a Gaussian PSF

The bivariate Gaussian is (where ρ is the correlation between X and Y):

$$f(x,y) = \frac{1}{2\pi\sigma_x\sigma_y\sqrt{1-\rho^2}} \exp\left(-\frac{1}{2(1-\rho^2)}\left[\frac{(x-\mu_x)^2}{\sigma_x^2} + \frac{(y-\mu_y)^2}{\sigma_y^2} + \frac{2\rho(x-\mu_x)(y-\mu_y)}{\sigma_x\sigma_y}\right]\right). \tag{B.1}$$

Adopting several assumptions, the above can be greatly simplified. Assume X and Y are uncorrelated ($\rho = 0$) with mean value 0 ($\mu_x = \mu_y = 0$). Further, assert circular symmetry such that $\sigma_x = \sigma_y = \sigma$. Under these conditions, the above reduces to:

$$f(x,y) = \frac{1}{2\pi\sigma^2} \cdot \exp\left(-\frac{1}{2}\left[\frac{x^2}{\sigma^2} + \frac{y^2}{\sigma^2} + 0\right]\right) = \frac{1}{2\pi\sigma^2} \cdot \exp\left(-\frac{(x^2+y^2)}{2\sigma^2}\right) \tag{B.2}$$

A "radial" version of this profile can be obtained by assuming circular symmetry and using $r^2 = x^2 + y^2$. After substitution, have:

$$f(r) = \frac{1}{2\pi\sigma^2} \cdot \exp\left(-\frac{r^2}{2\sigma^2}\right) \tag{B.3}$$

The bivariate Gaussian distribution is given in eq. B.3. If using this function to model a PSF, it is important to know what fraction of the full flux is contained within a radius $R = r/\sigma$. This fraction can be obtained by integrating (substituting $dA = 2\pi r\,dr$ and $x = r/\sigma$):

$$\text{flux}(r/\sigma < R) = \frac{1}{2\pi\sigma^2} \int_{r=0}^{r=R\sigma} \exp\left(\frac{-r^2}{2\sigma^2}\right) dA = \int_{r=0}^{r=R\sigma} \frac{r}{\sigma} \exp\left(\frac{-(r/\sigma)^2}{2}\right) \frac{dr}{\sigma} = \int_{x=0}^{x=R} x \exp\left(\frac{-x^2}{2}\right) dx \tag{B.4}$$

Evaluating, find:

$$\text{flux}(r/\sigma < R) = \left[-\exp\left(\frac{-x^2}{2}\right)\right]_0^R = \boxed{1 - \exp\left(\frac{-R^2}{2}\right) = \text{flux}(r/\sigma < R)} \tag{B.5}$$

Appendix C

KELT Centroid Precision Considerations

CDE-generated object lists provide centroid precision that exceeds what can be done using KELT photometry alone for a large number of stars. Effectively, this occurs because fainter stars ($V \lesssim 11$) have SNR that is too low to overcome the combined effects of bright sky and a relatively broad point spread function (PSF).

The KELT PSF varies in size across the detector and focal plane but has a typical FWHM of ~ 3.5 pixels and thus a σ_{PSF} of roughly 1.5 pixels (for a Gaussian profile, FWHM $\approx 2.35\,\sigma_{\mathrm{PSF}}$; see Appendix A for a derivation). The uncertainty in a centroid measurement is well described by $\sigma_x, \sigma_y = \sigma_{\mathrm{PSF}}/\mathrm{SNR_P}$, where $\mathrm{SNR_P}$ is the signal-to-noise ratio on the brightest (center) pixel (see e.g., Neuschaefer and Windhorst [1995] and Windhorst et al. [1984]). With $\sigma_{\mathrm{PSF}} \sim 1.5$, 0.1-pixel uncertainties require $\mathrm{SNR_P} = 15$.

Understanding this $\mathrm{SNR_P}$ requirement requires understanding what fraction of total starlight falls within the central pixel in question. The central pixel can be approximated by a circle of the same area (1 pixel^2) with radius $r = \sqrt{1/\pi}$ pixels ($r = 0.379\,\sigma$ with the nominal 1.5-pixel PSF). Appendix B derives a formula for integrated flux of a Gaussian PSF interior to a radius in standard deviation units (equation B.5). Using this formula we find:

$$\mathrm{center\_pixel\_flux\_fraction} = \mathrm{flux}(r < 0.379\,\sigma) \approx 0.0693 \tag{C.1}$$

$$\mathrm{center\_pixel\_SNR\_fraction} = \sqrt{\mathrm{center\_pixel\_flux\_fraction}} \approx 0.2632 \tag{C.2}$$

This in turn implies that a total source SNR of ~ 57 (photometric RMSD ~ 0.018, corresponding to $V \sim 10-11$ in KELT) is needed to match the centroiding performance of the WCS-derived star positions even when zero systematic errors due to blending are assumed.

Given that significant sources of uncertainty (sky level in particular) were ignored in this investigation, the positional improvement obtained with WCS-derived aperture positions is likely to be quite significant for most stars surveyed by KELT.

Appendix D

Combined CDE Light Curve File Structure

The end result of the CDE pipeline is a large set of CDE data products, individual FITS files each consisting of numerous HDUs containing either individual time series or image thumbnails. One such data product is produced per KELT photometry target. Each target is a single photometric aperture placement but generally each can be considered a distinct celestial object. The file format exists to consolidate disjoint KELT flux and magnitude time series in a way that streamlines our science work and also facilitates data sharing. A Python API built around the internal file structure exists to provide stable access to the time series within these data products.

D.1 FITS File Structure

A sample FITS file layout as reported by the `CFITSIO liststruc` utility follows below. Each Binary Table HDU in the listing below contains a KELT photometry time series from a specific telescope-pointing-orientation-fluxtype combination.

```
1
2 HDU #1  Array:  NAXIS = 0,  BITPIX = 8
3
4 HDU #2  Binary Table:  6 columns x 5475 rows
5  COL NAME             FORMAT
6    1 JD_TT            D
7    2 wflux            E
8    3 werr             E
9    4 flux             E
10   5 err              E
11   6 ksum             E
12
13 HDU #3  Binary Table:  4 columns x 5475 rows
14  COL NAME             FORMAT
```

```
    1 JD_TT             D
    2 mag               E
    3 err               E
    4 tfasig            E

HDU #4  Binary Table:  3 columns x 5475 rows
 COL NAME               FORMAT
    1 JD_TT             D
    2 mag               E
    3 err               E

HDU #5  Binary Table:  3 columns x 5475 rows
 COL NAME               FORMAT
    1 JD_TT             D
    2 mag               E
    3 err               E

HDU #6  Binary Table:  6 columns x 2402 rows
 COL NAME               FORMAT
    1 JD_TT             D
    2 wflux             E
    3 werr              E
    4 flux              E
    5 err               E
    6 ksum              E

HDU #7  Binary Table:  4 columns x 2402 rows
 COL NAME               FORMAT
    1 JD_TT             D
    2 mag               E
    3 err               E
    4 tfasig            E

HDU #8  Binary Table:  3 columns x 2402 rows
 COL NAME               FORMAT
    1 JD_TT             D
    2 mag               E
    3 err               E

HDU #9  Binary Table:  3 columns x 2402 rows
 COL NAME               FORMAT
```

```
    1 JD_TT             D
    2 mag               E
    3 err               E

HDU #10  Binary Table:  6 columns x 2644 rows
 COL NAME               FORMAT
    1 JD_TT             D
    2 wflux             E
    3 werr              E
    4 flux              E
    5 err               E
    6 ksum              E

HDU #11  Binary Table:  4 columns x 2644 rows
 COL NAME               FORMAT
    1 JD_TT             D
    2 mag               E
    3 err               E
    4 tfasig            E

HDU #12  Binary Table:  3 columns x 2644 rows
 COL NAME               FORMAT
    1 JD_TT             D
    2 mag               E
    3 err               E

HDU #13  Binary Table:  3 columns x 2644 rows
 COL NAME               FORMAT
    1 JD_TT             D
    2 mag               E
    3 err               E

HDU #14  Binary Table:  6 columns x 3617 rows
 COL NAME               FORMAT
    1 JD_TT             D
    2 wflux             E
    3 werr              E
    4 flux              E
    5 err               E
    6 ksum              E

```

```
HDU #15  Binary Table:  4 columns x 3617 rows
 COL NAME              FORMAT
    1 JD_TT            D
    2 mag              E
    3 err              E
    4 tfasig           E

HDU #16  Binary Table:  3 columns x 3617 rows
 COL NAME              FORMAT
    1 JD_TT            D
    2 mag              E
    3 err              E

HDU #17  Binary Table:  3 columns x 3617 rows
 COL NAME              FORMAT
    1 JD_TT            D
    2 mag              E
    3 err              E
```

D.2 FITS Header Listing

The FITS header content of a combined CDE light curve is shown below. The primary HDU, consisting of a header but no data, is used to store object-specific information relevant for all time series, including data such as sky position, proper motion, external catalog identifiers. Selected useful data from external catalogs, magnitudes in standard bandpasses for example, are also included. A synopsis of relevant data regarding known neighbors including object identifiers is also provided to facilitate blend detection and interpretation.

Light curves from the various fields and hemispheres are stored in separate HDUs for efficient access. For convenience, all available versions of each data set are included within the file. The variants include raw and detrended data as well as Earth-based and barycentric (BJD_{TDB}) time stamps to facilitate a variety of different science needs.

```
Header listing for HDU #1:
SIMPLE  =                    T / conforms to FITS standard
BITPIX  =                    8 / array data type
NAXIS   =                    0 / number of array dimensions
```

```
EXTEND  =                    T
VERSION = '0.1.0    '           / kelt_cde_tools module version
OBSERVER= 'KELT     '
RA_J2000=          277.11190056 / [degrees] UCAC4 Right Ascension (J2000)
RA_ERR  =                    16 / [mas] UCAC4 mean RA error at ICRS
EP_RA   =                1997.84 / central RA epoch
DE_J2000=           30.59918111 / [degrees] UCAC4 Declination (J2000)
DE_ERR  =                    13 / [mas] UCAC4 mean DE error at ICRS
EP_DE   =                1993.06 / central DE epoch
PMRA    =                  -3.4 / [mas/yr] proper motion in RA*cos(dec)
PMRA_ERR=                   1.2 / [mas/yr] proper motion in RA*cos(dec) error
PMDE    =                 -19.1 / [mas/yr] proper motion in DE
PMDE_ERR=                   0.6 / [mas/yr] proper motion in DE error
J_MAG   =     8.988999999999999 / [mag] 2MASS J magnitude
J_ERR   =                  0.02 / [mag] 2MASS J magnitude error
J_QFLAG =                     5 / 2MASS J quality flag
H_MAG   =                 8.439 / [mag] 2MASS H magnitude
H_ERR   =                  0.02 / [mag] 2MASS H magnitude error
H_QFLAG =                     5 / 2MASS H quality flag
K_MAG   =     8.282999999999999 / [mag] 2MASS K magnitude
K_ERR   =                  0.01 / [mag] 2MASS K magnitude error
K_QFLAG =                     5 / 2MASS K quality flag
AP_BMAG =                12.881 / [mag] APASS B magnitude
AP_BERR =                 0.099 / [mag] APASS B magnitude error
AP_VMAG =                 11.28 / [mag] APASS V magnitude
AP_VERR =                 0.099 / [mag] APASS V magnitude error
AP_GMAG =    -99.98999999999999 / [mag] APASS g magnitude
AP_GERR =                 0.099 / [mag] APASS g magnitude error
AP_RMAG =    -99.98999999999999 / [mag] APASS r magnitude
AP_RERR =                 0.099 / [mag] APASS r magnitude error
AP_IMAG =    -99.98999999999999 / [mag] APASS i magnitude
AP_IERR =                 0.099 / [mag] APASS i magnitude error
U_FMAG  =                10.773 / [mag] UCAC4 fitted magnitude
U_AMAG  =                10.748 / [mag] UCAC4 aperture magnitude
U_MERR  =                  0.03 / [mag] UCAC4 magnitude error (both)
U_OTYPE =                     0 / UCAC4 object type flag (0=good)
DBL_FLAG=                     0 / UCAC4 double star flag (0=good)
CAT_FLAG=             310110010 / catalog source/match flags
ID_UCAC4= '603-064121'          / UCAC4 catalog ID
ID_UCAC2= '242-087706'          / UCAC2 catalog ID
ID_2MASS=             216741779 / 2MASS catalog ID
```

```
IDNUMBER=            141955691 / UCAC4 unique internal identifier
ID_TYCHO= '2624-02469-1'       / Tycho-2 catalog ID
JMINUSH =                 0.55 / [mag] 2MASS J-H magnitude
JMINUSK =                0.706 / [mag] 2MASS J-K magnitude
NEIGHTOT=                    0 / number of neighbors identified in KTC
END

Header listing for HDU #2:
XTENSION= 'BINTABLE'           / binary table extension
BITPIX  =                    8 / array data type
NAXIS   =                    2 / number of array dimensions
NAXIS1  =                   28 / length of dimension 1
NAXIS2  =                 5475 / length of dimension 2
PCOUNT  =                    0 / number of group parameters
GCOUNT  =                    1 / number of groups
TFIELDS =                    6 / number of table fields
TTYPE1  = 'JD_TT   '
TFORM1  = 'D       '
TUNIT1  = 'JD (TT) mid-exposure'
TTYPE2  = 'wflux   '
TFORM2  = 'E       '
TUNIT2  = 'diff-flux'
TTYPE3  = 'werr    '
TFORM3  = 'E       '
TUNIT3  = 'diff-flux'
TTYPE4  = 'flux    '
TFORM4  = 'E       '
TUNIT4  = 'diff-flux'
TTYPE5  = 'err     '
TFORM5  = 'E       '
TUNIT5  = 'diff-flux'
TTYPE6  = 'ksum    '
TFORM6  = 'E       '
EXTNAME = 'KN10E_FLUX'         / extension name
END

Header listing for HDU #3:
XTENSION= 'BINTABLE'           / binary table extension
BITPIX  =                    8 / array data type
NAXIS   =                    2 / number of array dimensions
NAXIS1  =                   20 / length of dimension 1
```

```
NAXIS2  =                 5475 / length of dimension 2
PCOUNT  =                    0 / number of group parameters
GCOUNT  =                    1 / number of groups
TFIELDS =                    4 / number of table fields
TTYPE1  = 'JD_TT    '
TFORM1  = 'D        '
TUNIT1  = 'JD (TT) mid-exposure'
TTYPE2  = 'mag      '
TFORM2  = 'E        '
TUNIT2  = 'mag      '
TTYPE3  = 'err      '
TFORM3  = 'E        '
TUNIT3  = 'mag      '
TTYPE4  = 'tfasig   '
TFORM4  = 'E        '
TUNIT4  = 'mag stddev'
EXTNAME = 'KN10E_MTFA'          / extension name
END

Header listing for HDU #4:
XTENSION= 'BINTABLE'            / binary table extension
BITPIX  =                    8 / array data type
NAXIS   =                    2 / number of array dimensions
NAXIS1  =                   16 / length of dimension 1
NAXIS2  =                 5475 / length of dimension 2
PCOUNT  =                    0 / number of group parameters
GCOUNT  =                    1 / number of groups
TFIELDS =                    3 / number of table fields
TTYPE1  = 'JD_TT    '
TFORM1  = 'D        '
TUNIT1  = 'JD (TT) mid-exposure'
TTYPE2  = 'mag      '
TFORM2  = 'E        '
TUNIT2  = 'mag      '
TTYPE3  = 'err      '
TFORM3  = 'E        '
TUNIT3  = 'mag      '
EXTNAME = 'KN10E_LCS1'          / extension name
END

Header listing for HDU #5:
```

```
XTENSION= 'BINTABLE'           / binary table extension
BITPIX  =                    8 / array data type
NAXIS   =                    2 / number of array dimensions
NAXIS1  =                   16 / length of dimension 1
NAXIS2  =                 5475 / length of dimension 2
PCOUNT  =                    0 / number of group parameters
GCOUNT  =                    1 / number of groups
TFIELDS =                    3 / number of table fields
TTYPE1  = 'JD_TT    '
TFORM1  = 'D        '
TUNIT1  = 'JD (TT) mid-exposure'
TTYPE2  = 'mag      '
TFORM2  = 'E        '
TUNIT2  = 'mag      '
TTYPE3  = 'err      '
TFORM3  = 'E        '
TUNIT3  = 'mag      '
EXTNAME = 'KN10E_LCS2'         / extension name
END

Header listing for HDU #6:
XTENSION= 'BINTABLE'           / binary table extension
BITPIX  =                    8 / array data type
NAXIS   =                    2 / number of array dimensions
NAXIS1  =                   28 / length of dimension 1
NAXIS2  =                 2402 / length of dimension 2
PCOUNT  =                    0 / number of group parameters
GCOUNT  =                    1 / number of groups
TFIELDS =                    6 / number of table fields
TTYPE1  = 'JD_TT    '
TFORM1  = 'D        '
TUNIT1  = 'JD (TT) mid-exposure'
TTYPE2  = 'wflux    '
TFORM2  = 'E        '
TUNIT2  = 'diff-flux'
TTYPE3  = 'werr     '
TFORM3  = 'E        '
TUNIT3  = 'diff-flux'
TTYPE4  = 'flux     '
TFORM4  = 'E        '
TUNIT4  = 'diff-flux'
```

```
TTYPE5  = 'err      '
TFORM5  = 'E        '
TUNIT5  = 'diff-flux'
TTYPE6  = 'ksum     '
TFORM6  = 'E        '
EXTNAME = 'KN11W_FLUX'          / extension name
END

Header listing for HDU #7:
XTENSION= 'BINTABLE'            / binary table extension
BITPIX  =                    8 / array data type
NAXIS   =                    2 / number of array dimensions
NAXIS1  =                   20 / length of dimension 1
NAXIS2  =                 2402 / length of dimension 2
PCOUNT  =                    0 / number of group parameters
GCOUNT  =                    1 / number of groups
TFIELDS =                    4 / number of table fields
TTYPE1  = 'JD_TT    '
TFORM1  = 'D        '
TUNIT1  = 'JD (TT) mid-exposure'
TTYPE2  = 'mag      '
TFORM2  = 'E        '
TUNIT2  = 'mag      '
TTYPE3  = 'err      '
TFORM3  = 'E        '
TUNIT3  = 'mag      '
TTYPE4  = 'tfasig   '
TFORM4  = 'E        '
TUNIT4  = 'mag stddev'
EXTNAME = 'KN11W_MTFA'          / extension name
END

Header listing for HDU #8:
XTENSION= 'BINTABLE'            / binary table extension
BITPIX  =                    8 / array data type
NAXIS   =                    2 / number of array dimensions
NAXIS1  =                   16 / length of dimension 1
NAXIS2  =                 2402 / length of dimension 2
PCOUNT  =                    0 / number of group parameters
GCOUNT  =                    1 / number of groups
TFIELDS =                    3 / number of table fields
```

```
TTYPE1  = 'JD_TT    '
TFORM1  = 'D        '
TUNIT1  = 'JD (TT) mid-exposure'
TTYPE2  = 'mag      '
TFORM2  = 'E        '
TUNIT2  = 'mag      '
TTYPE3  = 'err      '
TFORM3  = 'E        '
TUNIT3  = 'mag      '
EXTNAME = 'KN11W_LCS1'          / extension name
END

Header listing for HDU #9:
XTENSION= 'BINTABLE'            / binary table extension
BITPIX  =                    8 / array data type
NAXIS   =                    2 / number of array dimensions
NAXIS1  =                   16 / length of dimension 1
NAXIS2  =                 2402 / length of dimension 2
PCOUNT  =                    0 / number of group parameters
GCOUNT  =                    1 / number of groups
TFIELDS =                    3 / number of table fields
TTYPE1  = 'JD_TT    '
TFORM1  = 'D        '
TUNIT1  = 'JD (TT) mid-exposure'
TTYPE2  = 'mag      '
TFORM2  = 'E        '
TUNIT2  = 'mag      '
TTYPE3  = 'err      '
TFORM3  = 'E        '
TUNIT3  = 'mag      '
EXTNAME = 'KN11W_LCS2'          / extension name
END

Header listing for HDU #10:
XTENSION= 'BINTABLE'            / binary table extension
BITPIX  =                    8 / array data type
NAXIS   =                    2 / number of array dimensions
NAXIS1  =                   28 / length of dimension 1
NAXIS2  =                 2644 / length of dimension 2
PCOUNT  =                    0 / number of group parameters
GCOUNT  =                    1 / number of groups
```

```
TFIELDS =                    6 / number of table fields
TTYPE1  = 'JD_TT    '
TFORM1  = 'D        '
TUNIT1  = 'JD (TT) mid-exposure'
TTYPE2  = 'wflux    '
TFORM2  = 'E        '
TUNIT2  = 'diff-flux'
TTYPE3  = 'werr     '
TFORM3  = 'E        '
TUNIT3  = 'diff-flux'
TTYPE4  = 'flux     '
TFORM4  = 'E        '
TUNIT4  = 'diff-flux'
TTYPE5  = 'err      '
TFORM5  = 'E        '
TUNIT5  = 'diff-flux'
TTYPE6  = 'ksum     '
TFORM6  = 'E        '
EXTNAME = 'KN10W_FLUX'           / extension name
END

Header listing for HDU #11:
XTENSION= 'BINTABLE'             / binary table extension
BITPIX  =                    8 / array data type
NAXIS   =                    2 / number of array dimensions
NAXIS1  =                   20 / length of dimension 1
NAXIS2  =                 2644 / length of dimension 2
PCOUNT  =                    0 / number of group parameters
GCOUNT  =                    1 / number of groups
TFIELDS =                    4 / number of table fields
TTYPE1  = 'JD_TT    '
TFORM1  = 'D        '
TUNIT1  = 'JD (TT) mid-exposure'
TTYPE2  = 'mag      '
TFORM2  = 'E        '
TUNIT2  = 'mag      '
TTYPE3  = 'err      '
TFORM3  = 'E        '
TUNIT3  = 'mag      '
TTYPE4  = 'tfasig   '
TFORM4  = 'E        '
```

```
TUNIT4  = 'mag stddev'
EXTNAME = 'KN10W_MTFA'          / extension name
END

Header listing for HDU #12:
XTENSION= 'BINTABLE'            / binary table extension
BITPIX  =                    8 / array data type
NAXIS   =                    2 / number of array dimensions
NAXIS1  =                   16 / length of dimension 1
NAXIS2  =                 2644 / length of dimension 2
PCOUNT  =                    0 / number of group parameters
GCOUNT  =                    1 / number of groups
TFIELDS =                    3 / number of table fields
TTYPE1  = 'JD_TT    '
TFORM1  = 'D        '
TUNIT1  = 'JD (TT) mid-exposure'
TTYPE2  = 'mag      '
TFORM2  = 'E        '
TUNIT2  = 'mag      '
TTYPE3  = 'err      '
TFORM3  = 'E        '
TUNIT3  = 'mag      '
EXTNAME = 'KN10W_LCS1'          / extension name
END

Header listing for HDU #13:
XTENSION= 'BINTABLE'            / binary table extension
BITPIX  =                    8 / array data type
NAXIS   =                    2 / number of array dimensions
NAXIS1  =                   16 / length of dimension 1
NAXIS2  =                 2644 / length of dimension 2
PCOUNT  =                    0 / number of group parameters
GCOUNT  =                    1 / number of groups
TFIELDS =                    3 / number of table fields
TTYPE1  = 'JD_TT    '
TFORM1  = 'D        '
TUNIT1  = 'JD (TT) mid-exposure'
TTYPE2  = 'mag      '
TFORM2  = 'E        '
TUNIT2  = 'mag      '
TTYPE3  = 'err      '
```

```
TFORM3  = 'E       '
TUNIT3  = 'mag     '
EXTNAME = 'KN10W_LCS2'          / extension name
END

Header listing for HDU #14:
XTENSION= 'BINTABLE'            / binary table extension
BITPIX  =                    8 / array data type
NAXIS   =                    2 / number of array dimensions
NAXIS1  =                   28 / length of dimension 1
NAXIS2  =                 3617 / length of dimension 2
PCOUNT  =                    0 / number of group parameters
GCOUNT  =                    1 / number of groups
TFIELDS =                    6 / number of table fields
TTYPE1  = 'JD_TT   '
TFORM1  = 'D       '
TUNIT1  = 'JD (TT) mid-exposure'
TTYPE2  = 'wflux   '
TFORM2  = 'E       '
TUNIT2  = 'diff-flux'
TTYPE3  = 'werr    '
TFORM3  = 'E       '
TUNIT3  = 'diff-flux'
TTYPE4  = 'flux    '
TFORM4  = 'E       '
TUNIT4  = 'diff-flux'
TTYPE5  = 'err     '
TFORM5  = 'E       '
TUNIT5  = 'diff-flux'
TTYPE6  = 'ksum    '
TFORM6  = 'E       '
EXTNAME = 'KN11E_FLUX'          / extension name
END

Header listing for HDU #15:
XTENSION= 'BINTABLE'            / binary table extension
BITPIX  =                    8 / array data type
NAXIS   =                    2 / number of array dimensions
NAXIS1  =                   20 / length of dimension 1
NAXIS2  =                 3617 / length of dimension 2
PCOUNT  =                    0 / number of group parameters
```

```
GCOUNT  =                    1 / number of groups
TFIELDS =                    4 / number of table fields
TTYPE1  = 'JD_TT    '
TFORM1  = 'D        '
TUNIT1  = 'JD (TT) mid-exposure'
TTYPE2  = 'mag      '
TFORM2  = 'E        '
TUNIT2  = 'mag      '
TTYPE3  = 'err      '
TFORM3  = 'E        '
TUNIT3  = 'mag      '
TTYPE4  = 'tfasig   '
TFORM4  = 'E        '
TUNIT4  = 'mag stddev'
EXTNAME = 'KN11E_MTFA'          / extension name
END

Header listing for HDU #16:
XTENSION= 'BINTABLE'            / binary table extension
BITPIX  =                    8 / array data type
NAXIS   =                    2 / number of array dimensions
NAXIS1  =                   16 / length of dimension 1
NAXIS2  =                 3617 / length of dimension 2
PCOUNT  =                    0 / number of group parameters
GCOUNT  =                    1 / number of groups
TFIELDS =                    3 / number of table fields
TTYPE1  = 'JD_TT    '
TFORM1  = 'D        '
TUNIT1  = 'JD (TT) mid-exposure'
TTYPE2  = 'mag      '
TFORM2  = 'E        '
TUNIT2  = 'mag      '
TTYPE3  = 'err      '
TFORM3  = 'E        '
TUNIT3  = 'mag      '
EXTNAME = 'KN11E_LCS1'          / extension name
END

Header listing for HDU #17:
XTENSION= 'BINTABLE'            / binary table extension
BITPIX  =                    8 / array data type
```

```
NAXIS   =                    2 / number of array dimensions
NAXIS1  =                   16 / length of dimension 1
NAXIS2  =                 3617 / length of dimension 2
PCOUNT  =                    0 / number of group parameters
GCOUNT  =                    1 / number of groups
TFIELDS =                    3 / number of table fields
TTYPE1  = 'JD_TT    '
TFORM1  = 'D        '
TUNIT1  = 'JD (TT) mid-exposure'
TTYPE2  = 'mag      '
TFORM2  = 'E        '
TUNIT2  = 'mag      '
TTYPE3  = 'err      '
TFORM3  = 'E        '
TUNIT3  = 'mag      '
EXTNAME = 'KN11E_LCS2'          / extension name
END
```

D.3 Python Code for CDE Light Curve Interaction

A Python Application Programming Interface (API) is provided to interact with combined CDE light curves. The API provides a stable, user-friendly means of identifying and extracting desired components from a multi-extension FITS data file. In effect, the API hides the details of file structure and data storage from the user. This separation allows the file structure to change in the future if needed without causing disruption to existing software developed to make use of CDE data. The Python script below is an early version of this API (corresponding to the file structure details in previous sections) that transparently extracts specific data subsets in a format identical to that used by KELT before the development of CDE.

```
#!/usr/bin/env python
# vim: set fileencoding=utf-8 ts=4 sts=4 sw=4 et tw=80 :
#
# A minimal API that provides access to CDE data products.
#
# Rob Siverd
```

```
# Created:       2019-07-03
# Last modified: 2019-07-04
#--------------------------------------------------------------------------
#**************************************************************************
#--------------------------------------------------------------------------

## Current version:
__version__ = "0.1.3"

## Python version-agnostic module reloading:
try:
    reload                              # Python 2.7
except NameError:
    try:
        from importlib import reload    # Python 3.4+
    except ImportError:
        from imp import reload          # Python 3.0 - 3.3

## Modules:
import os
import sys
import time
import numpy as np
from numpy.lib.recfunctions import append_fields
import pandas as pd
_have_np_vers = float('.'.join(np.__version__.split('.')[:2]))

##--------------------------------------------------------------------------##

##--------------------------------------------------------------------------##

## FITS I/O:
try:
    import astropy.io.fits as pf
except ImportError:
    try:
       import pyfits as pf
    except ImportError:
        sys.stderr.write("\nError!  No FITS I/O module found!\n"
               "Install either astropy.io.fits or pyfits and try again!\n\n")
        sys.exit(1)
```

```
48
49
50 ##--------------------------------------------------------------------##
51 ##-------------------    CDE (FITS) Data Product Handling   ----------##
52 ##--------------------------------------------------------------------##
53
54 class CDELoader(object):
55
56     def __init__(self, vlevel=0, stream=sys.stderr):
57         self._site_map = {'KN':'north', 'KS':'south'}
58         self._fresh_start()
59         self._stream = stream
60         self._vlevel = vlevel
61         self._def_norm = {'FLUX':'wflux', 'LCS1':'mag',
62                 'LCS2':'mag', 'LCS3':'mag', 'MTFA':'mag'}
63         return
64
65     # ------------------------------------------------------------------
66     # initialize things:
67     def _fresh_start(self):
68         self.targ_info = None
69         self.current_file = None
70         self.tab_info = None
71         self._ntables = 0
72         self._ufields = []
73         self._ultypes = []
74         return
75
76     # ------------------------------------------------------------------
77     @staticmethod
78     def _parse_extnames(ext_names):
79         kfields, lctypes = zip(*[x.split('_') for x in ext_names])
80         return np.core.records.fromarrays(
81                 [kfields, lctypes, ext_names], names='field,ltype,extn')
82
83     # ------------------------------------------------------------------
84     # verbosity level adjustment:
85     def set_vlevel(self, vv):
86         self._vlevel = vv
87
88     # load a table HDU:
```

```
89      def _load_tab_hdu_name(self, extname, cols=('data', 'hdrs')):
90          contents = pf.getdata(self.current_file, header=True, extname=extname)
91          contents[0] = contents[0].byteswap(inplace=True).newbyteorder()
92          return {cc:tt for cc,tt in zip(cols, contents)}
93
94      # ------------------------------------------------------------
95      # user-facing routine for file selection.  FITS table is analyzed
96      # and contents are summarized.  User then decides how to proceed:
97      def load_file(self, cde_table):
98          self.sprint(0, "Scanning %s ... " % cde_table)
99          with pf.open(cde_table) as hdulist:
100             self.targ_info = hdulist[0].header.copy(strip=True)
101             ext_names = [x.name for x in hdulist[1:]]
102         self.tab_info = self._parse_extnames(ext_names)
103         self._ntables = len(self.tab_info)
104         self.current_file = cde_table
105
106         # Unique fields and lctypes:
107         self._ufields = np.unique(self.tab_info['field'])
108         self._ultypes = np.unique(self.tab_info['ltype'])
109         self.sprint(0, "done.\n")
110
111         # Summary:
112         self.sprint(0, "Found %d data tables.\n" % self._ntables)
113         self.sprint(0, "KELT fields: %s\n" % str(self._ufields))
114         self.sprint(0, "LC flavors:  %s\n" % str(self._ultypes))
115         return
116
117     # ------------------------------------------------------------
118     # use median-subtraction to align the data sets:
119     def _msub_align_data(self, data_sets, ltype, normcol=None):
120         usenorm = normcol if normcol else self._def_norm[ltype]
121         sys.stderr.write("\nusenorm: %s\n" % usenorm)
122
123         # pre-add chunk identifier to individual data sets:
124         for i in range(len(data_sets)):
125             npts = len(data_sets[i])
126             dummy = np.zeros(npts, dtype='int') + i
127             data_sets[i] = append_fields(data_sets[i], 'lnum', dummy,
128                     usemask=False)
129
```

```
130         # flux/mag normalization:
131         med_vals, std_vals = [], []
132         for i,item in enumerate(data_sets):
133             flxvec = item[usenorm]
134             this_med = np.median(item[usenorm])
135             this_std =    np.std(item[usenorm])
136             item[usenorm] -= this_med
137             med_vals.append(this_med)
138             std_vals.append(this_std)
139         sys.stderr.write("med_vals: %s\n" % str(med_vals))
140         sys.stderr.write("std_vals: %s\n" % str(std_vals))
141         avg_mval = np.average(med_vals)
142         result = np.concatenate(data_sets)
143         result[usenorm] += avg_mval
144         return result
145 
146     # ------------------------------------------------------------------------
147     # load table HDU, optionally embed extension name:
148     @staticmethod
149     def _tab_with_xtras(fname, extname):
150         tdata = pf.getdata(fname, extname=extname)
151         tdata = tdata.byteswap().newbyteorder()
152         npnts = len(tdata)
153         dummy = npnts*[extname]
154         field, ltype = extname.split('_')
155         return append_fields(tdata, ('extn', 'field', 'ltype'),
156                 (npnts*[extname], npnts*[field], npnts*[ltype]), usemask=False)
157 
158     # Combine/extract all data of a specified type:
159     def extract_ltype(self, ltype, concat=True, align='med'):
160         if not isinstance(self.tab_info, np.ndarray):
161             self.sprint(-5, "No data file loaded!\n")
162             self.sprint(-5, "Use load_file() to choose a CDE file first.\n")
163             return None
164         lcheck = ltype.upper()
165         if not lcheck in self._ultypes:
166             self.sprint(-5, "Unrecognized type: '%s'\n" % lcheck)
167             return None
168         lwhich = (self.tab_info['ltype'] == lcheck)
169         subset = self.tab_info[lwhich]
170 
```

```
171         get_exts = subset['extn']
172         chunks = [self._tab_with_xtras(self.current_file, x) for x in get_exts]
173         if concat:
174             result = self._msub_align_data(chunks, ltype)
175             return result
176         else:
177             return chunks
178 
179     # ------------------------------------------------------------------------
180     # easily save a light curve in ASCII format:
181     def save_to_ascii(self, filename, data, ncols=0, delim=' '):
182         sys.stderr.write("Writing to: %s\n" % filename)
183         sys.stderr.write("columns: %s\n" % str(data.dtype.names))
184         cnames = data.dtype.names[:ncols] if ncols else data.dtype.names
185         vecs = [data[x] for x in cnames]
186         with open(filename, 'w') as f:
187             for rvals in zip(*[self._strformat(data[x]) for x in cnames]):
188                 f.write(delim.join(rvals) + '\n')
189                 pass
190             pass
191         return
192 
193     @staticmethod
194     def _strformat(array):
195         _known_fmts = ['U', 'S', 'f', 'i']
196         if not (array.dtype.kind in _known_fmts):
197             sys.stderr.write("Don't know this one: '%s'\n" % array.dtype.kind)
198             raise
199         if (array.dtype.kind is 'U'):
200             return array                    # already unicode
201         if (array.dtype.kind is 'S'):
202             newfmt = 'U%d' % array.dtype.itemsize
203             return array.astype(newfmt)     # into unicode
204         else:
205             return array.astype('U25')
206 
207     # ------------------------------------------------------------------------
208     # messaging helper:
209     def sprint(self, vlmin, text):
210         if (self._vlevel >= vlmin):
211             self._stream.write(text)
```

```
212
213 ##--------------------------------------------------------------------------##
214
215
216
217
218 ############################################################################
219 # CHANGELOG (cde_loader.py):
220 #-----------------------------------------------------------------------------
221 #
222 #   2019-07-04:
223 #       -- Increased __version__ to 0.1.2.
224 #       -- Now format strings to unicode for Python-3 compatibility.
225 #       -- Increased __version__ to 0.1.1.
226 #       -- Added 'U' kind to dtypes passed along as-is (may not always work).
227 #
228 #   2019-07-03:
229 #       -- Increased __version__ to 0.1.0.
230 #       -- First created cde_loader.py.
231 #
```

Appendix E

Photometric Precision vs. Magnitude: RMS Plots

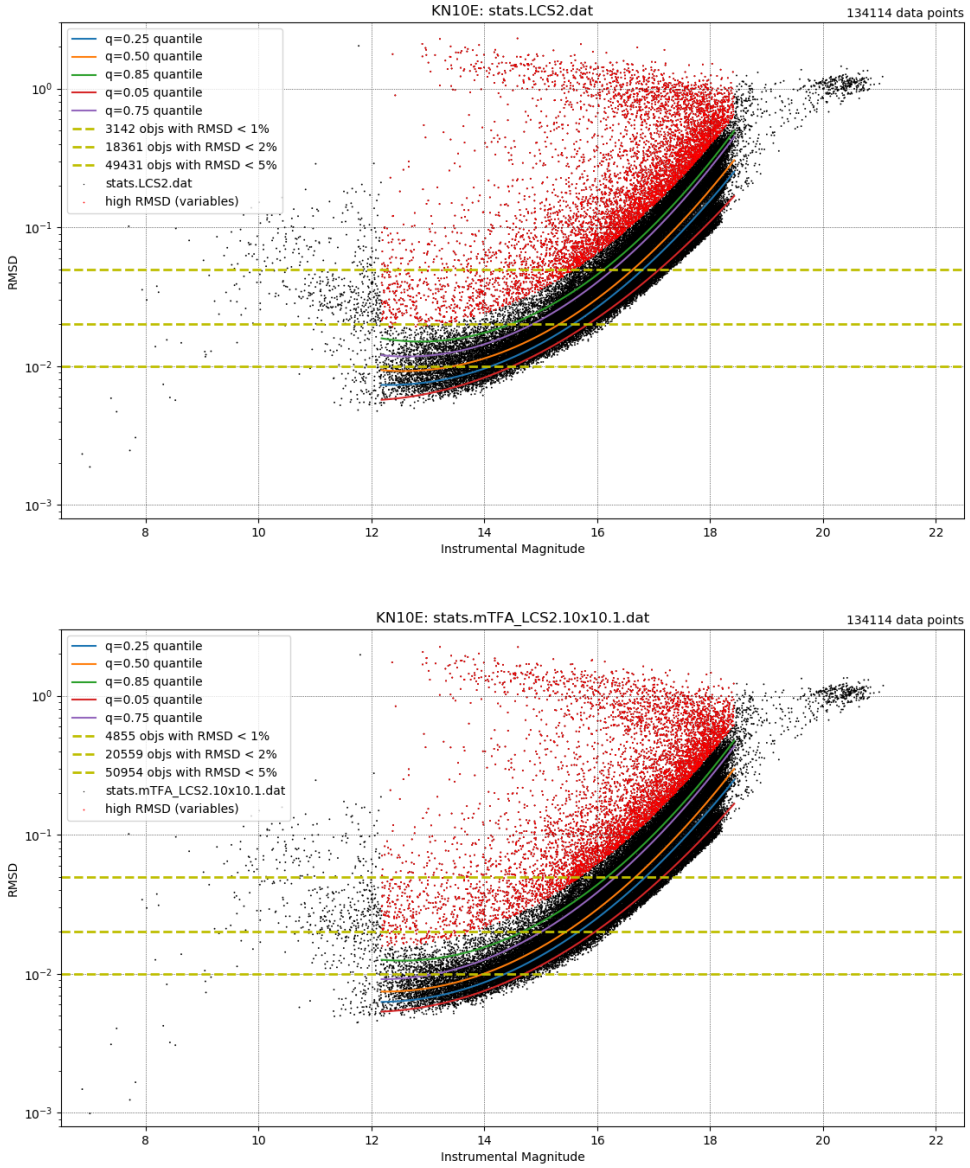

Figure E.1: RMS deviation vs. instrumental magnitude of raw (top) and TFA-detrended (bottom) light curves from Northern field KN10W using CDE. The black points trace the core instrument and system response from just prior to saturation on the bright end to the sky-dominated regime on the faint end. Quantile fits are drawn over the cloud of points up to the onset of saturation to help guide the eye. High-scatter points marked in red are likely to be variable stars.

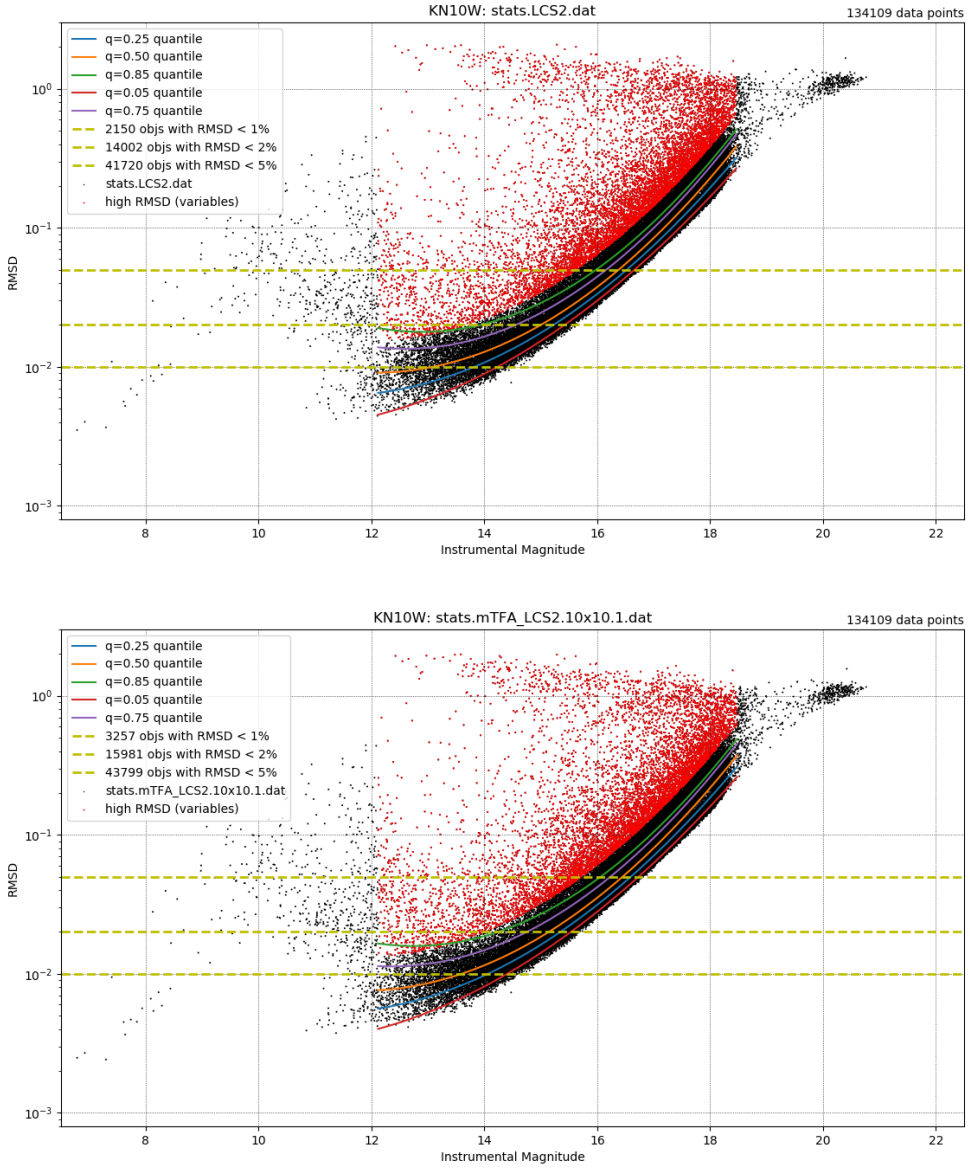

Figure E.2: RMS deviation vs. instrumental magnitude of raw (top) and TFA-detrended (bottom) light curves from Northern field KN10W using CDE. The black points trace the core instrument and system response from just prior to saturation on the bright end to the sky-dominated regime on the faint end. Quantile fits are drawn over the cloud of points up to the onset of saturation to help guide the eye. High-scatter points marked in red are likely to be variable stars.

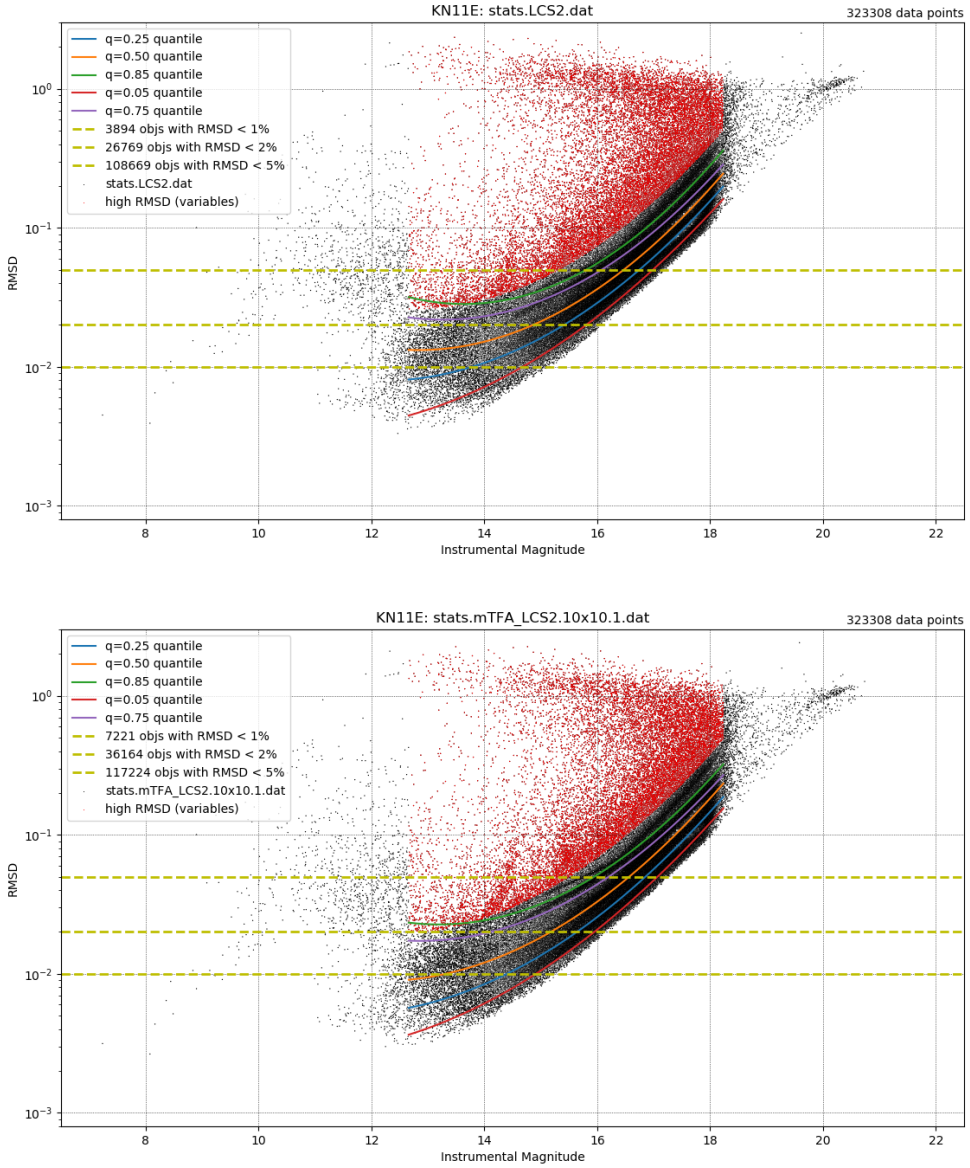

Figure E.3: RMS deviation vs. instrumental magnitude of raw (top) and TFA-detrended (bottom) light curves from Northern field KN11E using CDE. The black points trace the core instrument and system response from just prior to saturation on the bright end to the sky-dominated regime on the faint end. Quantile fits are drawn over the cloud of points up to the onset of saturation to help guide the eye. High-scatter points marked in red are likely to be variable stars.

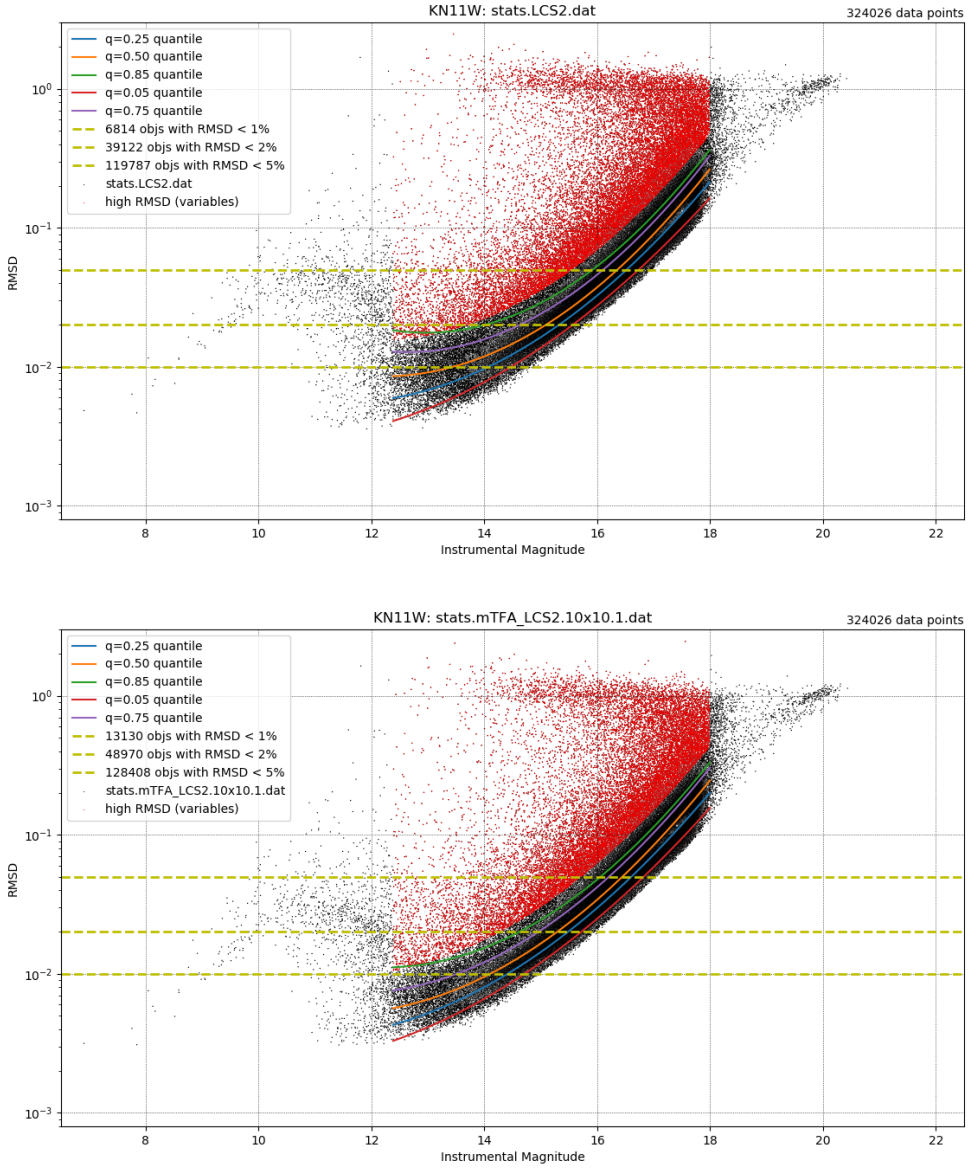

Figure E.4: RMS deviation vs. instrumental magnitude of raw (top) and TFA-detrended (bottom) light curves from Northern field KN11W using CDE. The black points trace the core instrument and system response from just prior to saturation on the bright end to the sky-dominated regime on the faint end. Quantile fits are drawn over the cloud of points up to the onset of saturation to help guide the eye. High-scatter points marked in red are likely to be variable stars.

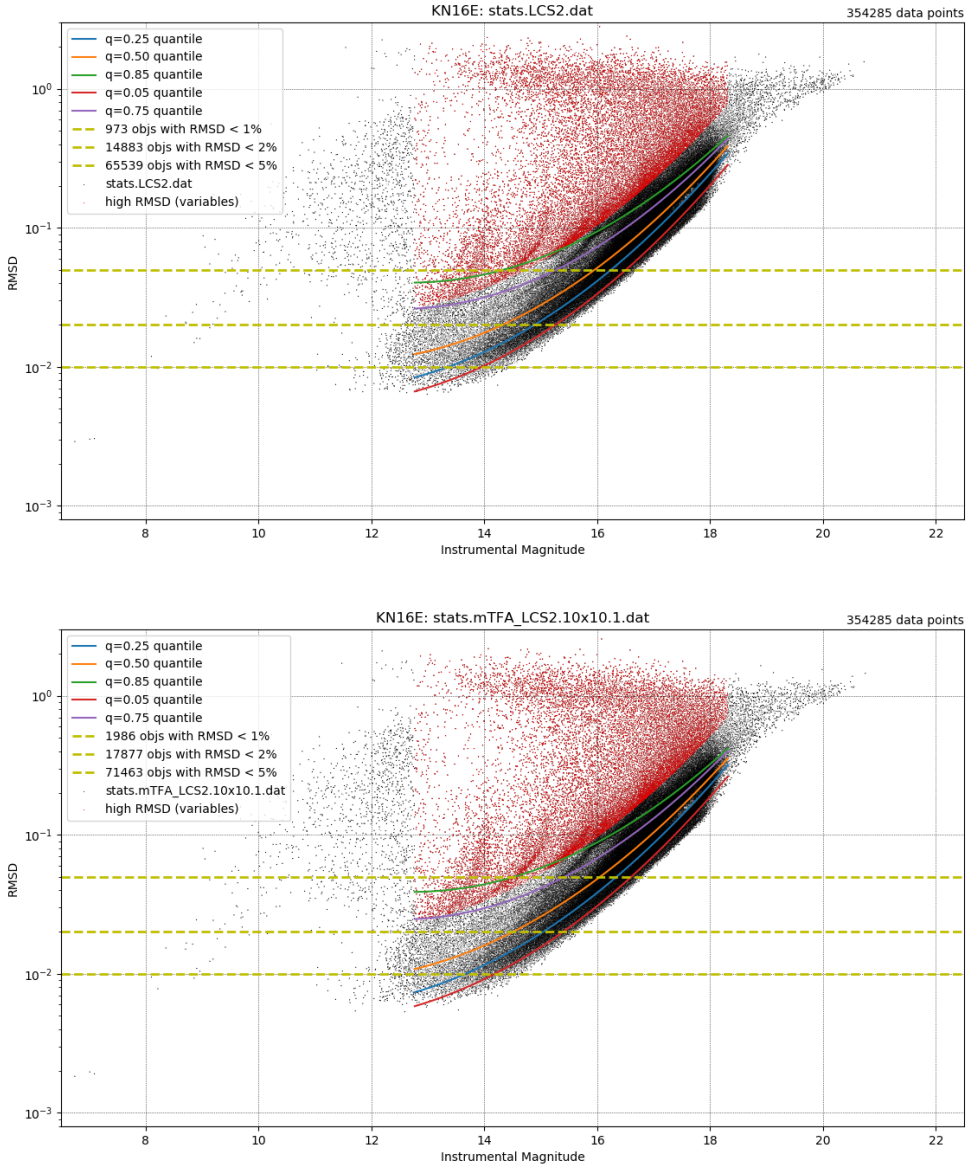

Figure E.5: RMS deviation vs. instrumental magnitude of raw (top) and TFA-detrended (bottom) light curves from Northern field KN16E using CDE. The black points trace the core instrument and system response from just prior to saturation on the bright end to the sky-dominated regime on the faint end. Quantile fits are drawn over the cloud of points up to the onset of saturation to help guide the eye. High-scatter points marked in red are likely to be variable stars.

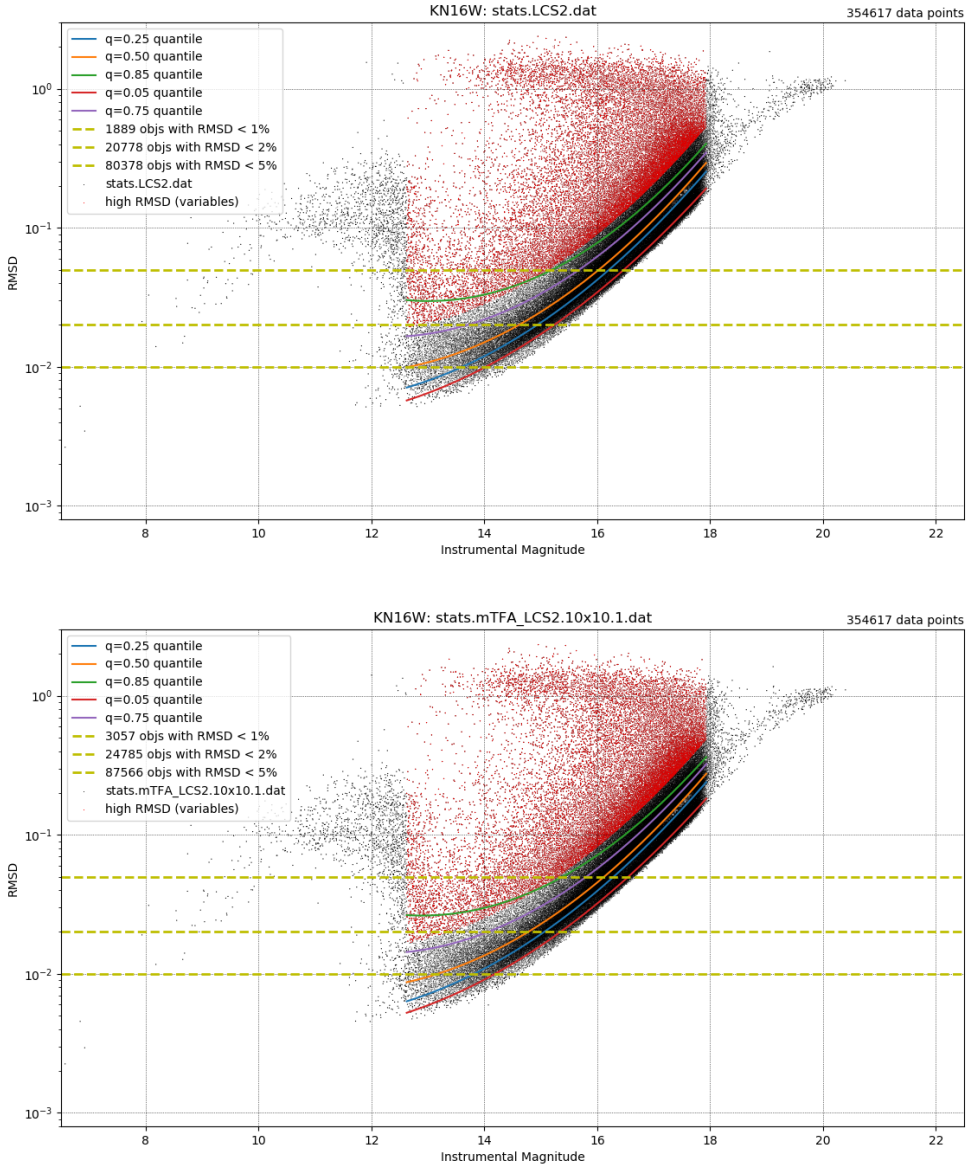

Figure E.6: RMS deviation vs. instrumental magnitude of raw (top) and TFA-detrended (bottom) light curves from Northern field KN16W using CDE. The black points trace the core instrument and system response from just prior to saturation on the bright end to the sky-dominated regime on the faint end. Quantile fits are drawn over the cloud of points up to the onset of saturation to help guide the eye. High-scatter points marked in red are likely to be variable stars.

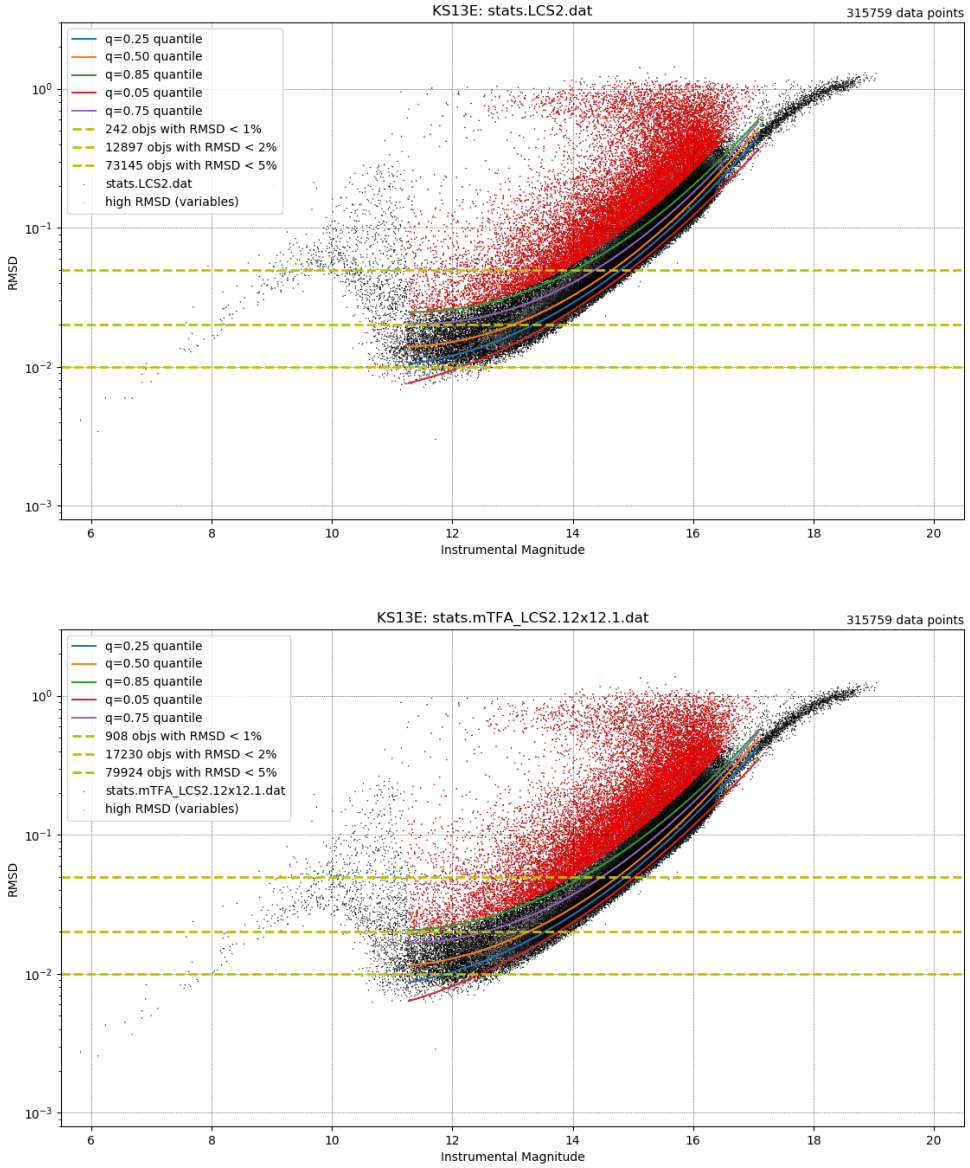

Figure E.7: RMS deviation vs. instrumental magnitude of raw (top) and TFA-detrended (bottom) light curves from Southern field KS13E using CDE. The black points trace the core instrument and system response from just prior to saturation on the bright end to the sky-dominated regime on the faint end. Quantile fits are drawn over the cloud of points up to the onset of saturation to help guide the eye. High-scatter points marked in red are likely to be variable stars.

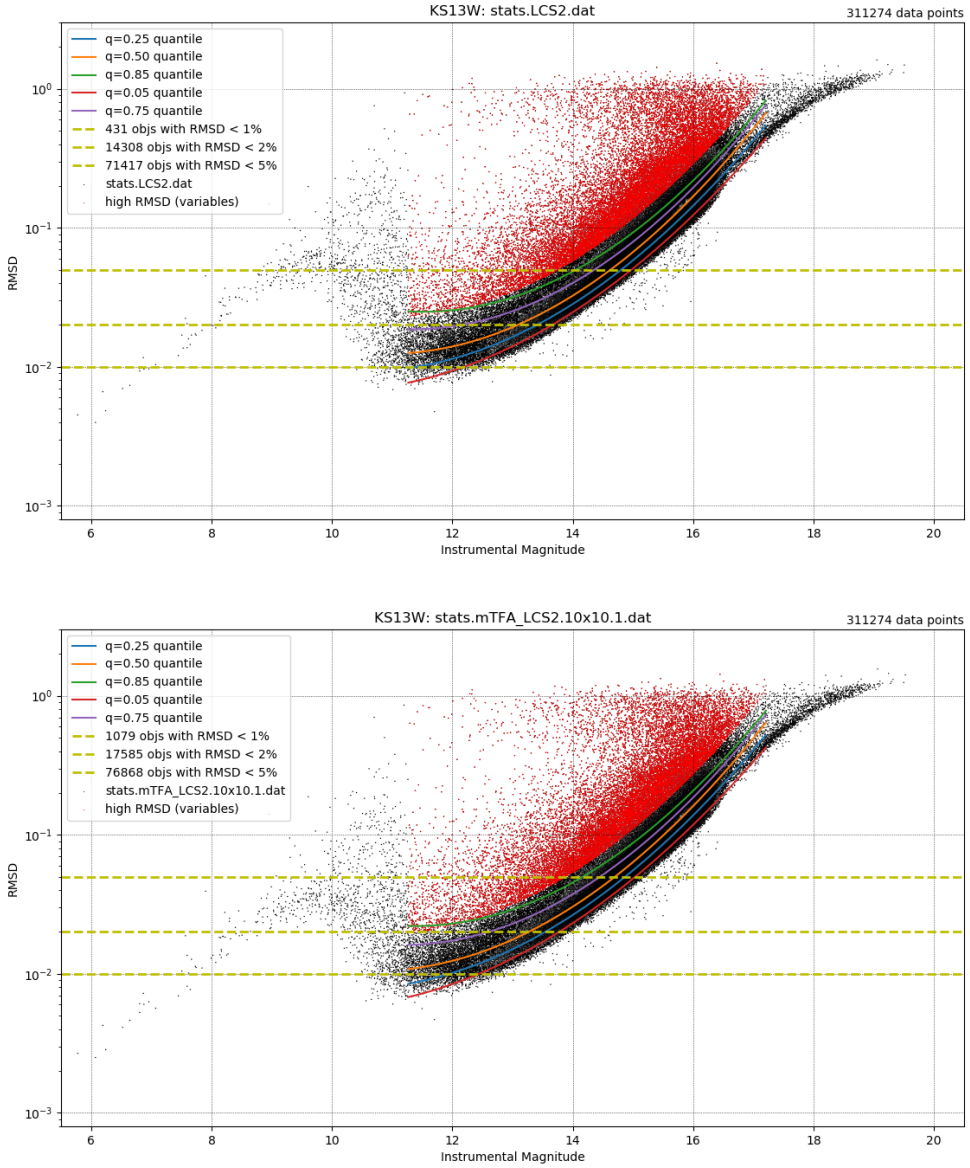

Figure E.8: RMS deviation vs. instrumental magnitude of raw (top) and TFA-detrended (bottom) light curves from Southern field KS13W using CDE. The black points trace the core instrument and system response from just prior to saturation on the bright end to the sky-dominated regime on the faint end. Quantile fits are drawn over the cloud of points up to the onset of saturation to help guide the eye. High-scatter points marked in red are likely to be variable stars.

REFERENCES

H. A. Abt and S. G. Levy. Improved study of metallic-line binaries. ApJS, 59:229–247, October 1985. doi: 10.1086/191070.

H. A. Abt and N. I. Morrell. The Relation between Rotational Velocities and Spectral Peculiarities among A-Type Stars. ApJS, 99:135, July 1995. doi: 10.1086/192182.

E. Agol and J. H. Steffen. A limit on the presence of Earth-mass planets around a Sun-like star. MNRAS, 374:941–948, January 2007. doi: 10.1111/j.1365-2966.2006.11213.x.

E. Agol, J. Steffen, R. Sari, and W. Clarkson. On detecting terrestrial planets with timing of giant planet transits. MNRAS, 359:567–579, May 2005. doi: 10.1111/j.1365-2966.2005.08922.x.

C. Alard. Image subtraction using a space-varying kernel. A&AS, 144:363–370, June 2000. doi: 10.1051/aas:2000214.

C. Alard and R. H. Lupton. A Method for Optimal Image Subtraction. ApJ, 503:325–331, August 1998. doi: 10.1086/305984.

R. Alonso, T. M. Brown, G. Torres, D. W. Latham, A. Sozzetti, G. Mandushev, J. A. Belmonte, D. Charbonneau, H. J. Deeg, E. W. Dunham, F. T. O'Donovan, and R. P. Stefanik. TrES-1: The Transiting Planet of a Bright K0 V Star. ApJ, 613:L153–L156, October 2004. doi: 10.1086/425256.

K. A. Alsubai, N. R. Parley, D. M. Bramich, R. G. West, P. M. Sorensen, A. Collier Cameron, D. W. Latham, K. Horne, D. R. Anderson, G. Á. Bakos, D. J. A. Brown, L. A. Buchhave, G. A. Esquerdo, M. E. Everett, G. Fżrész, J. D. Hartman, C. Hellier, G. M. Miller, D. Pollacco, S. N. Quinn, J. C. Smith, R. P. Stefanik, and A. Szentgyor-

gyi. Qatar-1b: a hot Jupiter orbiting a metal-rich K dwarf star. MNRAS, 417:709–716, October 2011. doi: 10.1111/j.1365-2966.2011.19316.x.

R. Amanullah, A. Goobar, J. Johansson, D. P. K. Banerjee, V. Venkataraman, V. Joshi, N. M. Ashok, Y. Cao, M. M. Kasliwal, S. R. Kulkarni, P. E. Nugent, T. Petrushevska, and V. Stanishev. The Peculiar Extinction Law of SN 2014J Measured with the Hubble Space Telescope. ApJ, 788:L21, June 2014. doi: 10.1088/2041-8205/788/2/L21.

D. R. Anderson, A. Collier Cameron, C. Hellier, M. Lendl, P. F. L. Maxted, D. Pollacco, D. Queloz, B. Smalley, A. M. S. Smith, I. Todd, A. H. M. J. Triaud, R. G. West, S. C. C. Barros, B. Enoch, M. Gillon, T. A. Lister, F. Pepe, D. Ségransan, R. A. Street, and S. Udry. WASP-30b: A 61 M $_{Jup}$ Brown Dwarf Transiting a V = 12, F8 Star. ApJ, 726: L19, January 2011. doi: 10.1088/2041-8205/726/2/L19.

D. R. Anderson, A. Collier Cameron, M. Gillon, C. Hellier, E. Jehin, M. Lendl, P. F. L. Maxted, D. Queloz, B. Smalley, A. M. S. Smith, A. H. M. J. Triaud, R. G. West, F. Pepe, D. Pollacco, D. Ségransan, I. Todd, and S. Udry. WASP-44b, WASP-45b and WASP-46b: three short-period, transiting extrasolar planets. MNRAS, 422:1988–1998, May 2012. doi: 10.1111/j.1365-2966.2012.20635.x.

A. Baglin. COROT: A minisat for pionnier science, asteroseismology and planets finding. *Advances in Space Research*, 31:345–349, 2003. doi: 10.1016/S0273-1177(02)00624-5.

G. Á. Bakos, R. W. Noyes, G. Kovács, D. W. Latham, D. D. Sasselov, G. Torres, D. A. Fischer, R. P. Stefanik, B. Sato, J. A. Johnson, A. Pál, G. W. Marcy, R. P. Butler, G. A. Esquerdo, K. Z. Stanek, J. Lázár, I. Papp, P. Sári, and B. Sipőcz. HAT-P-1b: A Large-Radius, Low-Density Exoplanet Transiting One Member of a Stellar Binary. ApJ, 656: 552–559, February 2007. doi: 10.1086/509874.

G. Á. Bakos, J. Hartman, G. Torres, D. W. Latham, G. Kovács, R. W. Noyes, D. A. Fischer, J. A. Johnson, G. W. Marcy, A. W. Howard, D. Kipping, G. A. Esquerdo, A. Shporer,

B. Béky, L. A. Buchhave, G. Perumpilly, M. Everett, D. D. Sasselov, R. P. Stefanik, J. Lázár, I. Papp, and P. Sári. HAT-P-20b-HAT-P-23b: Four Massive Transiting Extrasolar Planets. ApJ, 742:116, December 2011. doi: 10.1088/0004-637X/742/2/116.

G. Á. Bakos, J. D. Hartman, G. Torres, B. Béky, D. W. Latham, L. A. Buchhave, Z. Csubry, G. Kovács, A. Bieryla, S. Quinn, T. Szklenár, G. A. Esquerdo, A. Shporer, R. W. Noyes, D. A. Fischer, J. A. Johnson, A. W. Howard, G. W. Marcy, B. Sato, K. Penev, M. Everett, D. D. Sasselov, G. Fűrész, R. P. Stefanik, J. Lázár, I. Papp, and P. Sári. HAT-P-34b-HAT-P-37b: Four Transiting Planets More Massive than Jupiter Orbiting Moderately Bright Stars. AJ, 144:19, July 2012. doi: 10.1088/0004-6256/144/1/19.

I. Baraffe, G. Chabrier, T. S. Barman, F. Allard, and P. H. Hauschildt. Evolutionary models for cool brown dwarfs and extrasolar giant planets. The case of HD 209458. A&A, 402: 701–712, May 2003. doi: 10.1051/0004-6361:20030252.

J. W. Barnes. Transit Lightcurves of Extrasolar Planets Orbiting Rapidly Rotating Stars. ApJ, 705:683–692, November 2009. doi: 10.1088/0004-637X/705/1/683.

J. W. Barnes and J. J. Fortney. Transit Detectability of Ring Systems around Extrasolar Giant Planets. ApJ, 616:1193–1203, December 2004. doi: 10.1086/425067.

N. M. Batalha, J. F. Rowe, S. T. Bryson, T. Barclay, C. J. Burke, D. A. Caldwell, J. L. Christiansen, F. Mullally, S. E. Thompson, T. M. Brown, A. K. Dupree, D. C. Fabrycky, E. B. Ford, J. J. Fortney, R. L. Gilliland, H. Isaacson, D. W. Latham, G. W. Marcy, S. N. Quinn, D. Ragozzine, A. Shporer, W. J. Borucki, D. R. Ciardi, T. N. Gautier, III, M. R. Haas, J. M. Jenkins, D. G. Koch, J. J. Lissauer, W. Rapin, G. S. Basri, A. P. Boss, L. A. Buchhave, J. A. Carter, D. Charbonneau, J. Christensen-Dalsgaard, B. D. Clarke, W. D. Cochran, B.-O. Demory, J.-M. Desert, E. Devore, L. R. Doyle, G. A. Esquerdo, M. Everett, F. Fressin, J. C. Geary, F. R. Girouard, A. Gould, J. R. Hall, M. J. Holman, A. W. Howard, S. B. Howell, K. A. Ibrahim, K. Kinemuchi, H. Kjeldsen, T. C. Klaus,

J. Li, P. W. Lucas, S. Meibom, R. L. Morris, A. Prša, E. Quintana, D. T. Sanderfer, D. Sasselov, S. E. Seader, J. C. Smith, J. H. Steffen, M. Still, M. C. Stumpe, J. C. Tarter, P. Tenenbaum, G. Torres, J. D. Twicken, K. Uddin, J. Van Cleve, L. Walkowicz, and W. F. Welsh. Planetary Candidates Observed by Kepler. III. Analysis of the First 16 Months of Data. ApJS, 204:24, February 2013. doi: 10.1088/0067-0049/204/2/24.

T. G. Beatty, J. M. Fernández, D. W. Latham, G. Á. Bakos, G. Kovács, R. W. Noyes, R. P. Stefanik, G. Torres, M. E. Everett, and C. W. Hergenrother. The Mass and Radius of the Unseen M Dwarf Companion in the Single-Lined Eclipsing Binary HAT-TR-205-013. ApJ, 663:573–582, July 2007. doi: 10.1086/518413.

T. G. Beatty, J. Pepper, R. J. Siverd, J. D. Eastman, A. Bieryla, D. W. Latham, L. A. Buchhave, E. L. N. Jensen, M. Manner, K. G. Stassun, B. S. Gaudi, P. Berlind, M. L. Calkins, K. Collins, D. L. DePoy, G. A. Esquerdo, B. J. Fulton, G. Fűrész, J. C. Geary, A. Gould, L. Hebb, J. F. Kielkopf, J. L. Marshall, R. Pogge, K. Z. Stanek, R. P. Stefanik, R. Street, A. H. Szentgyorgyi, M. Trueblood, P. Trueblood, and A. M. Stutz. KELT-2Ab: A Hot Jupiter Transiting the Bright (V = 8.77) Primary Star of a Binary System. ApJ, 756:L39, September 2012. doi: 10.1088/2041-8205/756/2/L39.

T. Bensby, S. Feltzing, and I. Lundström. Elemental abundance trends in the Galactic thin and thick disks as traced by nearby F and G dwarf stars. A&A, 410:527–551, November 2003. doi: 10.1051/0004-6361:20031213.

E. Bertin and S. Arnouts. SExtractor: Software for source extraction. A&AS, 117:393–404, June 1996. doi: 10.1051/aas:1996164.

M. S. Bessell. UBVRI photometry II: the Cousins VRI system, its temperature and absolute flux calibration, and relevance for two-dimensional photometry. PASP, 91:589–607, Oct 1979. doi: 10.1086/130542.

A. Bieryla, K. Collins, T. G. Beatty, J. Eastman, R. J. Siverd, J. Pepper, B. S. Gaudi,

K. G. Stassun, C. Cañas, D. W. Latham, L. A. Buchhave, R. Sanchis-Ojeda, J. N. Winn, E. L. N. Jensen, J. F. Kielkopf, K. K. McLeod, J. Gregorio, K. D. Colón, R. Street, R. Ross, M. Penny, S. N. Mellon, T. E. Oberst, B. J. Fulton, J. Wang, P. Berlind, M. L. Calkins, G. A. Esquerdo, D. L. DePoy, A. Gould, J. Marshall, R. Pogge, M. Trueblood, and P. Trueblood. KELT-7b: A Hot Jupiter Transiting a Bright V = 8.54 Rapidly Rotating F-star. AJ, 150:12, July 2015. doi: 10.1088/0004-6256/150/1/12.

J. S. Bloom, D. Kasen, K. J. Shen, P. E. Nugent, N. R. Butler, M. L. Graham, D. A. Howell, U. Kolb, S. Holmes, C. A. Haswell, V. Burwitz, J. Rodriguez, and M. Sullivan. A Compact Degenerate Primary-star Progenitor of SN 2011fe. ApJ, 744:L17, January 2012. doi: 10.1088/2041-8205/744/2/L17.

W. J. Borucki, D. Koch, G. Basri, N. Batalha, T. Brown, D. Caldwell, J. Caldwell, J. Christensen-Dalsgaard, W. D. Cochran, E. DeVore, E. W. Dunham, A. K. Dupree, T. N. Gautier, J. C. Geary, R. Gilliland, A. Gould, S. B. Howell, J. M. Jenkins, Y. Kondo, D. W. Latham, G. W. Marcy, S. Meibom, H. Kjeldsen, J. J. Lissauer, D. G. Monet, D. Morrison, D. Sasselov, J. Tarter, A. Boss, D. Brownlee, T. Owen, D. Buzasi, D. Charbonneau, L. Doyle, J. Fortney, E. B. Ford, M. J. Holman, S. Seager, J. H. Steffen, W. F. Welsh, J. Rowe, H. Anderson, L. Buchhave, D. Ciardi, L. Walkowicz, W. Sherry, E. Horch, H. Isaacson, M. E. Everett, D. Fischer, G. Torres, J. A. Johnson, M. Endl, P. MacQueen, S. T. Bryson, J. Dotson, M. Haas, J. Kolodziejczak, J. Van Cleve, H. Chandrasekaran, J. D. Twicken, E. V. Quintana, B. D. Clarke, C. Allen, J. Li, H. Wu, P. Tenenbaum, E. Verner, F. Bruhweiler, J. Barnes, and A. Prsa. Kepler Planet-Detection Mission: Introduction and First Results. *Science*, 327:977, February 2010. doi: 10.1126/science.1185402.

F. Bouchy, A. S. Bonomo, A. Santerne, C. Moutou, M. Deleuil, R. F. Díaz, A. Eggenberger, D. Ehrenreich, C. Gry, T. Guillot, M. Havel, G. Hébrard, and S. Udry. SOPHIE velocimetry of Kepler transit candidates. III. KOI-423b: an 18 M_{Jup} transiting compan-

ion around an F7IV star. A&A, 533:A83, September 2011a. doi: 10.1051/0004-6361/201117095.

F. Bouchy, M. Deleuil, T. Guillot, S. Aigrain, L. Carone, W. D. Cochran, J. M. Almenara, R. Alonso, M. Auvergne, A. Baglin, P. Barge, A. S. Bonomo, P. Bordé, S. Csizmadia, K. de Bondt, H. J. Deeg, R. F. Díaz, R. Dvorak, M. Endl, A. Erikson, S. Ferraz-Mello, M. Fridlund, D. Gandolfi, J. C. Gazzano, N. Gibson, M. Gillon, E. Guenther, A. Hatzes, M. Havel, G. Hébrard, L. Jorda, A. Léger, C. Lovis, A. Llebaria, H. Lammer, P. J. MacQueen, T. Mazeh, C. Moutou, A. Ofir, M. Ollivier, H. Parviainen, M. Pätzold, D. Queloz, H. Rauer, D. Rouan, A. Santerne, J. Schneider, B. Tingley, and G. Wuchterl. Transiting exoplanets from the CoRoT space mission. XV. CoRoT-15b: a brown-dwarf transiting companion. A&A, 525:A68, January 2011b. doi: 10.1051/0004-6361/201015276.

D. M. Bramich. A new algorithm for difference image analysis. MNRAS, 386(1):L77–L81, May 2008. doi: 10.1111/j.1745-3933.2008.00464.x.

P. J. Brown, M. T. Smitka, L. Wang, A. Breeveld, M. de Pasquale, D. H. Hartmann, K. Krisciunas, N. P. M. Kuin, P. A. Milne, M. Page, and M. Siegel. Swift Ultraviolet Observations of Supernova 2014J in M82: Large Extinction from Interstellar Dust. *ArXiv e-prints*, August 2014.

T. M. Brown, D. Charbonneau, R. L. Gilliland, R. W. Noyes, and A. Burrows. Hubble Space Telescope Time-Series Photometry of the Transiting Planet of HD 209458. ApJ, 552:699–709, May 2001. doi: 10.1086/320580.

L. A. Buchhave, G. Á. Bakos, J. D. Hartman, G. Torres, G. Kovács, D. W. Latham, R. W. Noyes, G. A. Esquerdo, M. Everett, A. W. Howard, G. W. Marcy, D. A. Fischer, J. A. Johnson, J. Andersen, G. Fűrész, G. Perumpilly, D. D. Sasselov, R. P. Stefanik, B. Béky, J. Lázár, I. Papp, and P. Sári. HAT-P-16b: A 4 M_J Planet Transiting a Bright Star on an

Eccentric Orbit. ApJ, 720:1118–1125, September 2010. doi: 10.1088/0004-637X/720/2/1118.

C. J. Burke, B. S. Gaudi, D. L. DePoy, and R. W. Pogge. Survey for Transiting Extrasolar Planets in Stellar Systems. III. A Limit on the Fraction of Stars with Planets in the Open Cluster NGC 1245. AJ, 132:210–230, July 2006. doi: 10.1086/504468.

A. Burrows, M. Marley, W. B. Hubbard, J. I. Lunine, T. Guillot, D. Saumon, R. Freedman, D. Sudarsky, and C. Sharp. A Nongray Theory of Extrasolar Giant Planets and Brown Dwarfs. ApJ, 491:856–875, December 1997. doi: 10.1086/305002.

A. Burrows, L. Ibgui, and I. Hubeny. Optical Albedo Theory of Strongly Irradiated Giant Planets: The Case of HD 209458b. ApJ, 682:1277–1282, August 2008. doi: 10.1086/589824.

O. W. Butters, R. G. West, D. R. Anderson, A. Collier Cameron, W. I. Clarkson, B. Enoch, C. A. Haswell, C. Hellier, K. Horne, Y. Joshi, S. R. Kane, T. A. Lister, P. F. L. Maxted, N. Parley, D. Pollacco, B. Smalley, R. A. Street, I. Todd, P. J. Wheatley, and D. M. Wilson. The first WASP public data release. A&A, 520:L10, September 2010. doi: 10.1051/0004-6361/201015655.

J. A. Carter and J. N. Winn. Parameter Estimation from Time-series Data with Correlated Errors: A Wavelet-based Method and its Application to Transit Light Curves. ApJ, 704:51–67, October 2009. doi: 10.1088/0004-637X/704/1/51.

J. A. Carter and J. N. Winn. Empirical Constraints on the Oblateness of an Exoplanet. ApJ, 709:1219–1229, February 2010. doi: 10.1088/0004-637X/709/2/1219.

J. A. Carter, J. N. Winn, M. J. Holman, D. Fabrycky, Z. K. Berta, C. J. Burke, and P. Nutzman. The Transit Light Curve Project. XIII. Sixteen Transits of the Super-Earth GJ 1214b. ApJ, 730:82, April 2011. doi: 10.1088/0004-637X/730/2/82.

L. Casagrande, I. Ramírez, J. Meléndez, M. Bessell, and M. Asplund. An absolutely calibrated T_{eff} scale from the infrared flux method. Dwarfs and subgiants. A&A, 512:A54, March 2010. doi: 10.1051/0004-6361/200913204.

D. Charbonneau, T. M. Brown, R. W. Noyes, and R. L. Gilliland. Detection of an Extrasolar Planet Atmosphere. ApJ, 568:377–384, March 2002. doi: 10.1086/338770.

D. Charbonneau, L. E. Allen, S. T. Megeath, G. Torres, R. Alonso, T. M. Brown, R. L. Gilliland, D. W. Latham, G. Mandushev, F. T. O'Donovan, and A. Sozzetti. Detection of Thermal Emission from an Extrasolar Planet. ApJ, 626:523–529, June 2005. doi: 10.1086/429991.

D. R. Ciardi, C. A. Beichman, E. P. Horch, and S. B. Howell. Understanding the Effects of Stellar Multiplicity on the Derived Planet Radii from Transit Surveys: Implications for Kepler, K2, and TESS. ApJ, 805:16, May 2015. doi: 10.1088/0004-637X/805/1/16.

A. Claret. A new non-linear limb-darkening law for LTE stellar atmosphere models III. Sloan filters: Calculations for -5.0 $\leq$ log [M/H] $\leq$ +1, 2000 K $\leq$ T_{eff} $\leq$ 50 000 K at several surface gravities. A&A, 428:1001–1005, December 2004. doi: 10.1051/0004-6361:20041673.

A. Claret and S. Bloemen. Gravity and limb-darkening coefficients for the Kepler, CoRoT, Spitzer, uvby, UBVRIJHK, and Sloan photometric systems. A&A, 529:A75, May 2011. doi: 10.1051/0004-6361/201116451.

B. Coşkunoğlu, S. Ak, S. Bilir, S. Karaali, E. Yaz, G. Gilmore, G. M. Seabroke, O. Bienaymé, J. Bland-Hawthorn, R. Campbell, K. C. Freeman, B. Gibson, E. K. Grebel, U. Munari, J. F. Navarro, Q. A. Parker, A. Siebert, A. Siviero, M. Steinmetz, F. G. Watson, R. F. G. Wyse, and T. Zwitter. Local stellar kinematics from RAVE data - I. Local standard of rest. MNRAS, 412:1237–1245, April 2011a. doi: 10.1111/j.1365-2966.2010.17983.x.

B. Coşkunoğlu, S. Ak, S. Bilir, S. Karaali, E. Yaz, G. Gilmore, G. M. Seabroke, O. Bienaymé, J. Bland-Hawthorn, R. Campbell, K. C. Freeman, B. Gibson, E. K. Grebel, U. Munari, J. F. Navarro, Q. A. Parker, A. Siebert, A. Siviero, M. Steinmetz, F. G. Watson, R. F. G. Wyse, and T. Zwitter. Local stellar kinematics from RAVE data - I. Local standard of rest. MNRAS, 412:1237–1245, April 2011b. doi: 10.1111/j.1365-2966.2010.17983.x.

A. M. Cody and D. D. Sasselov. HD 209458: Physical Parameters of the Parent Star and the Transiting Planet. ApJ, 569:451–458, April 2002. doi: 10.1086/339281.

M. Cohen, W. A. Wheaton, and S. T. Megeath. Spectral Irradiance Calibration in the Infrared. XIV. The Absolute Calibration of 2MASS. AJ, 126:1090–1096, August 2003. doi: 10.1086/376474.

A. Collier Cameron, F. Bouchy, G. Hébrard, P. Maxted, D. Pollacco, F. Pont, I. Skillen, B. Smalley, R. A. Street, R. G. West, D. M. Wilson, S. Aigrain, D. J. Christian, W. I. Clarkson, B. Enoch, A. Evans, A. Fitzsimmons, M. Fleenor, M. Gillon, C. A. Haswell, L. Hebb, C. Hellier, S. T. Hodgkin, K. Horne, J. Irwin, S. R. Kane, F. P. Keenan, B. Loeillet, T. A. Lister, M. Mayor, C. Moutou, A. J. Norton, J. Osborne, N. Parley, D. Queloz, R. Ryans, A. H. M. J. Triaud, S. Udry, and P. J. Wheatley. WASP-1b and WASP-2b: two new transiting exoplanets detected with SuperWASP and SOPHIE. MNRAS, 375:951–957, March 2007a. doi: 10.1111/j.1365-2966.2006.11350.x.

A. Collier Cameron, F. Bouchy, G. Hébrard, P. Maxted, D. Pollacco, F. Pont, I. Skillen, B. Smalley, R. A. Street, R. G. West, D. M. Wilson, S. Aigrain, D. J. Christian, W. I. Clarkson, B. Enoch, A. Evans, A. Fitzsimmons, M. Fleenor, M. Gillon, C. A. Haswell, L. Hebb, C. Hellier, S. T. Hodgkin, K. Horne, J. Irwin, S. R. Kane, F. P. Keenan, B. Loeillet, T. A. Lister, M. Mayor, C. Moutou, A. J. Norton, J. Osborne, N. Parley, D. Queloz, R. Ryans, A. H. M. J. Triaud, S. Udry, and P. J. Wheatley. WASP-1b and WASP-2b:

two new transiting exoplanets detected with SuperWASP and SOPHIE. MNRAS, 375: 951–957, March 2007b. doi: 10.1111/j.1365-2966.2006.11350.x.

A. Collier Cameron, D. M. Wilson, R. G. West, L. Hebb, X.-B. Wang, S. Aigrain, F. Bouchy, D. J. Christian, W. I. Clarkson, B. Enoch, M. Esposito, E. Guenther, C. A. Haswell, G. Hébrard, C. Hellier, K. Horne, J. Irwin, S. R. Kane, B. Loeillet, T. A. Lister, P. Maxted, M. Mayor, C. Moutou, N. Parley, D. Pollacco, F. Pont, D. Queloz, R. Ryans, I. Skillen, R. A. Street, S. Udry, and P. J. Wheatley. Efficient identification of exoplanetary transit candidates from SuperWASP light curves. MNRAS, 380:1230–1244, September 2007c. doi: 10.1111/j.1365-2966.2007.12195.x.

A. Collier Cameron, E. Guenther, B. Smalley, I. McDonald, L. Hebb, J. Andersen, T. Augusteijn, S. C. C. Barros, D. J. A. Brown, W. D. Cochran, M. Endl, S. J. Fossey, M. Hartmann, P. F. L. Maxted, D. Pollacco, I. Skillen, J. Telting, I. P. Waldmann, and R. G. West. Line-profile tomography of exoplanet transits - II. A gas-giant planet transiting a rapidly rotating A5 star. MNRAS, 407:507–514, September 2010a. doi: 10.1111/j.1365-2966.2010.16922.x.

A. Collier Cameron, E. Guenther, B. Smalley, I. McDonald, L. Hebb, J. Andersen, T. Augusteijn, S. C. C. Barros, D. J. A. Brown, W. D. Cochran, M. Endl, S. J. Fossey, M. Hartmann, P. F. L. Maxted, D. Pollacco, I. Skillen, J. Telting, I. P. Waldmann, and R. G. West. Line-profile tomography of exoplanet transits - II. A gas-giant planet transiting a rapidly rotating A5 star. MNRAS, 407:507–514, September 2010b. doi: 10.1111/j.1365-2966.2010.16922.x.

K. A. Collins, J. F. Kielkopf, K. G. Stassun, and F. V. Hessman. AstroImageJ: Image Processing and Photometric Extraction for Ultra-precise Astronomical Light Curves. AJ, 153:77, February 2017. doi: 10.3847/1538-3881/153/2/77.

N. B. Cowan, P. Machalek, B. Croll, L. M. Shekhtman, A. Burrows, D. Deming, T. Greene,

and J. L. Hora. Thermal Phase Variations of WASP-12b: Defying Predictions. ApJ, 747: 82, March 2012. doi: 10.1088/0004-637X/747/1/82.

A. N. Cox. *Allen's astrophysical quantities*. The Athlone Press, Ltd., 2000.

A. Cumming, R. P. Butler, G. W. Marcy, S. S. Vogt, J. T. Wright, and D. A. Fischer. The Keck Planet Search: Detectability and the Minimum Mass and Orbital Period Distribution of Extrasolar Planets. PASP, 120:531, May 2008. doi: 10.1086/588487.

R. M. Cutri and et al. VizieR Online Data Catalog: WISE All-Sky Data Release (Cutri+ 2012). *VizieR Online Data Catalog*, 2311, 2012a.

R. M. Cutri and et al. VizieR Online Data Catalog: WISE All-Sky Data Release (Cutri+ 2012). *VizieR Online Data Catalog*, 2311, April 2012b.

R. M. Cutri and et al. VizieR Online Data Catalog: AllWISE Data Release (Cutri+ 2013). *VizieR Online Data Catalog*, 2328, November 2013.

R. M. Cutri, M. F. Skrutskie, S. van Dyk, C. A. Beichman, J. M. Carpenter, T. Chester, L. Cambresy, T. Evans, J. Fowler, J. Gizis, E. Howard, J. Huchra, T. Jarrett, E. L. Kopan, J. D. Kirkpatrick, R. M. Light, K. A. Marsh, H. McCallon, S. Schneider, R. Stiening, M. Sykes, M. Weinberg, W. A. Wheaton, S. Wheelock, and N. Zacarias. VizieR Online Data Catalog: 2MASS All-Sky Catalog of Point Sources (Cutri+ 2003). *VizieR Online Data Catalog*, 2246, June 2003a.

R. M. Cutri, M. F. Skrutskie, S. van Dyk, C. A. Beichman, J. M. Carpenter, T. Chester, L. Cambresy, T. Evans, J. Fowler, J. Gizis, E. Howard, J. Huchra, T. Jarrett, E. L. Kopan, J. D. Kirkpatrick, R. M. Light, K. A. Marsh, H. McCallon, S. Schneider, R. Stiening, M. Sykes, M. Weinberg, W. A. Wheaton, S. Wheelock, and N. Zacarias. VizieR Online Data Catalog: 2MASS All-Sky Catalog of Point Sources (Cutri+ 2003). *VizieR Online Data Catalog*, 2246:0, June 2003b.

S. Daemgen, F. Hormuth, W. Brandner, C. Bergfors, M. Janson, S. Hippler, and T. Henning. Binarity of transit host stars. Implications for planetary parameters. A&A, 498(2):567–574, May 2009. doi: 10.1051/0004-6361/200810988.

J. J. Dalcanton, B. F. Williams, A. C. Seth, A. Dolphin, J. Holtzman, K. Rosema, E. D. Skillman, A. Cole, L. Girardi, S. M. Gogarten, I. D. Karachentsev, K. Olsen, D. Weisz, C. Christensen, K. Freeman, K. Gilbert, C. Gallart, J. Harris, P. Hodge, R. S. de Jong, V. Karachentseva, M. Mateo, P. B. Stetson, M. Tavarez, D. Zaritsky, F. Governato, and T. Quinn. The ACS Nearby Galaxy Survey Treasury. ApJS, 183:67–108, July 2009. doi: 10.1088/0067-0049/183/1/67.

G. H. Darwin. The determination of the secular effects of tidal friction by a graphical method. *Proceedings of the Royal Society of London*, 29:168–181, 1879. ISSN 03701662. URL http://www.jstor.org/stable/113751.

H. J. Deeg, C. Moutou, A. Erikson, S. Csizmadia, B. Tingley, P. Barge, H. Bruntt, M. Havel, S. Aigrain, J. M. Almenara, R. Alonso, M. Auvergne, A. Baglin, M. Barbieri, W. Benz, A. S. Bonomo, P. Bordé, F. Bouchy, J. Cabrera, L. Carone, S. Carpano, D. Ciardi, M. Deleuil, R. Dvorak, S. Ferraz-Mello, M. Fridlund, D. Gandolfi, J.-C. Gazzano, M. Gillon, P. Gondoin, E. Guenther, T. Guillot, R. D. Hartog, A. Hatzes, M. Hidas, G. Hébrard, L. Jorda, P. Kabath, H. Lammer, A. Léger, T. Lister, A. Llebaria, C. Lovis, M. Mayor, T. Mazeh, M. Ollivier, M. Pätzold, F. Pepe, F. Pont, D. Queloz, M. Rabus, H. Rauer, D. Rouan, B. Samuel, J. Schneider, A. Shporer, B. Stecklum, R. Street, S. Udry, J. Weingrill, and G. Wuchterl. A transiting giant planet with a temperature between 250K and 430K. Nature, 464:384–387, March 2010. doi: 10.1038/nature08856.

M. Deleuil, H. J. Deeg, R. Alonso, F. Bouchy, D. Rouan, M. Auvergne, A. Baglin, S. Aigrain, J. M. Almenara, M. Barbieri, P. Barge, H. Bruntt, P. Bordé, A. Collier Cameron, S. Csizmadia, R. de La Reza, R. Dvorak, A. Erikson, M. Fridlund, D. Gandolfi, M. Gillon, E. Guenther, T. Guillot, A. Hatzes, G. Hébrard, L. Jorda, H. Lam-

mer, A. Léger, A. Llebaria, B. Loeillet, M. Mayor, T. Mazeh, C. Moutou, M. Ollivier, M. Pätzold, F. Pont, D. Queloz, H. Rauer, J. Schneider, A. Shporer, G. Wuchterl, and S. Zucker. Transiting exoplanets from the CoRoT space mission . VI. CoRoT-Exo-3b: the first secure inhabitant of the brown-dwarf desert. A&A, 491:889–897, December 2008. doi: 10.1051/0004-6361:200810625.

P. Demarque, J.-H. Woo, Y.-C. Kim, and S. K. Yi. Y^2 Isochrones with an Improved Core Overshoot Treatment. ApJS, 155:667–674, December 2004a. doi: 10.1086/424966.

P. Demarque, J.-H. Woo, Y.-C. Kim, and S. K. Yi. Y^2 Isochrones with an Improved Core Overshoot Treatment. ApJS, 155:667–674, December 2004b. doi: 10.1086/424966.

D. Deming, S. Seager, L. J. Richardson, and J. Harrington. Infrared radiation from an extrasolar planet. Nature, 434:740–743, March 2005. doi: 10.1038/nature03507.

B.-O. Demory and S. Seager. Lack of Inflated Radii for Kepler Giant Planet Candidates Receiving Modest Stellar Irradiation. ApJS, 197:12, November 2011. doi: 10.1088/0067-0049/197/1/12.

J. Devor. Solutions for 10,000 Eclipsing Binaries in the Bulge Fields of OGLE II Using DEBiL. ApJ, 628:411–425, July 2005. doi: 10.1086/431170.

S. Dhital, A. A. West, K. G. Stassun, and J. J. Bochanski. Sloan Low-mass Wide Pairs of Kinematically Equivalent Stars (SLoWPoKES): A Catalog of Very Wide, Low-mass Pairs. AJ, 139:2566–2586, June 2010. doi: 10.1088/0004-6256/139/6/2566.

S. E. Dodson-Robinson, D. Veras, E. B. Ford, and C. A. Beichman. The Formation Mechanism of Gas Giants on Wide Orbits. ApJ, 707:79–88, December 2009. doi: 10.1088/0004-637X/707/1/79.

J.-F. Donati, M. Semel, B. D. Carter, D. E. Rees, and A. Collier Cameron. Spec-

tropolarimetric observations of active stars. MNRAS, 291:658, November 1997. doi: 10.1093/mnras/291.4.658.

L. R. Doyle, J. A. Carter, D. C. Fabrycky, R. W. Slawson, S. B. Howell, J. N. Winn, J. A. Orosz, A. Přsa, W. F. Welsh, S. N. Quinn, D. Latham, G. Torres, L. A. Buchhave, G. W. Marcy, J. J. Fortney, A. Shporer, E. B. Ford, J. J. Lissauer, D. Ragozzine, M. Rucker, N. Batalha, J. M. Jenkins, W. J. Borucki, D. Koch, C. K. Middour, J. R. Hall, S. McCauliff, M. N. Fanelli, E. V. Quintana, M. J. Holman, D. A. Caldwell, M. Still, R. P. Stefanik, W. R. Brown, G. A. Esquerdo, S. Tang, G. Furesz, J. C. Geary, P. Berlind, M. L. Calkins, D. R. Short, J. H. Steffen, D. Sasselov, E. W. Dunham, W. D. Cochran, A. Boss, M. R. Haas, D. Buzasi, and D. Fischer. Kepler-16: A Transiting Circumbinary Planet. *Science*, 333:1602, September 2011. doi: 10.1126/science.1210923.

J. Eastman, R. Siverd, and B. S. Gaudi. Achieving Better Than 1 Minute Accuracy in the Heliocentric and Barycentric Julian Dates. PASP, 122:935–946, August 2010. doi: 10.1086/655938.

J. Eastman, B. S. Gaudi, and E. Agol. EXOFAST: A Fast Exoplanetary Fitting Suite in IDL. PASP, 125:83–112, January 2013. doi: 10.1086/669497.

D. Fabrycky and S. Tremaine. Shrinking Binary and Planetary Orbits by Kozai Cycles with Tidal Friction. ApJ, 669:1298–1315, November 2007. doi: 10.1086/521702.

S. Faigler and T. Mazeh. Photometric detection of non-transiting short-period low-mass companions through the beaming, ellipsoidal and reflection effects in Kepler and CoRoT light curves. MNRAS, 415:3921–3928, August 2011. doi: 10.1111/j.1365-2966.2011.19011.x.

G. Fűrész. *Design and Application of High Resolution and Multiobject Spectrographs: Dynamical Studies of Open Clusters*. PhD thesis, University of Szeged, September 2008.

E. L. Fitzpatrick. Correcting for the Effects of Interstellar Extinction. PASP, 111:63–75, January 1999. doi: 10.1086/316293.

S. W. Fleming, J. Ge, R. Barnes, T. G. Beatty, J. R. Crepp, N. De Lee, M. Esposito, B. Femenia, L. Ferreira, B. Gary, B. S. Gaudi, L. Ghezzi, J. I. González Hernández, L. Hebb, P. Jiang, B. Lee, B. Nelson, G. F. Porto de Mello, B. J. Shappee, K. Stassun, T. A. Thompson, B. M. Tofflemire, J. P. Wisniewski, W. M. Wood-Vasey, E. Agol, C. Allende Prieto, D. Bizyaev, H. Brewington, P. A. Cargile, L. Coban, K. S. Costello, L. N. da Costa, M. L. Good, N. Hua, S. R. Kane, G. R. Lander, J. Liu, B. Ma, S. Mahadevan, M. A. G. Maia, E. Malanushenko, V. Malanushenko, D. Muna, D. C. Nguyen, D. Oravetz, M. Paegert, K. Pan, J. Pepper, R. Rebolo, E. J. Roebuck, B. X. Santiago, D. P. Schneider, A. Shelden, A. Simmons, T. Sivarani, S. Snedden, C. L. M. Vincent, X. Wan, J. Wang, B. A. Weaver, G. M. Weaver, and B. Zhao. Very Low Mass Stellar and Substellar Companions to Solar-like Stars from MARVELS. II. A Short-period Companion Orbiting an F Star with Evidence of a Stellar Tertiary and Significant Mutual Inclination. AJ, 144:72, September 2012. doi: 10.1088/0004-6256/144/3/72.

R. J. Foley, O. Fox, C. McCully, M. M. Phillips, D. J. Sand, W. Zheng, P. Challis, A. V. Filippenko, G. Folatelli, W. Hillebrandt, E. Y. Hsiao, S. W. Jha, R. P. Kirshner, M. Kromer, G. H. Marion, M. Nelson, R. Pakmor, G. Pignata, F. K. Roepke, I. R. Seitenzahl, J. M. Silverman, M. Skrutskie, and M. D. Stritzinger. Extensive HST Ultraviolet Spectra and Multi-wavelength Observations of SN 2014J in M82 Indicate Reddening and Circumstellar Scattering by Typical Dust. *ArXiv e-prints*, May 2014.

E. B. Ford and B. S. Gaudi. Observational Constraints on Trojans of Transiting Extrasolar Planets. ApJ, 652:L137–L140, December 2006. doi: 10.1086/510235.

E. B. Ford and M. J. Holman. Using Transit Timing Observations to Search for Trojans of Transiting Extrasolar Planets. ApJ, 664:L51–L54, July 2007. doi: 10.1086/520579.

J. J. Fortney and N. Nettelmann. The Interior Structure, Composition, and Evolution of Giant Planets. Space Sci. Rev., 152:423–447, May 2010. doi: 10.1007/s11214-009-9582-x.

J. J. Fortney, M. S. Marley, and J. W. Barnes. Planetary Radii across Five Orders of Magnitude in Mass and Stellar Insolation: Application to Transits. ApJ, 659:1661–1672, April 2007a. doi: 10.1086/512120.

J. J. Fortney, M. S. Marley, and J. W. Barnes. Erratum: "Planetary Radii across Five Orders of Magnitude in Mass and Stellar Insolation: Application to Transits" (¡A href="/abs/2007ApJ...659.1661F"¿ApJ, 659, 1661 [2007]¡/A¿). ApJ, 668:1267–1267, October 2007b. doi: 10.1086/521435.

F. Fressin, T. Guillot, and L. Nesta. Interpreting the yield of transit surveys: are there groups in the known transiting planets population? A&A, 504:605–615, September 2009. doi: 10.1051/0004-6361/200810097.

F. Fressin, G. Torres, J. F. Rowe, D. Charbonneau, L. A. Rogers, S. Ballard, N. M. Batalha, W. J. Borucki, S. T. Bryson, L. A. Buchhave, D. R. Ciardi, J.-M. Désert, C. D. Dressing, D. C. Fabrycky, E. B. Ford, T. N. Gautier, III, C. E. Henze, M. J. Holman, A. Howard, S. B. Howell, J. M. Jenkins, D. G. Koch, D. W. Latham, J. J. Lissauer, G. W. Marcy, S. N. Quinn, D. Ragozzine, D. D. Sasselov, S. Seager, T. Barclay, F. Mullally, S. E. Seader, M. Still, J. D. Twicken, S. E. Thompson, and K. Uddin. Two Earth-sized planets orbiting Kepler-20. Nature, 482:195–198, February 2012. doi: 10.1038/nature10780.

M. Fukugita, T. Ichikawa, J. E. Gunn, M. Doi, K. Shimasaku, and D. P. Schneider. The Sloan Digital Sky Survey Photometric System. AJ, 111:1748, April 1996. doi: 10.1086/117915.

B. J. Fulton, A. Shporer, J. N. Winn, M. J. Holman, A. Pál, and J. Z. Gazak. Long-term

Transit Timing Monitoring and Refined Light Curve Parameters of HAT-P-13b. AJ, 142: 84, September 2011. doi: 10.1088/0004-6256/142/3/84.

B. J. Fulton, K. A. Collins, B. S. Gaudi, K. G. Stassun, J. Pepper, T. G. Beatty, R. J. Siverd, K. Penev, A. W. Howard, C. Baranec, G. Corfini, J. D. Eastman, J. Gregorio, N. M. Law, M. B. Lund, T. E. Oberst, M. T. Penny, R. Riddle, J. E. Rodriguez, D. J. Stevens, R. Zambelli, C. Ziegler, A. Bieryla, G. D'Ago, D. L. DePoy, E. L. N. Jensen, J. F. Kielkopf, D. W. Latham, M. Manner, J. Marshall, K. K. McLeod, and P. A. Reed. KELT-8b: A Highly Inflated Transiting Hot Jupiter and a New Technique for Extracting High-precision Radial Velocities from Noisy Spectra. ApJ, 810:30, September 2015. doi: 10.1088/0004-637X/810/1/30.

E. Furlan, D. R. Ciardi, M. E. Everett, M. Saylors, J. K. Teske, E. P. Horch, S. B. Howell, G. T. van Belle, L. A. Hirsch, T. N. Gautier, III, E. R. Adams, D. Barrado, K. M. S. Cartier, C. D. Dressing, A. K. Dupree, R. L. Gilliland, J. Lillo-Box, P. W. Lucas, and J. Wang. The Kepler Follow-up Observation Program. I. A Catalog of Companions to Kepler Stars from High-Resolution Imaging. AJ, 153:71, February 2017. doi: 10.3847/1538-3881/153/2/71.

Gaia Collaboration, A. G. A. Brown, A. Vallenari, T. Prusti, J. de Bruijne, F. Mignard, R. Drimmel, and 5. co-authors. Gaia Data Release 1. Summary of the astrometric, photometric, and survey properties. *ArXiv e-prints*, September 2016.

B. S. Gaudi and J. N. Winn. Prospects for the Characterization and Confirmation of Transiting Exoplanets via the Rossiter-McLaughlin Effect. ApJ, 655:550–563, January 2007. doi: 10.1086/509910.

B. S. Gaudi, S. Seager, and G. Mallen-Ornelas. On the Period Distribution of Close-in Extrasolar Giant Planets. ApJ, 623:472–481, April 2005. doi: 10.1086/428478.

B. S. Gaudi, K. G. Stassun, K. A. Collins, T. G. Beatty, G. Zhou, D. W. Latham, A. Bieryla,

J. D. Eastman, R. J. Siverd, J. R. Crepp, E. J. Gonzales, D. J. Stevens, L. A. Buchhave, J. Pepper, M. C. Johnson, K. D. Colon, E. L. N. Jensen, J. E. Rodriguez, V. Bozza, S. C. Novati, G. D'Ago, M. T. Dumont, T. Ellis, C. Gaillard, H. Jang-Condell, D. H. Kasper, A. Fukui, J. Gregorio, A. Ito, J. F. Kielkopf, M. Manner, K. Matt, N. Narita, T. E. Oberst, P. A. Reed, G. Scarpetta, D. C. Stephens, R. R. Yeigh, R. Zambelli, B. J. Fulton, A. W. Howard, D. J. James, M. Penny, D. Bayliss, I. A. Curtis, D. L. Depoy, G. A. Esquerdo, A. Gould, M. D. Joner, R. B. Kuhn, J. Labadie-Bartz, M. B. Lund, J. L. Marshall, K. K. McLeod, R. W. Pogge, H. Relles, C. Stockdale, T. G. Tan, M. Trueblood, and P. Trueblood. A giant planet undergoing extreme-ultraviolet irradiation by its hot massive-star host. Nature, 546:514–518, June 2017a. doi: 10.1038/nature22392.

B. Scott Gaudi, Keivan G. Stassun, Karen A. Collins, Thomas G. Beatty, George Zhou, David W. Latham, Allyson Bieryla, Jason D. Eastman, Robert J. Siverd, and Justin R. Crepp. A giant planet undergoing extreme-ultraviolet irradiation by its hot massive-star host. Nature, 546(7659):514–518, Jun 2017b. doi: 10.1038/nature22392.

A. M. Ghez, S. Salim, N. N. Weinberg, J. R. Lu, T. Do, J. K. Dunn, K. Matthews, M. R. Morris, S. Yelda, E. E. Becklin, T. Kremenek, M. Milosavljevic, and J. Naiman. Measuring Distance and Properties of the Milky Way's Central Supermassive Black Hole with Stellar Orbits. ApJ, 689:1044–1062, December 2008. doi: 10.1086/592738.

Y. Gómez Maqueo Chew, K. G. Stassun, A. Prša, and R. D. Mathieu. Near-infrared Light Curves of the Brown Dwarf Eclipsing Binary 2MASS J05352184-0546085: Can Spots Explain the Temperature Reversal? ApJ, 699:1196–1208, July 2009. doi: 10.1088/0004-637X/699/2/1196.

A. Goobar, J. Johansson, R. Amanullah, Y. Cao, D. A. Perley, M. M. Kasliwal, R. Ferretti, P. E. Nugent, C. Harris, A. Gal-Yam, E. O. Ofek, S. P. Tendulkar, M. Dennefeld, S. Valenti, I. Arcavi, D. P. K. Banerjee, V. Venkataraman, V. Joshi, N. M. Ashok, S. B. Cenko, R. F. Diaz, C. Fremling, A. Horesh, D. A. Howell, S. R. Kulkarni, S. Papado-

giannakis, T. Petrushevska, D. Sand, J. Sollerman, V. Stanishev, J. S. Bloom, J. Surace, T. J. Dupuy, and M. C. Liu. The Rise of SN 2014J in the Nearby Galaxy M82. ApJ, 784: L12, March 2014a. doi: 10.1088/2041-8205/784/1/L12.

A. Goobar, M. Kromer, R. Siverd, K. G. Stassun, J. Pepper, R. Amanullah, M. Kasliwal, J. Sollerman, and F. Taddia. Constraints on the origin of the first light from SN2014J. *ArXiv e-prints*, October 2014b.

A. Goobar, M. Kromer, R. Siverd, K. G. Stassun, J. Pepper, R. Amanullah, M. Kasliwal, J. Sollerman, and F. Taddia. Constraints on the Origin of the First Light from SN 2014J. ApJ, 799:106, January 2015. doi: 10.1088/0004-637X/799/1/106.

A. Gould and C. W. Morgan. Transit Target Selection Using Reduced Proper Motions. ApJ, 585:1056–1061, March 2003. doi: 10.1086/346131.

S. Grenier, R. Burnage, R. Faraggiana, M. Gerbaldi, F. Delmas, A. E. Gómez, V. Sabas, and L. Sharif. Radial velocities of HIPPARCOS southern B8-F2 type stars. A&AS, 135: 503–509, March 1999. doi: 10.1051/aas:1999186.

D. Grether and C. H. Lineweaver. How Dry is the Brown Dwarf Desert? Quantifying the Relative Number of Planets, Brown Dwarfs, and Stellar Companions around Nearby Sun-like Stars. ApJ, 640:1051–1062, April 2006. doi: 10.1086/500161.

D. B. Guenther, P. Demarque, Y.-C. Kim, and M. H. Pinsonneault. Standard solar model. ApJ, 387:372–393, March 1992. doi: 10.1086/171090.

T. Guillot. THE INTERIORS OF GIANT PLANETS: Models and Outstanding Questions. *Annual Review of Earth and Planetary Sciences*, 33:493–530, January 2005. doi: 10.1146/annurev.earth.32.101802.120325.

B. M. S. Hansen. Calibration of Equilibrium Tide Theory for Extrasolar Planet Systems. ApJ, 723:285–299, November 2010. doi: 10.1088/0004-637X/723/1/285.

B. M. S. Hansen and T. Barman. Two Classes of Hot Jupiters. ApJ, 671:861–871, December 2007. doi: 10.1086/523038.

J. D. Hartman and G. Á. Bakos. VARTOOLS: A program for analyzing astronomical time-series data. *Astronomy and Computing*, 17:1–72, October 2016. doi: 10.1016/j.ascom.2016.05.006.

J. D. Hartman, G. Bakos, K. Z. Stanek, and R. W. Noyes. HATNET Variability Survey in the High Stellar Density "Kepler Field" with Millimagnitude Image Subtraction Photometry. AJ, 128:1761–1783, October 2004. doi: 10.1086/423920.

J. D. Hartman, B. S. Gaudi, M. J. Holman, B. A. McLeod, K. Z. Stanek, J. A. Barranco, M. H. Pinsonneault, and J. S. Kalirai. Deep MMT Transit Survey of the Open Cluster M37. II. Variable Stars. ApJ, 675:1254–1277, March 2008. doi: 10.1086/527460.

J. D. Hartman, B. S. Gaudi, M. J. Holman, B. A. McLeod, K. Z. Stanek, J. A. Barranco, M. H. Pinsonneault, S. Meibom, and J. S. Kalirai. Deep MMT Transit Survey of the Open Cluster M37 IV: Limit on the Fraction of Stars with Planets as Small as $0.3R_J$. ApJ, 695:336–356, April 2009. doi: 10.1088/0004-637X/695/1/336.

J. D. Hartman, G. Á. Bakos, B. Sato, G. Torres, R. W. Noyes, D. W. Latham, G. Kovács, D. A. Fischer, A. W. Howard, J. A. Johnson, G. W. Marcy, L. A. Buchhave, G. Füresz, G. Perumpilly, B. Béky, R. P. Stefanik, D. D. Sasselov, G. A. Esquerdo, M. Everett, Z. Csubry, J. Lázár, I. Papp, and P. Sári. HAT-P-18b and HAT-P-19b: Two Low-density Saturn-mass Planets Transiting Metal-rich K Stars. ApJ, 726:52, January 2011. doi: 10.1088/0004-637X/726/1/52.

J. D. Hartman, G. Á. Bakos, L. A. Buchhave, G. Torres, D. W. Latham, G. Kovács, W. Bhatti, Z. Csubry, M. de Val-Borro, K. Penev, C. X. Huang, B. Béky, A. Bieryla, S. N. Quinn, A. W. Howard, G. W. Marcy, J. A. Johnson, H. Isaacson, D. A. Fischer, R. W. Noyes, E. Falco, G. A. Esquerdo, R. P. Knox, P. Hinz, J. Lázár, I. Papp, and

P. Sári. HAT-P-57b: A Short-period Giant Planet Transiting a Bright Rapidly Rotating A8V Star Confirmed Via Doppler Tomography. AJ, 150:197, December 2015. doi: 10.1088/0004-6256/150/6/197.

P. H. Hauschildt, F. Allard, and E. Baron. The NextGen Model Atmosphere Grid for $3000 \leq T_{eff} \leq$10,000 K. ApJ, 512:377–385, February 1999. doi: 10.1086/306745.

T. L. Hayward, B. Brandl, B. Pirger, C. Blacken, G. E. Gull, J. Schoenwald, and J. R. Houck. PHARO: A Near-Infrared Camera for the Palomar Adaptive Optics System. PASP, 113:105–118, January 2001. doi: 10.1086/317969.

C. Hellier, D. R. Anderson, A. Collier Cameron, M. Gillon, L. Hebb, P. F. L. Maxted, D. Queloz, B. Smalley, A. H. M. J. Triaud, R. G. West, D. M. Wilson, S. J. Bentley, B. Enoch, K. Horne, J. Irwin, T. A. Lister, M. Mayor, N. Parley, F. Pepe, D. L. Pollacco, D. Segransan, S. Udry, and P. J. Wheatley. An orbital period of 0.94days for the hot-Jupiter planet WASP-18b. Nature, 460:1098–1100, August 2009. doi: 10.1038/nature08245.

A. A. Henden, S. Levine, D. Terrell, and D. L. Welch. APASS - The Latest Data Release. In *American Astronomical Society Meeting Abstracts*, volume 225 of *American Astronomical Society Meeting Abstracts*, page 336.16, January 2015.

E. Hog, A. Kuzmin, U. Bastian, C. Fabricius, K. Kuimov, L. Lindegren, V. V. Makarov, and S. Roeser. The TYCHO Reference Catalogue. A&A, 335:L65–L68, July 1998.

E. Høg, C. Fabricius, V. V. Makarov, S. Urban, T. Corbin, G. Wycoff, U. Bastian, P. Schwekendiek, and A. Wicenec. The Tycho-2 catalogue of the 2.5 million brightest stars. A&A, 355:L27–L30, March 2000.

M. Holman, J. Touma, and S. Tremaine. Chaotic variations in the eccentricity of the planet orbiting 16 Cygni B. Nature, 386:254–256, March 1997. doi: 10.1038/386254a0.

M. J. Holman and N. W. Murray. The Use of Transit Timing to Detect Terrestrial-Mass Extrasolar Planets. *Science*, 307:1288–1291, February 2005. doi: 10.1126/science.1107822.

M. J. Holman, D. C. Fabrycky, D. Ragozzine, E. B. Ford, J. H. Steffen, W. F. Welsh, J. J. Lissauer, D. W. Latham, G. W. Marcy, L. M. Walkowicz, N. M. Batalha, J. M. Jenkins, J. F. Rowe, W. D. Cochran, F. Fressin, G. Torres, L. A. Buchhave, D. D. Sasselov, W. J. Borucki, D. G. Koch, G. Basri, T. M. Brown, D. A. Caldwell, D. Charbonneau, E. W. Dunham, T. N. Gautier, J. C. Geary, R. L. Gilliland, M. R. Haas, S. B. Howell, D. R. Ciardi, M. Endl, D. Fischer, G. Fürész, J. D. Hartman, H. Isaacson, J. A. Johnson, P. J. MacQueen, A. V. Moorhead, R. C. Morehead, and J. A. Orosz. Kepler-9: A System of Multiple Planets Transiting a Sun-Like Star, Confirmed by Timing Variations. *Science*, 330:51, October 2010. doi: 10.1126/science.1195778.

S. Hoyer, E. Pallé, D. Dragomir, and F. Murgas. Ruling out the Orbital Decay of the WASP-43b Exoplanet. AJ, 151:137, June 2016. doi: 10.3847/0004-6256/151/6/137.

E. Y. Hsiao, A. Conley, D. A. Howell, M. Sullivan, C. J. Pritchet, R. G. Carlberg, P. E. Nugent, and M. M. Phillips. K-Corrections and Spectral Templates of Type Ia Supernovae. ApJ, 663:1187–1200, July 2007. doi: 10.1086/518232.

P. J. Huber. *Robust statistics*. Wiley Series in Probability and Statistics. John Wiley and Sons, Inc., 1981. doi: 10.1002/0471725250.

J. D. Hunter. Matplotlib: A 2d graphics environment. *Computing in Science Engineering*, 9(3):90–95, May 2007. ISSN 1521-9615. doi: 10.1109/MCSE.2007.55.

T.-O. Husser, S. Wende-von Berg, S. Dreizler, D. Homeier, A. Reiners, T. Barman, and P. H. Hauschildt. A new extensive library of PHOENIX stellar atmospheres and synthetic spectra. A&A, 553:A6, May 2013. doi: 10.1051/0004-6361/201219058.

P. Hut. Stability of tidal equilibrium. A&A, 92:167–170, December 1980.

P. Hut. Tidal evolution in close binary systems. A&A, 99:126–140, June 1981.

I. Iben, Jr. and A. V. Tutukov. Supernovae of type I as end products of the evolution of binaries with components of moderate initial mass (M not greater than about 9 solar masses). ApJS, 54:335–372, February 1984. doi: 10.1086/190932.

L. Iorio. Classical and relativistic node precessional effects in WASP-33b and perspectives for detecting them. Ap&SS, 331:485–496, February 2011. doi: 10.1007/s10509-010-0468-x.

J. Irwin, L. Buchhave, Z. K. Berta, D. Charbonneau, D. W. Latham, C. J. Burke, G. A. Esquerdo, M. E. Everett, M. J. Holman, P. Nutzman, P. Berlind, M. L. Calkins, E. E. Falco, J. N. Winn, J. A. Johnson, and J. Z. Gazak. NLTT 41135: A Field M Dwarf + Brown Dwarf Eclipsing Binary in a Triple System, Discovered by the MEarth Observatory. ApJ, 718:1353–1366, August 2010. doi: 10.1088/0004-637X/718/2/1353.

B. Jackson, R. Greenberg, and R. Barnes. Tidal Evolution of Close-in Extrasolar Planets. ApJ, 678:1396–1406, May 2008. doi: 10.1086/529187.

E. Jensen. Tapir: A web interface for transit/eclipse observability. Astrophysics Source Code Library, June 2013.

C. M. Johns-Krull, P. R. McCullough, C. J. Burke, J. A. Valenti, K. A. Janes, J. N. Heasley, L. Prato, R. Bissinger, M. Fleenor, C. N. Foote, E. Garcia-Melendo, B. L. Gary, P. J. Howell, F. Mallia, G. Masi, and T. Vanmunster. XO-3b: A Massive Planet in an Eccentric Orbit Transiting an F5 V Star. ApJ, 677:657–670, April 2008. doi: 10.1086/528950.

D. R. H. Johnson and D. R. Soderblom. Calculating galactic space velocities and their uncertainties, with an application to the Ursa Major group. AJ, 93:864–867, April 1987. doi: 10.1086/114370.

J. A. Johnson, D. A. Fischer, G. W. Marcy, J. T. Wright, P. Driscoll, R. P. Butler, S. Hekker, S. Reffert, and S. S. Vogt. Retired A Stars and Their Companions: Exoplanets Orbiting Three Intermediate-Mass Subgiants. ApJ, 665:785–793, August 2007. doi: 10.1086/519677.

J. A. Johnson, K. Apps, J. Z. Gazak, J. R. Crepp, I. J. Crossfield, A. W. Howard, G. W. Marcy, T. D. Morton, C. Chubak, and H. Isaacson. LHS 6343 C: A Transiting Field Brown Dwarf Discovered by the Kepler Mission. ApJ, 730:79, April 2011. doi: 10.1088/0004-637X/730/2/79.

M. C. Johnson, W. D. Cochran, S. Albrecht, S. E. Dodson-Robinson, J. N. Winn, and K. Gullikson. A Misaligned Prograde Orbit for Kepler-13 Ab via Doppler Tomography. ApJ, 790:30, July 2014. doi: 10.1088/0004-637X/790/1/30.

Marshall C. Johnson, Joseph E. Rodriguez, George Zhou, Erica J. Gonzales, Phillip A. Cargile, Justin R. Crepp, Kaloyan Penev, Keivan G. Stassun, B. Scott Gaudi, and Knicole D. Colón. KELT-21b: A Hot Jupiter Transiting the Rapidly Rotating Metal-poor Late-A Primary of a Likely Hierarchical Triple System. AJ, 155(2):100, Feb 2018. doi: 10.3847/1538-3881/aaa5af.

S. R. Kane, S. Mahadevan, K. von Braun, G. Laughlin, and D. R. Ciardi. Refining Exoplanet Ephemerides and Transit Observing Strategies. PASP, 121:1386, December 2009. doi: 10.1086/648564.

D. Kasen. Seeing the Collision of a Supernova with Its Companion Star. ApJ, 708:1025–1031, January 2010. doi: 10.1088/0004-637X/708/2/1025.

B. Katz, S. Dong, and R. Malhotra. Long-Term Cycling of Kozai-Lidov Cycles: Extreme Eccentricities and Inclinations Excited by a Distant Eccentric Perturber. *Physical Review Letters*, 107(18):181101, October 2011. doi: 10.1103/PhysRevLett.107.181101.

P. L. Kelly, O. D. Fox, A. V. Filippenko, S. B. Cenko, L. Prato, G. Schaefer, K. J. Shen, W. Zheng, M. L. Graham, and B. E. Tucker. Constraints on the Progenitor System of the Type Ia Supernova 2014J from Pre-explosion Hubble Space Telescope Imaging. ApJ, 790:3, July 2014. doi: 10.1088/0004-637X/790/1/3.

S. J. Kenyon and L. Hartmann. Pre-Main-Sequence Evolution in the Taurus-Auriga Molecular Cloud. ApJS, 101:117, November 1995. doi: 10.1086/192235.

D. M. Kipping. Transit timing effects due to an exomoon. MNRAS, 392:181–189, January 2009. doi: 10.1111/j.1365-2966.2008.13999.x.

J. D. Kirkpatrick, C. R. Gelino, M. C. Cushing, G. N. Mace, R. L. Griffith, M. F. Skrutskie, K. A. Marsh, E. L. Wright, P. R. Eisenhardt, I. S. McLean, A. K. Mainzer, A. J. Burgasser, C. G. Tinney, S. Parker, and G. Salter. Further Defining Spectral Type "Y" and Exploring the Low-mass End of the Field Brown Dwarf Mass Function. ApJ, 753:156, July 2012. doi: 10.1088/0004-637X/753/2/156.

H. A. Knutson, D. Charbonneau, L. E. Allen, A. Burrows, and S. T. Megeath. The 3.6-8.0 μm Broadband Emission Spectrum of HD 209458b: Evidence for an Atmospheric Temperature Inversion. ApJ, 673:526–531, January 2008. doi: 10.1086/523894.

G. Kovács, S. Zucker, and T. Mazeh. A box-fitting algorithm in the search for periodic transits. A&A, 391:369–377, August 2002. doi: 10.1051/0004-6361:20020802.

G. Kovács, G. Bakos, and R. W. Noyes. A trend filtering algorithm for wide-field variability surveys. MNRAS, 356:557–567, January 2005. doi: 10.1111/j.1365-2966.2004.08479.x.

Y. Kozai. Secular perturbations of asteroids with high inclination and eccentricity. AJ, 67: 591, November 1962. doi: 10.1086/108790.

R. P. Kraft. Studies of Stellar Rotation. V. The Dependence of Rotation on Age among Solar-Type Stars. ApJ, 150:551, November 1967. doi: 10.1086/149359.

K. M. Kratter, R. A. Murray-Clay, and A. N. Youdin. The Runts of the Litter: Why Planets Formed Through Gravitational Instability Can Only Be Failed Binary Stars. ApJ, 710: 1375–1386, February 2010. doi: 10.1088/0004-637X/710/2/1375.

A. L. Kraus and L. A. Hillenbrand. The Stellar Populations of Praesepe and Coma Berenices. AJ, 134:2340–2352, December 2007. doi: 10.1086/522831.

R. B. Kuhn, J. E. Rodriguez, K. A. Collins, M. B. Lund, R. J. Siverd, K. D. Colón, J. Pepper, K. G. Stassun, P. A. Cargile, D. J. James, K. Penev, G. Zhou, D. Bayliss, T. G. Tan, I. A. Curtis, S. Udry, D. Segransan, D. Mawet, S. Dhital, J. Soutter, R. Hart, B. Carter, B. S. Gaudi, G. Myers, T. G. Beatty, J. D. Eastman, D. E. Reichart, J. B. Haislip, J. Kielkopf, A. Bieryla, D. W. Latham, E. L. N. Jensen, T. E. Oberst, and D. J. Stevens. KELT-10b: the first transiting exoplanet from the KELT-South survey - a hot sub-Jupiter transiting a V = 10.7 early G-star. MNRAS, 459:4281–4298, July 2016. doi: 10.1093/mnras/stw880.

R. L. Kurucz. Model atmospheres for G, F, A, B, and O stars. ApJS, 40:1–340, May 1979. doi: 10.1086/190589.

R. L. Kurucz. Model Atmospheres for Population Synthesis. In B. Barbuy and A. Renzini, editors, *The Stellar Populations of Galaxies*, volume 149 of *IAU Symposium*, page 225, 1992.

J. Labadie-Bartz, J. Pepper, M. V. McSwain, J. E. Bjorkman, K. S. Bjorkman, M. B. Lund, J. E. Rodriguez, K. G. Stassun, D. J. Stevens, D. J. James, R. B. Kuhn, R. J. Siverd, and T. G. Beatty. Photometric Variability of the Be Star Population. AJ, 153:252, June 2017. doi: 10.3847/1538-3881/aa6396.

J. Labadie-Bartz, S. D. Chojnowski, D. G. Whelan, J. Pepper, M. V. McSwain, M. Borges Fernandes, J. P. Wisniewski, G. S. Stringfellow, A. C. Carciofi, R. J. Siverd, A. L.

Glazier, S. G. Anderson, A. J. Caravello, K. G. Stassun, M. B. Lund, D. J. Stevens, J. E. Rodriguez, D. J. James, and R. B. Kuhn. Outbursts and Disk Variability in Be Stars. AJ, 155:53, February 2018. doi: 10.3847/1538-3881/aa9c7e.

D. Lang, D. W. Hogg, K. Mierle, M. Blanton, and S. Roweis. Astrometry.net: Blind Astrometric Calibration of Arbitrary Astronomical Images. AJ, 139:1782–1800, May 2010. doi: 10.1088/0004-6256/139/5/1782.

D. W. Latham, G. Á. Bakos, G. Torres, R. P. Stefanik, R. W. Noyes, G. Kovács, A. Pál, G. W. Marcy, D. A. Fischer, R. P. Butler, B. Sipőcz, D. D. Sasselov, G. A. Esquerdo, S. S. Vogt, J. D. Hartman, G. Kovács, J. Lázár, I. Papp, and P. Sári. Discovery of a Transiting Planet and Eight Eclipsing Binaries in HATNet Field G205. ApJ, 704:1107–1119, October 2009. doi: 10.1088/0004-637X/704/2/1107.

D. W. Latham, J. F. Rowe, S. N. Quinn, N. M. Batalha, W. J. Borucki, T. M. Brown, S. T. Bryson, L. A. Buchhave, D. A. Caldwell, J. A. Carter, J. L. Christiansen, D. R. Ciardi, W. D. Cochran, E. W. Dunham, D. C. Fabrycky, E. B. Ford, T. N. Gautier, III, R. L. Gilliland, M. J. Holman, S. B. Howell, K. A. Ibrahim, H. Isaacson, J. M. Jenkins, D. G. Koch, J. J. Lissauer, G. W. Marcy, E. V. Quintana, D. Ragozzine, D. Sasselov, A. Shporer, J. H. Steffen, W. F. Welsh, and B. Wohler. A First Comparison of Kepler Planet Candidates in Single and Multiple Systems. ApJ, 732:L24, May 2011. doi: 10.1088/2041-8205/732/2/L24.

J. Leconte, G. Chabrier, I. Baraffe, and B. Levrard. Is tidal heating sufficient to explain bloated exoplanets? Consistent calculations accounting for finite initial eccentricity. A&A, 516:A64, June 2010. doi: 10.1051/0004-6361/201014337.

B. L. Lee, J. Ge, S. W. Fleming, K. G. Stassun, B. S. Gaudi, R. Barnes, S. Mahadevan, J. D. Eastman, J. Wright, R. J. Siverd, B. Gary, L. Ghezzi, C. Laws, J. P. Wisniewski, G. F. Porto de Mello, R. L. C. Ogando, M. A. G. Maia, L. Nicolaci da Costa,

T. Sivarani, J. Pepper, D. C. Nguyen, L. Hebb, N. De Lee, J. Wang, X. Wan, B. Zhao, L. Chang, J. Groot, F. Varosi, F. Hearty, K. Hanna, J. C. van Eyken, S. R. Kane, E. Agol, D. Bizyaev, J. J. Bochanski, H. Brewington, Z. Chen, E. Costello, L. Dou, D. J. Eisenstein, A. Fletcher, E. B. Ford, P. Guo, J. A. Holtzman, P. Jiang, R. French Leger, J. Liu, D. C. Long, E. Malanushenko, V. Malanushenko, M. Malik, D. Oravetz, K. Pan, P. Rohan, D. P. Schneider, A. Shelden, S. A. Snedden, A. Simmons, B. A. Weaver, D. H. Weinberg, and J.-W. Xie. MARVELS-1b: A Short-period, Brown Dwarf Desert Candidate from the SDSS-III Marvels Planet Search. ApJ, 728:32, February 2011. doi: 10.1088/0004-637X/728/1/32.

A. Léger, D. Rouan, J. Schneider, P. Barge, M. Fridlund, B. Samuel, M. Ollivier, E. Guenther, M. Deleuil, H. J. Deeg, M. Auvergne, R. Alonso, S. Aigrain, A. Alapini, J. M. Almenara, A. Baglin, M. Barbieri, H. Bruntt, P. Bordé, F. Bouchy, J. Cabrera, C. Catala, L. Carone, S. Carpano, S. Csizmadia, R. Dvorak, A. Erikson, S. Ferraz-Mello, B. Foing, F. Fressin, D. Gandolfi, M. Gillon, P. Gondoin, O. Grasset, T. Guillot, A. Hatzes, G. Hébrard, L. Jorda, H. Lammer, A. Llebaria, B. Loeillet, M. Mayor, T. Mazeh, C. Moutou, M. Pätzold, F. Pont, D. Queloz, H. Rauer, S. Renner, R. Samadi, A. Shporer, C. Sotin, B. Tingley, G. Wuchterl, M. Adda, P. Agogu, T. Appourchaux, H. Ballans, P. Baron, T. Beaufort, R. Bellenger, R. Berlin, P. Bernardi, D. Blouin, F. Baudin, P. Bodin, L. Boisnard, L. Boit, F. Bonneau, S. Borzeix, R. Briet, J.-T. Buey, B. Butler, D. Cailleau, R. Cautain, P.-Y. Chabaud, S. Chaintreuil, F. Chiavassa, V. Costes, V. Cuna Parrho, F. de Oliveira Fialho, M. Decaudin, J.-M. Defise, S. Djalal, G. Epstein, G.-E. Exil, C. Fauré, T. Fenouillet, A. Gaboriaud, A. Gallic, P. Gamet, P. Gavalda, E. Grolleau, R. Gruneisen, L. Gueguen, V. Guis, V. Guivarc'h, P. Guterman, D. Hallouard, J. Hasiba, F. Heuripeau, G. Huntzinger, H. Hustaix, C. Imad, C. Imbert, B. Johlander, M. Jouret, P. Journoud, F. Karioty, L. Kerjean, V. Lafaille, L. Lafond, T. Lam-Trong, P. Landiech, V. Lapeyrere, T. Larqué, P. Laudet, N. Lautier, H. Lecann, L. Lefevre, B. Leruyet, P. Levacher, A. Magnan, E. Mazy, F. Mertens, J.-M. Mesnager, J.-C. Meunier, J.-P. Michel,

W. Monjoin, D. Naudet, K. Nguyen-Kim, J.-L. Orcesi, H. Ottacher, R. Perez, G. Peter, P. Plasson, J.-Y. Plesseria, B. Pontet, A. Pradines, C. Quentin, J.-L. Reynaud, G. Rolland, F. Rollenhagen, R. Romagnan, N. Russ, R. Schmidt, N. Schwartz, I. Sebbag, G. Sedes, H. Smit, M. B. Steller, W. Sunter, C. Surace, M. Tello, D. Tiphène, P. Toulouse, B. Ulmer, O. Vandermarcq, E. Vergnault, A. Vuillemin, and P. Zanatta. Transiting exoplanets from the CoRoT space mission. VIII. CoRoT-7b: the first super-Earth with measured radius. A&A, 506:287–302, October 2009. doi: 10.1051/0004-6361/200911933.

S. K. Leggett, D. A. Golimowski, X. Fan, T. R. Geballe, G. R. Knapp, J. Brinkmann, I. Csabai, J. E. Gunn, S. L. Hawley, T. J. Henry, R. Hindsley, Ž. Ivezić, R. H. Lupton, J. R. Pier, D. P. Schneider, J. A. Smith, M. A. Strauss, A. Uomoto, and D. G. York. Infrared Photometry of Late-M, L, and T Dwarfs. ApJ, 564:452–465, January 2002. doi: 10.1086/324037.

M. L. Lidov. The evolution of orbits of artificial satellites of planets under the action of gravitational perturbations of external bodies. Planet. Space Sci., 9:719–759, October 1962. doi: 10.1016/0032-0633(62)90129-0.

J. J. Lissauer, D. C. Fabrycky, E. B. Ford, W. J. Borucki, F. Fressin, G. W. Marcy, J. A. Orosz, J. F. Rowe, G. Torres, W. F. Welsh, N. M. Batalha, S. T. Bryson, L. A. Buchhave, D. A. Caldwell, J. A. Carter, D. Charbonneau, J. L. Christiansen, W. D. Cochran, J.-M. Desert, E. W. Dunham, M. N. Fanelli, J. J. Fortney, T. N. Gautier, III, J. C. Geary, R. L. Gilliland, M. R. Haas, J. R. Hall, M. J. Holman, D. G. Koch, D. W. Latham, E. Lopez, S. McCauliff, N. Miller, R. C. Morehead, E. V. Quintana, D. Ragozzine, D. Sasselov, D. R. Short, and J. H. Steffen. A closely packed system of low-mass, low-density planets transiting Kepler-11. Nature, 470:53–58, February 2011. doi: 10.1038/nature09760.

Y. Lithwick and S. Naoz. The Eccentric Kozai Mechanism for a Test Particle. ApJ, 742: 94, December 2011. doi: 10.1088/0004-637X/742/2/94.

A. Loeb and B. S. Gaudi. Periodic Flux Variability of Stars due to the Reflex Doppler Effect Induced by Planetary Companions. ApJ, 588:L117–L120, May 2003. doi: 10.1086/375551.

N. R. Lomb. Least-squares frequency analysis of unequally spaced data. Ap&SS, 39: 447–462, February 1976. doi: 10.1007/BF00648343.

M. B. Lund, J. E. Rodriguez, G. Zhou, B. S. Gaudi, K. G. Stassun, M. C. Johnson, A. Bieryla, R. J. Oelkers, D. J. Stevens, K. A. Collins, K. Penev, S. N. Quinn, D. W. Latham, S. Villanueva, Jr., J. D. Eastman, J. F. Kielkopf, T. E. Oberst, E. L. N. Jensen, D. H. Cohen, M. D. Joner, D. C. Stephens, H. Relles, G. Corfini, J. Gregorio, R. Zambelli, G. A. Esquerdo, M. L. Calkins, P. Berlind, D. R. Ciardi, C. Dressing, R. Patel, P. Gagnon, E. Gonzales, T. G. Beatty, R. J. Siverd, J. Labadie-Bartz, R. B. Kuhn, K. D. Colon, D. James, J. Pepper, B. J. Fulton, K. K. McLeod, C. Stockdale, S. Calchi Novati, D. L. DePoy, A. Gould, J. L. Marshall, M. Trueblood, and P. Trueblood. KELT-20b: A giant planet with a period of P˜ 3.5 days transiting the V˜ 7.6 early A star HD 185603. *ArXiv e-prints*, July 2017.

E. E. Mamajek and L. A. Hillenbrand. Improved Age Estimation for Solar-Type Dwarfs Using Activity-Rotation Diagnostics. ApJ, 687:1264-1293, November 2008. doi: 10.1086/591785.

K. Mandel and E. Agol. Analytic Light Curves for Planetary Transit Searches. ApJ, 580: L171–L175, December 2002. doi: 10.1086/345520.

G. Mandushev, G. Torres, D. W. Latham, D. Charbonneau, R. Alonso, R. J. White, R. P. Stefanik, E. W. Dunham, T. M. Brown, and F. T. O'Donovan. The Challenge of Wide-Field Transit Surveys: The Case of GSC 01944-02289. ApJ, 621:1061–1071, March 2005. doi: 10.1086/427727.

G. W. Marcy and R. P. Butler. Planets Orbiting Other Suns. PASP, 112:137–140, February 2000. doi: 10.1086/316516.

G. H. Marion, D. J. Sand, E. Y. Hsiao, D. P. K. Banerjee, S. Valenti, M. D. Stritzinger, J. Vinkó, V. Joshi, V. Venkataraman, N. M. Ashok, R. Amanullah, R. P. Binzel, J. J. Bochanski, G. L. Bryngelson, C. R. Burns, D. Drozdov, S. K. Fieber-Beyer, M. L. Graham, D. A. Howell, J. Johansson, R. P. Kirshner, P. A. Milne, J. Parrent, J. M. Silverman, R. J. Vervack, and J. C. Wheeler. Early Observations and Analysis of the Type Ia SN 2014J in M82. *ArXiv e-prints*, May 2014.

S. Matsumura, S. J. Peale, and F. A. Rasio. Tidal Evolution of Close-in Planets. ApJ, 725: 1995–2016, December 2010. doi: 10.1088/0004-637X/725/2/1995.

T. Mazeh and S. Faigler. Detection of the ellipsoidal and the relativistic beaming effects in the CoRoT-3 lightcurve. A&A, 521:L59, October 2010. doi: 10.1051/0004-6361/201015550.

T. Mazeh, G. Nachmani, G. Sokol, S. Faigler, and S. Zucker. Kepler KOI-13.01 - Detection of beaming and ellipsoidal modulations pointing to a massive hot Jupiter. A&A, 541: A56, May 2012. doi: 10.1051/0004-6361/201117908.

P. R. McCullough, J. E. Stys, J. A. Valenti, C. M. Johns-Krull, K. A. Janes, J. N. Heasley, B. A. Bye, C. Dodd, S. W. Fleming, A. Pinnick, R. Bissinger, B. L. Gary, P. J. Howell, and T. Vanmunster. A Transiting Planet of a Sun-like Star. ApJ, 648:1228–1238, September 2006. doi: 10.1086/505651.

Wes McKinney et al. Data structures for statistical computing in python. In *Proceedings of the 9th Python in Science Conference*, volume 445, pages 51–56. Austin, TX, 2010.

D. B. McLaughlin. Some results of a spectrographic study of the Algol system. ApJ, 60, July 1924. doi: 10.1086/142826.

S. A. Metchev and L. A. Hillenbrand. The Palomar/Keck Adaptive Optics Survey of Young Solar Analogs: Evidence for a Universal Companion Mass Function. ApJS, 181:62–109, March 2009. doi: 10.1088/0067-0049/181/1/62.

B. D. Metzger, D. Giannios, and D. S. Spiegel. Optical and X-ray transients from planet-star mergers. MNRAS, 425:2778–2798, October 2012. doi: 10.1111/j.1365-2966.2012.21444.x.

J. Patrick Miller, C. R. Pennypacker, and Graeme L. White. Optimal Image Subtraction Method: Summary Derivations, Applications, and Publicly Shared Application Using IDL. PASP, 120(866):449, Apr 2008. doi: 10.1086/588258.

N. Miller and J. J. Fortney. The Heavy-element Masses of Extrasolar Giant Planets, Revealed. ApJ, 736:L29, August 2011. doi: 10.1088/2041-8205/736/2/L29.

D. Mislis and S. Hodgkin. A massive exoplanet candidate around KOI-13: independent confirmation by ellipsoidal variations. MNRAS, 422:1512–1517, May 2012. doi: 10.1111/j.1365-2966.2012.20724.x.

S. Mohanty and K. G. Stassun. High-resolution Spectroscopy during Eclipse of the Young Substellar Eclipsing Binary 2MASS 0535-0546. II. Secondary Spectrum: No Evidence that Spots Cause the Temperature Reversal. ApJ, 758:12, October 2012. doi: 10.1088/0004-637X/758/1/12.

S. Mohanty, K. G. Stassun, and G. W. Doppmann. High-resolution Spectroscopy During Eclipse of the Young Substellar Eclipsing Binary 2MASS 0535-0546. I. Primary Spectrum: Cool Spots Versus Opacity Uncertainties. ApJ, 722:1138–1147, October 2010. doi: 10.1088/0004-637X/722/2/1138.

L. Molnár, A. Derekas, R. Szabó, J. M. Matthews, C. Cameron, A. F. J. Moffat, N. D. Richardson, B. Csák, Á. Dózsa, P. Reed, L. Szabados, B. Heathcote, T. Bohlsen, P. Cacella, P. Luckas, Á. Sódor, M. Skarka, G. M. Szabó, E. Plachy, J. Kovács, N. R. Evans,

K. Kolenberg, K. A. Collins, J. Pepper, K. G. Stassun, J. E. Rodriguez, R. J. Siverd, A. Henden, L. Mankiewicz, A. F. Żarnecki, A. Cwiek, M. Sokolowski, A. Pál, D. B. Guenther, R. Kuschnig, J. Rowe, S. M. Rucinski, D. Sasselov, and W. W. Weiss. V473 Lyr, a modulated, period-doubled Cepheid, and U TrA, a double-mode Cepheid, observed by MOST. MNRAS, 466:4009–4020, April 2017. doi: 10.1093/mnras/stw3345.

C. Mordasini, Y. Alibert, W. Benz, and D. Naef. Extrasolar planet population synthesis. II. Statistical comparison with observations. A&A, 501:1161–1184, July 2009. doi: 10.1051/0004-6361/200810697.

A. Mortier, N. C. Santos, S. G. Sousa, J. M. Fernandes, V. Z. Adibekyan, E. Delgado Mena, M. Montalto, and G. Israelian. New and updated stellar parameters for 90 transit hosts. The effect of the surface gravity. A&A, 558:A106, October 2013. doi: 10.1051/0004-6361/201322240.

A. Mortier, S. G. Sousa, V. Z. Adibekyan, I. M. Brandão, and N. C. Santos. Correcting the spectroscopic surface gravity using transits and asteroseismology. No significant effect on temperatures or metallicities with ARES and MOOG in local thermodynamic equilibrium. A&A, 572:A95, December 2014. doi: 10.1051/0004-6361/201424537.

P. S. Muirhead, J. A. Johnson, K. Apps, J. A. Carter, T. D. Morton, D. C. Fabrycky, J. S. Pineda, M. Bottom, B. Rojas-Ayala, E. Schlawin, K. Hamren, K. R. Covey, J. R. Crepp, K. G. Stassun, J. Pepper, L. Hebb, E. N. Kirby, A. W. Howard, H. T. Isaacson, G. W. Marcy, D. Levitan, T. Diaz-Santos, L. Armus, and J. P. Lloyd. Characterizing the Cool KOIs. III. KOI 961: A Small Star with Large Proper Motion and Three Small Planets. ApJ, 747:144, March 2012. doi: 10.1088/0004-637X/747/2/144.

D. J. Mullan and J. MacDonald. Magnetic Models of the Brown Dwarfs HD 130948b and HD 130948c. ApJ, 713:1249–1255, April 2010. doi: 10.1088/0004-637X/713/2/1249.

U. Munari, A. Henden, R. Belligoli, F. Castellani, G. Cherini, G. L. Righetti, and

A. Vagnozzi. BVRI lightcurves of supernovae SN 2011fe in M101, SN 2012aw in M95, and SN 2012cg in NGC 4424. New A, 20:30–37, April 2013. doi: 10.1016/j.newast.2012.09.003.

R. A. Murray-Clay, E. I. Chiang, and N. Murray. Atmospheric Escape From Hot Jupiters. ApJ, 693:23–42, March 2009. doi: 10.1088/0004-637X/693/1/23.

S. Naoz, W. M. Farr, Y. Lithwick, F. A. Rasio, and J. Teyssandier. Hot Jupiters from secular planet-planet interactions. Nature, 473:187–189, May 2011. doi: 10.1038/nature10076.

J. A. Nelder and R. Mead. A simplex method for function minimization. *The Computer Journal*, 7(4):308–313, 1965. doi: 10.1093/comjnl/7.4.308. URL http://comjnl.oxfordjournals.org/content/7/4/308.abstract.

Lyman W. Neuschaefer and Rogier A. Windhorst. Observation and Reduction Methods of Deep Palomar 200 Inch 4-Shooter Mosaics. ApJS, 96:371, Feb 1995. doi: 10.1086/192124.

P. E. Nugent, M. Sullivan, S. B. Cenko, R. C. Thomas, D. Kasen, D. A. Howell, D. Bersier, J. S. Bloom, S. R. Kulkarni, M. T. Kandrashoff, A. V. Filippenko, J. M. Silverman, G. W. Marcy, A. W. Howard, H. T. Isaacson, K. Maguire, N. Suzuki, J. E. Tarlton, Y.-C. Pan, L. Bildsten, B. J. Fulton, J. T. Parrent, D. Sand, P. Podsiadlowski, F. B. Bianco, B. Dilday, M. L. Graham, J. Lyman, P. James, M. M. Kasliwal, N. M. Law, R. M. Quimby, I. M. Hook, E. S. Walker, P. Mazzali, E. Pian, E. O. Ofek, A. Gal-Yam, and D. Poznanski. Supernova SN 2011fe from an exploding carbon-oxygen white dwarf star. Nature, 480:344–347, December 2011. doi: 10.1038/nature10644.

F. T. O'Donovan, D. Charbonneau, G. Torres, G. Mandushev, E. W. Dunham, D. W. Latham, R. Alonso, T. M. Brown, G. A. Esquerdo, M. E. Everett, and O. L. Creevey. Rejecting Astrophysical False Positives from the TrES Transiting Planet Survey: The Example of GSC 03885-00829. ApJ, 644:1237–1245, June 2006. doi: 10.1086/503740.

G. I. Ogilvie. Tidal Dissipation in Stars and Giant Planets. ARA&A, 52:171–210, August 2014. doi: 10.1146/annurev-astro-081913-035941.

G. I. Ogilvie and D. N. C. Lin. Tidal Dissipation in Rotating Giant Planets. ApJ, 610: 477–509, July 2004. doi: 10.1086/421454.

Y. Ohta, A. Taruya, and Y. Suto. The Rossiter-McLaughlin Effect and Analytic Radial Velocity Curves for Transiting Extrasolar Planetary Systems. ApJ, 622:1118–1135, April 2005. doi: 10.1086/428344.

K. Penev, M. Zhang, and B. Jackson. POET: A Model for Planetary Orbital Evolution Due to Tides on Evolving Stars. PASP, 126:553–564, June 2014. doi: 10.1086/677042.

J. Pepper, A. Gould, and D. L. Depoy. Using All-Sky Surveys to Find Planetary Transits. *Acta Astronomica*, 53:213–228, September 2003.

J. Pepper, R. W. Pogge, D. L. DePoy, J. L. Marshall, K. Z. Stanek, A. M. Stutz, S. Poindexter, R. Siverd, T. P. O'Brien, M. Trueblood, and P. Trueblood. The Kilodegree Extremely Little Telescope (KELT): A Small Robotic Telescope for Large-Area Synoptic Surveys. PASP, 119:923–935, August 2007. doi: 10.1086/521836.

J. Pepper, R. B. Kuhn, R. Siverd, D. James, and K. Stassun. The KELT-South Telescope. PASP, 124:230–241, March 2012. doi: 10.1086/665044.

D. Pollacco, I. Skillen, A. Collier Cameron, B. Loeillet, H. C. Stempels, F. Bouchy, N. P. Gibson, L. Hebb, G. Hébrard, and Y. C. Joshi. WASP-3b: a strongly irradiated transiting gas-giant planet. MNRAS, 385(3):1576–1584, Apr 2008. doi: 10.1111/j.1365-2966.2008.12939.x.

F. Pont, C. H. F. Melo, F. Bouchy, S. Udry, D. Queloz, M. Mayor, and N. C. Santos. A planet-sized transiting star around OGLE-TR-122. Accurate mass and radius near the

hydrogen-burning limit. A&A, 433:L21–L24, April 2005. doi: 10.1051/0004-6361:200500025.

F. Pont, C. Moutou, F. Bouchy, R. Behrend, M. Mayor, S. Udry, D. Queloz, N. Santos, and C. Melo. Radius and mass of a transiting M dwarf near the hydrogen-burning limit. OGLE-TR-123. A&A, 447:1035–1039, March 2006a. doi: 10.1051/0004-6361:20053692.

F. Pont, S. Zucker, and D. Queloz. The effect of red noise on planetary transit detection. MNRAS, 373:231–242, November 2006b. doi: 10.1111/j.1365-2966.2006.11012.x.

S. N. Quinn, G. Á. Bakos, J. Hartman, G. Torres, G. Kovács, D. W. Latham, R. W. Noyes, D. A. Fischer, J. A. Johnson, G. W. Marcy, A. W. Howard, A. Szentgyorgyi, G. Fűrész, L. A. Buchhave, B. Béky, D. D. Sasselov, R. P. Stefanik, G. Perumpilly, M. Everett, J. Lázár, I. Papp, and P. Sári. HAT-P-25b: A Hot-Jupiter Transiting a Moderately Faint G Star. ApJ, 745:80, January 2012. doi: 10.1088/0004-637X/745/1/80.

S. N. Quinn, R. J. White, D. W. Latham, L. A. Buchhave, G. Torres, R. P. Stefanik, P. Berlind, A. Bieryla, M. C. Calkins, G. A. Esquerdo, G. Fűrész, J. C. Geary, and A. H. Szentgyorgyi. HD 285507b: An Eccentric Hot Jupiter in the Hyades Open Cluster. ApJ, 787:27, May 2014. doi: 10.1088/0004-637X/787/1/27.

R. R. Rafikov. Can Giant Planets Form by Direct Gravitational Instability? ApJ, 621:L69–L72, March 2005. doi: 10.1086/428899.

F. A. Rasio, C. A. Tout, S. H. Lubow, and M. Livio. Tidal Decay of Close Planetary Orbits. ApJ, 470:1187, October 1996. doi: 10.1086/177941.

O. Richard, G. Michaud, and J. Richer. Iron Convection Zones in B, A, and F Stars. ApJ, 558:377–391, September 2001. doi: 10.1086/322264.

J. Richer, G. Michaud, and S. Turcotte. The Evolution of AMFM Stars, Abundance Anomalies, and Turbulent Transport. ApJ, 529:338–356, January 2000. doi: 10.1086/308274.

George R. Ricker, Joshua N. Winn, Roland Vanderspek, David W. Latham, Gáspár Á. Bakos, Jacob L. Bean, Zachory K. Berta-Thompson, Timothy M. Brown, Lars Buchhave, and Nathaniel R. Butler. Transiting Exoplanet Survey Satellite (TESS). *Journal of Astronomical Telescopes, Instruments, and Systems*, 1:014003, Jan 2015. doi: 10.1117/1.JATIS.1.1.014003.

L. A. Rogers and S. Seager. A Framework for Quantifying the Degeneracies of Exoplanet Interior Compositions. ApJ, 712:974–991, April 2010. doi: 10.1088/0004-637X/712/2/974.

R. A. Rossiter. On the detection of an effect of rotation during eclipse in the velocity of the brigher component of beta Lyrae, and on the constancy of velocity of this system. ApJ, 60, July 1924. doi: 10.1086/142825.

Peter J. Rousseeuw and Christophe Croux. Alternatives to the median absolute deviation. *Journal of the American Statistical Association*, 88(424):1273–1283, 1993. doi: 10.1080/01621459.1993.10476408. URL https://www.tandfonline.com/doi/abs/10.1080/01621459.1993.10476408.

J. F. Rowe, W. J. Borucki, D. Koch, S. B. Howell, G. Basri, N. Batalha, T. M. Brown, D. Caldwell, W. D. Cochran, E. Dunham, A. K. Dupree, J. J. Fortney, T. N. Gautier, III, R. L. Gilliland, J. Jenkins, D. W. Latham, J. J. Lissauer, G. Marcy, D. G. Monet, D. Sasselov, and W. F. Welsh. Kepler Observations of Transiting Hot Compact Objects. ApJ, 713:L150–L154, April 2010. doi: 10.1088/2041-8205/713/2/L150.

J. Sahlmann, D. Ségransan, D. Queloz, S. Udry, N. C. Santos, M. Marmier, M. Mayor,

D. Naef, F. Pepe, and S. Zucker. Search for brown-dwarf companions of stars. A&A, 525:A95, January 2011. doi: 10.1051/0004-6361/201015427.

J. D. Scargle. Studies in astronomical time series analysis. II - Statistical aspects of spectral analysis of unevenly spaced data. ApJ, 263:835–853, December 1982. doi: 10.1086/160554.

D. J. Schlegel, D. P. Finkbeiner, and M. Davis. Maps of Dust Infrared Emission for Use in Estimation of Reddening and Cosmic Microwave Background Radiation Foregrounds. ApJ, 500:525–553, June 1998. doi: 10.1086/305772.

J. Schneider, C. Dedieu, P. Le Sidaner, R. Savalle, and I. Zolotukhin. Defining and cataloging exoplanets: the exoplanet.eu database. A&A, 532:A79, August 2011. doi: 10.1051/0004-6361/201116713.

A. Schwarzenberg-Czerny. On the advantage of using analysis of variance for period search. MNRAS, 241:153–165, November 1989. doi: 10.1093/mnras/241.2.153.

S. Seager. *Exoplanet Atmospheres: Physical Processes*. Princeton University Press, 2010.

S. Seager and D. Deming. Exoplanet Atmospheres. ARA&A, 48:631–672, September 2010. doi: 10.1146/annurev-astro-081309-130837.

S. Seager and L. Hui. Constraining the Rotation Rate of Transiting Extrasolar Planets by Oblateness Measurements. ApJ, 574:1004–1010, August 2002. doi: 10.1086/340994.

S. Seager and G. Mallén-Ornelas. A Unique Solution of Planet and Star Parameters from an Extrasolar Planet Transit Light Curve. ApJ, 585:1038–1055, March 2003. doi: 10.1086/346105.

S. Seager and D. D. Sasselov. Theoretical Transmission Spectra during Extrasolar Giant Planet Transits. ApJ, 537:916–921, July 2000. doi: 10.1086/309088.

Pranab Kumar Sen. Estimates of the regression coefficient based on kendall's tau. *Journal of the American Statistical Association*, 63(324):1379–1389, 1968. ISSN 01621459. URL http://www.jstor.org/stable/2285891.

A. Shporer, J. M. Jenkins, J. F. Rowe, D. T. Sanderfer, S. E. Seader, J. C. Smith, M. D. Still, S. E. Thompson, J. D. Twicken, and W. F. Welsh. Detection of KOI-13.01 Using the Photometric Orbit. AJ, 142:195, December 2011. doi: 10.1088/0004-6256/142/6/195.

R. J. Siverd, T. G. Beatty, J. Pepper, J. D. Eastman, K. Collins, A. Bieryla, D. W. Latham, L. A. Buchhave, E. L. N. Jensen, J. R. Crepp, R. Street, K. G. Stassun, B. S. Gaudi, P. Berlind, M. L. Calkins, D. L. DePoy, G. A. Esquerdo, B. J. Fulton, G. Fűrész, J. C. Geary, A. Gould, L. Hebb, J. F. Kielkopf, J. L. Marshall, R. Pogge, K. Z. Stanek, R. P. Stefanik, A. H. Szentgyorgyi, M. Trueblood, P. Trueblood, A. M. Stutz, and J. L. van Saders. KELT-1b: A Strongly Irradiated, Highly Inflated, Short Period, 27 Jupiter-mass Companion Transiting a Mid-F Star. ApJ, 761:123, December 2012. doi: 10.1088/0004-637X/761/2/123.

Robert J. Siverd, Ariel Goobar, Keivan G. Stassun, and Joshua Pepper. Observations of the M82 SN 2014J with the Kilodegree Extremely Little Telescope. ApJ, 799(1):105, Jan 2015. doi: 10.1088/0004-637X/799/1/105.

Robert J. Siverd, Karen A. Collins, George Zhou, Samuel N. Quinn, B. Scott Gaudi, Keivan G. Stassun, Marshall C. Johnson, Allyson Bieryla, David W. Latham, and David R. Ciardi. KELT-19Ab: A P 4.6-day Hot Jupiter Transiting a Likely Am Star with a Distant Stellar Companion. AJ, 155(1):35, Jan 2018. doi: 10.3847/1538-3881/aa9e4d.

M. F. Skrutskie, R. M. Cutri, R. Stiening, M. D. Weinberg, S. Schneider, J. M. Carpenter, C. Beichman, R. Capps, T. Chester, J. Elias, J. Huchra, J. Liebert, C. Lonsdale, D. G. Monet, S. Price, P. Seitzer, T. Jarrett, J. D. Kirkpatrick, J. E. Gizis, E. Howard, T. Evans, J. Fowler, L. Fullmer, R. Hurt, R. Light, E. L. Kopan, K. A. Marsh, H. L. McCallon,

R. Tam, S. Van Dyk, and S. Wheelock. The Two Micron All Sky Survey (2MASS). AJ, 131:1163–1183, February 2006. doi: 10.1086/498708.

A. Socrates, B. Katz, S. Dong, and S. Tremaine. Super-eccentric Migrating Jupiters. ApJ, 750:106, May 2012. doi: 10.1088/0004-637X/750/2/106.

J. Southworth. Homogeneous studies of transiting extrasolar planets - II. Physical properties. MNRAS, 394:272–294, March 2009. doi: 10.1111/j.1365-2966.2008.14274.x.

D. S. Spiegel, Z. Haiman, and B. S. Gaudi. On Constraining a Transiting Exoplanet's Rotation Rate with Its Transit Spectrum. ApJ, 669:1324–1335, November 2007. doi: 10.1086/521921.

D. S. Spiegel, A. Burrows, and J. A. Milsom. The Deuterium-burning Mass Limit for Brown Dwarfs and Giant Planets. ApJ, 727:57, January 2011. doi: 10.1088/0004-637X/727/1/57.

K. G. Stassun and G. Torres. Evidence for a Systematic Offset of -0.25 mas in the Gaia DR1 Parallaxes. ApJ, 831:L6, November 2016. doi: 10.3847/2041-8205/831/1/L6.

K. G. Stassun, R. D. Mathieu, and J. A. Valenti. A Surprising Reversal of Temperatures in the Brown Dwarf Eclipsing Binary 2MASS J05352184-0546085. ApJ, 664:1154–1166, August 2007. doi: 10.1086/519231.

J. H. Steffen and E. Agol. An analysis of the transit times of TrES-1b. MNRAS, 364: L96–L100, November 2005. doi: 10.1111/j.1745-3933.2005.00113.x.

J. H. Steffen, N. M. Batalha, W. J. Borucki, L. A. Buchhave, D. A. Caldwell, W. D. Cochran, M. Endl, D. C. Fabrycky, F. Fressin, E. B. Ford, J. J. Fortney, M. J. Haas, M. J. Holman, S. B. Howell, H. Isaacson, J. M. Jenkins, D. Koch, D. W. Latham, J. J. Lissauer, A. V. Moorhead, R. C. Morehead, G. Marcy, P. J. MacQueen, S. N. Quinn, D. Ragozzine, J. F. Rowe, D. D. Sasselov, S. Seager, G. Torres, and W. F. Welsh. Five

Kepler Target Stars That Show Multiple Transiting Exoplanet Candidates. ApJ, 725: 1226–1241, December 2010. doi: 10.1088/0004-637X/725/1/1226.

J. H. Steffen, D. Ragozzine, D. C. Fabrycky, J. A. Carter, E. B. Ford, M. J. Holman, J. F. Rowe, W. F. Welsh, W. J. Borucki, A. P. Boss, D. R. Ciardi, and S. N. Quinn. Kepler constraints on planets near hot Jupiters. *Proceedings of the National Academy of Science*, 109:7982–7987, May 2012. doi: 10.1073/pnas.1120970109.

P. B. Stetson. DAOPHOT - A computer program for crowded-field stellar photometry. PASP, 99:191–222, March 1987. doi: 10.1086/131977.

P. B. Stetson. On the growth-curve method for calibrating stellar photometry with CCDs. PASP, 102:932–948, August 1990. doi: 10.1086/132719.

Daniel J. Stevens, Karen A. Collins, B. Scott Gaudi, Thomas G. Beatty, Robert J. Siverd, Allyson Bieryla, Benjamin J. Fulton, Justin R. Crepp, Erica J. Gonzales, and Carl T. Coker. KELT-12b: A P 5 day, Highly Inflated Hot Jupiter Transiting a Mildly Evolved Hot Star. AJ, 153(4):178, Apr 2017. doi: 10.3847/1538-3881/aa5ffb.

J. J. Swift, M. Bottom, J. A. Johnson, J. T. Wright, N. McCrady, R. A. Wittenmyer, P. Plavchan, R. Riddle, P. S. Muirhead, E. Herzig, J. Myles, C. H. Blake, J. Eastman, T. G. Beatty, S. I. Barnes, S. R. Gibson, B. Lin, M. Zhao, P. Gardner, E. Falco, S. Criswell, C. Nava, C. Robinson, D. H. Sliski, R. Hedrick, K. Ivarsen, A. Hjelstrom, J. de Vera, and A. Szentgyorgyi. Miniature Exoplanet Radial Velocity Array (MINERVA) I. Design, Commissioning, and First Science Results. *Journal of Astronomical Telescopes, Instruments, and Systems*, 1(2):027002, April 2015. doi: 10.1117/1.JATIS.1.2.027002.

G. J. J. Talens, S. Albrecht, J. F. P. Spronck, A.-L. Lesage, G. P. P. L. Otten, R. Stuik, V. Van Eylen, H. Van Winckel, D. Pollacco, J. McCormac, F. Grundahl, M. Fredslund Andersen, V. Antoci, and I. A. G Snellen. MASCARA-1 b: A hot Jupiter transiting a bright $m\_V = 8.3$ A-star in a misaligned orbit. *ArXiv e-prints*, July 2017a.

G. J. J. Talens, A. B. Justesen, S. Albrecht, J. McCormac, V. Van Eylen, G. P. P. L. Otten, F. Murgas, E. Palle, D. Pollacco, R. Stuik, J. F. P. Spronck, A.-L. Lesage, F. Grundahl, M. Fredslund Andersen, V. Antoci, and I. A. G. Snellen. MASCARA-2 b: A hot Jupiter transiting a $m\_V = 7.6$ A-star. *ArXiv e-prints*, July 2017b.

G. J. J. Talens, J. F. P. Spronck, A. L. Lesage, G. P. P. L. Otten, R. Stuik, D. Pollacco, and I. A. G. Snellen. The Multi-site All-Sky CAmeRA (MASCARA). Finding transiting exoplanets around bright (m_V < 8) stars. A&A, 601:A11, May 2017c. doi: 10.1051/0004-6361/201630319.

C. J. F. Ter Braak. A Markov Chain Monte Carlo version of the genetic algorithm Differential Evolution: easy Bayesian computing for real parameter spaces. *Statistics and Computing, Volume 16, Issue 3, pp 239-249, 2006*, 16, September 2006. doi: 10.1007/s11222-006-8769-1.

H. Theil. A rank-invariant method of linear and polynomial regression analysis, 3; confidence regions for the parameters of polynomial regression equations. *Indagationes Mathematicae*, 1(2):467–482, January 1950.

J. Titus and W. W. Morgan. On the Classification of the a Stars. I. The Spectral Types of the Brighter Members of the Hyades Cluster. ApJ, 92:256, September 1940. doi: 10.1086/144215.

G. Torres, J. Andersen, and A. Giménez. Accurate masses and radii of normal stars: modern results and applications. A&A Rev., 18:67–126, February 2010. doi: 10.1007/s00159-009-0025-1.

R. G. Tull, P. J. MacQueen, C. Sneden, and D. L. Lambert. The high-resolution cross-dispersed echelle white-pupil spectrometer of the McDonald Observatory 2.7-m telescope. PASP, 107:251–264, March 1995. doi: 10.1086/133548.

L. R. M. Tusnski and A. Valio. Transit Model of Planets with Moon and Ring Systems. ApJ, 743:97, December 2011. doi: 10.1088/0004-637X/743/1/97.

A. V. Tutukov and L. R. Yungelson. Evolutionary Scenario for Close Binary Systems of Low and Moderate Masses. *Nauchnye Informatsii*, 49:3, 1981.

S. van der Walt, S. C. Colbert, and G. Varoquaux. The numpy array: A structure for efficient numerical computation. *Computing in Science Engineering*, 13(2):22–30, March 2011. ISSN 1521-9615. doi: 10.1109/MCSE.2011.37. URL https://ieeexplore.ieee.org/document/5725236.

F. van Leeuwen. Validation of the new Hipparcos reduction. A&A, 474:653–664, November 2007. doi: 10.1051/0004-6361:20078357.

J. L. van Saders and M. H. Pinsonneault. The Sensitivity of Convection Zone Depth to Stellar Abundances: An Absolute Stellar Abundance Scale from Asteroseismology. ApJ, 746:16, February 2012. doi: 10.1088/0004-637X/746/1/16.

A. Vidal-Madjar, A. Lecavelier des Etangs, J.-M. Désert, G. E. Ballester, R. Ferlet, G. Hébrard, and M. Mayor. An extended upper atmosphere around the extrasolar planet HD209458b. Nature, 422:143–146, March 2003. doi: 10.1038/nature01448.

F. M. Walter and S. Bowyer. On the coronae of rapidly rotating stars. I - The relation between rotation and coronal activity in RS CVn systems. ApJ, 245:671–676, April 1981. doi: 10.1086/158842.

R. F. Webbink. Double white dwarfs as progenitors of R Coronae Borealis stars and Type I supernovae. ApJ, 277:355–360, February 1984. doi: 10.1086/161701.

W. F. Welsh, J. A. Orosz, J. A. Carter, D. C. Fabrycky, E. B. Ford, J. J. Lissauer, A. Prša, S. N. Quinn, D. Ragozzine, D. R. Short, G. Torres, J. N. Winn, L. R. Doyle, T. Barclay, N. Batalha, S. Bloemen, E. Brugamyer, L. A. Buchhave, C. Caldwell, D. A. Caldwell,

J. L. Christiansen, D. R. Ciardi, W. D. Cochran, M. Endl, J. J. Fortney, T. N. Gautier, III, R. L. Gilliland, M. R. Haas, J. R. Hall, M. J. Holman, A. W. Howard, S. B. Howell, H. Isaacson, J. M. Jenkins, T. C. Klaus, D. W. Latham, J. Li, G. W. Marcy, T. Mazeh, E. V. Quintana, P. Robertson, A. Shporer, J. H. Steffen, G. Windmiller, D. G. Koch, and W. J. Borucki. Transiting circumbinary planets Kepler-34 b and Kepler-35 b. Nature, 481:475–479, January 2012. doi: 10.1038/nature10768.

J. Whelan and I. Iben, Jr. Binaries and Supernovae of Type I. ApJ, 186:1007–1014, December 1973. doi: 10.1086/152565.

R. A. Windhorst, G. M. van Heerde, and P. Katgert. A deep Westerbork survey of areas with multicolor Mayall 4 M plates. I. The 1412 MHz catalogue, source counts and angular size statistics. A&AS, 58:1–37, Oct 1984.

J. N. Winn. Measuring accurate transit parameters. In F. Pont, D. Sasselov, and M. J. Holman, editors, *Transiting Planets*, volume 253 of *IAU Symposium*, pages 99–109, February 2009. doi: 10.1017/S174392130802629X.

J. N. Winn. *Exoplanet Transits and Occultations*, pages 55–77. University of Arizona Press, December 2010.

J. N. Winn, R. W. Noyes, M. J. Holman, D. Charbonneau, Y. Ohta, A. Taruya, Y. Suto, N. Narita, E. L. Turner, J. A. Johnson, G. W. Marcy, R. P. Butler, and S. S. Vogt. Measurement of Spin-Orbit Alignment in an Extrasolar Planetary System. ApJ, 631:1215–1226, October 2005. doi: 10.1086/432571.

J. N. Winn, M. J. Holman, G. Torres, P. McCullough, C. Johns-Krull, D. W. Latham, A. Shporer, T. Mazeh, E. Garcia-Melendo, C. Foote, G. Esquerdo, and M. Everett. The Transit Light Curve Project. IX. Evidence for a Smaller Radius of the Exoplanet XO-3b. ApJ, 683:1076–1084, August 2008. doi: 10.1086/589737.

J. N. Winn, D. Fabrycky, S. Albrecht, and J. A. Johnson. Hot Stars with Hot Jupiters Have High Obliquities. ApJ, 718:L145–L149, August 2010. doi: 10.1088/2041-8205/718/2/L145.

E. L. Wright, P. R. M. Eisenhardt, A. K. Mainzer, M. E. Ressler, R. M. Cutri, T. Jarrett, J. D. Kirkpatrick, D. Padgett, R. S. McMillan, M. Skrutskie, S. A. Stanford, M. Cohen, R. G. Walker, J. C. Mather, D. Leisawitz, T. N. Gautier, III, I. McLean, D. Benford, C. J. Lonsdale, A. Blain, B. Mendez, W. R. Irace, V. Duval, F. Liu, D. Royer, I. Heinrichsen, J. Howard, M. Shannon, M. Kendall, A. L. Walsh, M. Larsen, J. G. Cardon, S. Schick, M. Schwalm, M. Abid, B. Fabinsky, L. Naes, and C.-W. Tsai. The Wide-field Infrared Survey Explorer (WISE): Mission Description and Initial On-orbit Performance. AJ, 140:1868, December 2010. doi: 10.1088/0004-6256/140/6/1868.

J. T. Wright, O. Fakhouri, G. W. Marcy, E. Han, Y. Feng, J. A. Johnson, A. W. Howard, D. A. Fischer, J. A. Valenti, J. Anderson, and N. Piskunov. The Exoplanet Orbit Database. PASP, 123:412, April 2011. doi: 10.1086/659427.

J. T. Wright, G. W. Marcy, A. W. Howard, J. A. Johnson, T. D. Morton, and D. A. Fischer. The Frequency of Hot Jupiters Orbiting nearby Solar-type Stars. ApJ, 753:160, July 2012. doi: 10.1088/0004-637X/753/2/160.

Y. Wu, N. W. Murray, and J. M. Ramsahai. Hot Jupiters in Binary Star Systems. ApJ, 670: 820–825, November 2007. doi: 10.1086/521996.

N. Zacharias, D. G. Monet, S. E. Levine, S. E. Urban, R. Gaume, and G. L. Wycoff. The Naval Observatory Merged Astrometric Dataset (NOMAD). In *American Astronomical Society Meeting Abstracts*, volume 36 of *Bulletin of the American Astronomical Society*, page 1418, December 2004.

N. Zacharias, C. T. Finch, T. M. Girard, A. Henden, J. L. Bartlett, D. G. Monet, and M. I.

Zacharias. VizieR Online Data Catalog: UCAC4 Catalogue (Zacharias+, 2012). *VizieR Online Data Catalog*, 1322, July 2012.

N. Zacharias, C. T. Finch, T. M. Girard, A. Henden, J. L. Bartlett, D. G. Monet, and M. I. Zacharias. The Fourth US Naval Observatory CCD Astrograph Catalog (UCAC4). AJ, 145:44, February 2013. doi: 10.1088/0004-6256/145/2/44.

W. Zheng, I. Shivvers, A. V. Filippenko, K. Itagaki, K. I. Clubb, O. D. Fox, M. L. Graham, P. L. Kelly, and J. C. Mauerhan. Estimating the First-light Time of the Type Ia Supernova 2014J in M82. ApJ, 783:L24, March 2014. doi: 10.1088/2041-8205/783/1/L24.

G. Zhou, D. W. Latham, A. Bieryla, T. G. Beatty, L. A. Buchhave, G. A. Esquerdo, P. Berlind, and M. L. Calkins. Spin-orbit alignment for KELT-7b and HAT-P-56b via Doppler tomography with TRES. MNRAS, 460:3376–3383, August 2016a. doi: 10.1093/mnras/stw1107.

G. Zhou, J. E. Rodriguez, K. A. Collins, T. Beatty, T. Oberst, T. M. Heintz, K. G. Stassun, D. W. Latham, R. B. Kuhn, A. Bieryla, M. B. Lund, J. Labadie-Bartz, R. J. Siverd, D. J. Stevens, B. S. Gaudi, J. Pepper, L. A. Buchhave, J. Eastman, K. Colón, P. Cargile, D. James, J. Gregorio, P. A. Reed, E. L. N. Jensen, D. H. Cohen, K. K. McLeod, T. G. Tan, R. Zambelli, D. Bayliss, J. Bento, G. A. Esquerdo, P. Berlind, M. L. Calkins, K. Blancato, M. Manner, C. Samulski, C. Stockdale, P. Nelson, D. Stephens, I. Curtis, J. Kielkopf, B. J. Fulton, D. L. DePoy, J. L. Marshall, R. Pogge, A. Gould, M. Trueblood, and P. Trueblood. KELT-17b: A Hot-Jupiter Transiting an A-star in a Misaligned Orbit Detected with Doppler Tomography. AJ, 152:136, November 2016b. doi: 10.3847/0004-6256/152/5/136.

S. Zucker and T. Mazeh. Study of spectroscopic binaries with TODCOR. 1: A new two-dimensional correlation algorithm to derive the radial velocities of the two components. ApJ, 420:806–810, January 1994. doi: 10.1086/173605.

S. Zucker, T. Mazeh, N. C. Santos, S. Udry, and M. Mayor. Multi-order TODCOR: Application to observations taken with the CORALIE echelle spectrograph. I. The system HD 41004. A&A, 404:775–781, June 2003. doi: 10.1051/0004-6361:20030499.